diamond

Diamond-II | Conceptual Design Report

Diamond-II Conceptual Design Report

With contributions from

C. Abraham, L. Alianelli, M. Apollonio, R. Bartolini,
J. Bengtsson, C. Bloomer, L. Bobb, L.C. Chapon,
C. Christou, P. Coll, M.P. Cox, A.J. Dent, S.S. Dhesi,
S. Diaz-Moreno, J. Dymoke-Bradshaw, G. Evans,
R. Doull, R. Fielder, H. Ghasem, D.R. Hall, N.P. Hammond,
A. Harrison, M.T. Heron, J. Hriljac, S.E. Hughes, J. Kay,
V.C. Kempson, X. Liu, S.A. Macdonell, I. Martin,
S.R. Milward, A. Morgan, C.L. Nicklin, T. Olsson,
M. Popkiss, P. Quinn, R. Rambo, G. Rehm, A. Rose,
K.J. Sawhney, S.M. Scott, A. Shahveh, B. Singh, N. Tartoni,
R.P. Walker, M.A. Walsh

Editors

L.C. Chapon, I. Boscaro-Clarke, A.J. Dent, A. Harrison,
M. Launchbury, D.I. Stuart, R.P. Walker

Contents

1. Introduction

The use of synchrotron light to reveal the structure, composition and function of materials from biology to engineering components has been transformed over more than fifty years through the remarkable development of sources of synchrotron radiation. Such light was first produced parasitically at synchrotrons and storage rings designed for high-energy physics and demonstrated excellent research opportunities in its own right. This prompted and justified the development of 2nd generation sources whose primary purpose was to utilise synchrotron radiation. The first of these dedicated to produce X-rays was the Synchrotron Radiation Source (SRS) at Daresbury, which became operational in 1981. The start of operations at the European Synchrotron Radiation Facility (ESRF) in Grenoble in 1994 heralded the advent of 3rd generation sources with much lower emittance and the systematic use of insertion devices to produce an increase in photon brightness of many orders of magnitude.

We are now entering a new era of scientific opportunity with the advent of 4th generation sources, the so-called Diffraction Limited Storage Rings (DLSRs) [1]. This disruptive technology became a reality in 2016 with the start-up of operations of MAX IV, the world's first multibend-achromat (MBA) light source [2]. The progress in accelerator technology and the decrease of the electron horizontal emittance between one and two orders of magnitude, offers the scientific community the opportunity to exploit much brighter photon beams and an increased coherence over a large energy range. The gains are transformative in many areas of science, underpinning the science case for other new facilities such as SIRIUS [3] and HEPS [4], and upgrades of the storage ring at many major, 3rd generation synchrotron facilities including the EBS (Extremely Brilliant Source) upgrade at the ESRF [5], the Photon Source Upgrade, APS-U [6], the Swiss Light Source upgrade SLS 2.0 [7] and many others around the world. It is therefore vital that Diamond also realises such an upgrade in the years to come to remain competitive on the international scene and offer its academic and industrial users the very best opportunities in science enabled by synchrotron radiation.

Diamond has devised a novel implementation of MBA technology, offering not only dramatic gains in brightness and coherence but also additional source points (so-called mid-straight sections in each of the new cells) to install new photon sources based on insertion devices. This will enable the new machine - Diamond-II - to accommodate both high-performance beamlines that are currently based on bending magnets and additional sites for new beamlines, offering greater capacity and flexibility to accommodate new science drivers and communities well into the future. A further design feature, outlined in greater detail below, is an increase in electron beam energy from 3.0 GeV to 3.5 GeV, also driven by the new scientific opportunities provided by the consequential boost in photon flux at higher energies.

1.1. Outline Features of Diamond-II

Brightness is the photon flux per unit area in 4D phase space and per spectral bandwidth and is maximised by either increasing the flux (higher electron current or using a higher ring energy, provided that such a choice is compatible with the photon energy range targeted), or by decreasing the transverse phase space volume. The current vertical emittance of 8 pm at Diamond is state of the art, and most future gains in emittance are to be found in the horizontal direction.

We propose that the Diamond-II lattice will be based on Double Triple Bend Achromats (DTBAs). This "baseline" lattice, based on the 7BA lattice of the ESRF-EBS from which the central dipole has been removed, offers great advantages. It provides a reduction in horizontal emittance by a factor of ~20, with a resulting increase in photon brightness and coherent fraction that is described in greater detail below. In addition, it introduces 24 new "mid-straight" sections that can be used for short (1.5 m) in vacuum insertion devices (Figure 1-1). We will not be able to exploit all of these mid-straights for insertion device (ID) sources, however up to five new beamlines are possible in addition to repositioning beamlines I04-1, I20-EDE and B07-1, and converting any other existing bending magnet beamlines to ID sources (3-pole wigglers or undulators).
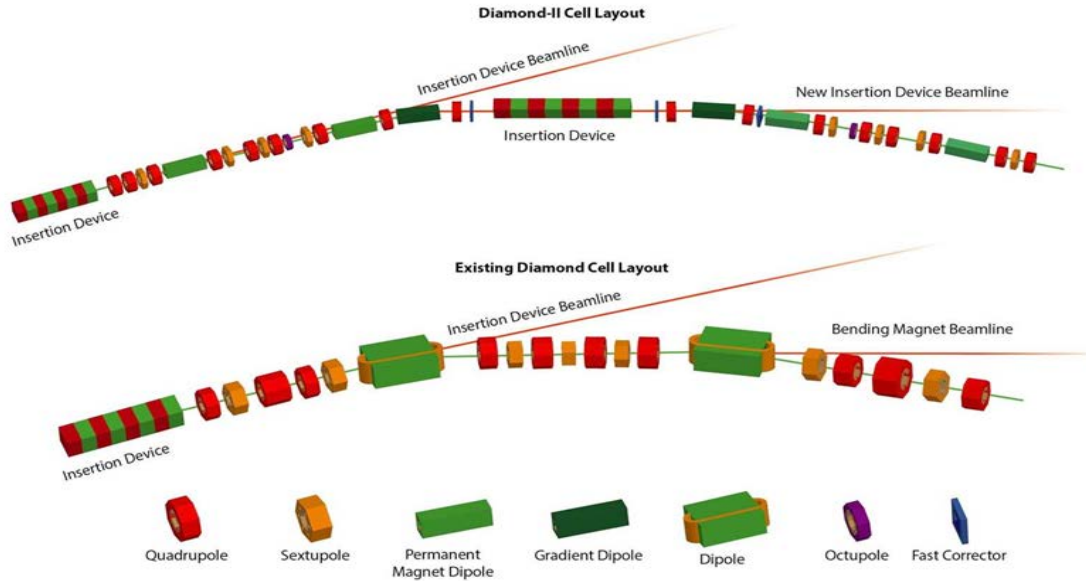
Figure 1-1 : Schematic of the current Diamond DBA (Double Bend Achromat) lattice (bottom), and the proposed design of a DTBA (Double Triple Bend Achromat) lattice for Diamond-II (top).

The brightness and coherent fraction of the photon beams for Diamond-II will be dramatically increased due to the reduction in electron emittance. Most experiments exploit brightness rather than coherence, particularly in the hard X-ray range where spatial filtering is always required, and so another defining feature of Diamond-II is an increase in machine energy to 3.5 GeV. The improved flux output from insertion devices with this ring energy results in a substantial increase in brightness at medium and high energies (Figure 1-2) despite the slight increase in horizontal emittance and reduction of the coherent fraction at low photon energy (Figure 1-3). This choice of ring energy still provides more than a factor of twenty reduction in horizontal emittance compared to the current machine. The photon brightness and coherent fraction are plotted in Figures 1-2 and 1-3 for a set of IDs covering the entire energy range accessible at Diamond. Whilst the coherent fraction decreases for the 3.5 GeV machine with respect to 3.0 GeV, it is marginal compared to the increase in brightness at higher energy (a factor of 4 at 25 keV for the Cryogenic Permanent Magnet Undulator (CPMU) to be installed on I11). Of course, increasing the electron current of the ring from 300 mA to 500 mA instead of increasing the energy was another option considered initially, but will not provide such a gain at the high energy end of the spectrum.
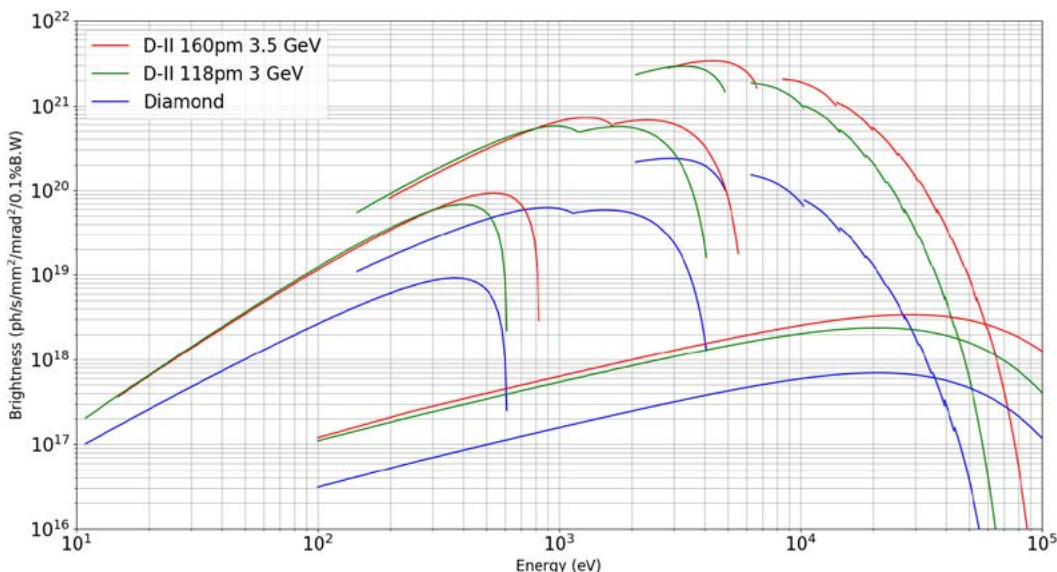
Figure 1-2 : Brightness for a set of selected sources at Diamond (blue curves), Diamond-II at 3 GeV (green curves) and Diamond-II at 3.5 GeV (red curves). In the UV regime, soft X-ray regime and hard X-ray, the brightness curves are shown respectively for the I05, I21, the future CPMU 15.6 mm period (to be installed on I11 and VMXm), and for the superconducting wiggler on I12 (JEEP). All calculations have been made with Spectra 9 using the Wigner function. A phase error of 3° for the undulators has been taken into account analytically.
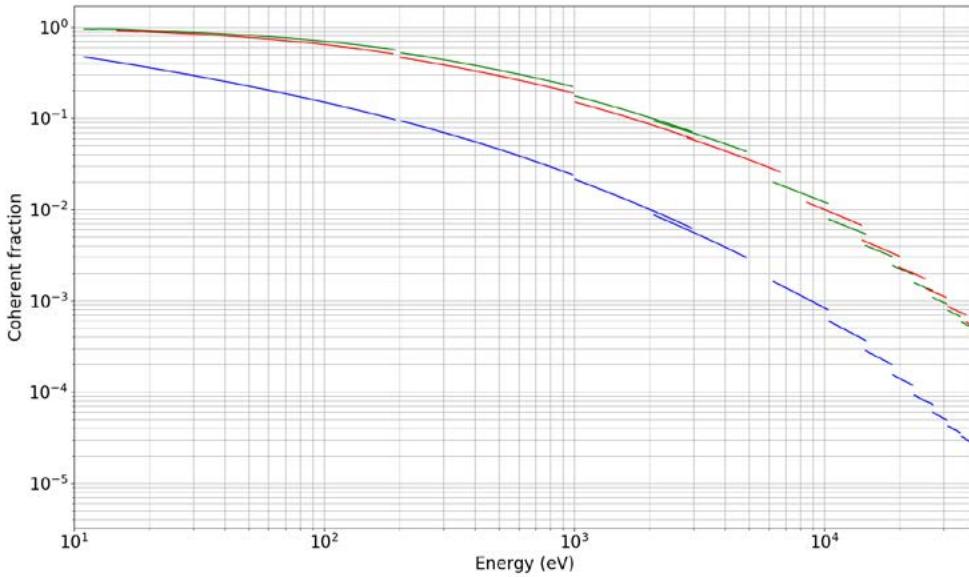
Figure 1-3 : Coherent fraction in the horizontal direction as a function of Energy for Diamond (blue), Diamond-II at 3 GeV (green) and Diamond-II at 3.5 GeV (red). All curves have been produced with Spectra using the Wigner function and approximating the coherent fraction as the ratio between the Brightness and the Brightness calculated in the limit of zero emittance and zero energy spread.

The Diamond-II Science Case contains strong drivers to increase the flux and brightness in the hard X-ray regime, as highlighted by consultations with the user community in recent workshops. The advent of pixelated counters with high-Z materials (GaAs, CdTe) and excellent quantum efficiencies at high X-ray energy allows the very effective exploitation of high flux in this energy range, which finds many applications in imaging, diffraction and spectroscopy. We foresee that, combined with the continuous improvement of short period IDs, the appetite for flux-hungry or brightness limited hard X-ray applications will continue to grow and justify the choice of ring energy. It should be noted that an upgrade to CPMU sources for several beamlines is already a major part of our current capital investment programme for the coming years (2019-2024). This ID upgrade programme will be extended and integrated as part of the Diamond-II project in order to fully exploit the benefit of the low-emittance upgrade and the increased energy of the ring. It is clear (Figure 1-4) that the gain in brightness provided by the proposed lattice at 3.5 GeV energy with 160 pm emittance is more advantageous for a large number of existing beamlines operating at Diamond than that offered by a similar lattice with an improved emittance (118 pm) but operating at 3 GeV. Clearly, the 3 GeV option provides only marginal gains in brightness below 800 eV, and would not be as transformative for high energies as the selected lattice design.
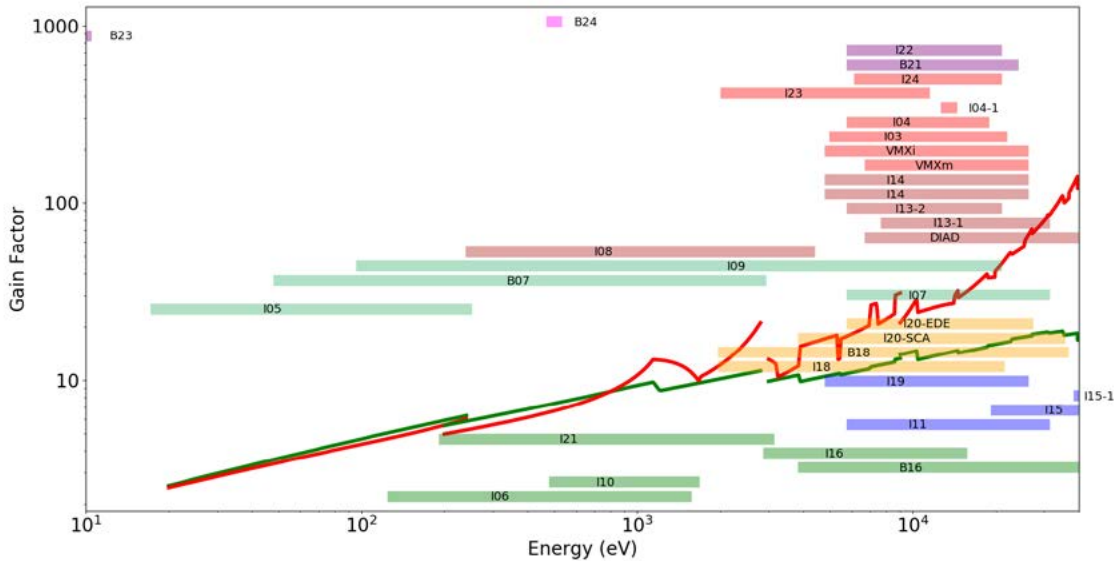
Figure 1-4: Gain in spectral brightness for a set of selected undulator sources for Diamond-II at 3 GeV, 118 pm emittance (green curves) and Diamond-II at 3.5 GeV, 160 pm emittance (red curves). In the UV regime, soft X-ray regime and hard X-ray, the brightness curves are shown respectively for the I05, I21, and the future CPMU 15.6 mm period (to be installed on I11 and VMXm). The photon energy ranges used for all current Diamond beamlines are represented by horizontal bars. Beamlines B22 (IR) and I12 (high-energy engineering) energies are outside of the range of this graph.

1.2. Long-term Upgrade Programme for Diamond

The project to upgrade the Diamond machine – the Diamond-II Machine Project – will offer disruptive new opportunities for science, outlined below and in the more comprehensive Diamond-II Science Case. However, full scientific exploitation of the new machine also requires optimisation of every step in the process from preparation for an experiment, through the X-ray measurement requiring a precise control of the beamline and user-defined parameters, to data management, processing and analysis and ultimately new scientific or technical insights. This larger programme requires complementary and coherent upgrades that include the development of X-ray sources, upgrade of beamlines or the construction of entirely new beamlines, new methods for data handling and computation, provision of sample environments with higher specifications, for example greater stability, and in many cases new sample preparation and delivery methods. It should also be emphasised that an important consideration in modifying an existing facility is minimisation of the disruption to operation of existing beamlines, with regard not only to the overall down-time of the entire facility as the storage ring is replaced, but also the time and cost associated with any necessary relocation of beamlines. The Diamond-II Machine Project should therefore be seen in the context of a much broader, long-term upgrade programme at Diamond that comprises, in addition to the machine upgrade, the following elements:

(i)   Upgrades critical for the continued operation of the existing suite of beamlines (see Table 1-1) on the new machine. For example, beamlines that are currently on bending magnets must move to new IDs, and a number of beamlines on IDs will also require significant engineering work; many beamlines will also need upgraded optics to cope with increased heat-load or change in the source position. There are also a number of other developments that should be considered critical for the exploitation of the enhanced beams provided by the new machine. For example, without significant upgrades to equipment to store, transfer and process data, it will be impossible to handle the step-change in data rates. Developments will also be required in the areas of optics and metrology, in detectors (e.g. integrating detectors), in beam diagnostics, and in sample environments (e.g. far more precise stage positioning and stability). All of these developments taken together constitute the Critical Upgrade Projects outlined in more detail in Chapter 3.

(ii)   Further improvements of beamlines and supporting infrastructure to maximise the benefit of the new machine, including a wider upgrade of IDs, optics and data handling and computation. These are distinct from the critical upgrade projects in that they could in principle enhance performance at any point in the next decade or so and have no particular relation to the machine upgrade, but are essential for many beamlines in order to take advantage of the benefits of Diamond-II. These are all part of the ongoing upgrade programme at Diamond, which started in 2018 and in future will be developed coherently with the machine upgrade and the Critical Upgrade Projects.

(iii)   The new MBA lattice geometry will not only allow us to maintain all existing beamlines, each of which is performing very well, but will also offer space for new IDs that will serve up to 5 additional, new beamlines. We have started the process of developing new concepts for such beamlines, in consultation with the user community, for prioritisation over the next few years.

This document presents the conceptual design for the Diamond-II machine upgrade. However, as changes to the machine have very significant impacts on many beamlines we also include an outline of the complementary upgrades that will be required to ensure that they will be developed too, along with the Critical Upgrade Projects to ensure that Diamond will be able to continue to handle the enhanced beam characteristics of the new machine.

Diamond's beamlines: current operational status April 2019

Beamline Name and Number	Main Techniques	Energy / Wavelength Range
I02-1 - Versatile MX micro (VMXm)	Micro- and nano-focus in vacuum cryo-macromolecular crystallography (VMXm)	7 - 28 keV
I02-2 - Versatile MX *in situ* (VMXi)	*In situ* microfocus macromolecular crystallography, Serial Synchrotron Crystallography	10 - 25 keV
I03 - MX	Macromolecular crystallography (MX), Multiwavelength Anomalous Diffraction (MAD)	5 - 25 keV
I04 - Microfocus MX	MX, MAD	6 - 18 keV
I04-1 - Monochromatic MX	MX, XChem fragment screening	13.53 keV (fixed wavelength)
I05 - ARPES	Angle-Resolved PhotoEmission Spectroscopy (ARPES) and nano-ARPES	18 - 240 eV; 500 eV
I06 - Nanoscience	X-ray Absorption Spectroscopy (XAS), X-ray photoemission microscopy and X-ray magnetic circular and linear dichroism	80eV - 2200eV
I07 - Surface and Interface Diffraction	Surface X-ray diffraction, Grazing Incidence X-ray Diffraction (GIXD), Grazing Incidence Small Angle X-ray Scattering (GISAXS), X-ray Reflectivity (XRR)	6 - 30 keV
B07 - VERSOX: Versatile Soft X-ray	Ambient Pressure XPS and NEXAFS	250 - 2800 eV
	NEXAFS and High-Throughput XPS	50 - 2200 eV
I08 - Scanning X-ray Microscopy	Scanning X-ray microscopy, NEXAFS/ XANES, X-ray fluorescence	I08 branch: 250 eV - 4.4 keV
		J08 - Soft and Tender X-ray Ptychography branch: 250 - 2000 eV
I09 - Atomic and Electronic Structure of Surfaces and Interfaces	XPS (including HAXPES), X-ray Standing Waves (XSW), Near Edge X-ray Absorption Fine Structure (NEXAFS), energy-scanned photoelectron diffraction	Hard X-rays: 2.1 - 18+ keV Soft X-rays: 0.1 - 2.1 keV (currently 0.1 - 1.9 keV)
I10 - BLADE: Beamline for Advanced Dichroism Experiments	Soft X-ray resonant scattering, XAS and X-ray magnetic circular and linear dichroism	Circular: 400-1600eV; Linear Horizontal: 250-1600eV; Linear Vertical: 480-1600eV
I11 - High Resolution Powder Diffraction	X-ray powder diffraction	6 - 25(30) keV (0.5 - 2.1 Å)
DIAD: Dual Imaging and Diffraction	Simultaneous imaging and diffraction	8 - 38 keV
I12 - JEEP: Joint Engineering, Environmental and Processing	Time-resolved imaging and tomography (phase- and attenuation-contrast), time-resolved powder diffraction, single crystal diffraction, diffuse scattering, energy dispersive X-ray diffraction (EDXD), high-energy small angle X-ray scattering (under development)	53 keV - 150 keV monochromatic or continuous white beam
I13 - X-ray Imaging and Coherence	Phase contrast imaging, tomography, full-field microscopy (under commissioning), coherent diffraction and imaging (CXRD,CDI), ptychography and photocorrelation spectroscopy (XPCS) (under commissioning), innovative microscopy and imaging	Imaging branch: 8 - 30keV
		Coherence branch: 7 - 20keV
I14 - Hard X-ray Nanoprobe	Scanning X-ray fluorescence, X-ray spectroscopy, ptychography and transmission diffraction	5 - 23 keV
I15 - Extreme Conditions	Powder diffraction, single crystal diffraction	Monochromatic and focused 20 - 80 keV White beam
I15-1 - XPDF	X-ray Pair Distribution Function (XPDF)	40, 65, and 76 keV
I16 - Materials and Magnetism	Resonant and magnetic single crystal diffraction, fundamental X-ray physics	2.5 - 15 keV
B16 - Test beamline	Diffraction, imaging and tomography, topography, reflectometry	4 - 20 keV monochromatic focused 4 - 45 keV monochromatic unfocused White beam
I18 - Microfocus Spectroscopy	Micro XAS, micro Extended X-ray Absorption Fine Structure (EXAFS), micro fluorescence tomography, micro XRD	2.05 - 20.5 keV
B18 - Core XAS	X-ray Absorption Spectroscopy (XAS)	2.05 - 35 keV
I19 - Small-Molecule Single-Crystal Diffraction	Small-molecule single-crystal diffraction	5 to 25 keV / 0.5 to 2.5 Å
I20 - LOLA: Versatile X-ray Spectroscopy	X-ray Absorption Spectroscopy (XAS), X-ray Emission Spectroscopy (XES) and Energy Dispersive EXAFS (EDE)	Dispersive branch: 6 - 26 keV
		Scanning branch: 4 - 20 keV
I21 - Inelastic X-ray Scattering	Resonant Inelastic X-ray Scattering (RIXS), X-ray Absorption Spectroscopy (XAS)	Currently 250 - 1500 eV (to be upgraded to 250 - 3000 eV)
B21 - High Throughput SAXS	BioSAXS, solution state small angle X-ray scattering	8 - 15 keV (set to 13.1 keV by default)
I22 - Small Angle Scattering and Diffraction	Small angle X-ray scattering and diffraction: SAXS, WAXS, USAXS, GISAXS. Micro-focus.	7 - 20 keV
B22 - MIRIAM: Multimode InfraRed Imaging And Mircrospectroscopy	IR micro- & nano-spectroscopy, IR imaging, THz spectroscopy	nanoFTIR : 4000-900 cm-1 (2.5-11 μm) microFTIR: 10,000-100 cm-1 (1-100 μm) Spectroscopy (FTIR): 10,000-10 cm-1 (1-1000 μm) Imaging (FPA): 10,000-900 cm-1 (1-11 μm)
I23 - Long Wavelength MX	Long wavelength macromolecular crystallography	3 - 8 keV (1.5 - 4.1 Å)
B23 - Circular Dichroism	Circular Dichroism (CD)	125-500 nm & 165-650 nm for CD Imaging at 50 μm resolution, 96-cell High-Throughput CD (HTCD) and High-Pressure CD up to 200 MPa
I24 - Microfocus and Serial MX	Macromolecular crystallography, MAD, Serial Crystallography	6.5 - 25.0 keV
B24 - Cryo Transmission X-ray Microscopy (TXM)	Full field X-ray imaging	200eV - 2600eV

1.3. New Scientific Opportunities

The Diamond-II machine upgrade, combined with essential complementary developments to beamlines, data handling and computational power, will offer important new scientific opportunities in a wide range of science of particular significance to our user community in universities and industry, now and tomorrow. The introduction of new mid-straight sections in the lattice will allow us not only to retain but also greatly enhance the performance of most beamlines that are currently located on bending magnets, as well as providing the possibility of building transformational new beamlines. The step-change in brightness and coherence, particularly at higher energies, will provide orders of magnitude improvement in resolution in time and space for diffraction, imaging and tomography, incorporating spectroscopic (high sensitivity, chemically specific) information. In some cases this will be by enabling completely new types of measurements to be performed, providing new physical insights, or allowing today's heroic or 'proof of principle' experiments to be performed routinely, and make their power accessible to a much larger user community. In other areas, it will allow much higher throughput measurements, accelerating current programmes in macromolecular crystallography, materials discovery and characterisation. And the importance of capacity and breadth of instrumentation should not be overlooked: the UK science community that depends on access to synchrotron radiation is very large and diverse, and served by only one national facility (as opposed to Germany with two major sources) as well as a small share of access to ESRF, especially for complementary work at even higher energies. The very high level of oversubscription by users with very highly rated proposals continues to rise across almost all beamlines and threatens to limit world-class research across mainly areas of science and engineering. Some of the key areas of impact are outlined below, with further details presented in the Diamond-II Science Case.

Integrated structural biology

Macromolecular crystallography (MX) remains essential for understanding the molecular basis of disease and plays an increasingly important role in identifying and developing drugs to prevent, cure or treat those diseases. MX accounts for approximately 50% of all academic and the majority of industrial users. Complementary techniques have grown in strength recently – Cryo-EM has enjoyed a meteoric rise, and MX at XFEL (X-ray Free Electron Laser) facilities is becoming increasingly available. However we expect MX to remain the driving force for smaller proteins, drug discovery, the exploration of milli-second and faster dynamics, and an essential element in understanding the hierarchy of structure and function from the atomic to the cellular. The Diamond-II Machine Project together with other upgrades of infrastructure will enhance or transform all MX beamlines, strengthen integration with imaging, *in vitro* and *in vivo*, including cryo-EM, and through Diamond's XFEL Hub, with XFELs. Enhanced capability at higher energy, complemented with high Z detectors and improved sources, may alter the default energy for MX. Key areas of impact include: much improved throughput in fragment screening on a new dedicated beamline and data collection from micron sized crystals will widen the target landscape; time-resolved MX experiments routinely down to the microsecond range to access the diffusion limit and complement XFEL experiments; and improved capability with seamless transition between MX and ED (electron diffraction). The extreme productivity of MX at Diamond-II will enhance applications in drug discovery, food security and biotech.

Biotechnology and biological systems

Biotechnology embraces the development and exploitation of a vast array of enzymes or biocatalysts in industry and medicine (the disruptive impact of Diamond-II in this field is outlined below under 'chemistry') as well as the rapidly growing field of biomaterials – bio-inspired, bio-mimetic or bio-derived substances. Diamond-II will transform the speed and sensitivity with which the structure and chemical composition of biomaterials may be scanned, over a wider range of length scales, in 3D and with reduced radiation damage using imaging, small-angle scattering and diffraction to track structure and function from tissue through cells to molecules in a single sample. For example, the enhanced flux and coherence of Diamond-II will enable true SAXS tensor tomography to map biomaterials at the sub-micron level, speeding experiments from days to an hour with applications in fields such as bone mechanics where a deeper of understanding of natural properties will help develop new biomaterials for bone repair and replacement, or polymer processing methods for components of longer-lived artificial organs, such as heart valves. Parallel improvements to our IR and CD beamlines will improve length and timescales for measurements to provide a better integrated, seamless suite of complementary techniques.

Health and well-being

Non-communicative diseases, which include cardiovascular disease, cancers, chronic respiratory diseases and diabetes are responsible for 63% of all deaths, including a significant percentage of those who die before they reach 60. Neurodegenerative diseases are also becoming an increasing concern, with about 35% of all human disease burden associated with brain disorders. Infectious diseases continue to present a severe challenge to human health, and to established treatment through antibiotics as resistant strains evolve. Synchrotron radiation techniques provide very powerful tools for imaging structure over many length scales, coupled with dynamic information, and Diamond-II will enable much faster scans with greater resolution, for example to understand the localisation and abundance of trace elements to study the mechanism and treatment for neurodegenerative disorders such as Alzheimer's disease. Diamond-II will also transform the capabilities and insights provided by coherent diffraction imaging and cryo-ptychography, lifting these techniques from 'proof of principle' to routine analysis of tissue, with both a wide field of view (~1 mm) and resolution down to 10's of nm, in combination with light and electron microscopies. As noted above, Diamond-II will also enable a dramatic acceleration of fragment screening, for example, enhancing translation into therapies as new targets for dementia and Alzheimer's are identified, and dissecting in chemical detail the mechanisms of specific cases of antimicrobial resistance (AMR), accelerating drug development as new forms of AMR arise.

Energy

The provision of sufficient energy, cleanly and sustainably, for the planet's needs requires new energy materials and devices. Synchrotron radiation provides the most incisive analytical method to study the structure, properties, manufacture and aging processes of materials critical to the next generation of devices for energy storage (batteries, hydrogen), energy harvesting (photo-catalysts, photovoltaics) and energy utilisation (fuel cells). Enhanced brilliance and flux, particularly at higher energy, will enable much faster *operando* measurements of chemical processes in devices such as batteries and photovoltaic materials on nano- to micrometre scales, elucidating the processes that compromise performance and helping improve manufacture and recycling. In battery research, for example, this includes processes that lead to mechanical (volume change or cracking) and atomistic (vacancies and disorder) failures after many charge-discharge cycles and will be transformative for the science and technology to be developed at the Faraday Institution. Diamond-II will also boost the power of techniques such as coherence diffraction to map stress and strain in materials to provide insights into changes in performance of devices as they are operated over long periods of time; this would be complemented by faster or higher resolution spectroscopies (for example multiplexed RIXS with soft X-rays promising 100 fold increases in data collection rates or a new X-Ray Raman Scattering beamline opening up studies around light elements such as Li which are likely to be critical for years to come) to enable much more sensitive and precise identification of chemical species and electronic character during device operation, again providing insights into how best to optimise performance.

Chemistry: catalysis, materials discovery and formulation

Catalysts – including biocatalysts - are essential to over 90% of processes in the chemical industry and play a crucial role in reducing energy consumption and opening up new chemical feedstocks. Progress will be accelerated through deeper insights into the mechanism of tailored catalytic processes provided by o*perando* 4D multimodal studies of nanoparticle catalysts on practical times scales (minutes not days) with resolution < 10 nm due to orders of magnitude increases in photon flux. Increased photon energy also extends such studies to important classes of catalysts containing the heavier elements Pd, Rh, Ru and Ag, while increased brightness will open up photon-hungry techniques such as valence to core X-ray emission spectroscopy, which could provide unique insights into catalysis and biocatalysis mechanisms involving small molecules of mainly light elements under *operando* conditions. Enhanced coherence will open up unique insights into nanoscale electronic structure and dynamics through ptychographic and XPCS (X-Ray photon correlation spectroscopy) techniques as well as the role of strain in catalyst particles through Bragg-CDI that should be enhanced by 2-3 orders of magnitude with improvements to coherent flux. Higher flux enables high throughput studies of libraries of compounds by diffraction and PDF methods, transforming the process of materials discovery, complemented by computation and modelling (and we could imagine developing a new, dedicated beamline optimised to accelerate such studies, both for the materials themselves and to gain insight into their functionality), for example to find new metal-organic framework compounds whose structure and composition has been optimised for a particular function such as catalysis or gas storage, and then to study the mechanism of such processes – all in a multiparameter space where surveys can only be performed if each point can be measured quickly. Finally, as a further example of activity in this very broad field, drug formulation is becoming a key challenge in the modern pharmaceutical industry, which aims to rapidly process specific cocktails of drugs for bespoke formulations to treat the needs of specific cohorts of patients as part of the drive towards personalised medicine. Diamond-II will enable faster, higher resolution insights into processes – for example crystallisation kinetics - in flow reactors and other elements of the formulation industry.

Quantum materials

Quantum materials – compounds with strong electronic correlations and emergent, co-operative properties that cannot be explained by the properties of individual electrons – offer some of the greatest challenges in fundamental science (e.g. superconductivity, spintronics, topological states of matter) as well as potentially disruptive new technology (e.g. for quantum computing and sensors). Their properties - and in particular the emergent phenomena that are both useful and pose challenges to our fundamental understanding of materials - generally depend on a subtle interplay between electronic, magnetic and structural degrees of freedom, often leading to self-organised structures and excitations spanning nano- and mesoscales. Diamond-II will enable the properties of such materials to be explored in multidimensional phase and parameter space (T,P,H,E) far faster, with an unprecedented range of spatial and temporal resolution including: nanoscale RIXS to trace the origin of emergent phenomena (e.g. superconductivity), perhaps down to <10 meV energy scales inside single domains; nano-ARPES to probe electronic properties in functioning devices; understanding magnetic properties at the nanoscale with unprecedented resolution using coherent diffraction imaging; establishing XPCS as a practical technique for sub-ns studies (e.g. dynamics of nano-domains in skyrmions). Finally, what is arguably the most vibrant and rapidly changing field of condensed matter physics at present is based on atomically-thin 2D materials (for example transition metal dichalcogenides such as WS_2) with novel properties that could provide the basis for electronic and magnetic devices with unique or unrivalled performance. Here ARPES provides an unrivalled means of mapping electronic states at or near the surface and Diamond-II together with beamline developments will offer orders of magnitude improvement in spatial resolution (down to 10 nm) with the ability to discriminate between spin-states with a new generation of spin detector.

Engineering materials and processing

Engineering materials are generally structurally complex, spatially heterogeneous materials whose properties depend on structure over many length scales – e.g. atomic or nanoscale defects produced in manufacturing or through heavy use, often through states far from equilibrium, can induce macroscopic failure in mechanical components. Diamond-II will increase by orders of magnitude the resolution or rate of mapping structural information through the provision of highly efficient project-based nano-tomography and high resolution scanning probe diffraction to bridge the gap between scanning electron microscopy (SEM), with a much wider field of view and additional probe information. CDI and Bragg ptychography techniques will also be greatly enhanced through improvements to the coherent flux and enable them to be applied as practical techniques to survey structure and strain in multivariate systems at sub-nm scales. All of these methods will be applied to a plethora of areas including: characterisation, improvement and validation of advanced manufacturing technologies such as additive manufacturing through *operando* studies; development of new metals and alloys through innovative casting methods, mapping structure, strain and bonding at interfaces; elucidating corrosion mechanisms at surfaces through fast, high-resolution mapping to identify and characterise micron to submicron nucleation sites and develop protective coatings or corrosion resistant materials. In many cases complementary TEM measurements may also be performed in the ePSIC (electron Physical Sciences Imaging Centre) at Diamond.

Earth, environment and planetary science

Minimising the impact that human activity has on our environment requires the most sensitive tools to measure, map and model trace quantities of contaminants in the ground, water and air, as well as their take-up in plants and animals, including humans. Synchrotron X-rays provide the most versatile tools to determine chemical speciation and structure well below the micron scale. The finer, brighter beams of Diamond-II will provide unprecedented sensitivity in structural and chemical analysis using greatly enhanced diffraction measurements (faster or finer real-space resolution) as well as spectroscopy where Diamond-II will provide greatly enhanced brightness at hard and soft X-ray wavelengths, and much smaller probe sizes. Such improved spectroscopy capability will provide access to heavier elements such as Ag and Tc and actinides U, Np, Pu, and Am, and much more sensitive detection limits - <ppb) at 10's of nm. Key applications include: understanding degradation processes and developing new materials for geological depository facilities for nuclear waste; understanding the mechanism and treatment for take-up of toxins in plants to improve food security; monitoring the structure, transport and activity of potentially hazardous nanoparticles in the environment with unprecedented sensitivity and (<5 nm) resolution; understanding better the reactivity and cycling of organic carbon on this planet, between the oceans, the earth and the atmosphere, requiring enhanced resolution and detections limits for this particular element. The greater flux at high energies of Diamond-II will also open up new areas of extreme conditions science, for example the behaviour of planetary interiors, including but not limited to that of our Earth. Here, it is the reduction in sample size through the use of finer, sub-micron beams that is critical, allowing much higher pressures to be applied, often in conjunction with other conditions such as high temperatures through laser heating.

References

[1] M. Eriksson, J.F. Van Der Veen & C. Quitmann, Diffraction-limited storage rings - A window to the science of tomorrow. *J. Synchrotron Radiat*. 21, 837–842 (2014).

[2] https://www.maxiv.lu.se/about-us/.

[3] https://www.lnls.cnpem.br/sirius-en/.

[4] Yi Jiao et al., The HEPS project, *J. Synchrotron Radiat*. **25,** 1611–1618 (2018).

[5] http://www.esrf.eu/Apache_files/Upgrade/ESRF-orange-book.pdf.

[6] https://www.aps.anl.gov/APS-Upgrade.

[7] http://www.lib4ri.ch/archive/nebis/PSI_Berichte_000478272/PSI-Bericht_17-03.pdf.

2. Accelerator and Sources

2.1. Diamond-II Machine Overview

This chapter describes the evolution of the machine design proposed for Diamond-II. Constraints and objectives are presented as they developed in time over the last seven years, so that their rationale acquires a clearer justification. In fact, unlike other upgrade designs, the lowering of the emittance has not been the exclusive guideline for the optimisation of the lattice; other factors such as the increase in the capacity of the ring and increase in the electron beam energy have played a major role in the definition of the final lattice structure. Nevertheless, the Diamond-II lattice still provides a competitive small emittance, given the available circumference in the existing tunnel, compared to other projects worldwide, with the additional bonus of a much larger straight sections to circumference ratio (see Figure 2-1).
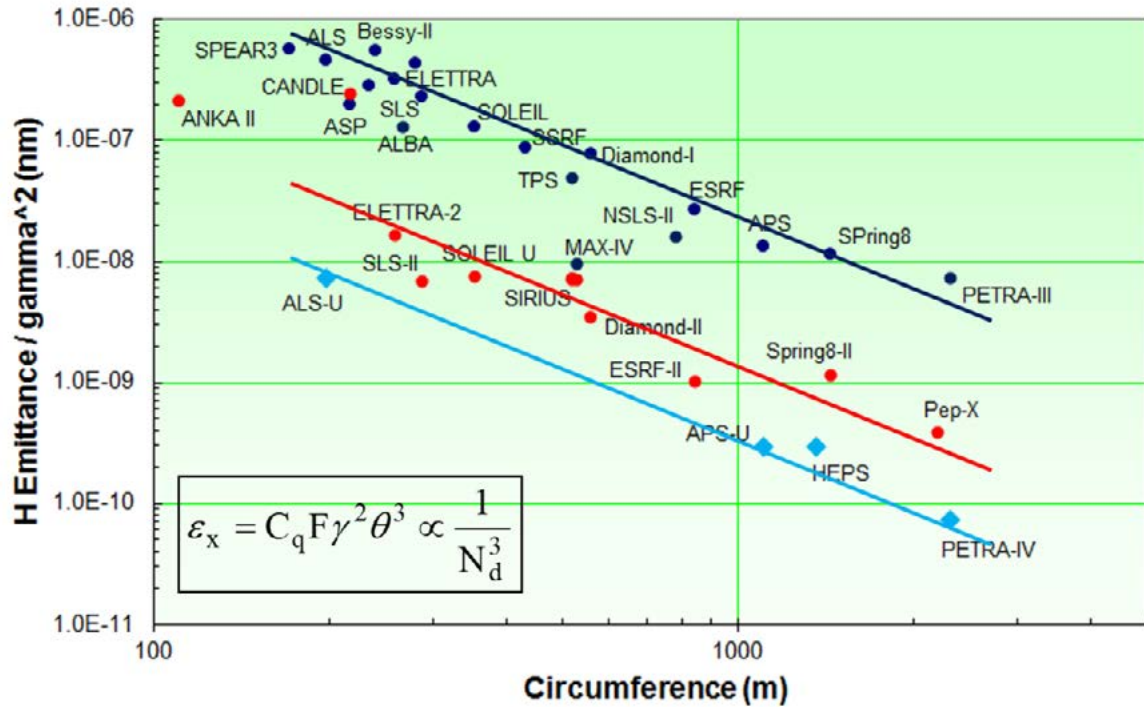
Figure 2-1 : Normalised emittance as a function of circumference: (blue) light sources in operation; (red) new projects with off-axis injection; (cyan) new projects with on-axis injection.

2.1.1. Constraints and Objectives

Diamond started the study of low-emittance lattices for a possible upgrade of the storage ring in 2013 [1]. The initial research was focussed on assessing the relative merit of different versions of the so-called multi-bend-achromat (MBA) lattice. Along the course of this work it transpired that a significant reduction of the emittance over the existing Diamond lattice (2.7 nm rad for the bare lattice) could be achieved with a modified MBA cell that provides an additional straight section in the middle of the arc. This concept was named double-double-bend-achromat (DDBA) and was the initial baseline design for Diamond-II, allowing a 10-fold reduction of the emittance (270 pm) and doubling the number of straight sections (48 straights, corresponding to 45% of the total circumference). Figure 2-2 shows the schematic layout of the DDBA lattice while Figure 2-3 shows the lattice functions of DDBA compared to the original Diamond DBA.

The advantage of the additional straight section in the middle of the arc triggered a project proposal for the actual implementation of one DDBA cell in the existing lattice, replacing one of the DBA cells. This project was delivered in three years 2013-2016 [2]. While the emittance of the ring does not change significantly with the swap of only one cell, a new beamline could be built which has operated successfully since April 2018. The DDBA project also gave the opportunity of gaining R&D experience on strong gradient, small bore aperture magnets, small aperture vacuum pipes and other key subsystems that underpin the design and operation of low emittance lattices.
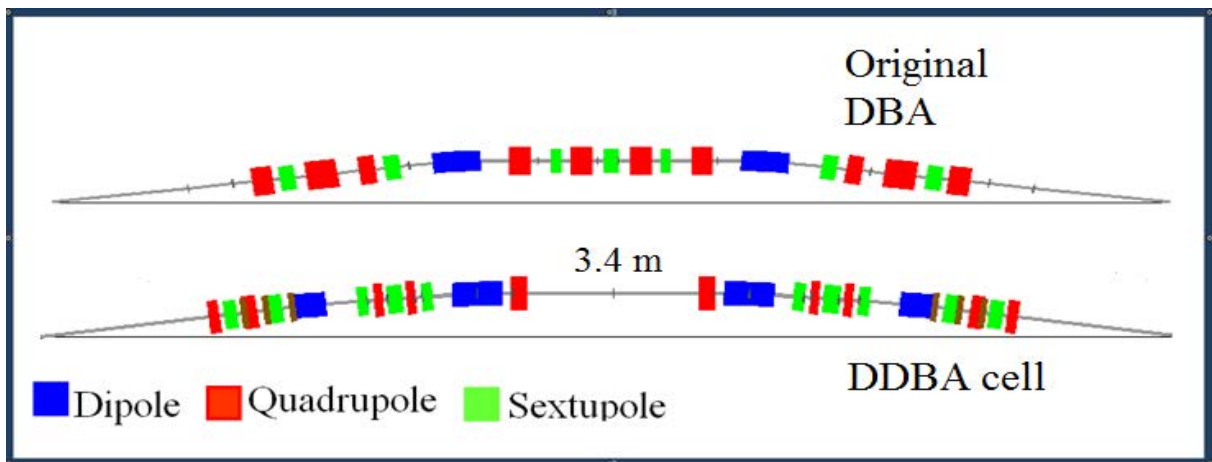
Figure 2-2 : Schematic showing the DDBA cell arrangement compared to the original DBA.
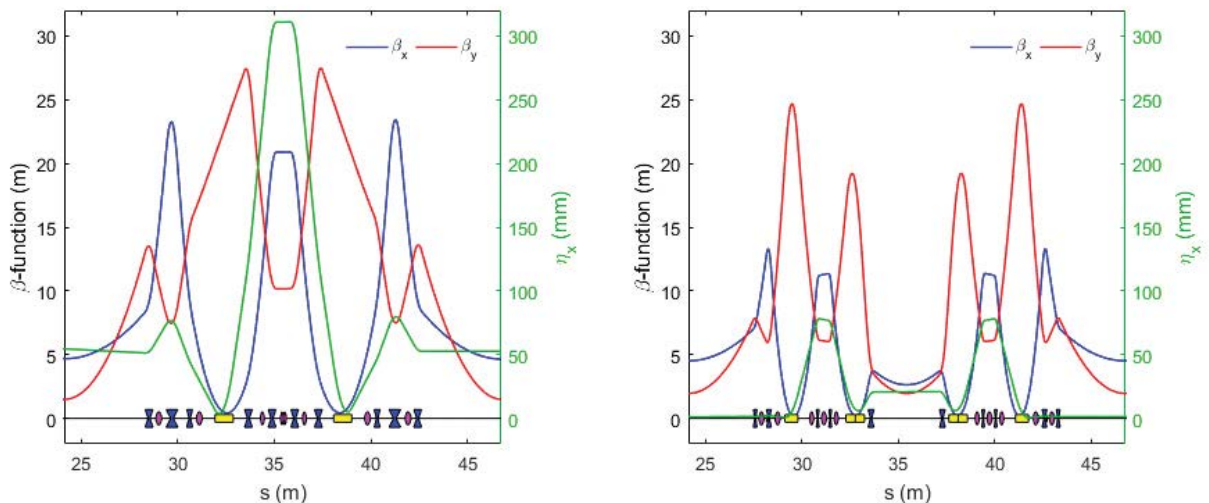
Figure 2-3 : Optics functions of the Diamond DBA cell (left) and DDBA cell (right).

Later on, the concept of a 6BA was explored and following a fruitful collaboration with the ESRF Accelerator Physics team, the so-called Modified Hybrid-Multi-Bend-Achromat (M-HMBA) cell design was proposed [3] and was subsequently promoted to the baseline lattice. The M-HMBA cell merges the concepts of the HMBA cell designed for the ESRF-EBS upgrade [4] based on:

• longitudinal gradient dipoles (DL)
• dispersion bump for chromatic sextupoles and –I sextupole pairing

with the DDBA concept of splitting the arc cell to introduce an additional straight section. The resulting cell is a modification of the 7BA cell of the ESRF-EBS where the middle dipole has been removed to create a mid-straight section and the adjacent gradient dipole magnet (DQ) tuned to control the optics functions. A comparison of the two cells is shown in Figure 2-4. The initial M-H6BA lattice delivered an emittance of 130 pm at 3 GeV. The performance of this lattice in terms of dynamic aperture and momentum aperture is compatible with the implementation of an off-axis injection scheme. In fact, one of the requirements of the baseline design is to maintain top-up injection with an off-axis injection scheme.
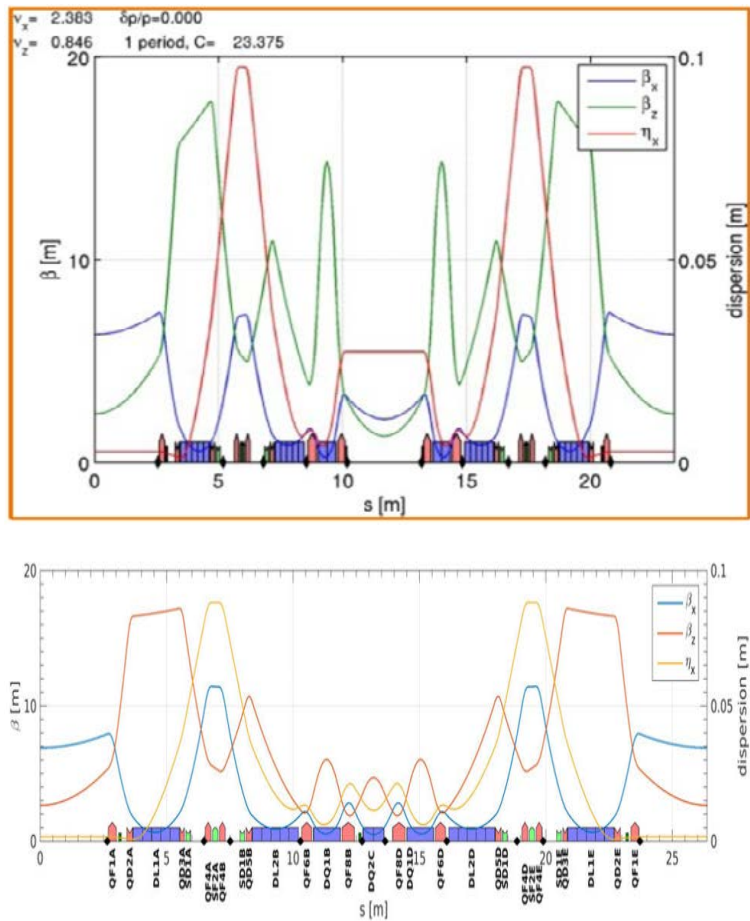
Figure 2-4 : ESRF-EBS cell (lower) and M-H6BA cell (upper).

The rationale for this choice is as follows. Off-energy injection requires a much larger momentum aperture than the current baseline Diamond-II lattice can provide. It also requires the development of very fast kicker magnets and power supplies with less than 2 ns pulse duration. Multi-bunch swap-out injection would require an accumulator ring located in the Diamond ring tunnel so that beams can be interchanged between the two rings, which is not feasible from an engineering point of view. It would also lead to significant intensity jumps (~ 10%) which would disturb certain beamlines, e.g. if performing continuous scanning, when part of the low emittance beam is replaced with a beam with much increased emittance. Single-bunch swap-out wouldn't require an accumulator and would have less impact on beamlines because of the large number of bunches, and so might be acceptable. Like off-energy injection however, it does require fast kicker magnets and power supplies able to produce the required strength with less than 4 ns pulse duration.

The primary advantage of swap-out injection is that it allows the lattice to be optimised for smaller dynamic aperture and thereby achieve a lower emittance. Studies show however that the possible further reduction in emittance is a relatively small factor compared to the gain of the proposed Diamond-II lattice over the current Diamond machine. As regards other quoted advantages of swap-out injection, the fact that it permits full-coupling while maintaining small insertion device gaps is not relevant in our case as small vertical beam sizes are preferred. Another advantage, that of permitting small round insertion device vacuum vessels, is not entirely exclusive to swap-out. The proposed injection scheme results in a small residual oscillation of the injected beam, 2.5 mm in the standard straights and 1.5 mm in the mid-straights, which does not preclude small circular ID vessels. In summary, the baseline design is based on a conventional injection scheme using improved, but existing technology, which we believe is therefore lower risk. We will however explore alternatives further during the TDR (Technical Design Report) phase.

The inclusion of mid-straights is clearly a major decision, as it is a severe constraint on the optics design and leads to a higher emittance than would otherwise be achievable, however there are strong reasons for including them:

1. it allows the new beamline VMXm (K02) created through the DDBA project [2] to be retained, otherwise it would be lost.

2. it allows beamlines I04-1 and I20-2, based on short IDs which follow the main IDs in a standard straight, to be re-located to new positions in the Experimental Hall, and fed by new more powerful IDs in mid-straights, otherwise they would either be lost, due to the shorter straight sections in Diamond-II, or, if the straight sections had to be long enough to keep them, this would then limit the emittance reduction that could be obtained.

3. the latest Diamond beamline, DIAD (K11) created through the "missing sextupole" scheme [5] has a short 10-pole wiggler as its source, which limits its capabilities. The use of a mid-straight undulator would be a major gain.

4. several bending magnet beamlines can convert to more powerful insertion devices as the radiation source.

5. up to 5 additional new insertion device beamlines can be created using mid-straights and available space on the experimental hall floor.

In summary, the 24 new mid-straights will be utilised as follows:

- 6 bending magnet beamlines will be modified to operate with a three-pole wiggler or insertion device source located in the nearby mid-straights (K07, K16, K18, K21, K22, K23).

- 1 bending magnet experimental station (B07-1) will be re-located on a new beamline using an insertion device source in the mid-straight (K08).

- 2 insertion device beamlines (I04-1, I20-2) will be relocated on new beamlines using insertion devices in mid straights (K04, K14).

- 2 insertion device beamlines currently using mid-straights (K02, K11) will remain (with modifications).

- 2 mid-straights will be used for RF cavities.

- 5 mid-straights will be available for future new beamlines.

Thus, of the 24 mid-straights, we foresee that eventually only 6 will not be utilised.

Further internal discussions led to a proposal to increase the energy of Diamond-II to 3.5 GeV in order to enhance the radiation brightness at medium and high photon energies. The strategy to incorporate mid-straights and increase the energy of the machine was later endorsed by our Science Advisory Committee in May 2018 and our Industrial Science Committee in October 2018.

One of the major constraints of the lattice design was not to reduce too much the space available for the straight sections, because this would have a direct impact on the length of the undulators. Of the six long straights, I09 and I13 pose particular problems since they both have two undulators at offset angles produced by three-magnet chicanes. In addition, a quadrupole doublet at the centre of the straight produces two minima in the vertical beta function at the position of the IDs ("double mini-beta" [6]). This cannot be accommodated in Diamond-II and so the decision was taken to eliminate the double mini-beta, move the IDs and chicane magnets as close together as possible, keeping the same angles. The 24 standard straights also had to be reduced in length, the limit being set by still being able to accommodate at least a 3.5 m long APPLE device in straights I06, I08 and I10. In the case of the new mid-straights it proved impossible to keep the same length as that installed through the DDBA project, which can accommodate a 2 m long in-vacuum undulator, instead the limit was set by being able to install a 1.5 m long device in these straights. Table 2-1 summarises the straight section lengths in Diamond and Diamond-II.

Table 2-1 : Length of the straight sections from quadrupole-to-quadrupole (hard edge model) in Diamond and Diamond-II.

Straight Section	Diamond	Diamond-II
long straight sections (LSS)	11.3 m	7.54 m
standard straight sections (SSS)	8.3 m	5.19 m
mid-straight sections (MSS)	3.4 m (DDBA)	2.92 m

Another important factor emerged during the early stages of the engineering integration of the lattice, namely that wherever possible the source points and angle of the existing beamlines should remain the same in Diamond-II in order to minimise the disruption to beamlines and hence the overall length of the shutdown period. This was achieved by fine tuning the three straight section lengths.

The Diamond-II lattice has therefore been designed with the lowest possible emittance with the constraints of:

- doubling the number of straight sections by including a mid-straight at the centre of each cell
- increasing the energy to 3.5 GeV
- maintaining certain minimum straight section lengths
- making minimal changes in position and angle of source points
- preserving off-axis injection with top-up.

The resulting lattice, described in detail in Section 2.3, is a modified hybrid 6BA (M-H6BA) which delivers a natural emittance of 160 pm at 3.5 GeV, 17 times lower than that of the current machine (2.7 nm rad), comparing the bare lattices, but more than a factor of 20 when IDs are taken into consideration.

2.1.2. Other Main Design Decisions

The machine design described in this Conceptual Design Report hinges on a number of other significant design decisions:

- vacuum vessel apertures are such that they exceed the dynamic aperture, are small enough to allow the required magnetic fields to be realised, but no smaller than necessary in order to limit the effects of Resistive Wall impedance. This has resulted in a circular vessel, 20 mm internal diameter, and quadrupoles and sextupoles with an inscribed diameter of 24 mm.
- vacuum vessels of this size have very limited conductance and so to achieve the required vacuum pressures the vessels will be NEG coated.
- we have chosen to include in-situ bakeout in the design to allow faster recovery in case of vacuum incidents.
- magnets and vessels will be installed on two 7 m long girders per cell. This minimises handling operations and also minimises the sensitivity to girder alignment errors.
- after a careful analysis we have selected 500 MHz as the RF frequency; this also enables us to meet a user requirement to provide bunches of less than 100 ps FWHM time duration in hybrid mode.
- it has been agreed that there is no requirement for regularly-spaced filling patterns, which has allowed the closest match to the existing rf frequency to be achieved with a harmonic number of 934.
- the precise value of RF frequency precludes use of the existing superconducting cavities, however, we had already taken the decision to base the RF system on normal conducting cavities, powered by separate solid-state amplifiers for greater reliability and resilience.
- in order to reduce emittance growth due to Intra-Beam Scattering, reduce RF heating, improve beam lifetime and help combat instabilities, a superconducting 3rd harmonic cavity is part of the baseline design.
- the "anti-septum" injection scheme will be used for injection into the limited dynamic aperture of the new lattice.
- a new booster is required with smaller emittance and shorter bunch length to allow efficient injection into Diamond-II.

References

[1] R. Bartolini et al., Proc. IPAC 2013, Shanghai, China, MOPEA067, p. 237.

[2] R. Bartolini et al., Phys. Rev. Accel. Beams **21**, 050701 (2018).

[3] A. Alekou et al., Proc. IPAC 2016, Busan, Korea, WEPOW044, p. 2940.

[4] P. Raimondi, Proc. IPAC 2016, Busan, Korea, WEXA01, p. 2023.

[5] B. Singh et al., Proc. IPAC 2016, Busan, Korea, THPMR050, p. 3518.

[6] B. Singh et al., Proc. IPAC 2011, San Sebastian, Spain, WEPC042, p. 2103.

2.2. Photon Sources

2.2.1. Insertion Devices

As a third generation synchrotron light source, Diamond was designed from the outset to accommodate insertion devices (IDs) as the principal X-ray sources. As it has matured the complement of IDs has grown to fill all of the available accelerator straight sections. Table 2-2 lists the IDs that will be required in Diamond-II. IDs highlighted in green indicate upgrades to existing IDs planned for completion before Diamond-II. IDs highlighted in red will be replaced for Diamond-II. Those in yellow represent desired upgrades to IDs to gain full benefit from Diamond-II. All other devices are existing ones that will be re-used on Diamond-II. Parameters of all new devices are preliminary and will be refined during the TDR phase.

Current IDs located in standard or long straight sections are prefixed by the letter I, whereas the devices that will be installed in the new mid-straight sections are prefixed by K. There are two devices currently installed in these locations, K02 in the mid-straight created by the DDBA project, and K11, a short multipole wiggler which occupies the space created by removing a sextupole magnet.

The seven current bending magnet (BM) beamlines (one with two end stations, B07-1 and B07-2) will move either to three-pole wigglers (K18, K22, K23), insertion devices (K07, K08, K16, K21) or a DQ bending magnet (B24) in Diamond-II; further details of the three-pole wigglers and the bending magnet source are given in Section 2.2.2.

2.2.1.1. Modifications to Existing IDs

Standard straight sections in Diamond-II are 3.1 m shorter than in Diamond, and hence the APPLE IDs currently in straights I06, I08 and I10 can no longer be accommodated and new devices will have to be designed and built. A standard straight is, however, long enough for existing in-vacuum IDs and the two superconducting wigglers (SCWs). Long straight sections are also shorter, but will still accommodate the 5 m APPLE-II devices in straights I05 and I21, as well as the twin devices in I09 and I13. New mid straights are 0.5 m shorter than the mid-straight introduced recently through the DDBA project, and hence the in-vacuum ID in K02 will also have to be replaced.

Existing in-vacuum IDs, that don't have to change for Diamond-II, will remain in the storage ring when Diamond is turned off for upgrade to Diamond-II and may not require modification. It is possible however that changes may need to be made to the taper transitions inside the ends of in-vacuum IDs to accommodate the change in beam aperture between Diamond and Diamond-II. These modifications will be defined during the TDR phase.

We intend to operate in-vacuum IDs in Diamond-II down to a minimum 4 mm gap, thus compensating for increased photon energies resulting from the higher electron beam energy and so allowing existing low photon energy limits to be reached. The most recent IDs with "black" support structures designed and built at Diamond can be operated at 4 mm and it is likely that older "purple" structure IDs can also be closed to 4 mm but analysis and testing with IDs removed for upgrade will provide confirmation during the detailed design phase. Once feasibility of 4 mm gap operation is confirmed the only modifications required are to set limit switches and hard-stops to the appropriate gap and to change the control system software limits.

Table 2-2 : Insertion Devices required in Diamond-II. Parameters of new devices are preliminary. (H)PMU: (hybrid) permanent magnet undulator, CPMU: cryogenic permanent magnet undulator, MPW: multipole wiggler, SCU: superconducting undulator, SCW: superconducting wiggler, 3PW: three-pole wiggler. Total power is for 300 mA.

ID	Type	Period (mm)	N	L (m)	Gap (mm)	B (T)	K	Emin1 (keV)	Emin3 (keV)	Diamond-II energy range (keV)	Ptot (kW)
I02 (VMXi)	CPMU	17.6	113	2.0	4.0	1.36	2.24	1.9	5.6	5-30	8.6
K02 (VMXm)	CPMU	17.6	85	1.5	4.0	1.36	2.24	1.9	5.7	5-30	6.4
I03	CPMU	17.6	113	2.0	4.0	1.36	2.24	1.9	5.6	5-30	8.6
I04	CPMU	17.6	113	2.0	4.0	1.32	2.17	2.0	5.9	6-30	8.1
K04 (I04-1)	HPMU	19.7	76	1.5	4.0	1.22	2.24	1.7	5.1	10-25	5.2
I05	APPLE-II	192.0	26	5.0	-	0.45	8.07	0.018	0.054	0.018-0.24	2.4
I06	APPLE-II	56.0	62	3.5	12.5	0.73	3.82	0.25	0.750	0.25-2.1	4.3
I07	CPMU	17.7	113	2.0	4.6	1.04	1.72	2.6	7.9	8-35	5.0
K07 (B07-2)	APPLE-II									0.05-2.2	
I08	APPLE-II	56.0	62	3.5	12.5	0.73	3.82	0.25	0.75	0.25-4.2	4.3
K08 (B07-1)	(H)PMU									0.25-5	
I09-1	HPMU	25.3	79	2.0	6.4	1.06	2.50	1.1	3.3	2.1-18	5.2
I09-2	APPLE-II	60.0	40	2.4	10.6	1.08	6.07	0.1	0.3	0.1-2	6.5
I10	APPLE-II	48.0	73	3.5	13.2	0.93	4.19	0.25	0.75	0.25-1.6	7.1
I11	SCU/CPMU	15.6	128	2.0	4.0	1.20	1.75	2.9	8.8	9-35	6.7
K11 (DIAD)	CPMU	16.5	90	1.5	4.0	1.30	2.00	2.3	7.0	7-38	5.8
I12	SCW	48.0	23	1.1	-	4.20	18.83			53-150	45.5
I13-1	HPMU	22.6	119	2.7	6.4	0.97	2.04	1.7	5.0	5-25	5.9
I13-2	CPMU	20.0	100	2.0	6.4	1.04	1.94	2.0	6.0	6-38	5.0
I14	CPMU	17.6	113	2.0	4.0	1.36	2.24	1.9	5.6	5-25	8.6
K14 (I20-2)	MPW	83.0	9	0.7	15.0	1.30	10.08			6-26	2.8
I15	SCW	60.0	23	1.4	-	3.50	19.61			20-80	39.5
I16	PMU	27.0	72	1.9	5.0	1.00	2.52	1.0	3.1	2.5-15	4.5
K16	CPMU	17.3	86	1.5	4.0	1.35	2.18	2.0	6.0	6-45	6.3
I18	HPMU	19.5	102	2.0	4.0	1.21	2.20	1.7	5.2	2-27	6.8
I19	HPMU	18.7	106	2.0	4.0	1.17	2.05	2.0	6.0	6-30	6.4
I20-1	MPW	83.0	24	2.0	11.0	1.92	14.88			4-34	17.1
I21	APPLE-II	56.0	89	5.0	17.6	0.7	3.83	0.2	0.7	0.25-3	6.2
K21	HPMU	18.7	80	1.5	4.0	1.17	2.05	2.0	6.0	6-14.5	4.8
I22	HPMU	18.7	106	2.0	4.0	1.17	2.05	2.0	6.0	6-30	6.4
I23	PMU	27.0	74	2.0	5.0	1.00	2.52	1.0	3.1	2-11	4.6
I24	CPMU	17.6	113	2.0	4.0	1.36	2.24	1.9	5.6	5-30	8.6

Key:							
	Existing ID		Approved upgrade before Diamond-II		Desired new ID for Diamond-II		Essential new ID for Diamond-II

2.2.1.2. New IDs

I02 (VMXi)

The current 2 m long U23 permanent magnet in-vacuum undulator is compatible with Diamond-II, however an upgrade is desired, provisionally a CPMU with 17.6 mm period as planned for the other MX beamlines (I03, I04, I24).

K02 (VMXm)

The current 2 m long U21 permanent magnet in-vacuum undulator in the mid-straight created by DDBA will be replaced by a 1.5 m CPMU for Diamond-II, provisionally with 17.6 mm period.

K04

The current 30.8 mm period short ex-vacuum undulator (I04-1) will be replaced with a 1.5 m 19.7 mm period in-vacuum hybrid undulator, possibly before Diamond-II as part of the ID upgrade programme.

I05

Presently I05 is an APPLE-II ex-vacuum undulator with a quasi-periodic magnet arrangement to reduce higher order contamination. An increase in ID period is likely to be needed for Diamond-II to preserve the beamline energy range down to the current minimum of 18 eV. For example, increasing the period from 140mm to 192mm allows the low energy limit to be preserved without increasing the total power density from the ID over that in Diamond. This would be at the cost of reduced flux with respect to Diamond although still with an increase in brightness.

Another option being studied is an APPLE-II Knot device [1] which offers the advantage of reduced beam power to front end and beamline optics and reduced higher harmonic contamination.

I06

A new ID (or IDs) is required as the length of the straight is shorter than before. A design will be developed during the TDR phase, for example a period of 56 mm, with 0.73 T field, offers the same total power density as the current ID in Diamond with a minimum photon energy of 250 eV. Options will be studied for fast polarisation switching.

K07

The current bending magnet source B07-2 will be replaced by an APPLE-II, with magnetic length up to 1.8 m and period optimised for the required energy range during the TDR phase.

I08

As for I06, a new ID suitable for a shorter straight will be designed during the TDR phase.

K08

The bending magnet source B07-1 will be replaced by a PMU, possibly a hybrid design, with 1.5 m magnetic length and period optimised for the required energy range during the TDR phase.

I09-1

The current in-vacuum ID will be replaced by a hybrid undulator with a provisional 25.3 mm period.

I10

The current two APPLE-II HU48 IDs will be replaced by a single 3.5m APPLE-II without the five fast polarisation switching magnets that are currently installed. It is likely the new ID will have a longer period to preserve the low photon energy limit.

K11 (DIAD)

The current fixed gap MPW will provisionally be replaced by a 1.5 m long CPMU with a 16.5 mm period.

I13-1

The existing in-vacuum PMU will cover the required photon energy range in Diamond-II, however an increased flux is requested from a device optimised for the expected minimum gap of 6.4 mm, provisionally a hybrid device with 22.6 mm period.

I13-2

The existing in-vacuum PMU will not cover the required photon energy range in Diamond-II, and will be replaced by a device optimised for the expected minimum gap of 6.4 mm, provisionally a CPMU with 20 mm period.

K14

The current I20-2 (EDE) side-station will be re-built in a new beamline wedge at K14, initially using the same insertion device as at present.

K16

The B16 bending magnet source will be replaced by a 1.5 long CPMU, provisionally with 17.3 mm period.

I18

The current ID, a U27 in-vacuum PMU, could provide photons over the required range in Diamond-II however an upgrade is needed at some stage in order to be able to meet the scientific requirements.

I21

For I21 the minimum energy range can be recovered by a modest reduction in ID gap from 20 mm in Diamond to 17 mm in Diamond-II so the ID would not have to be changed. I21 will therefore only need to be replaced if a APPLE Knot ID is considered the best option for reducing heat loads and higher harmonic contamination.

K21

The B21 bending magnet source will be replaced by a 1.5 long HPMU, provisionally with 18.7 mm period.

2.2.2. Thee-Pole Wiggler and Bending Magnet Sources

Four beamlines initially requested a study of a three-pole wiggler to replace the current bending magnet source. The required energy ranges and angular acceptances are listed in Table 2-3.

Table 2-3 : Energy ranges and acceptances for the present Diamond BM beamlines and the Diamond-II 3PW sources located in the new mid-straights.

Beamline	Energy range		Acceptance (mrad²)	
	Diamond	Diamond-II	Diamond	Diamond-II
B18	2-35 keV		2.7 x 0.165	
B22	1 meV-1 eV		50x30	40x30
B23	1-10 eV		20x8	10x8
B24	0.2-2.6 keV	0.3-4.5 keV	2x2	

In the following paragraphs we examine each beamline with its specific requests. The change towards a source inserted in the mid-straight is reflected in the naming convention, where a 'B' bending magnet beamline becomes a 'K' mid-straight ID beamline.

The initial standard concept of a three-pole wiggler has evolved to be a sequence of a steerer-radiator-steerer poles (S-R-S) where the 'R' pole is typically the main element used to produce the useful radiation for the downstream line.

Figure 2-5 illustrates the wide variety of energy ranges for the beamlines discussed in this Section.
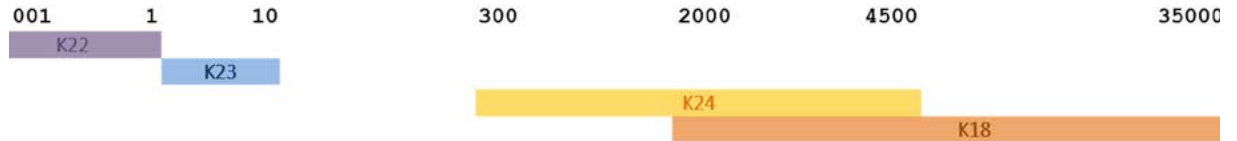
Figure 2-5 : Energy range for the four BM beamlines considering adopting a 3PW as a radiation source.

All of the calculations for the SR generated by the new sources have been carried out using SRW [2]. This code allows utilising an arbitrary source by defining a magnetic $B_y(s)$ field as a function of its longitudinal position. Radiation is initially propagated to the front-end of the beamline after which the wave-front can be followed through an arbitrary optical system.

The new devices will be located in the mid-straight region where there is an available length of 2.5m. One important aspect that emerged in this study is the effect of the dipoles located in the downstream/upstream regions of the cell, at about ±2.4m from the centre of the straight. Figure 2-6 highlights the positions of the 'DQ' gradient dipoles (purple) whose radiation can fall within the horizontal acceptance of the proposed beamlines.

In the following paragraphs we will illustrate the effects of these spurious sources.
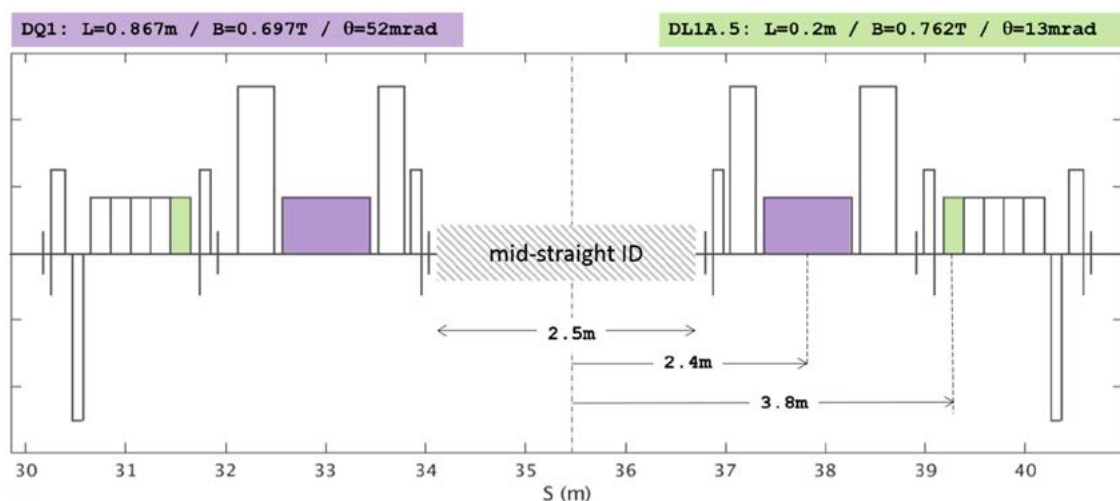
Figure 2-6 : View of the M-H6BA standard cell around the mid-straight region where the new devices will be located. The hatched grey box in the centre defines the 2.5m clearance where the new 3PWs can be located. Highlighted in purple, at ± 2.4m from the mid-point of the straight, are the DQ gradient dipoles with a field of 0.7T.

2.2.2.1. Beamline K18

This beamline is characterised by a relatively large energy span (2 to 35 keV) where as smooth as possible flux should be produced within an acceptance of 2.68 x 0.165 mrad². SR reaches a double slit at 18.5 m, each aperture accepting 1.12 mrad horizontally, see Figure 2-7.

Several configurations of 3PW devices were simulated with SRW, concluding that an effective way to minimise the interference between the S-poles and the central radiator consists in lowering the field of the steerers, hence reducing their critical energy.
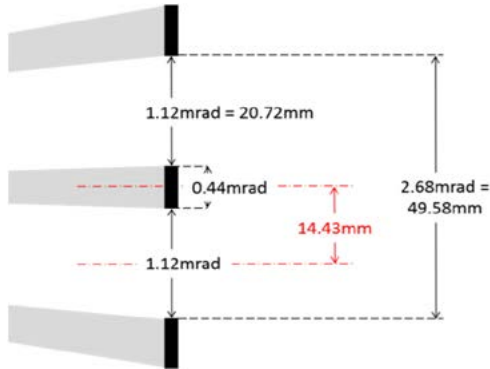
Figure 2-7 : Double slit opening for K18 for light collected at 18.5 m from the centre of the source.

Figure 2-8 shows fluxes at large statistics of 100K/1M macro-electrons (to avoid computational artefacts) for three different configurations of the device. When reducing the B_y field of the steerers the left peak moves towards smaller energies, considerably mitigating the interference between the S and R poles. This has driven our choice towards a device with long and weak S poles (78 cm x 0.04 T) while keeping the radiator at around 1.45 T, which is the field for the present BM at Diamond. As seen in Figure 2-8 for the case SRS-1 (blue curve), this choice substantially decouples the effects of the S and R poles, mimicking the behaviour of a plain dipole (red curve) for energies larger than 2keV.
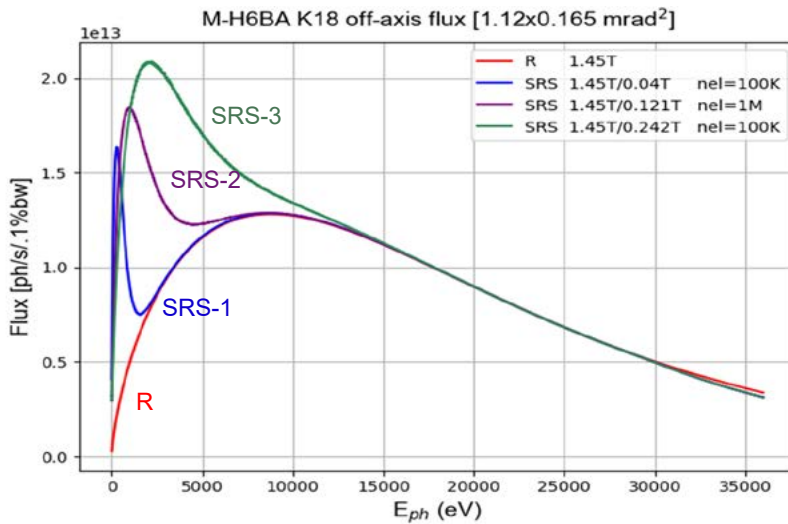
Figure 2-8 : Flux through one of the slits shown in Fig. 2, for different 3PW models. (SRS-1: blue) 3PW with 0.04T long S-poles, (SRS-2: purple) 0.121T S-poles, (SRS-3: green) 0.242T S-poles. The red curve (R) represents a 1.45T dipole.

The main parameters of the chosen device are summarised in Table 2-4. B_y field, trajectory and angle of the electron beam as a function of the longitudinal coordinate s are shown in Figure 2-9.

Table 2-4 : Main parameters of the 3PW considered for K18 (case SRS-1 in Figure 2-8).

	R-pole	S-pole
Peak-field (T)	-1.45	+0.04
pole-width (cm)	4.3	78
pole-position (cm)	0	86
R-S drift (cm)	44.85	
Length (cm)	250	
R-θ (mrad)	5.2	
E_{crit} (keV)	11.844	0.326
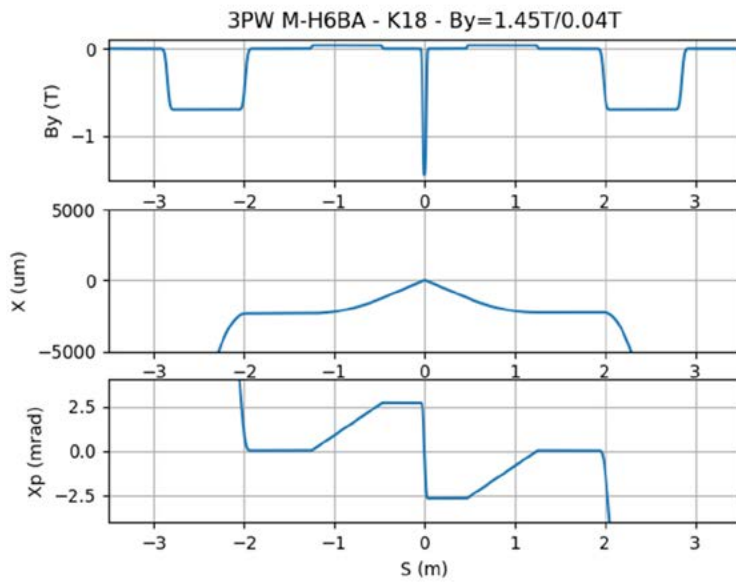
Figure 2-9 : Field (top), electron trajectory (middle) and angle (bottom) of the proposed 3PW for K18. The DQ dipoles are visible at ± 2.4 m.

Intensities at the slit plane computed for the two ends of the energy spectrum (2-35 keV) are shown in Figure 2-10.

Figure 2-11 shows the power density on a surface located at 18.5 m and orthogonal to the photon beam direction for both the sum of the plain source and the DQ gradient dipoles (A) and for the 3PW device alone (B). For the former case we observe the effect of the DQ dipoles entering the central region from the left/right sides and incrementing the power density by about 60%. The total emitted power for this device is 348 W.

$E_{ph} = 2$ keV   **$E_{ph} = 35$ keV**
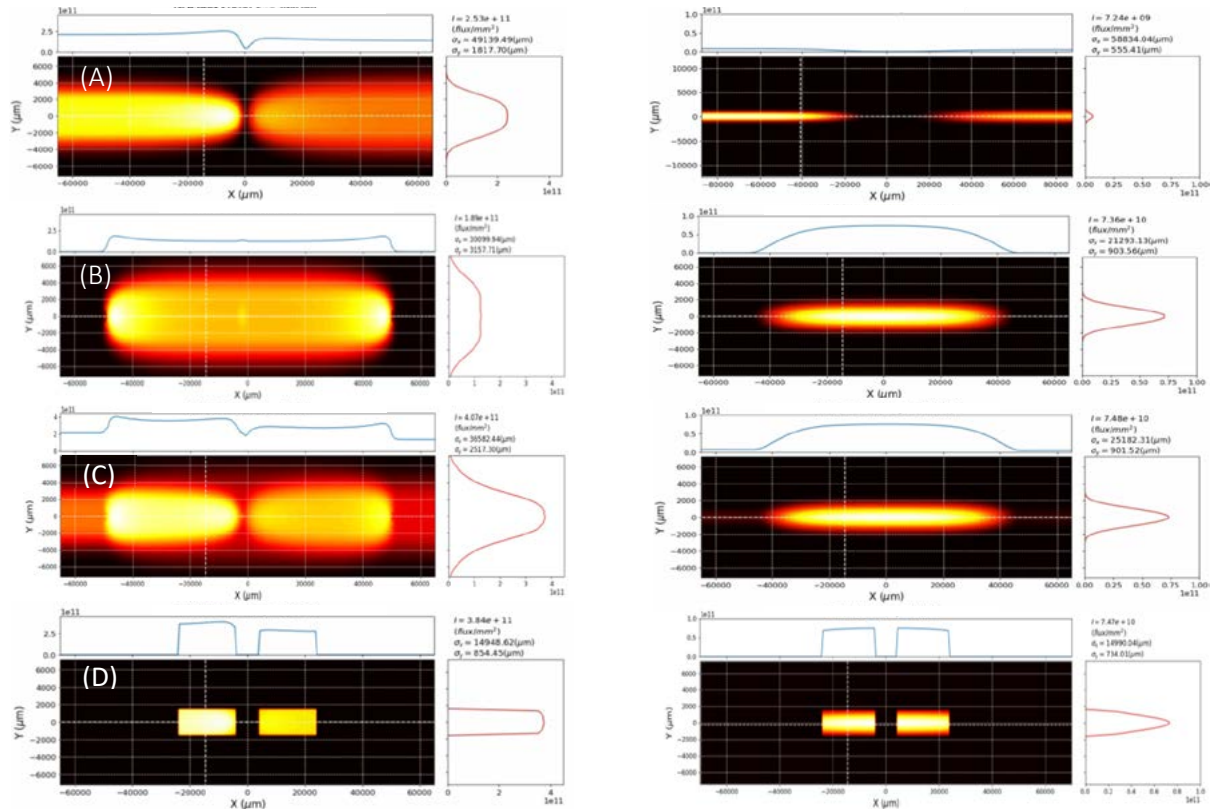
Figure 2-10 : Photon flux density (ph/s/0.1%bw/mm²) for the K18 3PW at 18.5 m, at 2keV (left column) and 35 keV (right column). (A) 'DQ' dipoles only, (B) plain 3PW source, (C) sum of the two sources (A+B), (D) SR from case (C) past the double slit as shown in Figure 2-7. The effect of the DQ dipoles is less dramatic at 35 keV due to their critical energy (5.7 keV).
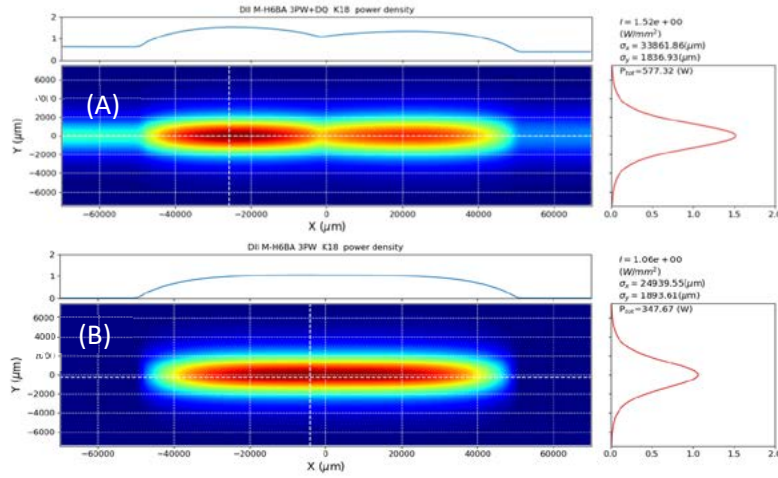
Figure 2-11 : Power density for the K18 3PW at 18.5 m from the centre of the source; (A) 3PW and DQ dipoles, (B) 3PW only. The effect of the DQ dipoles can be clearly seen on the sides.

An initial investigation on the feasibility of such device has been carried out. A RADIA model of the device is shown in Figure 2-12.
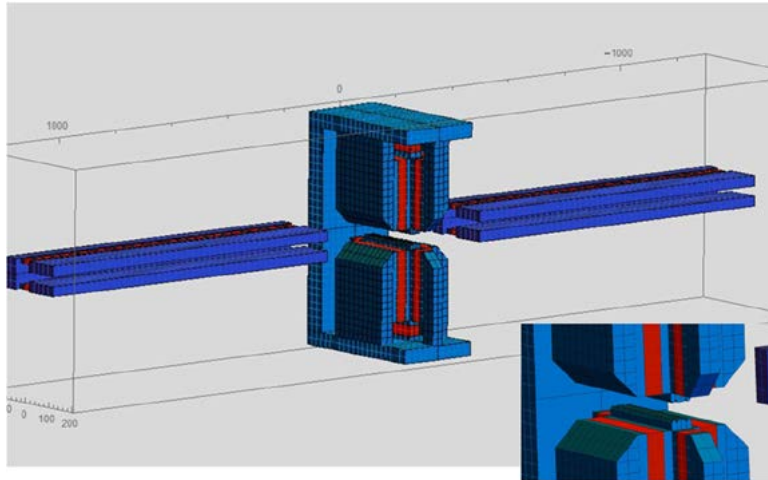
Figure 2-12 : RADIA model of the K18 3PW. The main picture shows the full device, while the inset shows a detail of the central radiator.

2.2.2.2. Beamline K22

Within the group of beamlines studied in this Section, K22 is the one operating at the lowest photon energies and largest spectral range between 1 meV and 1 eV, and has requested an angular acceptance of up to 40 mrad (horizontally) in Diamond-II in order to gain flux, with a lower critical energy source for optimal brightness. The desired SR is mixed with a component from the pure bending element and an edge radiation point mostly for far IR and THz spectroscopy. The edge radiation in addition to the bending one is also meant to provide two sources for two endstations as currently in B22.

In order to fulfil these needs, we considered a long pole (1.63 m) at a low field (-0.35 T), and two 40 cm long strong steerers (0.72T) to close the orbit. This configuration was derived taking into account the need to minimise the increase in emittance essentially driven by the steerers in a dispersive region.

The present K22 3PW parameters are summarised in Table 2-5, while Figure 2-13 displays the field and electron trajectory.

Table 2-5 : Main parameters of the 3PW considered for K22.

	R-pole	S-pole
Peak-field (T)	-0.35	+0.72
pole-width (cm)	163	40
pole-position (cm)	0	117
R-S drift (cm)	3.5	
Length (cm)	250	
R-θ (mrad)	49	
E_{crit} (keV)	2.85	5.86
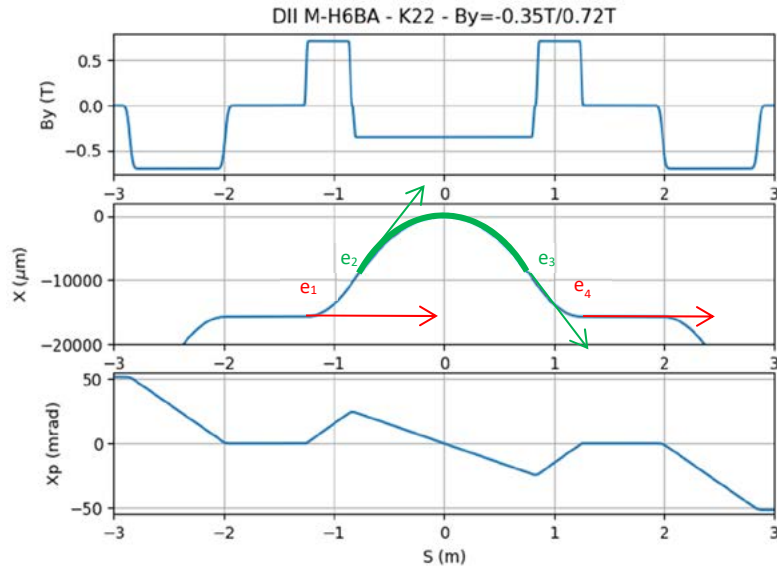
Figure 2-13 : Field (top), electron trajectory (middle) and angle (bottom) of the proposed 3PW for K22. The long radiating arc is highlighted in green. Edge radiation points are marked (red/green) indicating the direction of the beam. The DQ dipoles are visible at ±2.4 m. Useful radiation might be collected by an upward pointing mirror placed just after the device (1.3m from the centre of the source).
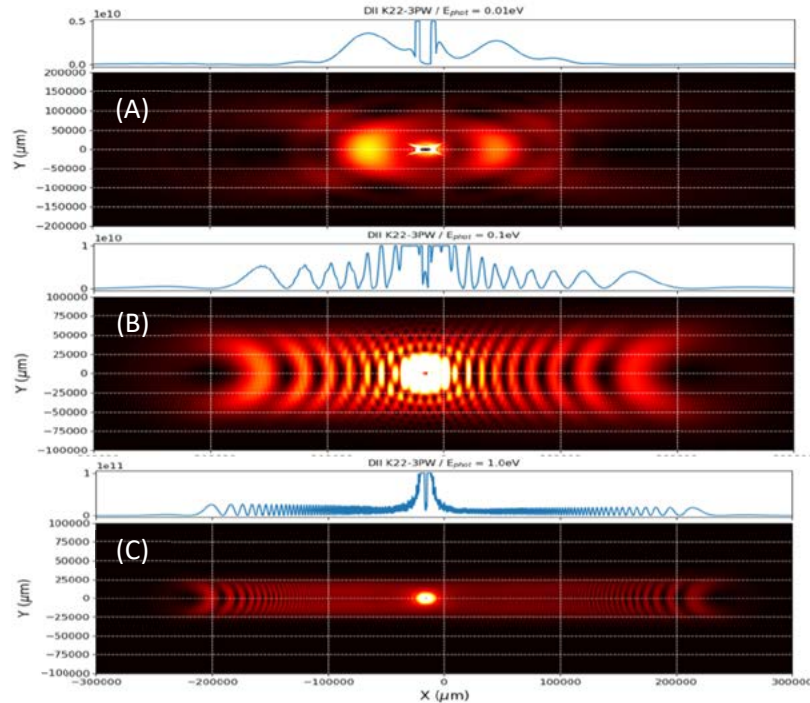
Figure 2-14 : Photon flux density (ph/s/0.1%bw/mm²) for several energies 10m away from the K22 3PW device. (A) 0.01 eV, (B) 0.1 eV, (C) 1.0 eV. Some typical features are recognized: the strong hollow cone from the edge radiation sources (e1, e4) the long radiation band generated by the 'R' pole sweep and the edge radiation edges from the same main radiator (e2, e3).

Figure 2-14 shows the intensity pattern at 10 m for various photon energies (0.01, 0.1, 1.0eV), for the plain device. Strong interference patterns (not shown here) are enhanced when the SR from the lattice gradient dipoles is included, as described in more detail in [3]. The use of edge radiation, particularly marked for low photon energies, is a desired feature for K22, which is interested in capturing the edge radiation generated by the gradient in the B_y field at e2 (see Figure 2-13). The edge radiation due to the gradient field at e1 and e4 is instead responsible for the strong hollow cone at about x = -15.6 mm in the chosen reference frame, where x=0 corresponds to the mid-point of the long radiating arc (centre of the device), and is a typical feature of these kind of devices (as seen in the case of K23 also).
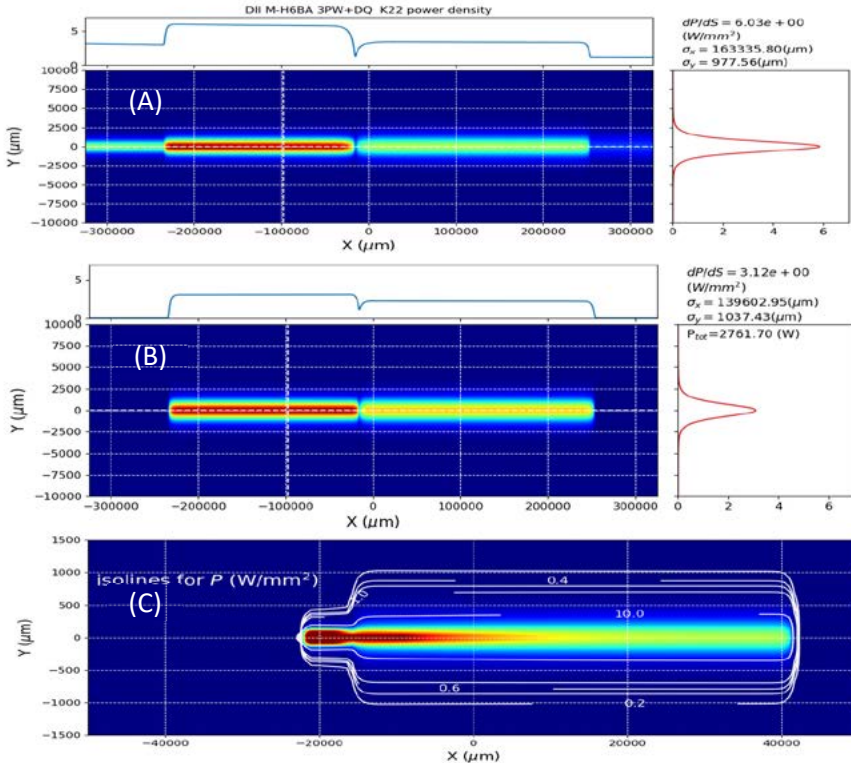
Figure 2-15 : Power density for the K22 3PW at 10m from the centre of the source; (A) 3PW and DQ dipoles, (B) 3PW only. (C) displays the power density for the plain source at 1.3 m from the centre of the device, where a mirror could be possibly placed to collect the SR useful to the beamline.

We are currently investigating ways of extracting the wide fan of radiation. One possibility being examined entails the use of a mirror positioned just downstream of the device and as close as possible to the electron orbit in order to increase the usable flux (1.3 m from s=0 in Figure 2-13). Another possibility is the use of a 1st mirror several metres away as in the current B22 beamline configuration at Diamond.

Figure 2-15 shows the power density on a surface located at 10 m and orthogonal to the photon beam direction for the 3PW with and without the DQ gradient dipoles. The 0.72T steerers play an important role in defining the power pattern, with a total emitted power for this device reaching 2.8 kW. The right lobe in Figure 2-15(B) (outboard side), shows a reduced power load, which might be an advantage if using a mirror close to the electron beam axis to capture the SR just after the K22 device.

The power at a plane placed 1.3 m from the source centre is shown in Figure 2-15(C). Power density for |y|>0.8mm is less than 0.6 W/mm^2 (0.4 W/mm^2 if collected by a 45° oriented mirror). This concept requires further investigation to assess its technical feasibility.

Figure 2-16 shows the flux for this device calculated for an aperture of 27 x 30 mrad^2, with a horizontal offset of 13.5 mrad chosen to avoid the hard radiation cone at 0 mrad, while capturing the outboard edge radiation (e2 in Figure 2-13) from the entry point of the central pole. The flux exceeds that obtained from the present BM source in Diamond. Also shown is the output from a DQ magnet which is also being investigated as a possible source for K22, which would have the advantage of no extra structure in the spectrum and spatial distribution, but with somewhat less flux.
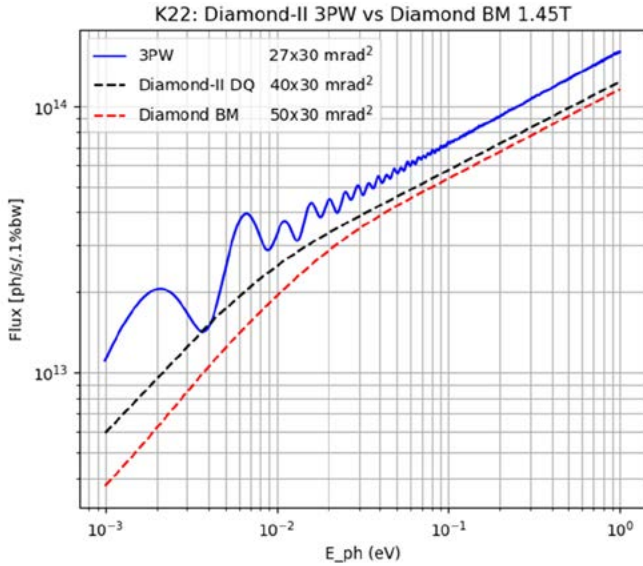
Figure 2-16 : K22 3PW flux (blue) compared with the present BM source at Diamond (red dashed) and a DQ gradient dipole (black dashed).

2.2.2.3. Beamline K23

This beamline will operate between 1 and 10 eV, with a requested aperture of the order of 10 mrad in the horizontal plane. The parameters defining this device are reported in Table 2-6 while the $B_y(s)$ field, electron trajectory and angle are shown in Figure 2-17.

Table 2-6 : Main parameters of the 3PW considered for K23.

	R-pole	S-pole
Peak-field (T)	-0.7	+0.175
pole-width (cm)	35	70
pole-position (cm)	0	90
R-S drift (cm)	37.5	
Length (cm)	250	
R-θ (mrad)	20.9	
E_{crit} (keV)	5.7	1.43
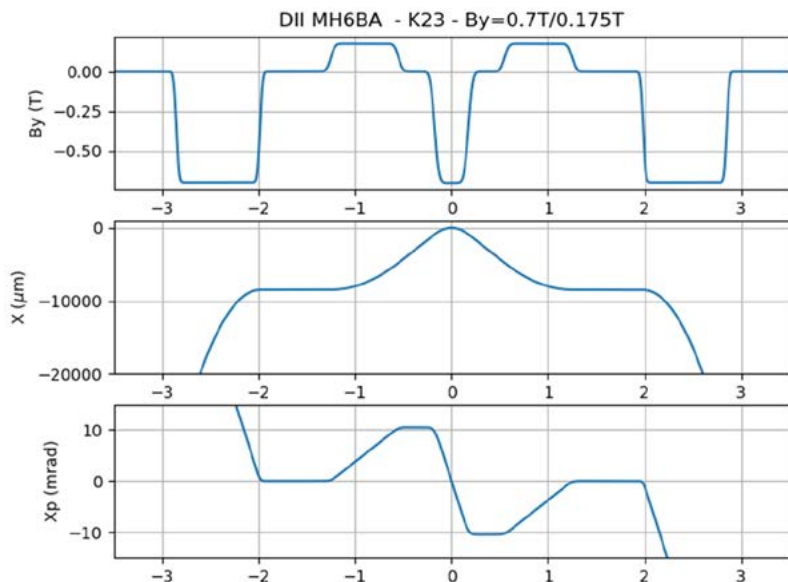
Figure 2-17 : Field (top), electron trajectory (middle) and angle (bottom) of the proposed 3PW for K23, exploiting a central dipole at soft field (-0.7T) and two steerers (0.175T) to close the orbit. The DQ dipoles are visible at ±2.4m.

Intensity patterns collected at 10 m from the source at the two edges of the spectrum, 1 and 10 eV, are shown in Figure 2-18.
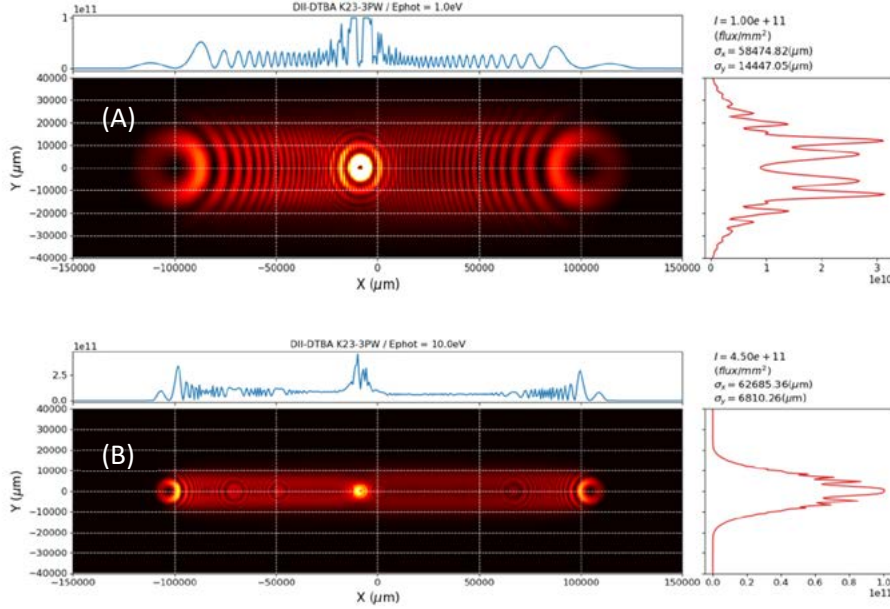
Figure 2-18 : Photon flux density (ph/s/0.1%bw/mm²) at 10 m from the source point for the K23 3PW device at 1 eV (A) and 10 eV (B).

In the present machine an 8 mm diameter cold finger is placed at the median plane of the 1st mirror (10m from the source) to combat the high power from the X-ray component. In Diamond-II we might adopt a solution similar to the case for K22, where a horizontally cut mirror would be placed in the space between the end of the device and the first elements of equipment (1.3 m from the source).

The power density at 10m is shown in Figure 2-19 both with and without the contribution of the gradient dipoles. Fig. 2-19 (C) shows the power density at 1.3 m, where its value for |y|>0.8mm would be less than 155 mW/mm² on the surface of a 45° oriented mirror. The total power for this device is about 887 W.
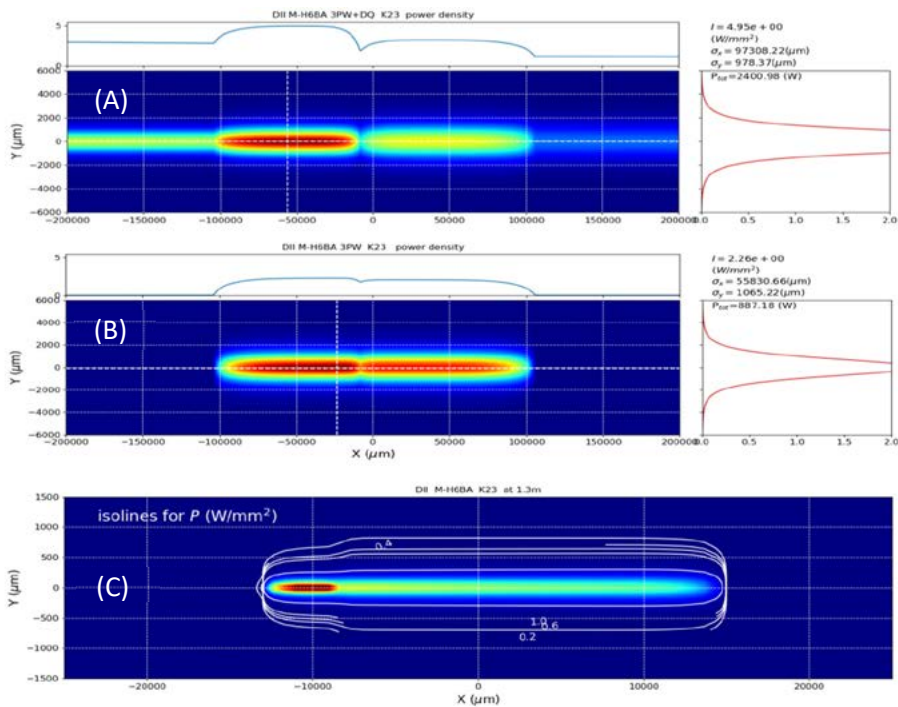
Figure 2-19 : Power density for the K23 3PW at 10m from the centre of the source; (A) 3PW and DQ dipoles, (B) 3PW only. (C) shows the plain 3PW source at 1.3 m, just past the last steerer of the device.

An alternative to the use of a close mirror would require a reduction in the horizontal and vertical acceptance for the beamline in order to transport the SR fan through the downstream magnets. Both the use of a close mirror or the transport through a crotch vessel require further investigation to assess their technical feasibility.

2.2.2.4. Beamline B24

The main requests for this beamline are an aperture of 2x2 mrad^2 and an energy range of 0.3 - 4.5 keV. In addition, it is also required that there are no interference effects in the collected light and no double sources. This is an issue for a relatively low photon energy beamline such as B24, since effects of interference could still be present due to the nature of the device [4]. Another effect that could be detrimental for this beamline is the SR from the DQ dipoles, which could appear as an unwanted multiple source. Interference enhanced by the DQ dipoles was indeed confirmed in the 3PW model for this beamline, which prompted a study for an alternative source exploiting the radiation from the 4th dipole in the 6BA cell, the 0.7T DQ gradient dipole. Preliminary calculations with a simple (no-gradient) model suggest that the flux in the energy range of interest is greater than the one obtained today for the same 2x2 mrad^2 acceptance (see Figure 2-20) making it an appealing candidate. Thanks to the small required acceptance, engineering studies confirm that the downstream DQ lends itself well as a source to reach the present front-end aperture of the beamline with minor modifications.

Given the ability at generating a smooth broadband spectrum without spurious effects caused by many poles, the good flux properties and the ease at transporting the useful SR towards the beamline, the DQ solution has been chosen as the baseline for B24.
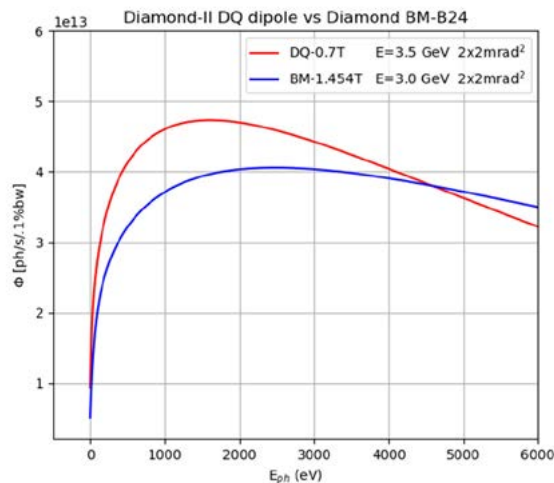
Figure 2-20 : Flux from the present B24 bending magnet (blue curve) and a DQ magnet in Diamond-II (red curve).

2.2.2.5. Summary

A summary of the field strengths and total power emitted by the 3PW's is reported in Table 2-7.

Table 2-7 : Total power emitted by the new devices placed in the relevant mid-straights.

Beamline	3PW Field Strengths (T)	Total Power (W)
K18	0.04 / -1.45 / 0.04	348
K22	0.72 / -0.35 / 0.72	2762
K23	0.175 / -0.7 / 0.175	887

Several items require further study during the TDR phase. The intrinsic interference nature of such a device may represent a problem for some beamlines, which could be exacerbated by the SR produced by the two lattice gradient dipoles. In this respect B24 has opted for the use of the downstream DQ dipole. For the low energy beamlines (K22, K23) one important issue is the extraction of the large SR fan, and a mirror close to the electron orbit placed upstream of the last steerer of the device, could direct the useful radiation towards the beamline front end. This aspect needs further studies. Full SR propagation through the beamlines is needed in order to understand how the image is formed at the sample and what the effect of the DQ dipoles is. Finally the use of DQ as a source for K22 and K23 is under consideration.

References

[1]   Qiaogen Zhou et al.; IEEE Transactions in Applied Superconductivity, Vol. 26, NO. 4, June 2016.

[2]   O. Chubar and P. Elleaume, "Accurate And Efficient Computation Of Synchrotron Radiation In The Near Field Region", Proc. EPAC98 Conference, p.1177-1179.

[3]   M. Apollonio, Technical Note in preparation.

[4]   R.J. Dejus and K.J. Kim, "Sharpness of Interference pattern of the 3-pole wiggler", AIP Conf. Proc. 1741, 020015 (2016).

2.3. Accelerator Physics

2.3.1. Lattice Design

The lattice is based on the MBA structure with 24 cells and maintains the 6-fold symmetry of Diamond with a long straight section every four cells. One mid-straight section is introduced in each arc, making a total of 24 mid-straight sections. Figure 2-21 shows a schematic block diagram of the super-period layout.
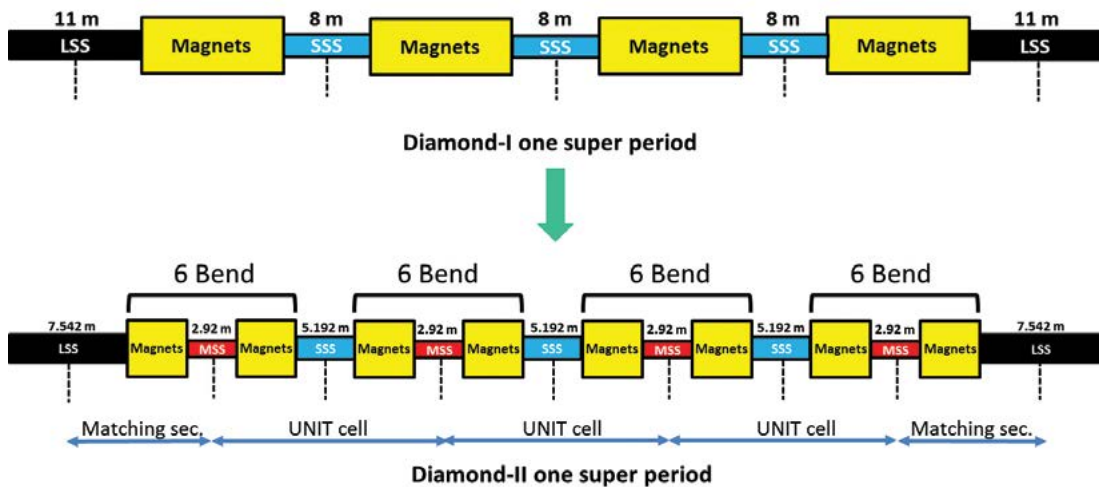
Figure 2-21 : Diamond-II super-period layout and comparison with Diamond.

Each cell is (roughly) mirror symmetric with respect to the mid-straight section and is composed of:

- four longitudinal gradient dipoles (DL)
- two gradient dipoles (DQ)
- sixteen quadrupoles (with an additional pair in each long straight)
- twelve sextupoles with embedded H/V correctors
- two octupoles
- discrete correctors facing the long-straight sections.

Doublets of quadrupoles face the standard straight section while triplets are used in the long straight sections to ease the matching of the optics functions and produce zero dispersion.

Longitudinal gradient dipoles are used to reduce the emittance, while gradient dipoles which embed a vertically focussing quadrupole reduce space requirements. In this way only high gradient horizontally focussing quadrupoles remain in the arcs.

The dispersion bump that characterises the ESRF-EBS [1] cell is maintained in the M-H6BA, albeit slightly reduced in length and in the peak value of the dispersion, and chromatic sextupoles are located only in the dispersion bumps. The phase advance between sextupoles is maintained to be a multiple of π (i.e. 3π in horizontal and 1π in the vertical plane). This condition provides a very effective cancellation of the higher order terms in the sextupole aberration also in the M-H6BA cell.

The field of the DL magnets was tailored to minimise the contribution of the dispersion invariant (the "curly-H" function) to the emittance as was done in the ESRF-EBS design. The longitudinal profile is shown in the inset in Figure 2-22. The DL is made of five slices of the same length (20 cm) with the highest field of 1T located at the ends where the dispersion function is minimum and the contribution to the emittance is lowest.

A careful exercise was necessary to tailor the optics functions to take into account the loss of the central DQ. The optics functions in the mid-straight sections should have a minimum to accommodate a possible in-vacuum insertion device. It was found that also the dispersion function must be carefully controlled as it generates a strong impact on the emittance depending on the ID field strength. It was found that the dispersion function should not exceed 2.5 cm in the mid-straight sections. These constraints produce rather strong DQs on either side of the mid-straight section, combining a relatively

high field 0.7 T with a gradient of 30 T/m. The local quadrupoles are also rather strong reaching 65 T/m. The implication of these requirements on the magnet design is discussed in Section 2.4.

Inevitably the lattice design tends to require that many of the magnets are as close together as possible. A minimum separation of 7.5 cm (iron-to-iron in the hard edge model) was specified as a constraint.

In summary the main constraints for the optics design have been:

- maintain the required minimum straight section lengths
- dispersion bump in arcs and -I pairing of phase advance between sextupoles
- zero dispersion in the standard and long straight sections
- dispersion less than 2.5 cm in mid-straights and small beta functions
- minimise the maximum β functions in the arcs
- provide suitably small beta functions at the locations of the insertion devices
- maintain a minimum magnet-to-magnet spacing of 7.5 cm.
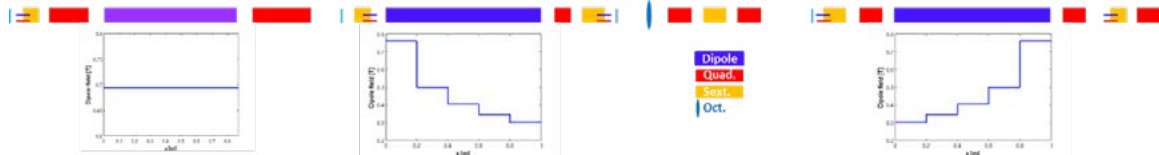
Figure 2-22 : Downstream half of the M-H6BA cell: quads (red), sextupoles (green), gradient dipoles (violet), dipole (blue): the insets show the value of the dipole field as a function of the longitudinal position.

2.3.1.1. Lattice Optics Functions and Source Parameters

The main lattice parameters are shown in Table 2-8 compared to those of the current Diamond lattice; in both cases these are the bare lattices with IDs off. The natural bunch length for both cases was calculated for a RF voltage corresponding to a 3.5% energy acceptance. The optics functions for one superperiod are shown in Figure 2-23.

The optics functions at the centre of the straight sections are given in Table 2-9.

The corresponding electron beam source size and divergence, and the reduction with respect to Diamond, are presented in Table 2-10.

Table 2-8 : Main lattice parameters of Diamond and Diamond-II without IDs.

Parameter	Diamond @ 3 GeV	Diamond-II @ 3.5 GeV
Emittance [pm]	2700	160
Circumference [m]	561.571	560.574
Harmonic number	936	934
RF frequency [MHz]	499.680	499.499
Momentum compaction	1.57e-04	1.17e-04
Energy loss per turn [MeV] (dipoles)	0.988	0.670
Energy spread [%]	0.096	0.078
Horizontal damping partition	1.0014	1.3739
Vertical damping partition	1.0000	1.0000
Longitudinal damping partition	1.9986	1.6261
Horizontal damping time (ms)	11.28	14.21
Vertical damping time (ms)	11.38	19.53
Longitudinal damping time (ms)	5.71	12.01
Natural bunch length (ps)	11.55 @ 2.17 MV	9.86 @ 1.66 MV
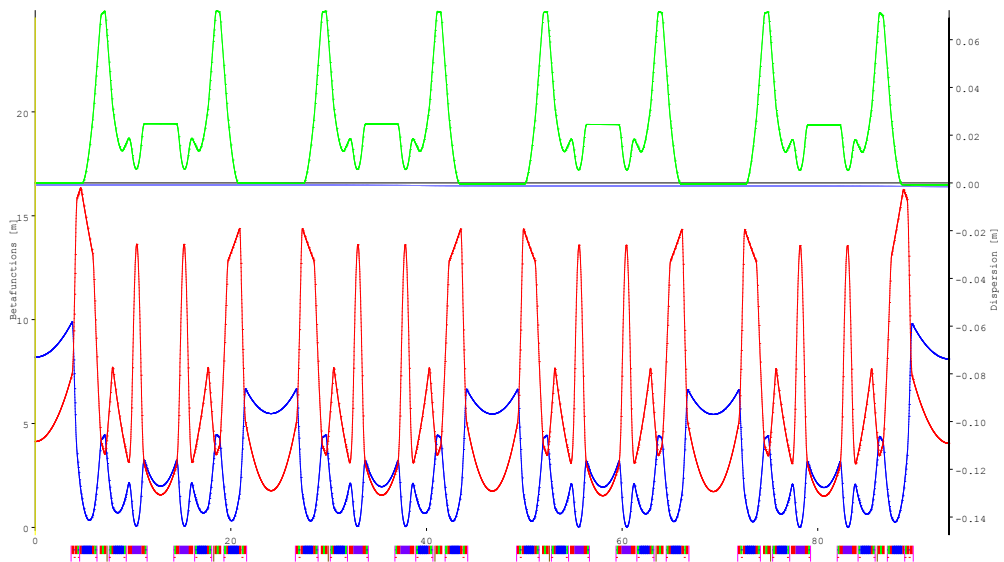
Figure 2-23 : Optics functions in a super-period; dispersion function (green), βx (blue) and βy (red).

Table 2-9 : Optics functions at the centre of the straight sections.

Straight type	β_x(m)	β_y(m)	α_x(rad)	α_y(rad)	D_x(m)	D_x'(rad)
standard straights	5.67	2.06	0.00	0.00	0.00	0.00
mid-straights	2.17	1.86	0.00	0.00	0.025	0.00
long straights	8.36	4.40	0.00	0.00	0.00	0.00

Table 2-10 : Electron beam source size and divergence at the middle of the straight sections. A vertical emittance of 8 pm is assumed. In parenthesis is the ratio of reduction with respect to the current Diamond values.

Straight type	σ_x (μm)	$\sigma_{x'}$ (μrad)	σ_y (μm)	$\sigma_{y'}$ (μrad)
standard straight	29.8 (x 4.1)	5.2 (x4.6)	4.1 (x0.9)	1.0 (x0.9)
mid-straight	26.8	8.5	3.8	2.1
long straights	36.1 (x 4.9)	4.3 (x3.8)	5.9 (x1.2)	1.4 (x1.2)

The gain in electron brightness over Diamond is a factor of ~17. Note that this increase is due exclusively to the reduction of the horizontal source size and divergence, since Diamond is already operating at an emittance of 8 pm in the vertical plane, which is the nominal "diffraction limit" ($\lambda/4\pi$) for a wavelength λ = 1 Å. As shown in Chapter 1 however, the gain in brightness of the emitted photons is significantly larger than this, particularly in the medium and high photon energy range, due to the additional effect of the increase in electron energy.

The set of IDs foreseen for Diamond-II is described in Section 2.2.1. The modification to the main lattice parameters due to the operation of the IDs is summarised in Table 2-11. The reduction in emittance between Diamond and Diamond-II in this case is a factor 25. The natural bunch length for both cases was calculated for a RF voltage corresponding to a 3.5% energy acceptance.

Table 2-11 : Main lattice parameters of Diamond and Diamond-II for with the full complement of IDs.

Parameter	Diamond (all IDs)	Diamond-II (all IDs)
Emittance [pm]	3100	125
Momentum compaction	1.56e-4	1.16e-04
Energy loss per turn [MeV]	1.52	1.53
Energy spread [%]	0.10	0.10
Horizontal damping partition	1.006	1.164
Vertical damping partition	1.000	1.000
Longitudinal damping partition	1.994	1.836
Horizontal damping time (ms)	7.36	7.37
Vertical damping time (ms)	7.40	8.58
Longitudinal damping time (ms)	3.71	4.67
Natural bunch length (ps)	10.99 @ 2.80 MV	10.78 @ 2.69 MV)

2.3.1.2. Lattice Optimisation

The strategy adopted for the Diamond-II lattice optimisation is based on a number of state-of-the-art tools that have been developed over the last 15-20 years, namely:

- semi-analytical tools based on the (computer-aided) analysis of terms in the Hamiltonian of nonlinear betatron motion, i.e. detuning terms, resonance driving terms, both geometric and chromatic;

- numerical tools for the complete solution and post processing of the nonlinear motion, i.e. 6D tracking, including errors and engineering apertures, Frequency Map Analysis (FMA), realistic injection efficiency simulations;

- numerical tools based on genetic multi-objective algorithms (MOGA-type) that allow an efficient exploration of a large multi-dimensional parameter space to find optimal solutions.

It has long been recognised that an effective optimisation of the lattice should proceed with a combined analysis of the linear and non-linear beam dynamics. In this sense we have adopted the approach used in the optimisation of the ESRF-EBS cell where a thorough search of linear optics handles is carried out to identify the best correlations with non-linear quantities such as dynamic aperture, detuning with amplitude and detuning with momentum, while still keeping the emittance under control.

In summary we found that:

- phase advance between sextupoles impacts the dynamic aperture (DA)

- alpha at the sextupoles impacts the cross detuning terms

- beta at the straight sections impacts the emittance

- dispersion in the mid-straights impacts the dependence of emittance with IDs.

In addition to this scheme, nonlinear optics quantities are directly targeted with sextupoles and octupoles to achieve a tighter control of the detuning with amplitude and with momentum ("tune confinement"). As a rule of thumb, we tried to confine the tune deviation with amplitude to 0.1 and tune deviation with momentum to be less than 0.1 for 2% momentum deviation respectively. The rationale behind this choice is that the phase space region satisfying such a condition is likely to be robust against errors. Several attempts were also made to achieve an additional compensation of the resonant driving terms by defining the cell phase advance so that, over N cells, the driving terms up to second order are reduced to zero. The main route attempted was the compensation of all second order driving term after 8 cells by using a phase advance of

$$\mu_x = 2.375; \qquad \mu_y = 0.875;$$

In this way the main third and fourth order resonances will compensate after 8 cells as

$$8*(M\mu_x + N\mu_y) = P$$

is satisfied with M, N and P integers. While this condition guarantees the compensation of the driving terms to zero every 8 cells, it often required deviation from the –I paring, and as a consequence, it produced worse results.

Further optimisation was attempted using the multi-objective genetic algorithms (MOGA) to optimise the sextupoles and octupoles using directly the injection efficiency and the Touschek lifetime as objectives.

It is clear however that the ultimate benchmark on the robustness of a lattice optimisation is a full simulation of the beam dynamics, with engineering aperture and realistic errors. These can simulate the actual injection process as well as the computation of dynamic aperture (DA) and momentum aperture (MA).

Bare lattice simulations were used to have a first assessment of the performance of the ring, define the correction schemes for orbit, optics and coupling and to inform the first round of engineering integration of the various components. Some basic design choices were taken as a result:

- minimise as much as possible the movement of the source points
- adjust the magnet positions to allow the insertion of absorbers, vacuum pumps and flanges, Beam Position Monitors, where necessary
- avoid clashes due to coil overhangs or accidental overlap of elements
- maintain the circumference of the ring compatible with the adjustment range of the RF frequency of the injector complex
- design the injection section keeping the same lattice symmetry based on the antis-septum concept [2].

Figure 2-24 shows the dynamic aperture (DA) (x, y) and the on-momentum Frequency Map (FM) of the bare lattice. It shows a comfortable +/- 8 mm DA albeit with a strong detuning pushing the FM toward the half integer resonance $Q_y = \frac{1}{2}$. The lattice was optimised using a chromaticity of (1.2,1.2) with the assumption that a slight positive chromaticity will be needed to damp collective instabilities. The lattice optimisation for larger positive chromaticity, up to (2,2) as required from Section 2.3.4.3, will be part of future work
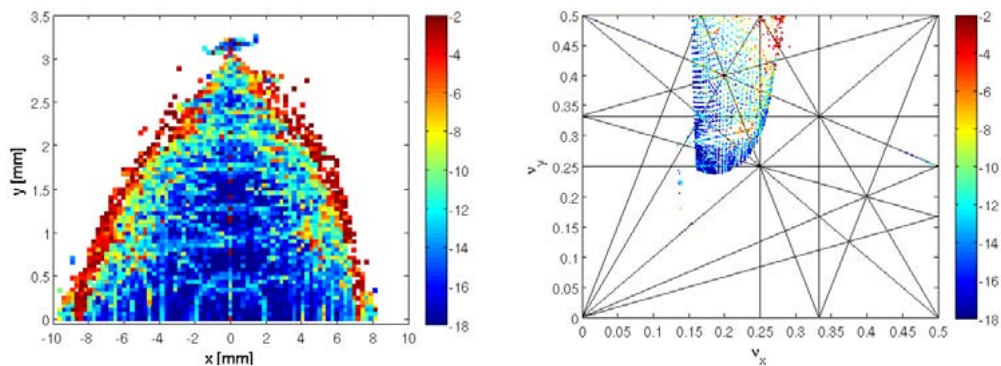
Figure 2-24 : Bare lattice DA and the on-momentum Frequency Map (FM).

In Figure 2-25 we show the off-momentum DA (x, dp/p) and the corresponding FM. Again a comfortable +/-4% appears but the detuning with amplitude is large and hard to control given the second order chromaticity terms that are driven by the –I pairing of the chromatic sextupoles.
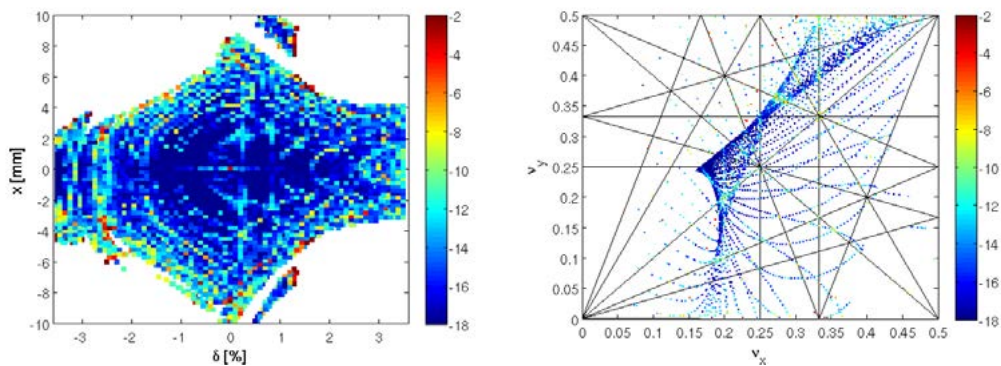
Figure 2-25 : Bare lattice MA and the off-momentum Frequency Map (FM).

35

The details of the off momentum tune deviation is reported in Figure 2-26 which shows how the tune confinement criteria is violated below +/- 2%.
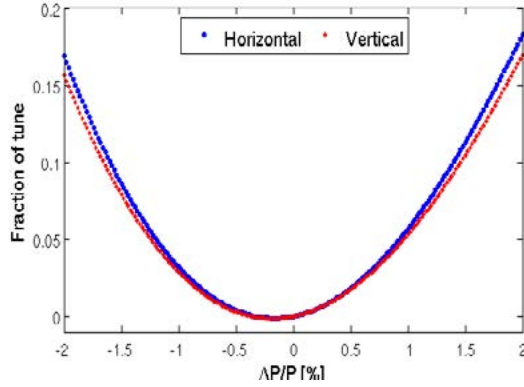
Figure 2-26 : Bare lattice off-momentum tune deviation.

The MA was calculated from tracking with elegant [3] and is presented in Figure 2-27. The RF voltage was chosen to provide 3.5% energy acceptance. The natural bunch length is 2.95 mm, and the corresponding Touschek lifetime assuming 300 mA stored in 934 bunches and a vertical emittance of 8 pm is about 3.1 h. The relevant parameters for this calculation are given in Table 2-12. More information on the Touschek lifetime is presented in Section 2.3.3 where the impact of the errors is analysed and in Section 2.3.4 including the effect of a 3rd harmonic cavity. Despite such a relatively small value of the lifetime, the proposed solution is an acceptable starting point. Work will continue during the TDR phase to improve the momentum aperture.
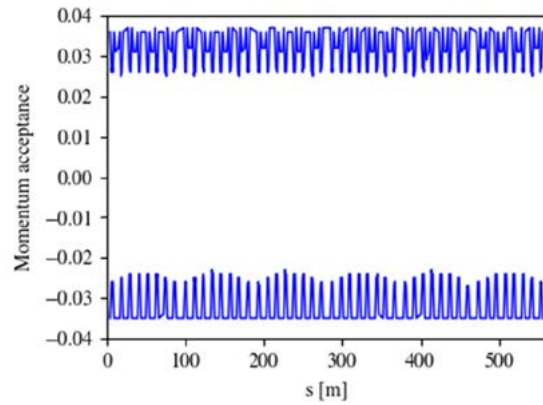
Figure 2-27 : Bare lattice momentum aperture.

Table 2-12 : Parameters for Touschek lifetime calculations.

Parameter	Value
RF voltage (MV)	1.66
Harmonic number	934
RF frequency (MHz)	499.499
RF synchronous phase (deg)	156.18
Beam current (mA)	300
Number of bunches	934
Vertical emittance (pm)	8
Bunch length (mm)	2.95
Energy spread (%)	0.78

References

[1] P. Raimondi, Proc. IPAC 2016, Busan, Korea, WEXA01, p. 2023.

[2] C. Gough and M. Aiba, Proc. IPAC 2017, Copenhagen, Denmark, MOPIK104, p. 774.

[3] M. Borland, "elegant: A Flexible SDDS-Compliant Code for Accelerator Simulation," Advanced Photon Source LS-287, September 2000.

2.3.2. Apertures and Magnet Parameters

2.3.2.1. Magnet and Vessel Apertures

The criteria that have been used to define the machine apertures are the following:

•   a sufficiently small magnet aperture that achieves the required field strengths, while keeping the field inside the yoke below 1.8 T and pole tip field below 1 T

•   a vessel aperture that is larger than the dynamic aperture, is compatible with the magnet aperture, but which is no smaller than necessary, in order to limit Resistive Wall effects

•   allowance for in-situ bakeout.

This has resulted in a vacuum vessel with an internal radius of 10 mm, external radius of 11 mm and a magnet bore radius of 12 mm. This leaves 1mm between vessel and poles which is adequate to install a thin in-situ bakeout system. Such dimensions are technologically feasible and not dissimilar to values chosen by other 4th generation low emittance light sources. The resulting aperture amply contains the dynamic aperture which is ~5 mm horizontal and ~2 mm vertical (with errors) at the injection point where $(\beta_x, \beta_y) = (8.4\ m, 4.4\ m)$ which translates to ~5.5 mm horizontal and ~4 mm vertical, at the locations of maximum $\beta_x = $ ~10 m and $\beta_y = $~17 m in quadrupoles of the long insertion straights.

The in-vacuum IDs in the standard and mid-straight sections will operate with a minimum vertical gap of 4 mm, lower than the 5 mm used currently in Diamond. The ID vertical aperture is more restrictive than the one defined by the internal radius of the vacuum pipe in the quadrupoles but still amply contains the dynamic aperture. Scaling the 4 mm aperture in the standard straight, to the case of straights I09 and I13, where the IDs will be off-centred, will still allow a minimum gap of 6.4 mm. The horizontal apertures will be defined taking into account the minimum deviation from the dimension of the circular pipe to reduce the contribution to the geometric impedance.

2.3.2.2. Magnet Parameters

Table 2-13 presents the nominal magnet parameters for an ideal lattice without errors. The design and related challenges are discussed in Section 2.4.

Table 2-13 : Magnet parameters.

Name	#	Description	L (m)	θ [°]	B [T]	B′ [T/m]	1/2B″ [T/m²]	1/6B‴ [T/m³]
DL	96	LGB	1.0	2.27	0.461	0	0	0
DQ	48	Grad. Bend	0.87	2.97	0.695	-32.6	0	0
Q1	216	Quadrupoles	0.15	0	0	85	0	0
Q2	60	„	0.105	0	0	„	0	0
Q3	24	„	0.185	0	0	„	0	0
Q4	48	„	0.25	0	0	„	0	0
Q5	48	„	0.36	0	0	„	0	0
S1	144	Sextupoles	0.14	0	0	0	3850	0
S2	144	„	0.10	0	0	0	„	0
O1	48	Octupoles	0.09	0	0	0	0	110300
CH, CV	252	Correctors	0.08	0.057	0	0	0	0

There are 240 correctors, produced by extra windings in the sextupoles, as well as 12 discrete corrector magnets located at either end of the long straight sections. The maximum strength of the correctors is 1 mrad.

2.3.3. Lattice Imperfections and Corrections

The impact of a realistic distribution of errors of the magnetic elements and BPMs on the performance of the ring has been assessed by means of a statistical analysis of the closed orbit, linear optics and of the key performance parameters of the nonlinear beam dynamics.

The error analysis of ultra-low emittance lattices has shown that such lattices are generally more sensitive to magnet positioning and gradient errors as the emittance is lowered [1]. However, it has been acknowledged that beam-based correction techniques have proven very successful in compensating the error effects and restoring the nominal lattice performance, at least in third generation light sources [2]. For this reason, the error analysis has been split in two parts: relatively large initial errors have been used to simulate the commissioning strategy replicating in detail the exact steps that will be taken in establishing first turn, first stored beam, first orbit correction, first beam-based alignment (BBA) and first optics correction. This analysis is used to inform the tolerances on magnets and BPMs errors. A second table with reduced errors has been used to quickly check the robustness of the lattice optimisation, to simulate the effect of residual errors, after the beam-based correction have been applied. The criteria to define this reduced error table is that the residual beta beating is less than ±15% which we believe is pessimistic, but provides a safe margin for our tests. Such errors are enough to excite resonances that would normally be completely transparent in the bare lattice, as is the case of the half integer resonance $Q_y = 1/2$ that limits the dynamic and momentum aperture. We stress that the reduced error table is meant to provide only a first and fast check on the robustness of the optimisation, without the full simulation of the commissioning procedure, but does not define the tolerance on the magnet and BPM errors. The two error tables used are reported in Table 2-14 and Table 2-15 respectively. The values quoted are the rms of a Gaussian distribution which is cut at ±2 sigma.

Table 2-14 : Machine errors used in the commissioning simulation.

Parameter	Value
Girder misalignment /roll [μm /μrad]	150/150
Dipole misalignment / roll within girder [μm /μrad]	50/100
Quad., Sext., Oct. misalignment /roll within girder [μm /μrad]	25/100
BPM misalignment /roll within girder [μm /μrad]	150/150
Dipole/Quad./Sext./Oct. fractional strength error	$5\times10^{-4}/10^{-3}/10^{-3}/10^{-3}$

Table 2-15 : Reduced errors used for the simulations of the corrected machine.

Parameter	Value
Dipole misalignment / roll within girder [μm /μrad]	15/100
Quad., Sext., Oct. misalignment /roll within girder [μm /μrad]	15/100
BPM misalignment /roll within girder [μm /μrad]	5/10
Dipole/Quad./Sext./Oct. fractional strength error	$10^{-4}/10^{-3}/10^{-3}/10^{-3}$

This Section presents the results of the commissioning simulations, analyses the required engineering tolerances, and describes the effect of the lattice imperfections on the beam dynamics. The analysis of the lattice imperfections confirmed that the tolerances on magnets and BPMs positioning and precision can be significantly relaxed by a step-by-step beam-based correction strategy. We then consider the effect of the multipole errors and IDs to establish the tolerances of the nonlinear dynamics optimisation.

2.3.3.1. Distribution of BPMs, Correctors and Skew quadrupoles

In order to correct the orbit and the optics and to control the coupling, a set of beam position monitors (BPMs), combined horizontal and vertical correctors (HVCORs) and skew quadrupoles (SQUADs) have been distributed along the cell, as

shown in Figure 2-28. The position of such corrector elements was carefully chosen to provide a sufficiently dense sampling of the phase advance along the cell, so that an effective orbit correction can be achieved, reducing the orbit close to zero at the BPMs without correctors fighting each other (see Sec. 2.3.3.4) and effectively controlling the coupling.
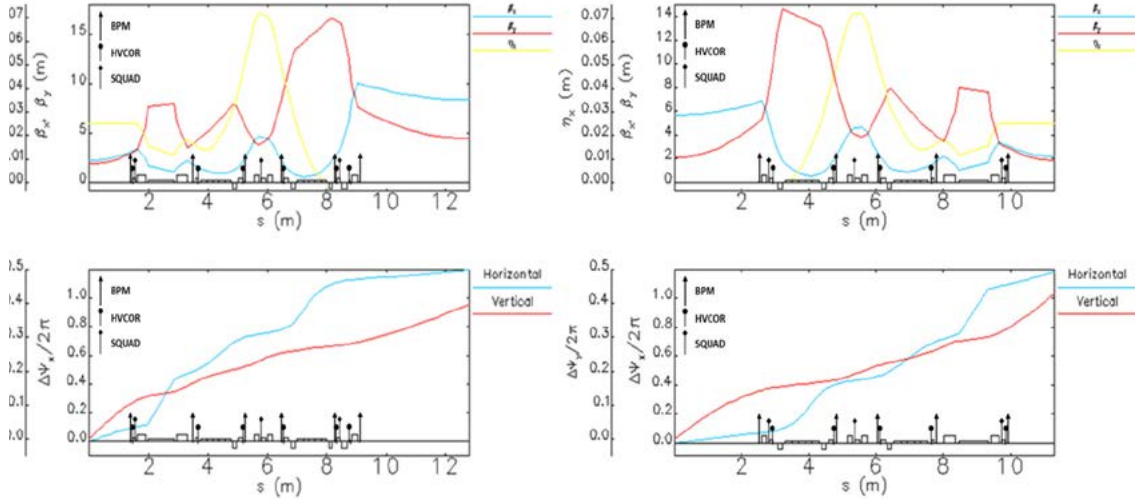
Figure 2-28 : Distribution of the BPMs, HVCORs and SQUADs in the (left) matching section, (right) half a unit section.

Using the decomposition of the superperiod in three unit cells and two matching cells at the ends. Each cell contains 10 BPMs, 10 HVCORs and 6 SQUADs except for the cells at the end of the superperiod which have 12 BPMs, 12 HVCORs and 6 SQUADs. There are 252 BPMs, 252 HVCORs and 144 SQUADs in total for the whole ring. For precise orbit control at the insertion devices (IDs), BPMs are placed at either end of the straight sections. A group of 240 correctors is embedded in the sextupoles by means of additional windings, while the remaining 12 will be standalone correctors combining both horizontal and vertical correction. All the 144 skew quadrupoles have been considered as additional windings inside the sextupoles. Two thirds of the skew quadrupoles (96 SQUADs) are positioned in locations of non-zero dispersion while the remaining third (48 SQUADs) are located in the dispersion-free straights.

2.3.3.2. Commissioning Simulation Procedure

The commissioning of the storage ring is based on the following steps [3]-[5]: 1) Establish the first turns with quads and dipole only and perform basic trajectory correction while the sextupoles have been switched off, 2) power on the sextupoles and RF to capture the beam, (adjust tune and chromaticity if necessary) 3) Preliminary BPM calibration and quadrupole centering (also known as beam based alignment or BBA), 4) correct the closed orbit, 5) correction of the beta-beating, 6) correction of the vertical dispersion and coupling errors, 7) accumulation. All the correction steps are based on the response matrix method and SVD algorithm.

While usually orbit corrections are tackled from a set of random errors directly using the orbit response matrix (ORM), the orbit correction is significantly aided by a first beam threading for one or more turns in the ring. In this way, random seeds that cannot be corrected with a single standalone orbit correction via the ORM, can actually be corrected after the beam threading procedure. In this way the tolerance on the magnets and BPMs errors can be relaxed. The beam-based correction strategy can be fully simulated on the computer, replicating the actions that are taken during the commissioning of the accelerator, from establishing the first turn, to store the beam, quadrupole centering, and optics corrections.

All simulations of the lattice imperfections and the commissioning strategies were made using ELEGANT [6] and AT [7].

2.3.3.3. Trajectory Correction

In the first step, the errors are randomly imposed to the lattice elements according to Table 2-14 using a Gaussian distribution with 2σ cut off in 100 error seeds. The errors include transverse misalignment and fractional strength of the magnets and higher order multipoles [3]. The longitudinal misalignment and jitter of the incoming beam have not yet been considered. It is assumed that the inner diameter of the vacuum chamber is 20 mm and the beam will be lost when its transverse oscillation amplitude exceeds $\pm$10 mm. An example of the distribution of the girder and magnet alignment errors for one arbitrary seed is displayed in Figure 2-29.
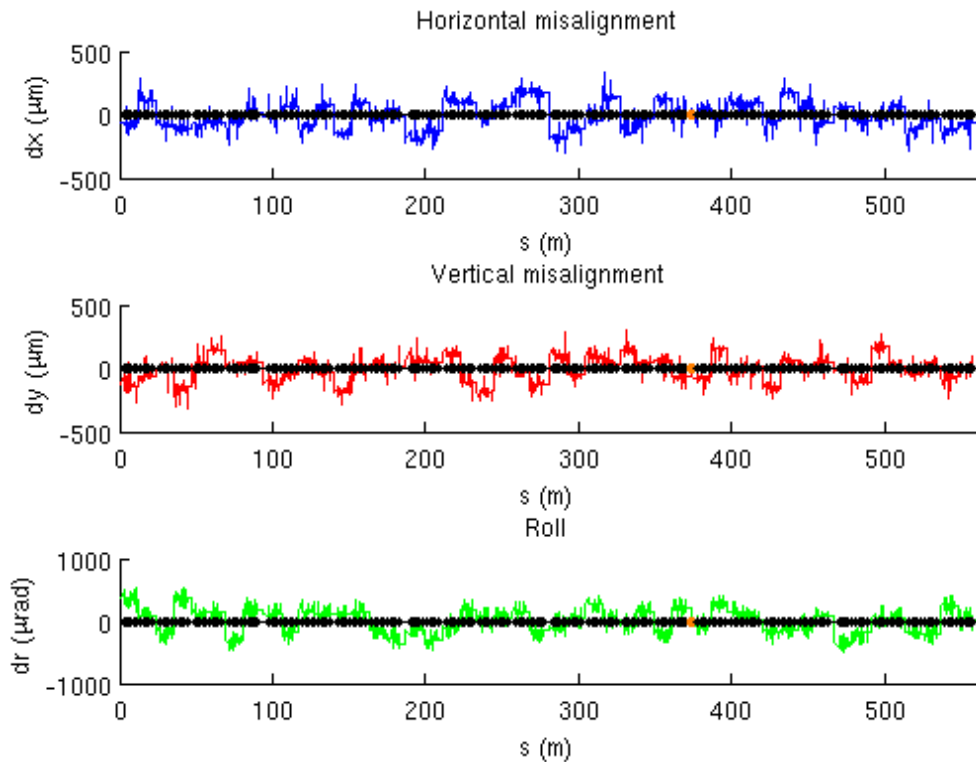
Figure 2-29 : Distribution of the girder and magnet alignment errors in the ring for an arbitrary seed.

After generating the errors, the transverse trajectory has been corrected with the goal of closing the first turn. The sextupole magnets are off in this step to increase the likelihood of beam transfer and to follow more realistically the actual commissioning procedure. In order to correct the trajectory in the ring, the response of horizontal/vertical (H/V) trajectory is measured at the BPMs by changing the horizontal/vertical correctors' strength. The H/V trajectory response matrix and its inverse matrix are plotted in Figure 2-30.
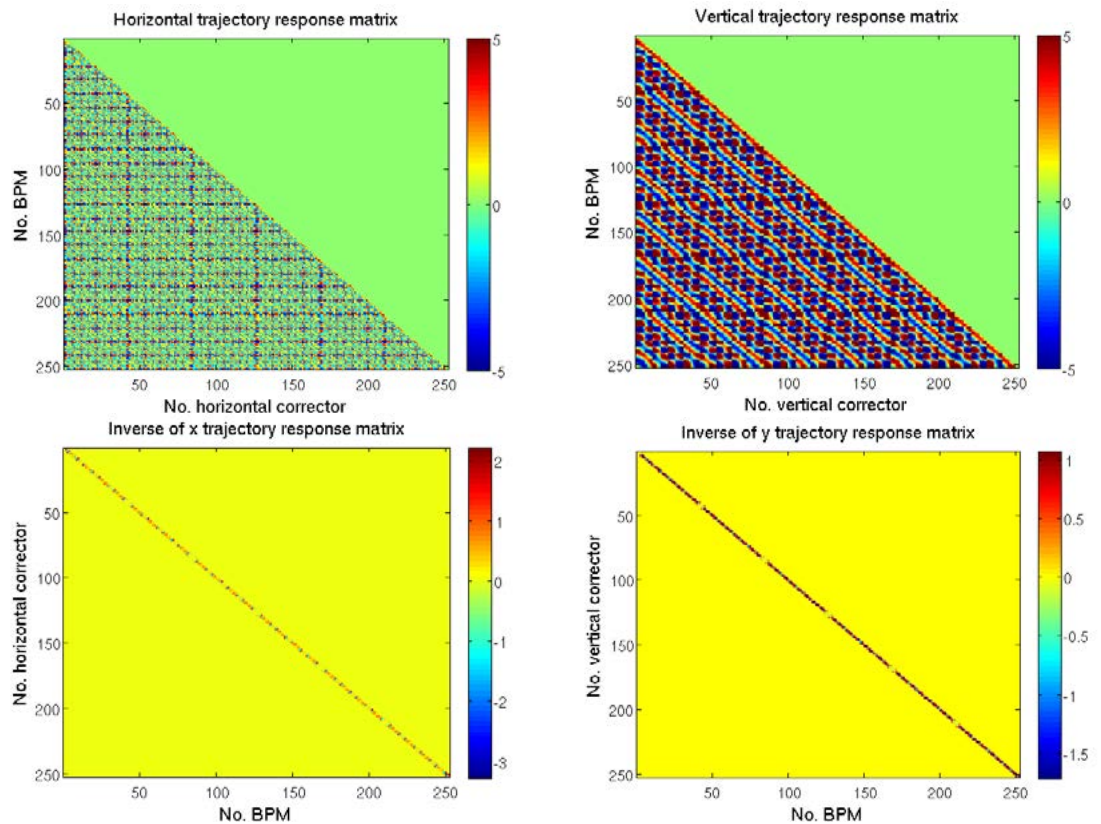
Figure 2-30 : Horizontal and vertical trajectory response matrix and corresponding inverse matrixes.

The distorted and corrected trajectory along the ring are displayed in Figure 2-31 and the corresponding corrector strengths are displayed in Figure 2-32 respectively for all the error seeds. The maximum value of the correctors over 100 seeds is less than 0.7 mrad.
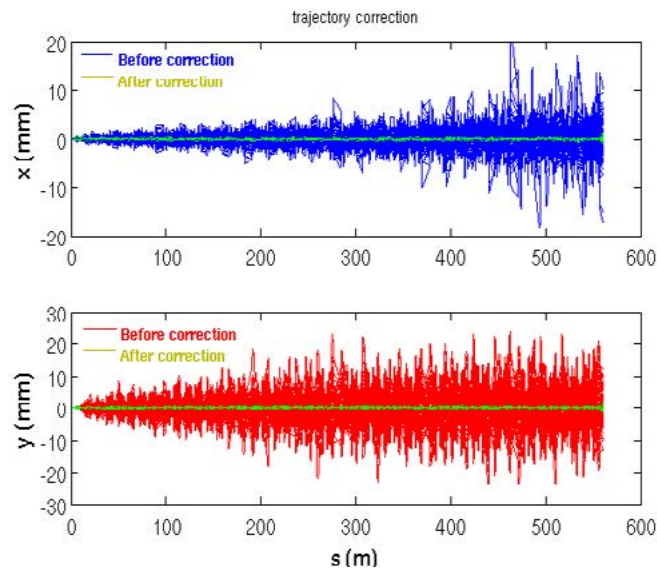
Figure 2-31 : Transverse trajectory of the beam before and after the correction. It is assumed that x0=y0=0, x0'=y0'=0 as initial conditions.
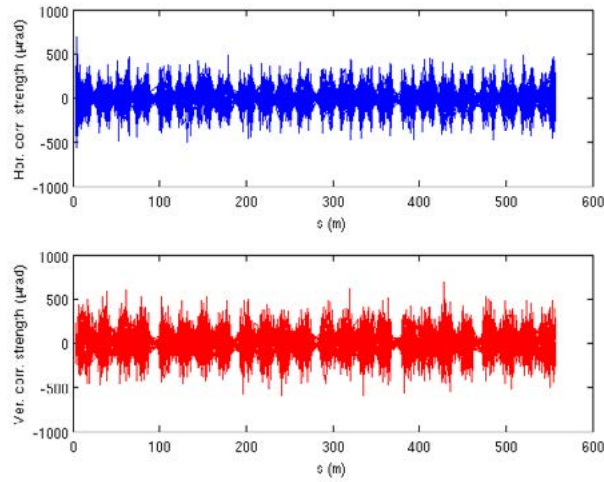
Figure 2-32 : Corrector strengths after trajectory correction for all the error seeds.

2.3.3.4. Closed Orbit Correction

The first turn trajectory correction provides corrector settings that are used as a starting point for the subsequent orbit correction. First we compute the orbit with sextupoles on and then a global closed orbit correction is performed. The closed orbit along the ring before and after correction is displayed in Figure 2-33 and the corresponding corrector strengths are given in Figure 2-34. In this step, 8% of the machine samples are lost and for the remaining 92%, the closed orbit is found. If we start directly with the closed orbit correction on the same 100 seeds, about 70% of the machines cannot be corrected.
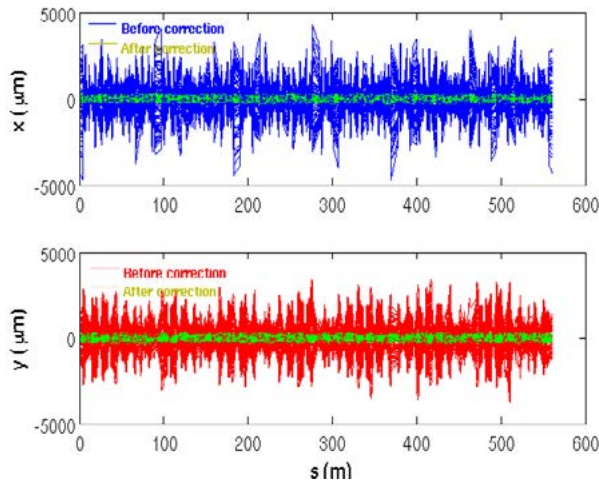
Figure 2-33 : The closed orbit before and after correction.
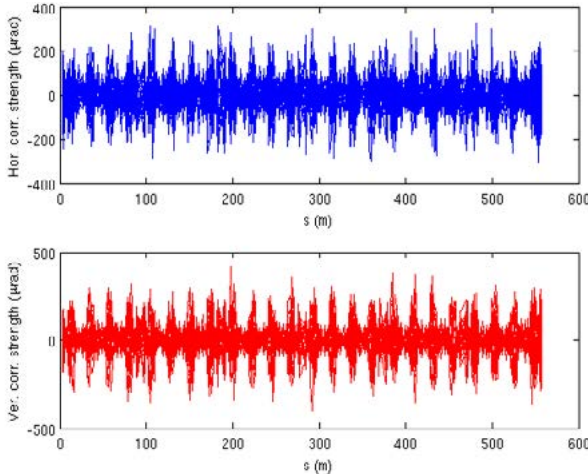
Figure 2-34 : Corrector strengths after closed orbit correction for all the error seeds.

The RMS and MAX values of the corrected orbit and corrector strength for all the seeds and in the all elements are given in Table 2-16. As shown, the RMS x/y value of the corrected orbit over all elements of the machine is less than 50 μm, while at the BPMs the orbit is virtually corrected to zero. The rms corrector strength is 100 μrad.

Table 2-16 : The RMS and MAX values of H/V orbit at all elements after correction and corresponding corrector's strength.

Parameter	X rms	X max	Y rms	Y max
Orbit deviation [μm]	42.5	336.97	47.3	357.33
Corrector strength [μrad]	76.47	360.2	90.02	460.5

2.3.3.5. Optics Correction

Once the orbit is corrected we proceed with the correction of the linear optics. Several alternative methods of correction can be used and in what follows we present an example of the application of the well known LOCO (Linear Optics from Closed Orbit) package [2]. The applicability of these techniques is enabled by having independent power supplies on all the quadrupoles, including quadrupole trim capabilities in the DQs. LOCO provides the corrections required to the gradients of the normal and skew quadrupoles. The application of LOCO has been tested in a simple case where we assign well defined errors to a subset of elements to check the ability of LOCO to pinpoint where the errors are. This analysis identified a degeneracy in the LOCO matrix, producing quadrupole corrections fighting each other as is the case of the QF4 pair of quads in the dispersion bump. As a result such quadrupoles are now locked together in the LOCO error fit procedure. A typical example of optic correction with LOCO is described in Figure 2-35 where we plot the optics function before and after correction for a random set of errors from Table 2-15.
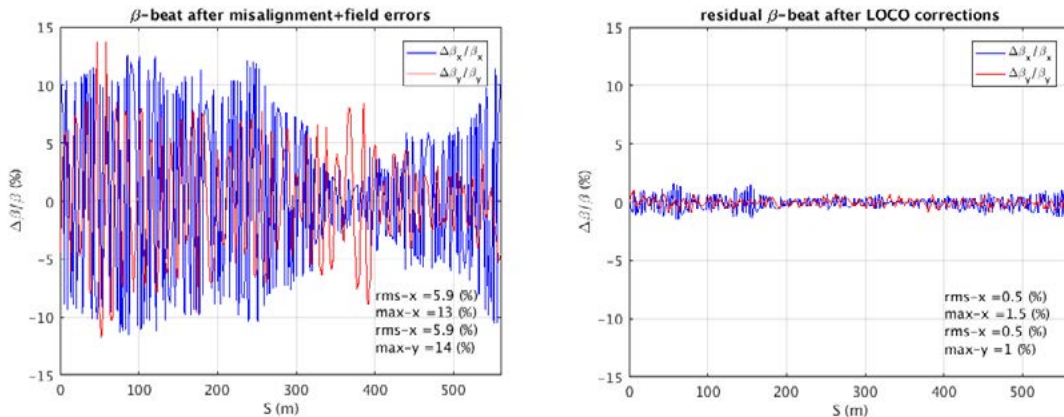
Figure 2-35 : H/V beta-beat before (left) and after (right) correction.

The corresponding correction required to the quadrupole gradients are shown in Figure 2-36
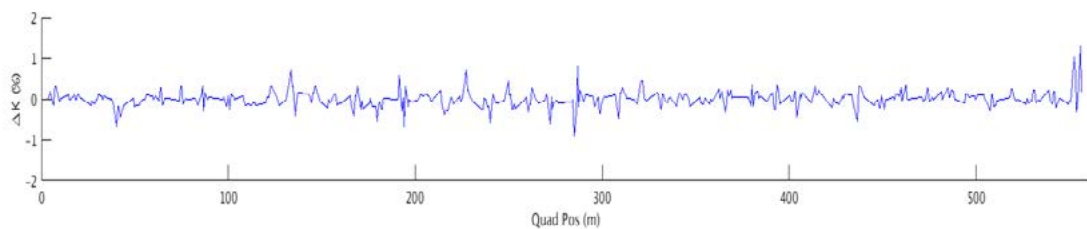
Figure 2-36 : Random quadruple gradient error (in %) reconstructed with LOCO.

The results reveal that the peak-to-peak of the uncorrected H/V beta-beating is within ±15% and can be corrected to below 1% in both planes with quadrupoles variation well below 1%. This procedure guarantees also the correction of the horizontal dispersion (not shown).

2.3.3.6. Vertical Dispersion and Linear Coupling Correction

Vertical dispersion and linear coupling have to be corrected in order to control the value of the vertical emittance. It is likely that operations will aim at providing a small vertical emittance in the single digit pm, provided the impact on the Touschek lifetime is manageable. Taking as an example 8 pm, as in our present lattice, this value corresponds to a coupling ratio of 5% in Diamond-II. The coupling correction is also based on the LOCO package, and uses 96 skew quadrupoles in dispersive regions and 48 skew quadrupoles located in zero dispersion regions to control the betatron coupling.

The effectiveness of the coupling correction with LOCO was tested on a set of random errors from Table 2-15. After orbit correction the emittance ratio k = $\varepsilon_y/\varepsilon_x$ averaged over 30 seeds is 12.3% corresponding to a vertical emittance of 19.4 pm. The dispersion function before and after correction is displayed in Figure 2-37.
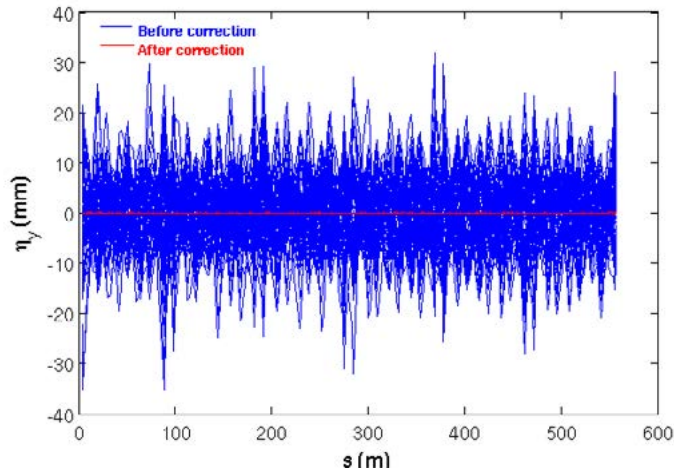
Figure 2-37 : Vertical dispersion along the ring before and after correction.

With this correction algorithm, the peak dispersion function is corrected by more than one order of magnitude, from around a few tens of millimetres to few hundreds of micrometres. The rms value of the distorted and corrected dispersion function is 7.5 mm and 80 μm respectively. A full LOCO correction reduces the coupling to K = 0.6% corresponding to a vertical emittance of ~1pm. The corresponding strength of the skew quadrupoles is shown in Figure 2-38.
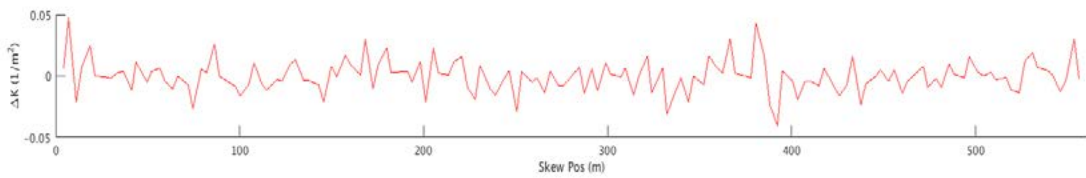
Figure 2-38 : The strength of skew quadrupoles for vertical dispersion and coupling correction.

As displayed, the maximum strength of skew quadrupole is 0.05 m^{-2} which corresponds to an integrated gradient of 0.08 m^{-1}, comparable to that used in Diamond, 0.12 m^{-1}. The skew quadrupoles can be comfortably powered to produce any betatron coupling up to 12.3% (19.4 pm).

2.3.3.7. Impact of Imperfections on the Nonlinear Dynamics

With the successful correction of the orbit, optics and coupling, we turn now to the analysis of the impact of the errors on the nonlinear beam dynamics to complete the commissioning simulations.

Due to the intensive computing nature of this chain of simulations, the nonlinear beam dynamics has been mostly analysed using the reduced set of errors of Table 2-15. The rationale for this is also the fact that the commissioning simulation tends invariably to produce very well corrected lattices with a level of symmetry that is not generally maintained during standard operation. The error set of Table 2-15 which produces larger optics errors than the output of the commissioning simulation is therefore seen as pessimistic and will ensure that the non-linear dynamics is robust enough to tolerate "real life" optics

errors. We have however checked for a limited number of cases that a full non-linear dynamics simulation starting from the output of the commissioning procedure is consistent with this approach. Simulations made in these conditions are explicitly mentioned below.

Particle tracking has been carried out for 30 random error seeds of Table 2-15 and the nonlinear beam dynamics has been investigated. The on-momentum dynamic aperture (DA) is displayed in Figure 2-39.
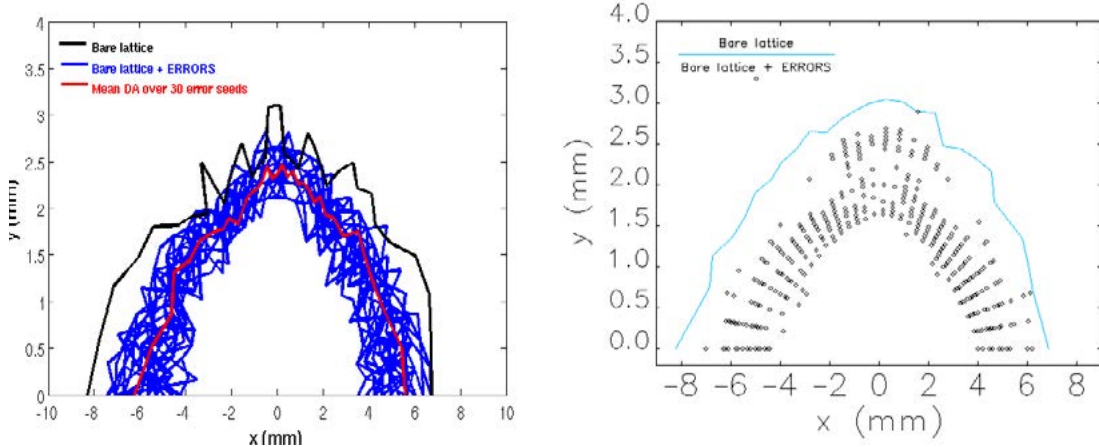
Figure 2-39 : The dynamic aperture with the errors of Table 2-14 after correction (left) and with the errors of Table 2-15 (right).

The dynamic aperture is on average ±6 mm in the horizontal and ±2 mm in the vertical planes which is sufficient for off axis injection. Frequency maps and tune diffusion plots are shown in Figure 2-40 for one representative seed.
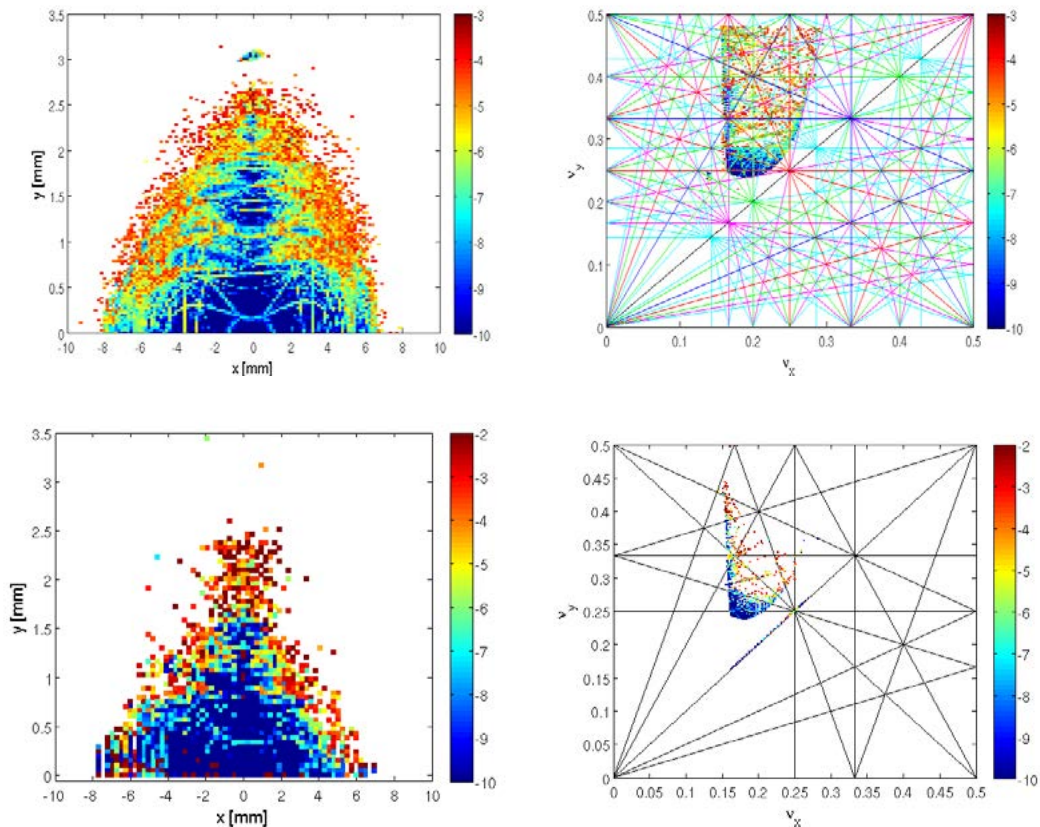
Figure 2-40 : Tune diffusion map of the dynamic aperture and corresponding frequency map with the errors of Table 2-14 after correction (top) and with the errors of Table 2-15 (bottom).

The dependence of the tune with energy deviation for the bare lattice has been shown in Figure 2-26. It was highlighted that the tunes drift towards the Qy = ½ resonance at approximately ±2% energy deviation. The addition of errors produces a strong limitation in the momentum aperture (MA). Figure 2-41 shows the off-energy dynamic aperture and corresponding frequency map both after the commissioning correction and for the reduced error set of Table 2-15, showing the potential harm of the hole in the off-momentum aperture at -2.5%. Figure 2-42 shows the contours of the off-momentum apertures in the (x, dp/p) and (y, dp/p) planes corresponding to 30 seeds.
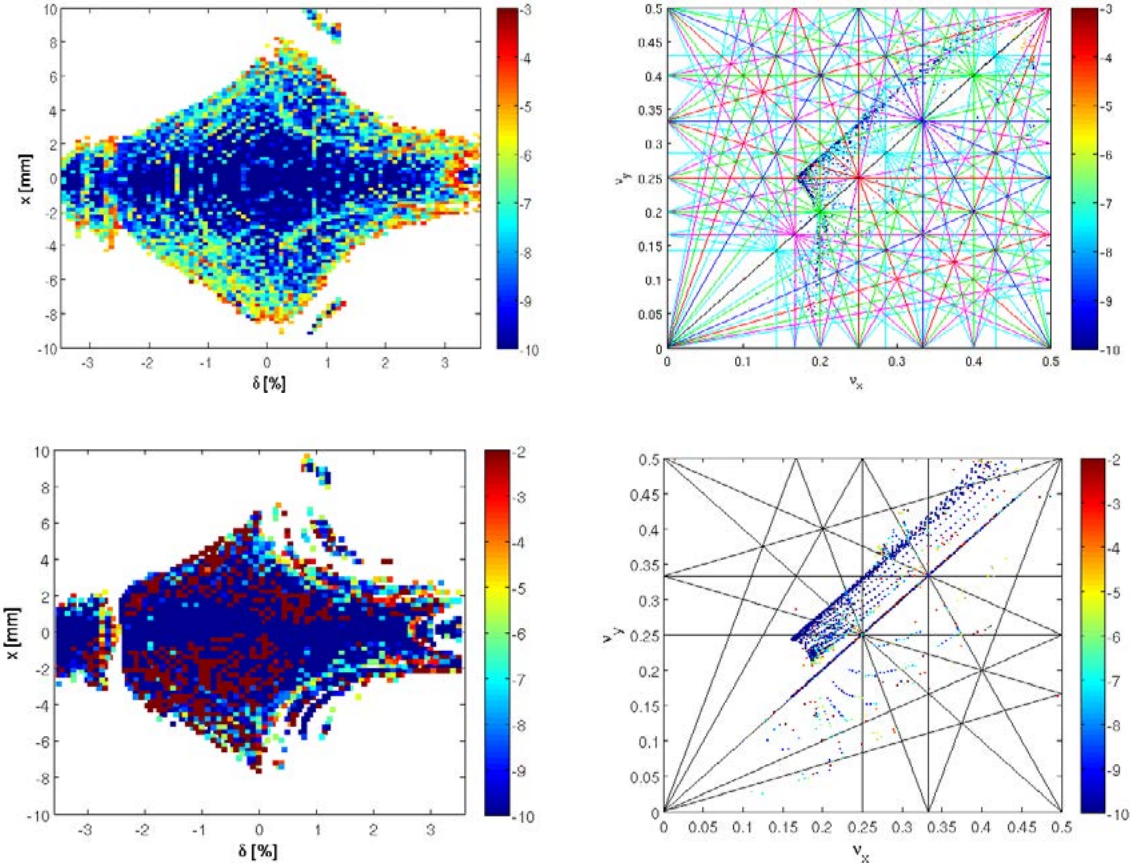
Figure 2-41 : Tune diffusion map of the off-momentum dynamic aperture and corresponding frequency map with the errors of Table 2-14 after correction (top) and with the errors of Table 2-15 (bottom).
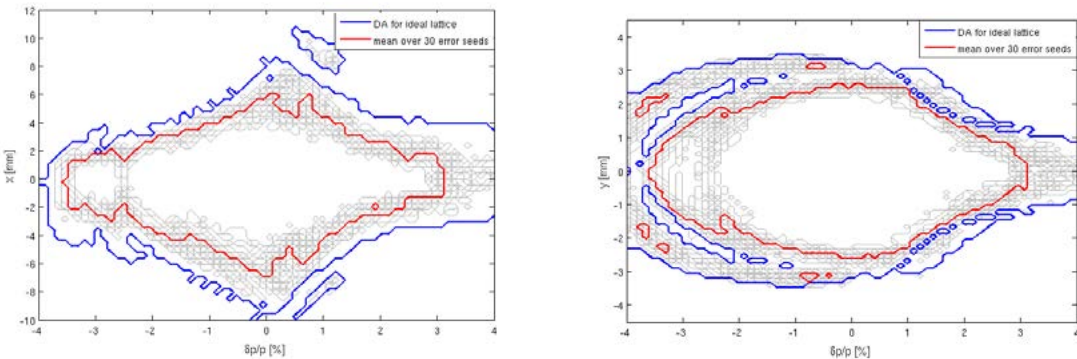
Figure 2-42 : Contours of the off-momentum dynamic aperture for 30 seeds from Table 2-14 after correction, in (x, dp/p) (left) and (y, dp/p) (right).
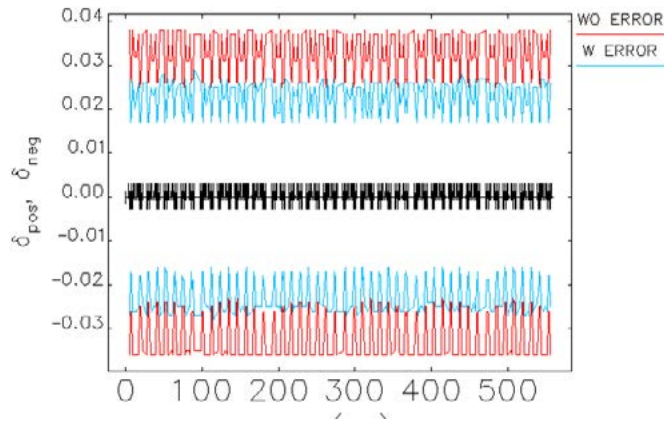
Figure 2-43 : Momentum aperture for the bare lattice (as in Figure 2-27) and for one of the worst error seeds in Table 2-15.

An example of the impact of the errors on the MA is shown in Figure 2-43. The resulting lifetime over 20 seeds is 0.95 h ± 0.12 h (see Section 2.3.4.9). The reduction is due to the crossing of the $Q_y = 1/2$ resonance for off-momentum particles. It is clear however that further optimisation work is needed to improve this value. In addition, the use of a higher harmonic cavity has been analysed in depth in Section 2.3.4. However, preliminary studies of including reverse bends in the lattice show significant improvements in both lifetime and dynamic aperture can be achieved. Detailed studies of the beam dynamics and engineering implications will be carried out during the technical design phase.

2.3.3.8. Lattice with Errors and Insertion Devices

Beam dynamics simulations using the insertion devices (IDs) model in elegant and the ID "kick maps" for the Apple-II devices show that the perturbation of all proposed IDs for Diamond-II (see Section 2.2.1) on the linear optics can be well controlled with quadrupole corrections based on LOCO or simpler approach constraining only quadrupoles close to the IDs.

To single out the effect of the proposed Diamond-II IDs, we have computed the DA on the bare lattice plus the IDs only (no errors) without any correction. The results are reported in Figure 2-44 which show that, even without optics correction, the effect of the IDs only is not too detrimental on the DA.
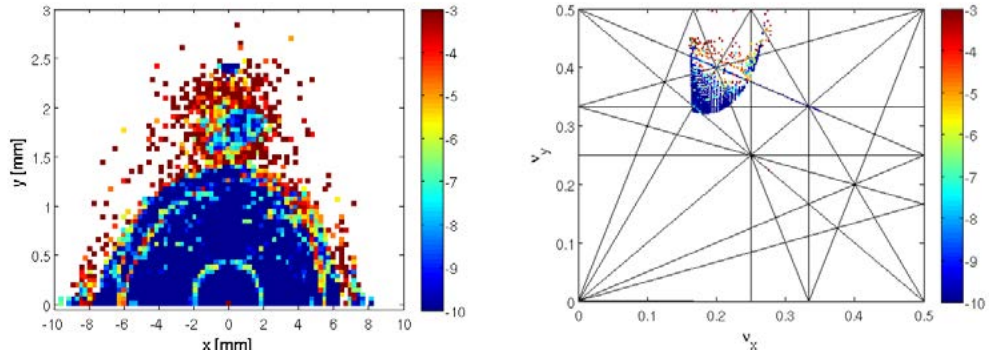
Figure 2-44 : DA and FM with no errors and with all IDs. No correction of the linear optics (to be compared to Figure 2-24; note the tune shift in the vertical plane).

A more realistic case was simulated including all IDs and the reduced errors of Table 2-15. The beta beating after orbit correction is reported in Figure 2-45 for one representative error seed. The perturbation to the optics function is within ±10% in the horizontal plane and ±15% in the vertical plane, the last one mostly dominated by the effect of the two wigglers I12 (4.2 T) and I15 (3.5T).The corresponding DA and FM are reported in Figure 2-46 before LOCO correction. The DA is reduced because of the uncorrected beta beating.
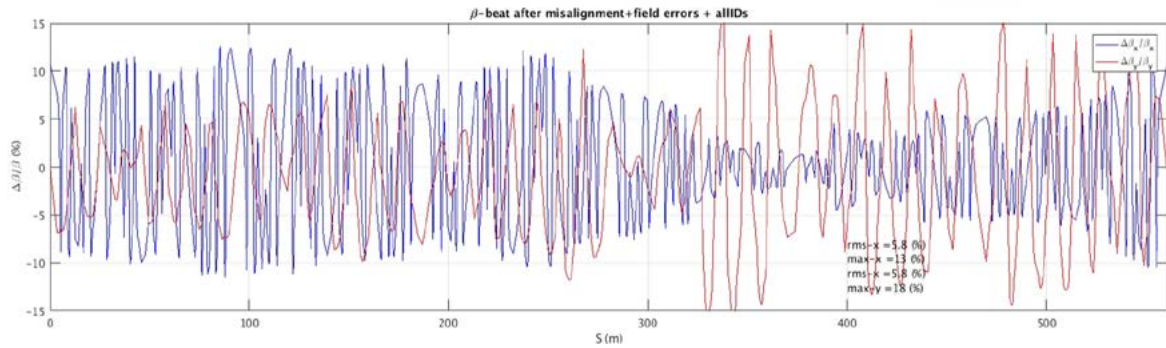
Figure 2-45 : Beta-beating with all IDs and errors from Table 2-15 after orbit correction.
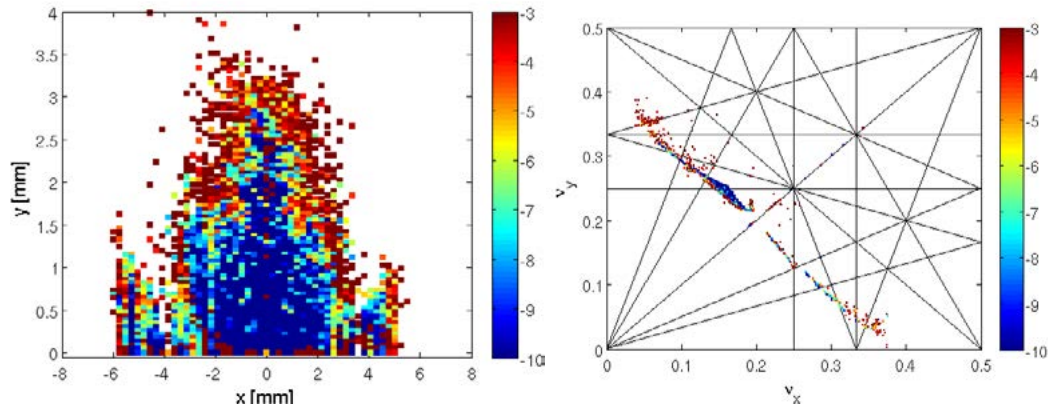
Figure 2-46 : DA and FM with IDs and errors after orbit corrections (to be compared to Figure 2-40).
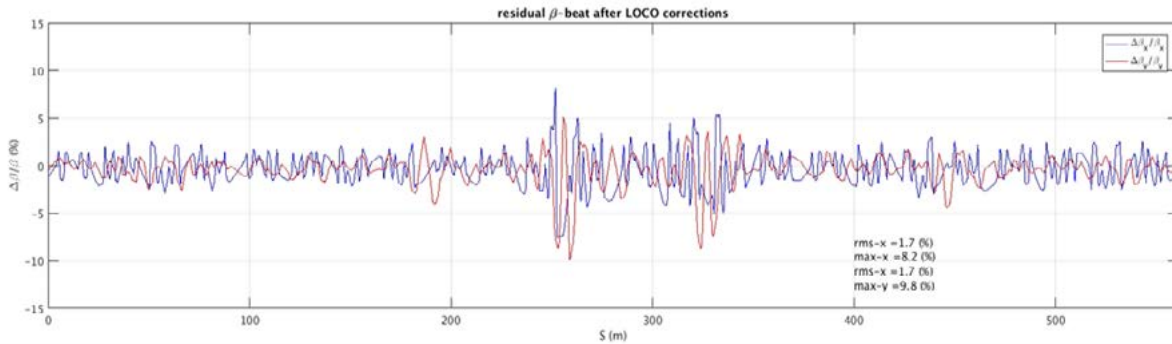
Figure 2-47 : Residual beta-beating of the lattice with all IDs and errors after LOCO correction (to be compared to Figure 2-45).

The beta beating and linear optics were fully corrected with LOCO. An example of one error seed is reported in Figure 2-47. Some local beta-beating remains around the wigglers in straights 12 and 15. This will be improved at a later stage. It should be mentioned that the vertical emittance for the lattice in Figure 2-47 is corrected to less than 1 pm. Figure 2-48 shows the DA and the FM after applying LOCO correction to the machine with all IDs and errors.
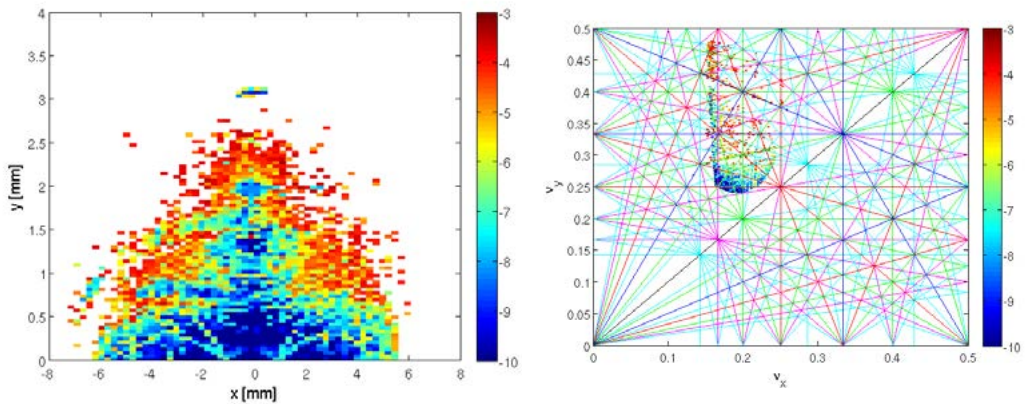
Figure 2-48 : DA and FM with IDs and errors after a full correction of the linear optics with LOCO (to be compared to Figure 2-46).

The impact of the IDs and errors on the MA has been studied using 20 seeds from Table 2-15 assuming a coupling correction to 5%. The results are shown in Figure 2-49. The corresponding lifetime is 1.29 h ± 0.13 h for 300 mA, 934 bunch, operation, somewhat larger than the one obtained with all errors only. The reason for this change is related to the combined impact of the IDs on the energy spread, bunch length and emittance.
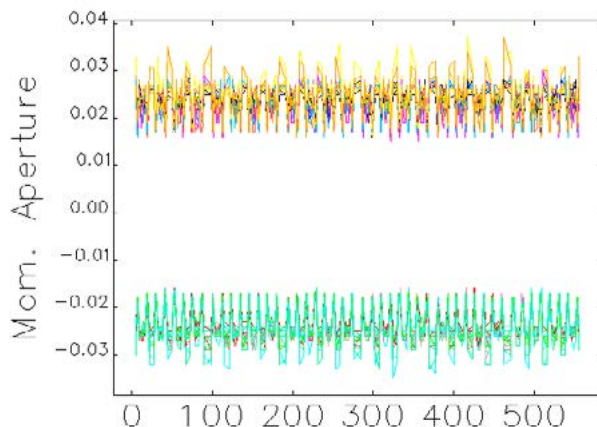
Figure 2-49 : Momentum aperture with IDs and reduced errors from Table 2-15.

IDs have a strong impact on the equilibrium bunch properties of the Diamond-II lattice. In fact the full complement of IDs reduces the emittance from 160 pm to 125 pm and increases the energy spread from 0.078% to 0.1%; the RF voltage required also generates a longer bunch length from 9.86 ps to 10.78 ps. As a consequence the lifetime with IDs and errors (1.29 h) is larger than the lifetime of the lattice with errors (0.95 h).

References

[1]   Presentations at the Workshop on Diffraction Limited Storage Rings (DLSR 2013), SLAC National Accelerator Laboratory, Stanford, USA, Dec. 2013 https://portal.slac.stanford.edu/sites/conf_public/dlsr2013/Pages/default.aspx.

[2]   J. Safranek, "Experimental determination of storage ring optics using closed orbit response measurements", Nucl. Inst. and Meth. A388, (1997), p. 27-36.

[3]   R. Bartolini et. al., *Double-double bend achromat cell upgrade at the Diamond Light Source: From design to commissioning*, PRAB 21, 050701 (2018).

[4]   V. Sajaev and M. Borland, *Commissioning simulations for the APS upgrade lattice*, IPAC2015, Richmond, USA., p. 553-553 (2015).

[5]   T. Hellert et al., *Simulation of trajectory correction in early commissioning of the Advanced Light Source upgrade*, IPAC2018, Vancouver, BC, Canada, p. 4256-4258 (2018).

[6]   M. Borland, *Elegant: a flexible sdds-compliant code for accelerator simulation*, Advanced Photon Source, Argonne National Laboratory, USA, Report No. LS-287 (2000).

[7]   A. Terebilo, *Accelerator toolbox for MATLAB*, in Proc. Workshop on Performance Issues at Synchrotron Light Sources Berkeley, California, October 2-4, 2000.

2.3.4. Collective Effects and Lifetime

2.3.4.1. Introduction

The Diamond-II design raises a number of concerns with regard to collective effects and instabilities. The required magnet gradients lead to reduced bore radius, which in turn requires a narrow vacuum pipe. The proposed 10 mm radius circular pipe will greatly increase the resistive wall impedance compared to the current Diamond ring. This can be partially compensated by utilising a copper pipe instead of stainless steel, but this would in turn be degraded by introducing NEG coating to improve vacuum pumping and reduce gas desorption. In addition, other vessel materials than copper will be necessary in areas where lower conductivity is required (see Section 2.5.6.1).

The multibend achromat structure of Diamond-II results in longer damping times compared to the current ring, as shown in Table 2-8. Loading the lattice with all IDs reduces the damping times to be similar to those in the existing ring (see Table 2-11), but at the cost of significantly increased resistive wall impedance.

In the current ring, instabilities are compensated to some extent by operating at positive chromaticity in both planes. The chromaticity has recently been reduced in the horizontal plane to improve lifetime and injection efficiency, and it is anticipated that the nonlinear dynamics for Diamond-II may impose further constraints on chromaticity.

The current ring requires multibunch feedback in both transverse planes to ensure stable operation for users. A longitudinal feedback system was recently installed, but it is not required in normal operation. Diamond-II will certainly need these systems, but other than investigating how much corrective power will be required, it is not anticipated for there to be any need for qualitative change to the multibunch feedback systems.

The Diamond-II lattice has a significantly lower Touschek lifetime than the current ring, which poses operational problems regarding the frequency of top-up injection and possible disturbance to user beam. This has driven the case for operating with a harmonic cavity for bunch lengthening, which can improve lifetime as well as reducing the impact of intrabeam scattering (IBS) and RF heating of vacuum components. In addition, operation with a harmonic cavity increases the synchrotron frequency spread, which damps instabilities. For a double RF system the voltage seen by the beam is given by:

$$V(\varphi) = V_{\mathrm{rf}} \sin(\varphi + \phi_s) + kV_{\mathrm{rf}}(n\varphi + n\phi_h),$$

where V_{rf} is the main cavity voltage, ϕ_s the synchronous phase, kV_{rf} the harmonic cavity voltage, n the order of the harmonic cavity and ϕ_h the harmonic phase. If the voltage and phase of the harmonic cavity is chosen such that both the first and second derivative of the total voltage at the synchronous phase is zero a quadratic potential well is formed, resulting in long bunches. The parameters for when this occurs are given by:

$$k_{\mathrm{fp}} = \sqrt{\frac{1}{n^2} - \frac{1}{n^2-1}\left(\frac{U_0}{eV_{\mathrm{rf}}}\right)^2}$$

$$\tan\left(n\phi_{h,\mathrm{fp}}\right) = -\frac{\dfrac{nU_0}{eV_{\mathrm{rf}}}}{\sqrt{(n^2-1)^2 - \left(n^2 \dfrac{U_0}{eV_{\mathrm{rf}}}\right)^2}},$$

where U_0 is the energy loss per turn and e the electron charge [1]. These conditions are commonly called flat potential conditions and are used for comparisons in this report. In the case of a passive harmonic cavity, the flat potential conditions require a certain shunt impedance, which depends on the beam current as:

$$R_{s,\mathrm{fp}} = \frac{k_{\mathrm{fp}}V_{\mathrm{rf}}}{2IF_{\mathrm{fp}}\left|\cos\psi_{h,\mathrm{fp}}\right|},$$

where I is the beam current, F_{fp} the bunch form factor and $\psi_{h,\text{fp}}$ the cavity tuning angle given by:

$$\psi_{h,\text{fp}} = \frac{\pi}{2} - n\phi_{h,\text{fp}}.$$

This means a single passive harmonic cavity cannot be employed to achieve the flat potential conditions at more than one beam current [2]. This can however be achieved by employing several cavities tuned differently with respect to each other. Another option is to relax the conditions to only require the first derivative of the voltage to be zero.

2.3.4.2. Impedance Model

An impedance model has been developed which takes into account the expected larger contributions to the impedance. Since detailed engineering design work has not yet taken place, geometric contributions in particular must be considered a first approximation. A summary of included components can be found in Table 2-17.

The Diamond-II ring has a total length of 560.6 m. There will be 20 in-vacuum undulators with ~38 m total length, compared to 16 in-vacuum IDs with 32.4 m total length in the current ring. The IDs currently installed mostly have a minimum full gap of 5 mm, but this is planned to be reduced to 4 mm in Diamond-II. The magnet arrays are covered with a copper foil to provide electrical continuity. Transitions to the normal vacuum pipe will need redesigning, but it is assumed that the overall impedance will remain similar.

Diamond-II will use NEG coating on the vacuum pipe. However, there are many varieties of NEG with greatly varying electrical properties, and there are competing claims regarding the effects of thin coatings of varying thickness. In the best case, NEG could be effectively transparent at the frequencies relevant to the bunch lengths Diamond-II will have, while in worst cases there could be a significant increase in resistive wall (RW) impedance. At this stage in the design process, the approach has therefore been chosen to study the consequences of a range of conductivities to determine the limitations, rather than attempting to assign specific properties to the pipe material at this stage. The conductivities for copper ($\sigma = 5.96$ 10^7 S/m) and stainless steel ($\sigma = 1.37$ 10^6 S/m) were chosen as upper and lower limits for the range. Analytical calculations of the resistive wall impedance of a two-layered circular pipe [3] using a 0.5 - 1 µm NEG layer ($\sigma = 1.099$ 10^6 S/m) show an impedance which is significantly lower than for a pure stainless steel pipe and therefore the effective conductivity of a copper pipe with NEG coating can be assumed to be well within the studied range. More detailed studies of the impedance effect of NEG coating will be conducted during the technical design phase including a more detailed model of the vacuum chamber geometry and materials.

Table 2-17 : Impedance database showing significant components, the number in the ring, transverse dipole kick factors (k_x, k_y) and longitudinal loss factor (k_z). The number of bellows and pumping ports is yet to be determined so the number used is only for preliminary simulations, indicated by an asterisk.

Component	Number in ring	k_x (V/pC/m)	k_y (V/pC/m)	k_z (V/pC)
BPM	252	1.6e-3	1.6e-3	8.5e-3
Dipole chamber	144	1.8e-3	9.1e-4	5.9e-3
ID transitions	20	0.014	0.013	7.0e-3
Bellows	tbd (252*)	6.9e-4	3.8e-4	4.3e-3
Horizontal stripline	1	1.6e5	1.6e-5	1.06
Vertical stripline	1	1.5e-5	1.5-e5	0.837
Longitudinal kicker cavity	1	0.000	0.038	1.044
Pumping ports	tbd (252*)	0.013	1.2e-3	4.6e-3

So far, the resistive wall impedance has been taken to consist of 522.6 m of vacuum pipe with 10 mm radius and various possible materials, and 38 m of copper pipe with varying vertical aperture as shown in Table 2-2. For simplicity, the horizontal radius has been kept to 10 mm in all cases whereas in reality the horizontal aperture will likely be larger through the in-vacuum ID straights.

The Diamond-II upgrade will change the storage ring RF system from CESR-B superconducting cavities to EU HOM-damped normal conducting (NC) cavities. Due to the decreased voltage and power per cavity, there will be 8 NC cavities, compared to the two superconducting cavities currently in use. Two NC cavities have recently been installed in the existing Diamond ring to increase resilience, and studies show that they are well HOM-damped and contribute little to the machine impedance.

Notably, while the superconducting cavities themselves are relatively benign, the transition tapers are a significant source of impedance. Since the normal conducting cavities are much smaller and have correspondingly less extreme transitions, the overall impedance of RF components is expected to be less for Diamond-II.

The Diamond ring currently contains 173 BPMs, and this will increase to 252 in Diamond-II. BPMs added more recently to the Diamond ring for the DDBA upgrade are of a newer type based on an ESRF design with much reduced impedance compared to the original Diamond design. A rough preliminary design for Diamond-II BPMs has been created based on putting the ESRF-style buttons into the cylindrical Diamond-II beam pipe. More detailed design work would be expected to reduce impedance further, particularly in the transverse plane.

Flanges in the existing Diamond ring mostly use a CF flange which is essentially seen by the beam as a pillbox cavity with a nominal length of 0.1 mm. In practice, the size of the cavity is not well controlled, and heating has been observed in several locations. This remains true for a different design of helicoflex flanges used in the DDBA upgrade, where RF heating has also been observed. Preliminary studies for Diamond-II suggest several possible flange designs which should produce a true zero gap and therefore be virtually invisible to the beam. Flanges have therefore not been included in the impedance model at this point.

Design work has not yet been done in detail for other components such as bellows, dipole chambers, pumping ports, etc. These have been assumed to be similar to the existing Diamond designs, or have had simple approximate models created for the purposes of impedance simulations. For the pumping ports, a design was created based on those used in the DDBA upgrade, adapted to the circular beam pipe for Diamond-II. This has significant impedance in the horizontal plane, so it is clear further work will be required to produce an optimised design suitable for Diamond-II.

Simulations for geometric impedances were carried out in CST Studio, using a 3 mm (10 ps) bunch length. Future work with more time available for simulations will use a reduced bunch length (1 mm or less) to ensure the impedance is well sampled. For single and multibunch simulations, these impedances were fitted to a small number of resonators for input into tracking codes. Due to engineering tolerances, simply multiplying the impedance of a single component by the number in the ring is not a fair representation, resulting in shaper peaks with greater amplitude than would be expected in reality. A full simulation including all error tolerances is beyond the scope of this report, so this effect was approximated by applying an error to the resonator frequency in a Gaussian distribution with sigma equal to 1% of the simulated frequency. An example is shown for BPMs in Figure 2-50.
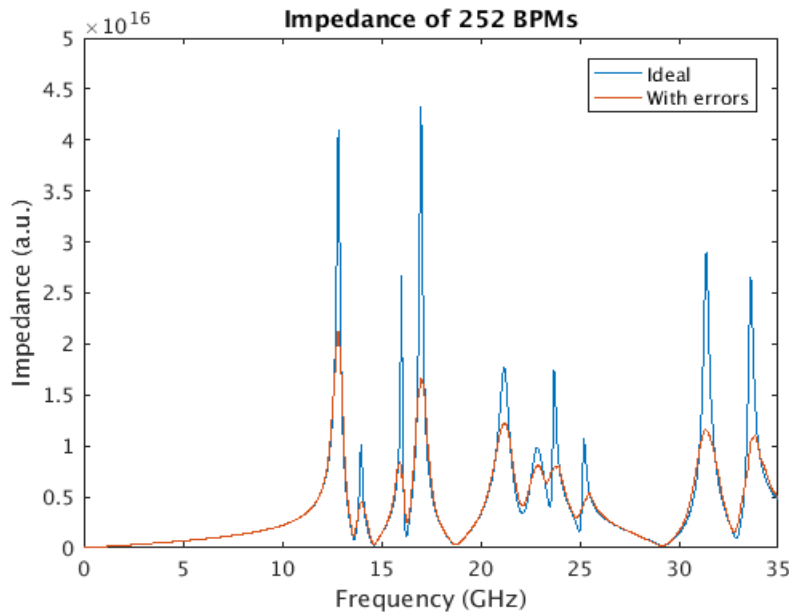
Figure 2-50 : Total impedance of 252 BPMs, comparing ideal and Gaussian error distribution of resonator frequency.

2.3.4.3. Single Bunch Instabilities

Single bunch instability thresholds were simulated using both the sbtrack [4] and mbtrack [5] macroparticle tracking

codes. Simulations were carried out for the nominal bunch length without harmonic cavity and considering a range of chromaticities. The longitudinal instability threshold is considered to be the current at which the energy spread begins increasing, indicating the onset of a microwave instability. Transverse instability thresholds are considered to be the current at which the transverse beam size or centre of mass motion continuously increases. The fill patterns are discussed in more detail in Section 2.3.4.10, but for comparison to the instability thresholds, the bunch current requirements for the two fill patterns that have been considered so far are displayed in Table 2-18. For a standard fill pattern of 900 bunches at 300 mA total current, the required single bunch current is 0.33 mA. For a hybrid fill pattern consisting of a train of 685 bunches plus a single 3 nC high charge bunch, the required single bunch current is 0.44 mA for the train and 1.6 mA for the camshaft bunch.

Table 2-18 : Bunch charge and current for different fill patterns. The values for a uniform fill are included for comparison.

Fill pattern	Bunch charge [nC]	Bunch current [mA]
Uniform fill (934 bunches)	0.60	0.32
Standard mode (900 bunches)	0.62	0.33
Hybrid mode (685 bunches)	3.0 (camshaft), 0.82 (train)	1.6 (camshaft), 0.44 (train)

Figure 2-51 displays the phase shift and bunch lengthening as a function of bunch current including various effects for a circular copper pipe with 10 mm radius. Table 2-19 shows the simulated microwave thresholds for both stainless steel and copper pipes. The instability thresholds are lower for a stainless steel pipe compared to copper, but for all the simulated cases the microwave instability threshold is well above the bunch current needed for both the standard and hybrid mode. It can also be seen that the thresholds increase when the IDs are closed.
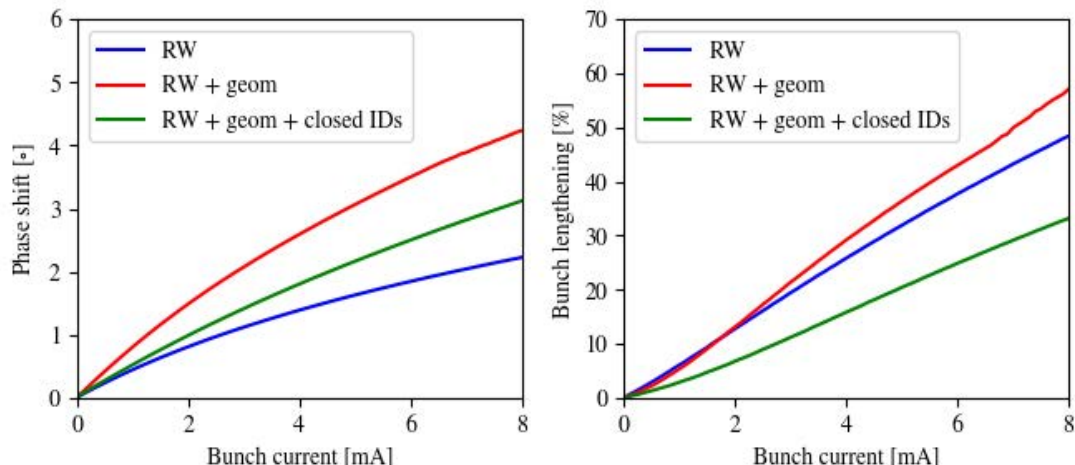
Figure 2-51 : Phase shift (left) and bunch lengthening (right) for a copper pipe with 10 mm radius for the bare lattice including resistive wall (RW), bare lattice including resistive wall and geometric impedances and the lattice including resistive wall, geometric impedance and all IDs closed.

Table 2-19 : Microwave instability thresholds.

	Stainless steel	Copper
Bare lattice, resistive wall	4 mA	> 8 mA
Bare lattice, resistive wall + geometric impedance	3 mA	6.5 mA
Closed IDs, resistive wall + geometric impedance	6 mA	> 8 mA

Transverse instability thresholds are shown in Figure 2-52. As for the longitudinal plane, three cases have been considered, just resistive wall impedance, the full impedance model including resistive wall and resonators, and the full impedance model including IDs, including both their effects on impedance and the ring optics. Including only the resistive wall impedance, both copper and stainless steel meet the bunch current requirement for a 900 bunch fill even at zero

chromaticity in both planes. For a hybrid fill, copper meets all requirements at zero chromaticity, whereas stainless steel needs a chromaticity between 1 - 2 in the horizontal and at least 2 in the vertical plane to meet the requirement for the camshaft bunch. Including resonators makes only minor differences to the instability thresholds, and can even increase the threshold in some cases. Including the effects of IDs makes a significant difference in both planes, especially reducing the vertical threshold to 1.1 mA at zero chromaticity for copper, which is no longer enough for the camshaft bunch in hybrid mode. Resistive wall appears to be the dominant impedance source for the ring, and the reduced damping times from ID radiation is not sufficient to compensate for the narrow vertical apertures when the in-vacuum IDs are closed. However, using a chromaticity of ~1.5 could allow stable operation without need for active feedback.
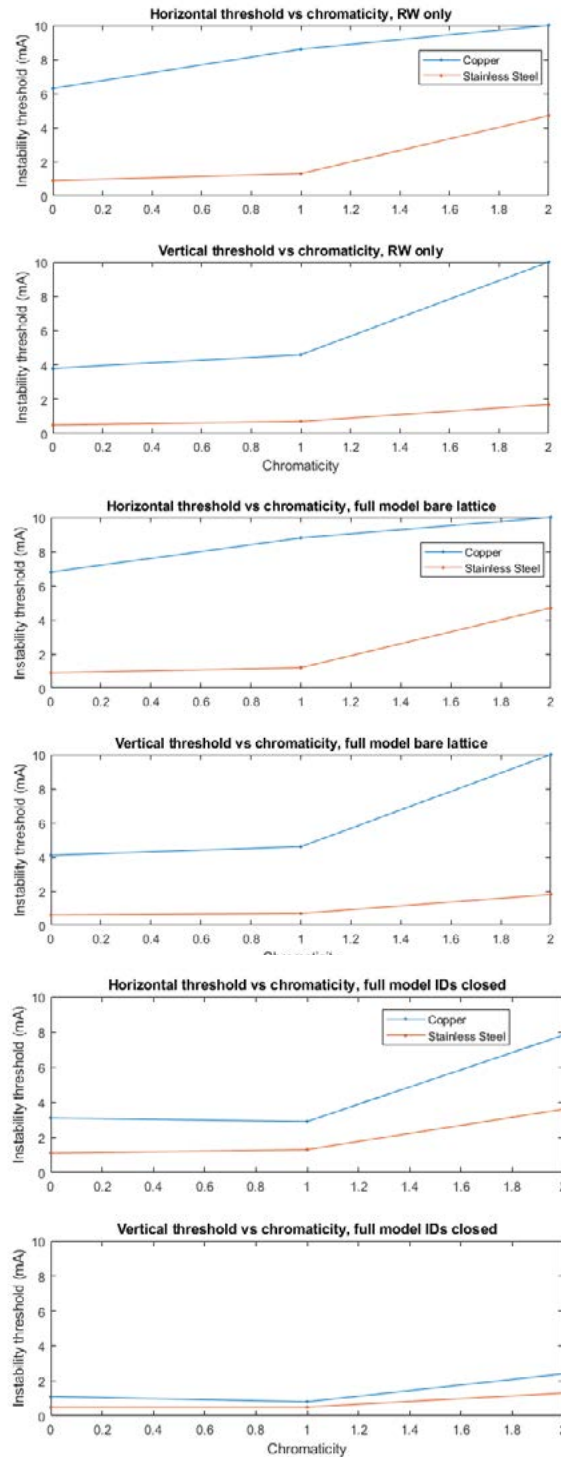
Figure 2-52 : Single bunch instability thresholds vs. chromaticity with copper and stainless steel beam pipe for resistive wall only (top), full impedance model (RW + resonators) (middle) and full impedance model with IDs closed (bottom).

The effect on the single bunch instability thresholds due to a passive harmonic cavity including the effect of transient beam loading when having a gap in the fill pattern will be studied during the technical design phase, but it is expected that a harmonic cavity will help to increase the single bunch instability thresholds.

2.3.4.4. Multibunch Instabilities

Simulations of multibunch instabilities remain to be conducted for Diamond-II, but experience from the current ring provides indication on which effects that can be expected to be most significant.

Diamond historically operated without a longitudinal multibunch feedback (LMBF) system. Recently two normal conducting cavities have been installed to increase resilience to a main cavity failure. At the same time, an LMBF system was installed in order to compensate for any HOMs excited by these. However, measurements show that the HOMs are well damped, see Figure 2-53, and therefore longitudinal feedback is not required to provide stable beam to users. Diamond-II will use 8 similar NC cavities, and due to this experience from the current ring, it is expected that resistive wall impedance will remain the most important factor for longitudinal instabilities.
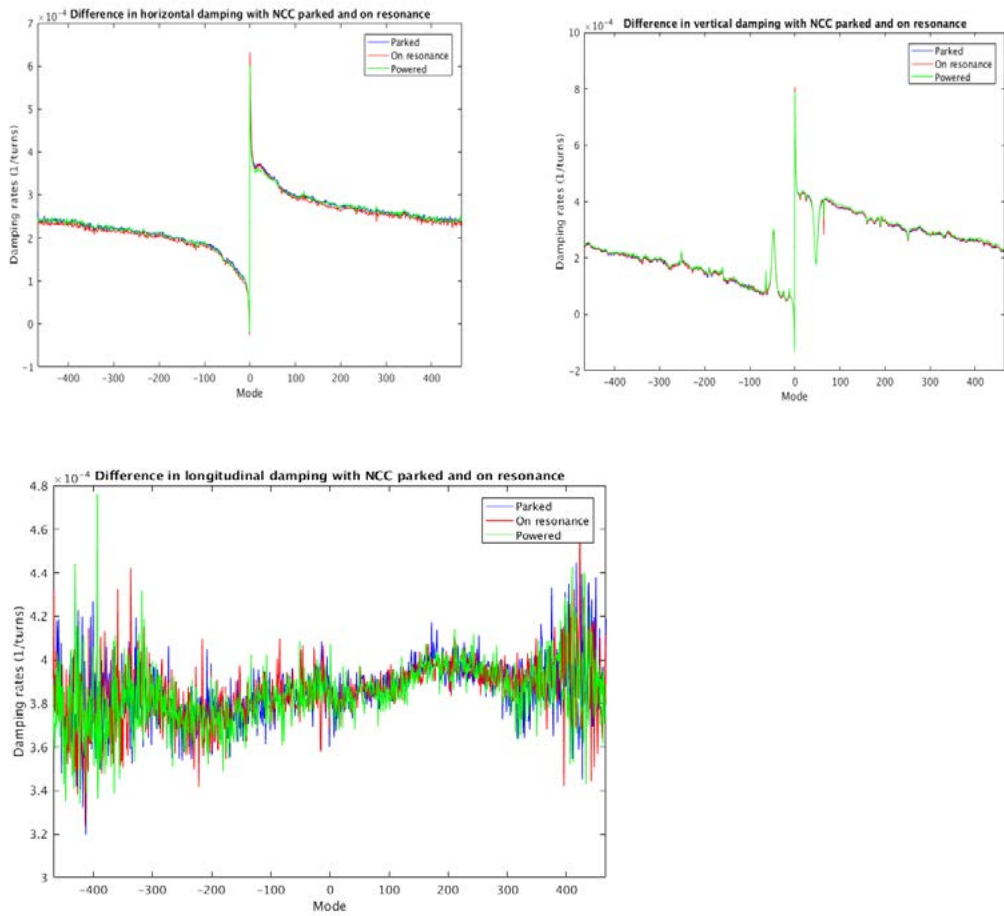
Figure 2-53 : Measured damping rate vs. mode with a normal conducting cavity in different states: horizontal plane (top left), vertical plane (top right) and longitudinal plane (bottom).

In early operations at Diamond, a chromaticity of 2.0 in both horizontal and vertical plane was sufficient to provide stable beam under user conditions. Installation of more in-vacuum IDs, narrow-gap vessels for some ex-vacuum IDs, and various other installations, especially DDBA, have reduced the instability thresholds to the point that transverse multibunch feedback (TMBF) is required in both planes to provide a stable beam. In addition, the optics constraints resulting from DDBA and the more recent DIAD "missing sextupole" scheme have required lowering the horizontal chromaticity to 1.6 to optimise lifetime and injection efficiency. Multibunch instability thresholds after installation of DDBA are shown in Figure 2-54.
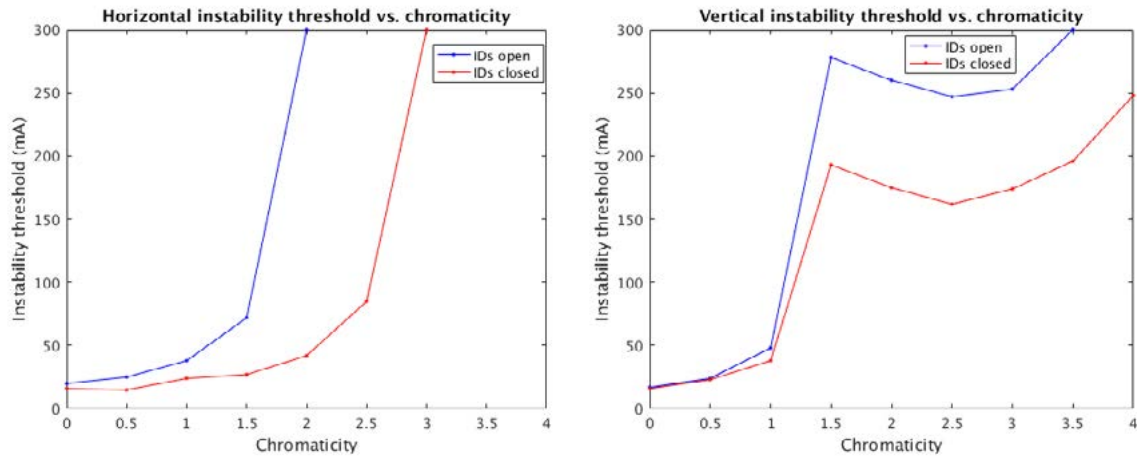
Figure 2-54 : Multibunch instability thresholds vs. chromaticity in the existing Diamond ring for the horizontal (left) and vertical (right) planes.

In the current Diamond ring, the in-vacuum IDs and the vertical collimator are the main narrowband resonators contributing to transverse impedance as seen in Figure 2-55. There is also one high-Q resonator that remains unidentified. Diamond-II will use similar ID transitions and tapers, so there is not expected to be any significant change to the impedance in that regard, although reduced minimum gaps for in-vacuum IDs will increase the resistive wall contribution. A new design for a vertical collimator will be a necessity, since this is the single largest source of transverse impedance in the ring, and although in its current position the effect is benign, a change in position could result in serious detrimental effects to the vertical beam dynamics.
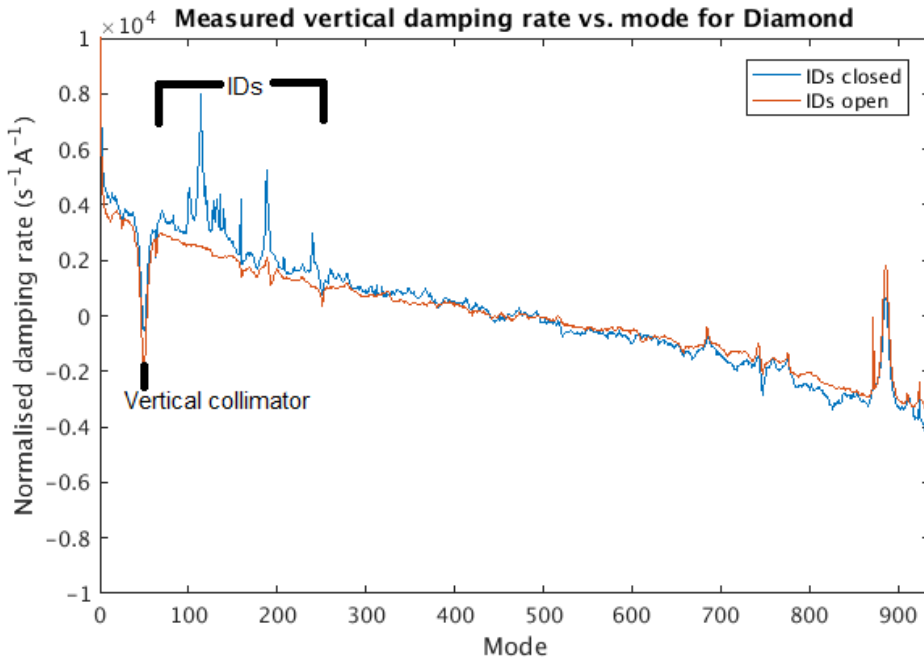
Figure 2-55 : Measured vertical damping rate vs. mode in the existing Diamond ring, with major resonators labelled.

In the light of this, it is expected that resistive wall impedance will be the main driver of transverse multibunch instabilities in Diamond-II, especially when considering the reduction of the beam pipe radius compared to the current ring. Analytical calculations [6], [7] of damping rate as function of mode number at 300 mA current for a 10 mm radius circular copper or stainless steel pipe are shown in Figure 2-56. In the stainless steel case, the most unstable mode has a growth rate of 1,800 s^{-1} in the horizontal plane and 3,300 s^{-1} in the vertical plane, which is similar to measured data in the existing ring. For copper this is reduced to 272 s^{-1} in the horizontal plane and 500 s^{-1} in the vertical plane. While the increased radiation damping with IDs closed brings the transverse damping rates (137 s^{-1} and 118 s^{-1} in the horizontal and vertical planes, respectively) to comparable values as in the current ring, it is not sufficient for Diamond-II to be naturally stable in either plane even for an

all copper beam pipe. Most likely, some combination of positive chromaticity and transverse multibunch feedback will be required as is the case in the current ring. The multibunch instability thresholds including the effect of a passive harmonic cavity and different fill patterns will be studied in more detail during the technical design phase. It is expected that this will help to damp multibunch instabilities, but to which degree remains to be determined.
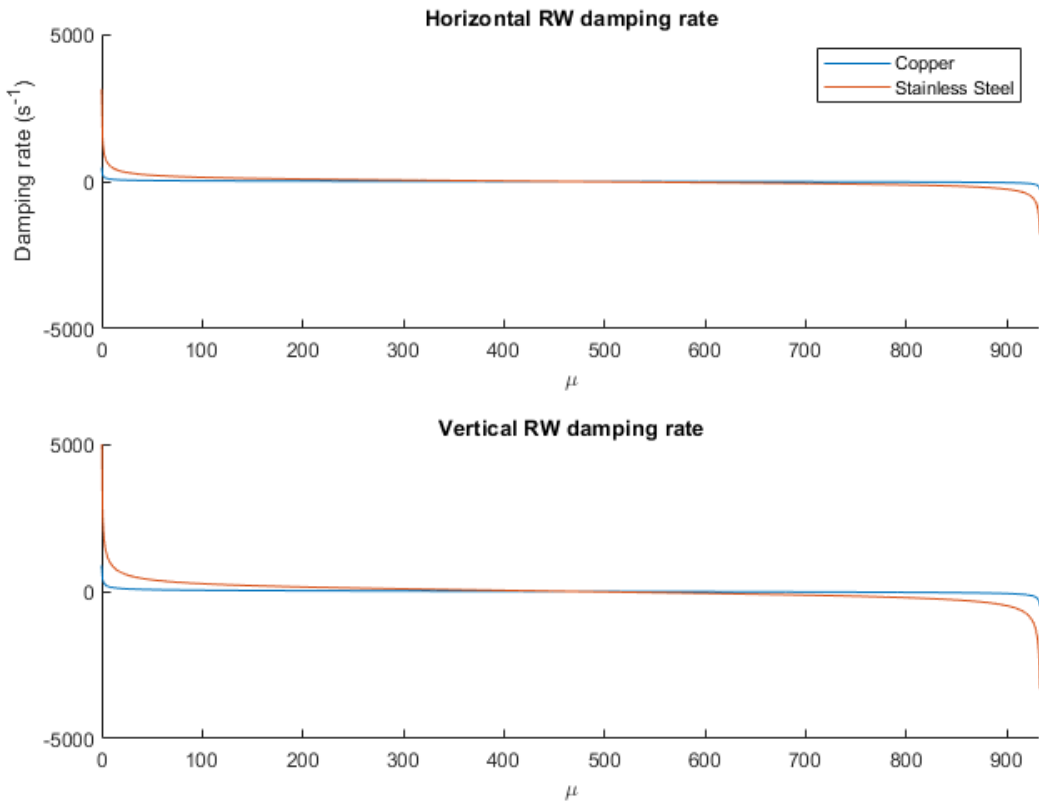
Figure 2-56 : Analytically calculated damping rates vs. mode for different beam pipe materials only including resistive wall impedance.

2.3.4.5. Ion Instabilities

The current Diamond ring operates with a gap in the fill pattern (see Section 2.3.4.10), which serves to both reduce transverse coupled-bunch instabilities and provide ion clearing, and it is expected that a gap will also be required for Diamond-II.

The presence of ion instabilities is a function of vacuum quality in a storage ring. During early operation of the current ring, the beam current was mainly limited by gas lifetime and conditioning of the superconducting RF cavities, with ion instabilities being a lesser concern. Since then, ion instabilities have only been observed for short periods following vacuum interventions, usually conditioning out within a matter of hours or days during dedicated start-up time. The NEG coating to be used in Diamond-II should greatly reduce the initial conditioning period. However, the overall vacuum quality is not expected to be significantly better so the smaller transverse bunch size will increase the effects of ions on beam stability. Simulations of ion instabilities for Diamond-II will be conducted during the technical design phase for optimisation of the fill pattern in conjunction with transient beam loading in a passive harmonic cavity.

2.4.5.6. Harmonic Cavity Parameters

Simulations of the effect of a harmonic cavity have so far been conducted for intrabeam scattering and Touschek lifetime and will presented in the following sections. For comparisons, different sets of cavity parameters have been used as displayed in Table 2-20. The parameters for the normal conducting cavity cases correspond to the flat potential conditions at 300 mA, whereas the parameters for the superconducting cases correspond to the Super-3HC cavity (SLS and Elettra design) [8] tuned to zero the first derivative of the voltage at the synchronous phase and reach similar bunch length.

Table 2-20 : Cavity parameters used in simulations. The tuning angle, detuning and bunch length for a uniform fill are given for 300 mA current.

		Normal conducting		Superconducting	
		Bare	Incl. IDs	Bare	Incl. IDs
Shunt impedance $\left(P = \dfrac{V^2}{2R}\right)$		5.41185 MΩ	4.92679 MΩ	17.68 GΩ	17.68 GΩ
Q factor		20 000	20 000	2.10^8	2.10^8
R/Q		270.6	246.3	88.4	88.4
Tuning angle		99.647°	105.447°	90.00301°	90.00453°
Detuning		220.427 kHz	135.584 kHz	71.238 kHz	47.399 kHz
Bunch length (RMS) when tuned in (uniform fill)		43 ps	46 ps	46 ps	53 ps

2.3.4.7. Intrabeam Scattering

The increase of the horizontal emittance due to intrabeam scattering (IBS) as a function of the RF voltage is displayed in Figure 2-57 for both 500 MHz and 100 MHz RF frequency. The calculations were performed using the IBS algorithm available in elegant [9], which is based on the Bjorken and Mtingwa's formula [10]. The growth of the horizontal emittance is calculated compared to the zero-current horizontal emittance with 8 pm vertical emittance. The calculations were done for the bare lattice with 300 mA total current (corresponding to 0.6 nC and 3 nC bunch charge in a uniform fill pattern for 500 MHz and 100 MHz RF frequency, respectively). The effect of a harmonic cavity was determined by taking into account the increase of the RMS bunch length due to a third order harmonic cavity tuned to the flat potential conditions. Similarly, the increase of the energy spread is displayed in Figure 2-58.
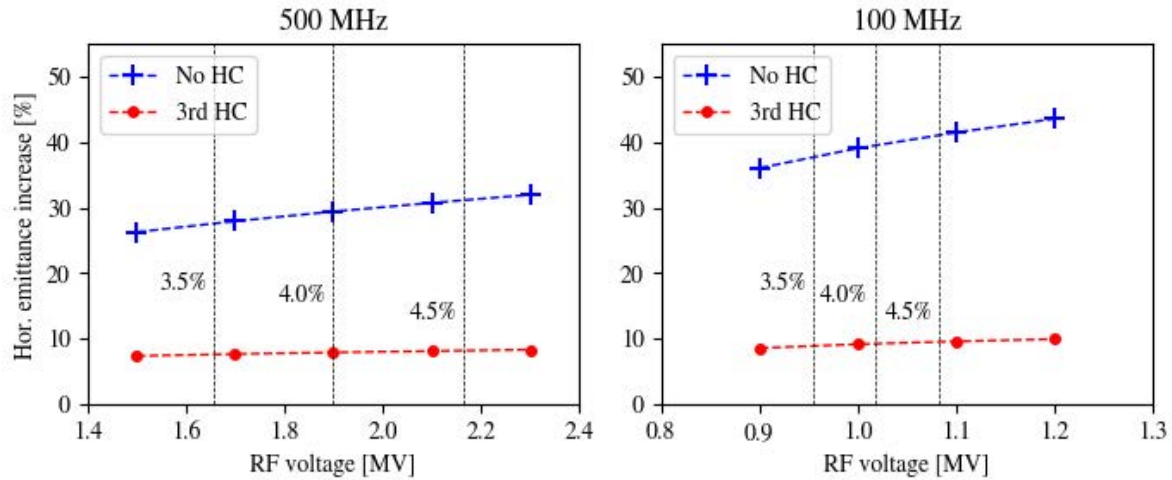
Figure 2-57 : Horizontal emittance increase as function of RF voltage due to intrabeam scattering. The voltages corresponding to 3.5%, 4.0% and 4.5% RF acceptance are marked for comparisons (black dashed lines).
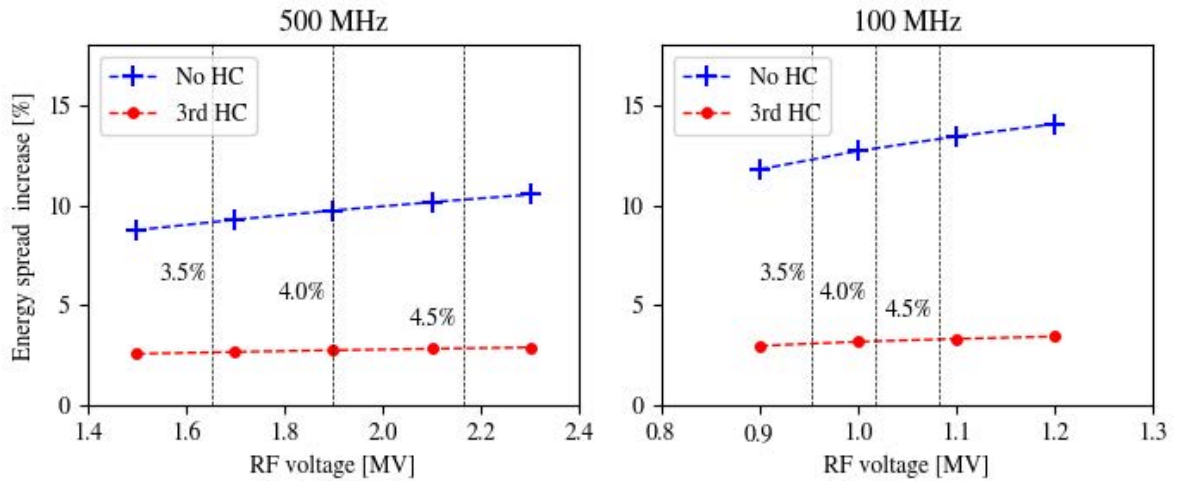
Figure 2-58 : Energy spread increase as a function of RF voltage due to intrabeam scattering. The voltages corresponding to 3.5%, 4.0% and 4.5% RF acceptance are marked for comparisons (black dashed lines).

The results show that the effect of IBS without harmonic cavity is more severe for a RF frequency of 100 MHz than for 500 MHz assuming the voltage is adjusted to achieve the same RF acceptance. The difference is reduced when including the harmonic cavity due to longer bunch lengthening for 100 MHz than 500 MHz (see Section 2.3.4.9), but this does not fully compensate for the difference in bunch charge. The simulations show that a harmonic cavity is required to reduce both the increase of emittance and energy spread due to IBS when operating at the nominal 300 mA current.

Figure 2-59 displays the increase of horizontal emittance and energy spread as a function of bunch charge for 500 MHz RF frequency. The calculation was performed for a voltage of 1.66 MV corresponding to 3.5% RF acceptance and 8 pm vertical emittance. The effect of a harmonic cavity was calculated assuming that the flat potential conditions (resulting in the same bunch lengthening) can be achieved independently of the beam current.
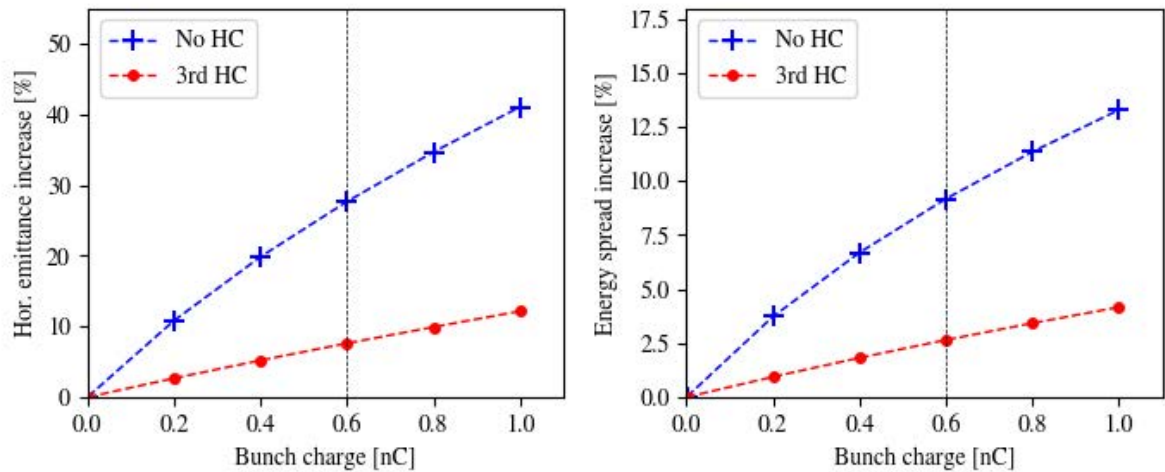
Figure 2-59 : Horizontal emittance and energy spread increase as a function of bunch charge due to intrabeam scattering. The nominal bunch charge corresponding to 300 mA total current in a uniform fill is marked for comparison (black dashed lines).

The effect of intrabeam scattering taking into account the effect of the insertion devices and a non-uniform fill pattern remains to be studied.

2.3.4.8. Robinson Stability

Robinson instability occurs when the beam loading in RF cavities renders the beam unstable. The instability can be separated into two different types:

- DC (zero-frequency) Robinson instability: occurs when the beam loading is so large compared to the generator voltage that a bunch sits at the crest of the generator voltage. This results in loss of phase stability and exponential growth of the bunch phase [11].

- AC Robinson instability: occurs when the beam interacts with the cavity impedance such that a bunch with higher energy than the nominal gains more energy and a bunch with lower energy loses more energy. This leads to a growing bunch oscillation. For a storage ring with positive momentum compaction factor this occurs when the resonance frequency of a RF cavity is tuned above a multiple of the RF frequency. Correspondingly, damping of the oscillation can be achieved by tuning the resonance frequency of a cavity below a multiple of the RF frequency [12].

For a RF system only including main cavities, Robinson stability is automatically obtained when tuning the cavities to minimise the reflected power since this requires tuning the cavities below the RF frequency. When including harmonic cavities in the system the condition for stability becomes more complex, especially in the case of passive harmonic cavities since stability has to be ensured while tuning in the cavity. In addition, to allow flexibility of the machine operation, stability should be ensured at all considerable operating currents and main cavity settings. To achieve bunch lengthening, the harmonic cavities need to be tuned to the Robinson unstable side, leading to instability growth. In case the radiation damping is not sufficient to achieve AC Robinson stability, this can (depending on the main cavity parameters), be compensated by tuning the main cavities to achieve increased Robinson damping. This, however, does not guarantee DC Robinson stability since that also depends on the generator voltage.

Figure 2-60 displays a comparison of the stability in tracking simulations as function of the Q factor of the harmonic cavity. The harmonic cavity parameters used in the simulations are as shown in Table 2-20, but with the detuning adjusted to provide the same tuning angle as the Q factor is varied. The simulations were performed for a 300 mA uniform fill pattern including beam loading in 8 normal conducting main cavities as described in Section 2.9.3. The main cavities were assumed to operate at optimal coupling and tuned to achieve no reflected power. The simulations show that for a normal conducting harmonic cavity with the required shunt impedance to achieve flat potential conditions at 300 mA current, common Q values for normal conducting cavities (20,000–30,000) are too low to avoid Robinson instability when the harmonic cavity is fully tuned in because of the large required R/Q. Stability can, however, be obtained for a superconducting cavity tuned to achieve the same bunch lengthening. For a superconducting cavity, stability is provided even without taking into account the damping provided by the main cavities, which allows for a flexible operation of the number of main cavities and their detuning.
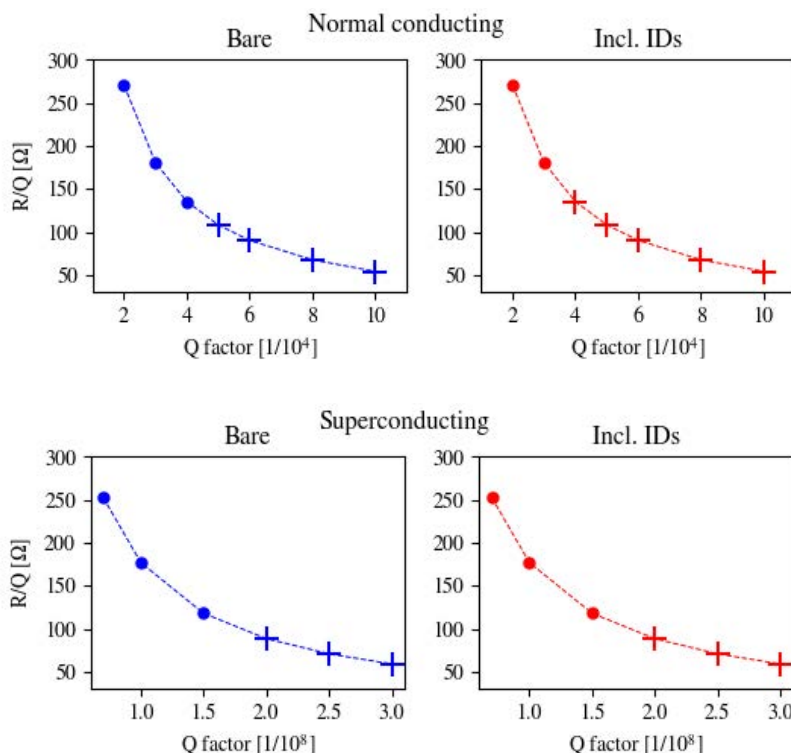
Figure 2-60 : Stable (+) and unstable (•) harmonic cavity parameters in tracking simulations for 300 mA current, the settings in Table 2-20 and a uniform fill including Robinson damping from the main cavities.

Tracking simulations for a superconducting cavity also show that stable bunch lengthening can be achieved already at low current by tuning the cavity, which could be of importance in case of heating issues during commissioning.

2.3.4.9. Touschek Lifetime

Comparisons were performed of the effect on Touschek lifetime due to the choice of RF frequency. Figure 2-61 displays the Touschek lifetime for the bare lattice as a function of RF voltage for 100 MHz and 500 MHz RF frequency, both with and without a harmonic cavity. The lifetime without harmonic cavity was obtained by determining the local momentum aperture around the ring with 6D tracking and then calculating the lifetime assuming 934 bunches, a total current of 300 mA and a vertical emittance of 8 pm. Here, the lifetime with harmonic cavity is an estimation assuming a third order harmonic cavity set to the flat potential conditions and approximating the increase of lifetime to be proportional to the increase of the RMS bunch length compared to the case without harmonic cavity. Both the effect of the modification of the bunch profile and the change of the momentum aperture due to the harmonic cavity are thus neglected.
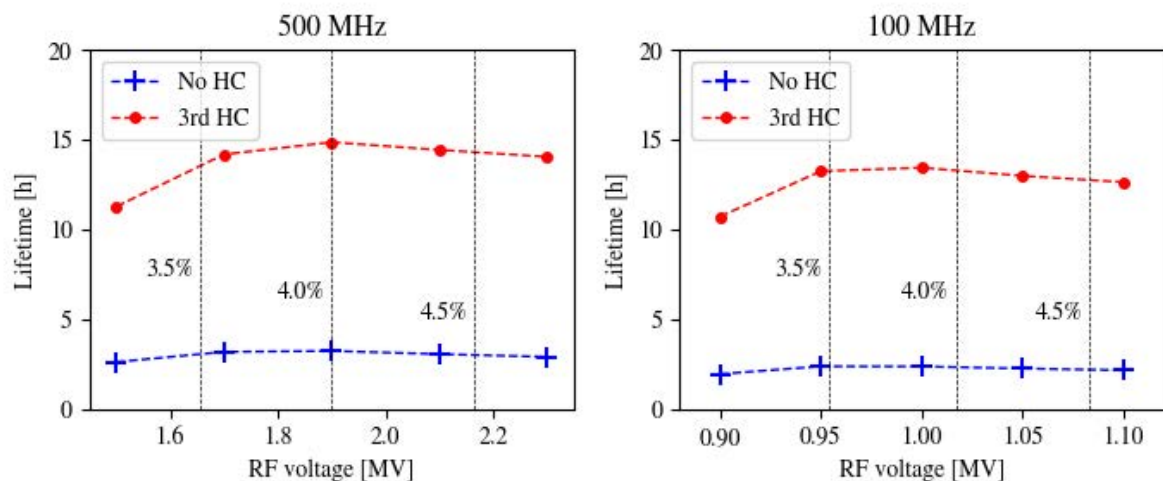
Figure 2-61 : Lifetime for the bare lattice as a function of RF voltage. The RF acceptance is marked (black dashed) for comparisons.

For a given RF acceptance, the Touschek lifetime without harmonic cavity is longer for a RF frequency of 500 MHz compared to 100 MHz. This is due to the lower charge per bunch, which is not fully counterbalanced by the shorter bunch length. When including a harmonic cavity, the Touschek lifetime increases because of the bunch lengthening. Figure 2-62 displays the bunch lengthening for a third order harmonic cavity set to the flat potential conditions as function of RF voltage. Larger bunch lengthening is achieved for a RF frequency of 100 MHz compared to 500 MHz, but as can be seen in Figure 2-61, this does not fully compensate for the lower Touschek lifetime and therefore the lifetime is still slightly longer for 500 MHz. It is therefore preferable for the lifetime to keep the 500 MHz RF frequency for Diamond-II as operated in the current ring. In addition, since the nominal bunch length at 3.5% RF acceptance for 100 MHz frequency is 33 ps, operation at 100 MHz together with a third harmonic cavity would result in bunch lengths that are too long compared to a user requirement of maximum 100 ps FWHM bunch length for the camshaft bunch in the hybrid mode already when the harmonic cavity is only slightly tuned in, meaning the lifetime increase achieved by the harmonic cavity would be minor since it cannot be fully tuned in while still meeting this user requirement.
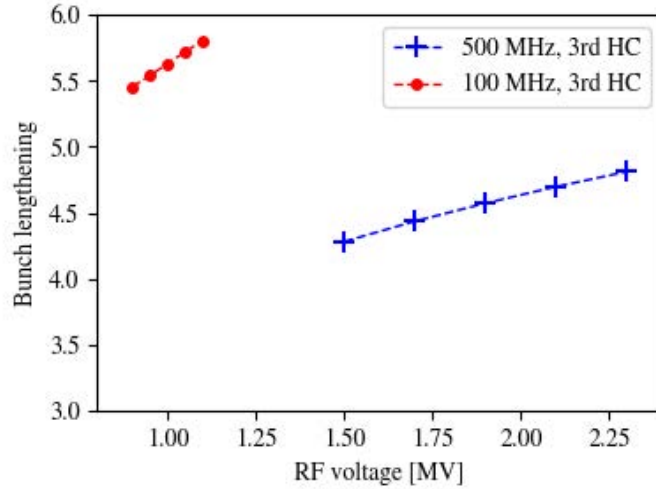
Figure 2-62 : Bunch lengthening for a third order harmonic cavity set to the flat potential conditions as function of RF voltage.

As described in Section 2.3.4.8, tracking simulations show Robinson instability for a normal conducting harmonic cavity tuned to achieve the flat potential conditions. To ensure stability it is therefore required to employ a superconducting harmonic cavity. For a superconducting cavity it is not possible to achieve the flat potential conditions due to a too large shunt impedance, but similar bunch lengthening can be achieved by only requiring the first derivative of the voltage at the synchronous phase to be zero. Figure 2-63 displays the bunch length as function of detuning for the bare lattice and the superconducting cavity parameters displayed in Table 2-20. The corresponding bunch profiles for different detunings are displayed in Figure 2-64. As shown, similar bunch lengthening can be achieved as for the flat potential conditions, but the bunch profile is not symmetric. As discussed further in Section 2.3.4.10, the bunch profiles will be asymmetric in any case when there is a gap in the fill pattern and therefore the consequence of choosing a superconducting cavity has no effect in practise for Diamond-II where a gap most likely will be required to avoid instabilities.
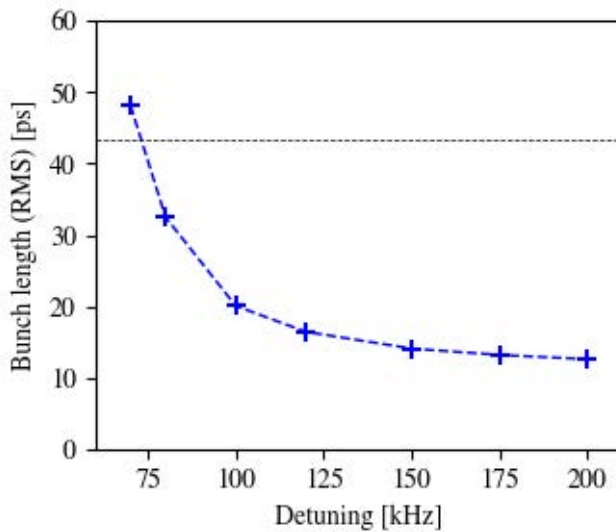
Figure 2-63 : Bunch length (RMS) as a function of detuning for the Super-3HC harmonic cavity for 1.66 MV voltage, 300 mA current and the bare lattice. The bunch length achieved by the flat potential conditions is marked (black dashed) for comparison.
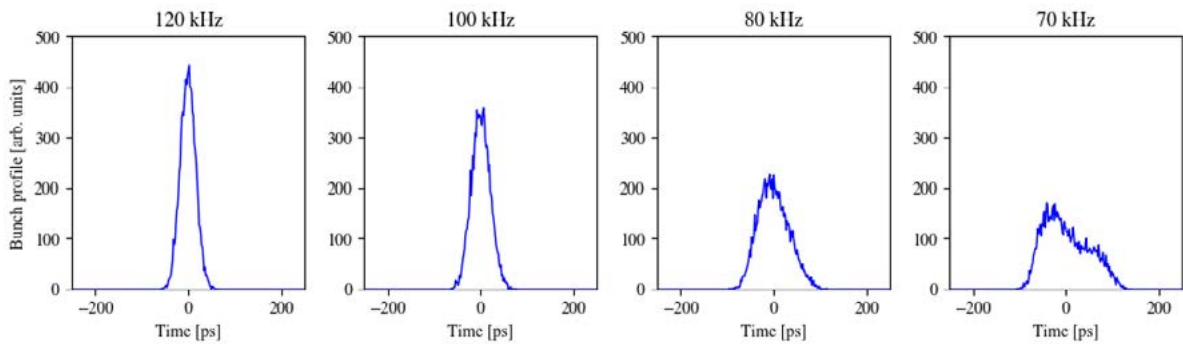
Figure 2-64 : Bunch profile for different detunings for the Super-3HC harmonic cavity for 1.66 MV, 300 mA current and the bare lattice. The nominal detuning for this case is 71.238 kHz as stated in Table 2-20.

When including errors, the Touschek lifetime is reduced compared to the bare lattice due to the reduction of the momentum aperture (see Section 2.3.3.7) and a RF voltage corresponding to a lower RF acceptance can be chosen before the momentum acceptance becomes limited by the RF. Lower RF voltage, however, results in reduced bunch lengthening from the harmonic cavity and the choice of RF voltage therefore has to be based on both the momentum aperture and the bunch lengthening from the harmonic cavity. To balance this, the nominal RF voltage was therefore chosen as the 3.5% RF acceptance limit, corresponding to 1.66 MV for the bare lattice. At this voltage, a bunch lengthening of 4.4 times can be achieved for a uniform fill when the harmonic cavity is fully tuned in. Taking into account the modification of the bunch profile, the lifetime increase becomes 4.6 times.

Table 2-21 displays the Touschek lifetime for the bare lattice with and without errors. In all of these simulations, the estimated errors after correction were used (see Table 2-15). The lifetime with harmonic cavity is for a uniform fill. The reduction of this lifetime due to transient beam loading when having a gap in the fill pattern is discussed in the following section.

Table 2-21 : Touschek lifetime for the bare lattice including errors. A voltage of 1.66 MV and zero chromaticity was used in the simulations. The lifetime with harmonic cavity is for the Super-3HC cavity tuned according to the settings in Table 2-20.

	Touschek lifetime
No errors, no harmonic cavity	3.1 h
With errors, no harmonic cavity	0.95 ± 0.12 h
With errors, with harmonic cavity (uniform fill)	4.37 ± 0.56 h

2.3.4.10. Fill Patterns and Transient Beam Loading

Operation of non-uniform fill patterns gives rise to transient beam loading, which leads to a variation of synchronous phase over the bunch train. When operating with a harmonic cavity this will in addition lead to both a reduction of the average bunch lengthening and a variation of the bunch length over the bunch train [13]. The reduction of the bunch lengthening is a concern for lifetime and instability thresholds whereas the phase variation over the bunch train affects the injection efficiency and the performance of the bunch-by-bunch feedback systems. For Diamond-II no issues are expected for the bunch-by-bunch feedback systems because of sufficient phase range, but the injection efficiency is reduced if the phase variation is too large unless the whole injection chain is re-phased between injections into different RF buckets. To avoid this, a maximum time variation corresponding to 100 ps over the whole bunch train is estimated as a limit. This estimation has been obtained by simulating the injection efficiency off-phase and will be studied in more detail during the technical design phase.

The current Diamond ring is operated with a gap in the fill pattern (900 bunches out of 936) to avoid instabilities and it is foreseen that this will also be the case for Diamond-II. In addition to this, the current ring is operated a couple of weeks per year in hybrid mode (686 bunches) for timing users with a longer gap including a 3 nC camshaft bunch. A similar mode to serve timing users will likely also be required for Diamond-II. A bunch length below 100 ps FWHM is expected to be

required for the camshaft bunch. So far, only fill patterns similar to those operated in the current ring have been considered for Diamond-II, i.e. a standard mode consisting of 900 bunches (out of 934) and a hybrid mode consisting of 685 bunches and a 3 nC camshaft bunch placed in the middle of the gap. Table 2-18 shows the bunch charge and bunch current for these two fill patterns.

Figure 2-65 displays the time shift and RMS bunch length over the bunch train for the two fill patterns using 300 mA current, the bare lattice and the Super-3HC cavity parameters (see Table 2-20). In these simulations the transient beam loading in the main cavities has not yet been included to be able to study only the effect of the harmonic cavity. However, it is already evident that the estimated requirements for Diamond-II are not fulfilled since the time deviation over the bunch train is above 100 ps for both fill patterns.
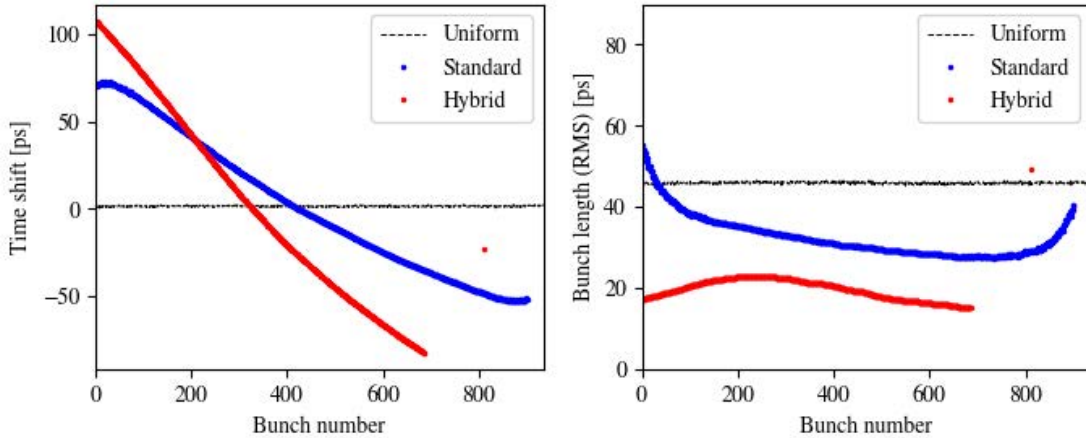
Figure 2-65 : Time shift (left) and RMS bunch length (right) over the bunch train for 1.66 MV voltage, 300 mA current, the bare lattice and the Super-3HC harmonic cavity tuned according to Table 2-20. The results for a uniform fill are displayed for comparison. In these simulations the transient beam loading in the main cavities has not been included.

Figure 2-66 displays the corresponding bunch profiles. As can be noted, the bunch profiles become significantly asymmetric due to the transient beam loading. This is also the case for the camshaft bunch, which indicate that only a FWHM requirement on the bunch length might not be sufficient to describe the bunch profile requirements of the timing users. More detailed requirements for the camshaft bunch will be discussed during the technical design phase.
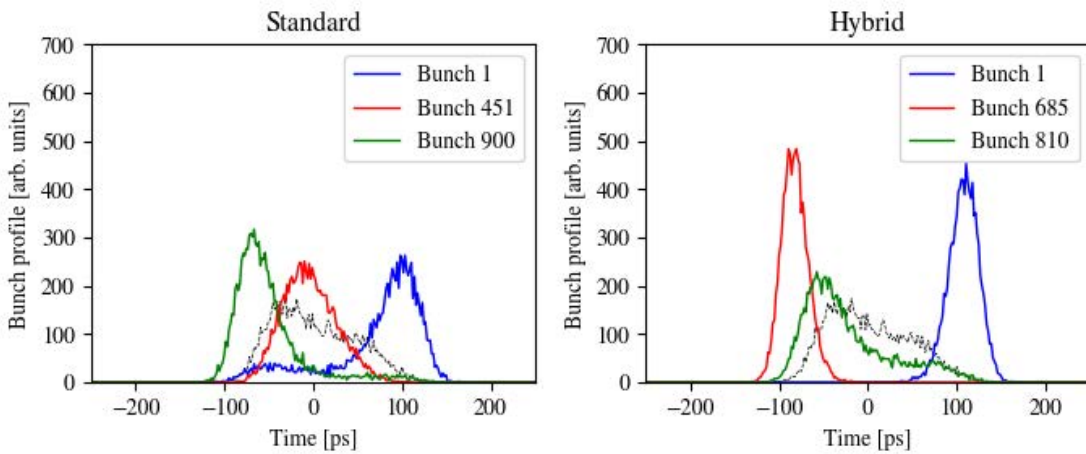
Figure 2-66 : Bunch profiles for the standard (left) and hybrid (right) mode for 1.66 MV voltage, 300 mA current, the bare lattice and the Super-3HC harmonic cavity tuned according to Table 2-20. The profile for a uniform fill is displayed for comparison (black dashed).

Since the bunch profiles become significantly different from a Gaussian bunch, the modification of the bunch profiles has to be taken into account when assessing the lifetime increase. This can be done according to

$$\frac{\tau_{HC}}{\tau_0} = \frac{\varepsilon_{HC}^2}{\varepsilon_0^2} \frac{\int \rho_0^2 (dz) dz}{\int \rho_{HC}^2 (dz) dz}$$

where τ_0, ε_0 and ρ_0 are the Touschek lifetime, momentum aperture and bunch profile without harmonic cavity and $\tau_{HC}, \varepsilon_{HC}$ and ρ_{HC} the corresponding values including the cavity [1]. Note that this is the Touschek lifetime of individual bunches and not of the whole beam. The effect on the momentum aperture due to the harmonic cavity was estimated to be ~5% and therefore neglected. Figure 2-67 displays the FWHM bunch length and the lifetime increase of individual bunches corresponding to the results presented in Figure 2-65. As can be noted, the lifetime increase follows the same pattern as the FWHM bunch length and not as the RMS bunch length due to the asymmetry of the bunches.
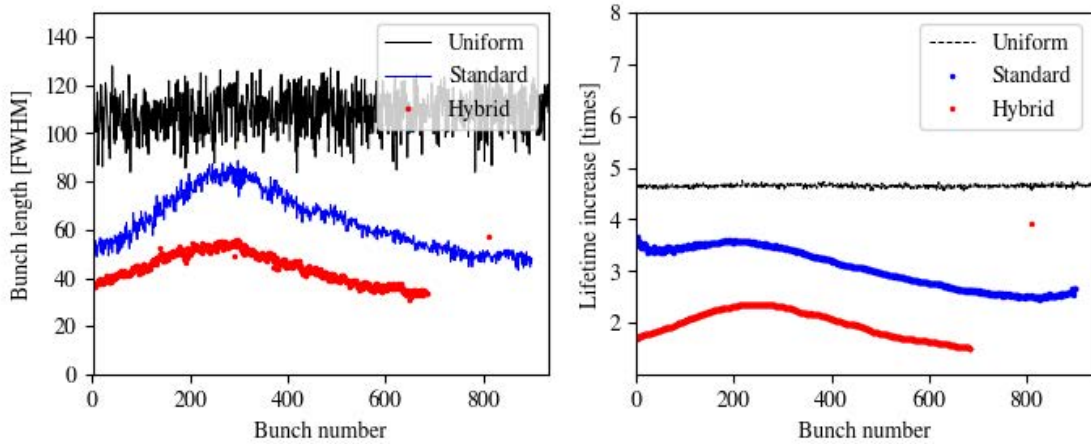
Figure 2-67 : FWHM bunch length (left) and estimated lifetime increase (right) over the bunch train for 1.66 MV voltage, 300 mA current, the bare lattice and the Super-3HC harmonic cavity tuned according to Table 2-20. The corresponding values for a uniform fill patterns are marked for comparison (black dashed). The noise on the FWHM bunch length values comes from the numerical resolution of the bunch profiles. In these simulations the transient beam loading in the main cavities has not been included.

The lifetime increase of individual bunches for the different fill patterns both for ideal main cavities and when including the transient beam loading in them is shown in Table 2-22. It is evident that the contribution from the main cavities is significant.

Table 2-22 : Lifetime increase of individual bunches for the different fill patterns both for ideal main cavities and when including the transient beam loading in them for the Super-3HC harmonic cavity tuned according to the settings in Table 2-20.

	Uniform	Standard	Hybrid
Ideal main cavities	4.6 times	3.1 ± 0.4 times	2.0 ± 0.3 times
Real main cavities	4.6 times	2.1 ± 0.3 times	1.3 ± 0.1 times

Figure 2-68 shows the time deviation over the bunch train and the lifetime increase of individual bunches as function of harmonic cavity R/Q for the standard mode both for ideal main cavities and including the transient beam loading in them. The results show that a reduction of the harmonic cavity R/Q would improve the situation, but also that the contribution from the main cavity is significant and efforts to reduce the R/Q of the harmonic cavity would be in vain unless a feedback can be implemented to reduce the transient in the main cavities. However, the situation for the hybrid mode would be more severe and most likely difficult to sufficiently improve by only these means.
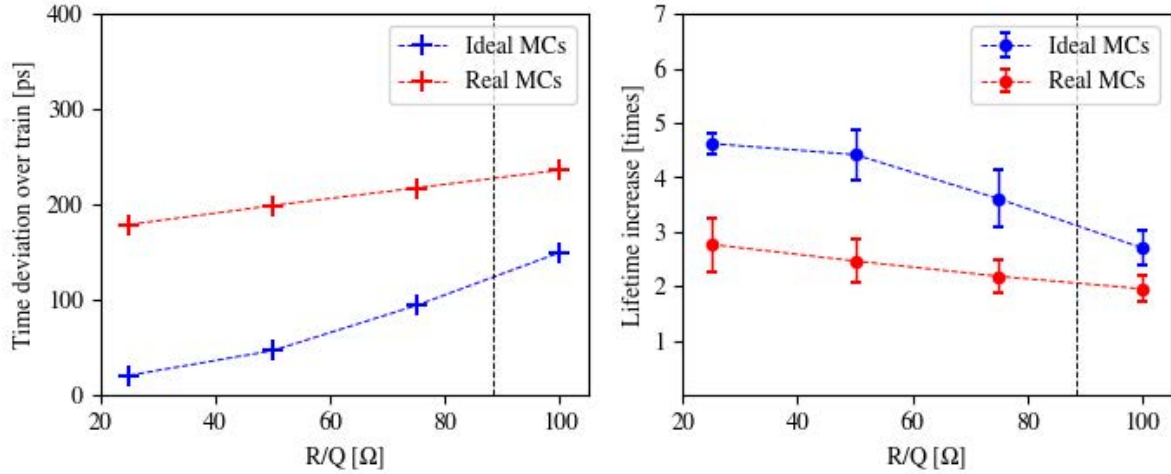
Figure 2-68 : Time deviation (left) and lifetime increase of individual bunches (right) as function of harmonic cavity R/Q for the standard mode for 1.66 MV voltage, 300 mA and the bare lattice. The R/Q of the Super-3HC harmonic cavity is marked (black dashed). Results are shown for both ideal main cavities and when including the transient beam loading in them.

Due to the time and cost requirements to design and prototype a superconducting cavity it is preferable to choose an existing harmonic cavity design. The simulations show that this is not compatible with operating similar fill patterns as in the current Diamond ring. Studies of options for new fill patterns for Diamond-II has been initiated and will be studied in detail during the technical design phase. The aim of these studies is to develop a standard mode which meets the requirements of maximum 100 ps time deviation over the bunch train and an average lifetime increase of 4 times for existing harmonic cavity designs by utilising several short gaps for ion-clearing instead of one long gap. Discussions about requirements and solutions for the hybrid mode have also begun.

2.3.4.11. Total Lifetime

Gas lifetimes have been calculated for the vacuum chamber options presented in Section 2.5.4 (pipe without NEG coating, pipe with activated NEG and pipe with saturated NEG) all at 300 mA current, 100 Ah condition and the corresponding calculated pressure profiles. For these calculations, 20 seeds were considered where the dynamic and momentum apertures were calculated using the errors in Table 2-15. The resulting gas lifetimes are displayed in Table 2-23. As concluded in Section 2.5.4, the gas lifetime for the uncoated chamber would not be acceptable for Diamond-II since the vacuum quality would drastically affect the total lifetime, which confirms the requirement of NEG coating.

Table 2-23. Summary of the gas lifetime values computed from pressure profiles. The two main processes (elastic, bremsstrahlung) are shown together with the overall result for three different options of the vacuum chamber, 300 mA current and 100 Ah conditioning.

Vacuum chamber	Elastic (h)	Bremsstrahlung (h)	Gas lifetime (h)
No NEG	1.57 ± 0.38	1.88 ± 0.02	0.86 ± 0.11
Activated NEG	738.8 ± 147.9	849.2 ± 23.5	395.1 ± 42.6
Saturated NEG	73.6 ± 17.2	97.6 ± 1.32	41.9 ± 5.6

The total lifetime is determined according to

$$\tau_{\text{tot}} = \left(\frac{1}{\tau_{\text{T}}} + \frac{1}{\tau_{\text{G}}} \right)^{-1}$$

where τ_{T} is the Touschek lifetime and τ_{G} the gas lifetime. For a uniform fill with or without harmonic cavity, the Touschek contribution will be the same for all bunches, meaning the average Touschek lifetime of the whole beam will be equal to

the Touschek lifetime of an individual bunch. For a fill pattern with a variation of the lifetime over the bunch train this is no longer the case as the average Touschek lifetime is given by

$$\bar{\tau} = \left(\frac{1}{N} \sum_{i=1}^{N} \frac{1}{\tau_i} \right)^{-1}$$

where τ_i is the Touschek lifetime of an individual bunch and N the number of bunches. Table 2-24 shows the calculated average Touschek lifetime for the different fill patterns taking into account the Touschek lifetime of individual bunches, as well as the resulting total lifetime including the gas contribution.

Table 2-24 : Average Touschek lifetime and total lifetime for the bare lattice. The Touschek lifetimes with harmonic cavity are for the Super-3HC harmonic cavity tuned according to the settings in Table 2-20 and including the transient beam loading in 8 normal conducting main cavities operated at optimal power coupling and detuning.

	Average Touschek lifetime	Total lifetime activated NEG	Total lifetime saturated NEG
No HC	0.95 ± 0.12 h	0.95 ± 0.12 h	0.93 ± 0.11 h
With HC, uniform fill	4.37 ± 0.56 h	4.32 ± 0.55 h	3.96 ± 0.46 h
With HC, standard mode	1.91 ± 0.24 h	1.90 ± 0.24 h	1.83 ± 0.22 h

References

[1]   J. M. Byrd and M. Georgsson, "Lifetime increase using passive harmonic cavities in synchrotron light sources," *Physical Review Special Topics - Accelerators and Beams,* vol. 4, no. 3, 2001.

[2]   P. F. Tavares et al., "Equilibrium bunch density distribution with passive harmonic cavities in a storage ring," *Physical Review Special Topics - Accelerators and Beams,* vol. 14, no. 6, 2014.

[3]   N. Wang and Q. Qin, "Resistive-wall impedance of two-layer tube", *Physical Review Special Topics - Accelerators and Beams,* vol. 10, 111003, 2007.

[4]   R. Nagaoka, "Instability Studies Using Evaluated Wake Fields and Comparison with Observations at Soleil," in *EPAC*, 2006.

[5]   G. Skripka et al., "Simultaneous computation of intrabunch and interbunch collective beam motions in storage rings," *Nuclear Instruments and Methods in Physics Research, Section A: Accelerators, Spectrometers, Detectors and Associated Equipment,* vol. 206, 2016.

[6]   A. W. Chao, Physics of Collective Beam Instabilities in High Energy Accelerators, New York: Wiley, 1993.

[7]   R. Bartolini et al., "Analysis of Multi-bunch Instabilities at the Diamond Storage Ring," in *IPAC*, 2016.

[8]   M. Pedrozzi et al., "SLS Operational Performance with Third Harmonic Superconducting System," in *Proceedings of the 11th Workshop on RF Superconductivity*, 2003.

[9]   M. Borland, "elegant: A Flexible SDDS-Compliant Code for Accelerator Simulation," in *The 6th International Computational Accelerator Physics Conference*, 2000.

[10]   J. D. Bjorken and S. K. Mtingwa, "Intrabeam Scattering," *Part. Acc.,* vol. 13, pp. 115-143, 1983.

[11]   Chao et. al., Handbook of Accelerator Physics and Engineering, World Scientific Publishing Co, 2013, pp. 646-647.

[12]   Lee, Accelerator Physics, World Scientific Publishing Co, 2012, pp. 336-339.

[13]   J. M. Byrd et al., "Transient beam loading effects in harmonic rf systems for light sources," *Physical Review Special Topics - Accelerators and Beams,* vol. 5, no. 9, 2002.

2.3.5. Injection

2.3.5.1. Introduction

The latest generation of electron storage rings are characterised by a substantial reduction in dynamic aperture compared to their predecessors. This presents a challenge for capturing the injected beam, and a variety of new methods have been proposed in order to cope with this. These schemes can be split into two broad categories, namely on or off-axis injection methods. The most recent off-axis injection schemes seek to maintain accumulation by compensating for the reduced transverse acceptance in some way, either by installing a dedicated high-beta injection straight [1] [2], using a nonlinear kicker [3], or by reducing the separation between stored and injected beams with a thin septum [4] or an 'anti-septum' magnet [5] [6]. On-axis injection schemes can be operated with smaller dynamic apertures, and some allow accumulation by offsetting the injected beam in time and energy from the stored beam [7] [8]. Alternatively, a full swap-out injection [9] [10] can be performed.

For the Diamond-II storage ring, an off-axis accumulation injection scheme is preferred. This type of injection has many advantages over swap-out injection, such as a reduced charge per shot from the injector and it avoids the need for pulsed magnets with nanosecond rise/fall times [11]. Swap-out injection schemes suffer from an intrinsic drop in brightness as the injected beam emittance damps to the stored beam emittance. Provided the kicker magnets do not perturb the stored beam, accumulation injection schemes can avoid this problem. Adopting an accumulation injection scheme also has the advantage that the depleted electron bunches remain in the storage ring, removing the need to either install a beam dump, or to recapture the swapped-out electron bunches. The present storage ring design does not provide sufficient momentum aperture to allow the off-energy injection schemes to be considered, meaning any accumulation scheme must be off-axis. In principle, this could be eased by installing a dedicated high-beta injection straight, however, this would require substantial engineering modifications to the adjacent arcs and would break the symmetry of the ring, reducing the momentum aperture.

The baseline proposal for the Diamond-II storage ring injection scheme is therefore to use the anti-septum scheme originally proposed for the SLS-2 project [12]. The main benefit of this scheme is that the separation between stored and injected beams can be reduced compared to a standard off-axis injection scheme, which in combination with a low-emittance booster makes off-axis accumulation compatible with the available storage ring dynamic aperture.

The proposed layout for the injection straight contains a 4-kicker bump and septum magnet, similar to the one used for Diamond. The main difference is that the kicker following the septum magnet will contain a thin anti-septum plate in order to shield the injected beam from the kicker field [6], effectively turning the kicker magnet into a drift space for the injected beam. The stored beam will still receive the full deflection, thereby ensuring a closed bump and minimal beam disturbance for the users. In the design proposed here, the magnetic field in the kicker magnets is substantially lower than that in the main septum (0.18 T compared to 1.04 T), allowing an anti-septum plate of ~1 mm thickness in the kicker compared to the 3 mm required in the main septum magnet. An illustration of the injection straight layout and the paths of the stored and injected beams is given in Figure 2-69 and Figure 2-70 below, and the pulsed magnet requirements are summarised in Table 2-25.

Alternative injection methods that replace the anti-septum with a thick / thin main septum magnet, or that replace the 4-kicker bump with a nonlinear kicker will continue to be investigated.

Table 2-25 : Summary of pulsed magnet parameters in standard operating conditions.

Parameter	Unit	Septum	Kicker
Magnetic length	m	1.67	0.6
Bend angle	mrad	148.4	9.3
Bend radius	m	11.3	64.5
Magnetic field	T	1.04	0.18
Pulse shape	-	Full-sine	Half-sine
Pulse duration	μs	160 μs	6 μs
Repetition rate	Hz	5	5

2.3.5.2. Injection Process

The basic steps in the injection process are as follows. Firstly, the four kicker magnets used to bump the stored beam are triggered. Assuming the kicker pulses are identical half-sine, 6 μs full-width waveforms (similar to the existing kicker magnets), the closed orbit bump is at its maximum amplitude 2 turns after triggering, bringing the stored beam close to the septum plates. At this point, the injected bunch is transferred from the booster, exiting the anti-septum magnet at ~3 mm displacement from the stored beam. The final kicker magnet deflects both stored and injected beams, placing them both parallel to the magnet centreline with the stored beam remaining on-axis. The amplitude of the closed orbit bump reduces to approximately half the maximum value on the following turn, allowing the injected bunch to clear both the main and anti-septum plates. By the time the next revolution is completed, the kicker magnets are off and the injected beam can continue to oscillate around the stored beam, eventually damping down to be captured. Phase-space plots illustrating the injection process on the initial few turns are shown in Figure 2-71.
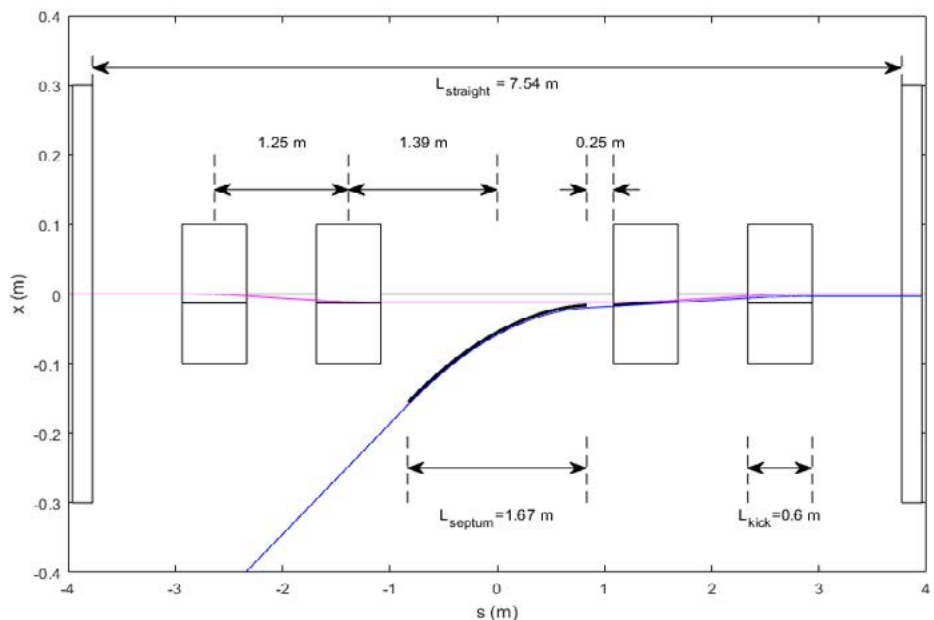
Figure 2-69 : Layout of the injection straight using the 'anti-septum' scheme. The basic structure of the straight remains unchanged compared to the Diamond storage ring, after allowing for the reduced straight length and updated magnet parameters.
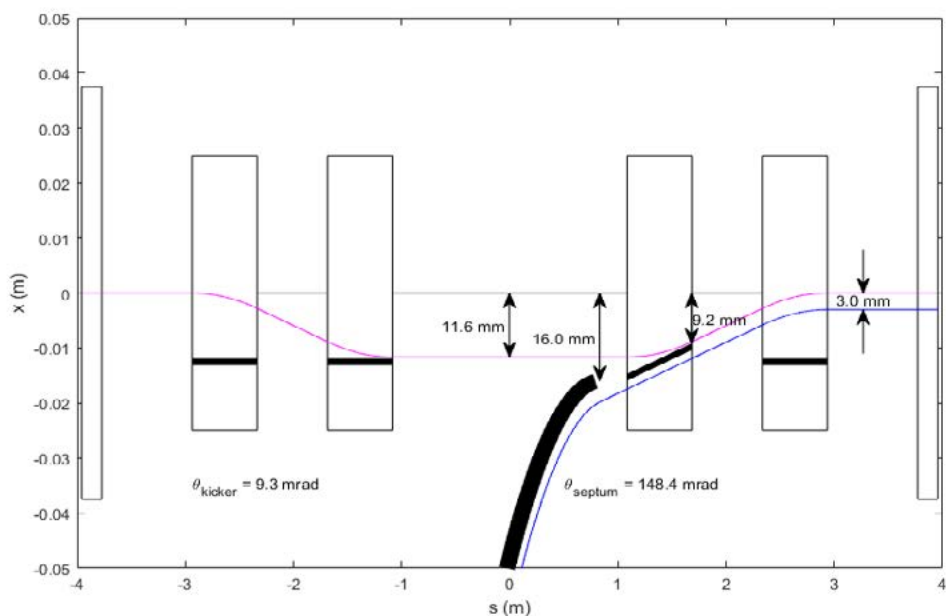
Figure 2-70 : Illustration of the paths taken by the stored and injected beams. The lower field in the kicker magnet compared to the main septum magnet allows a thinner anti-septum plate to be used, thereby reducing the separation between stored and injected beams.
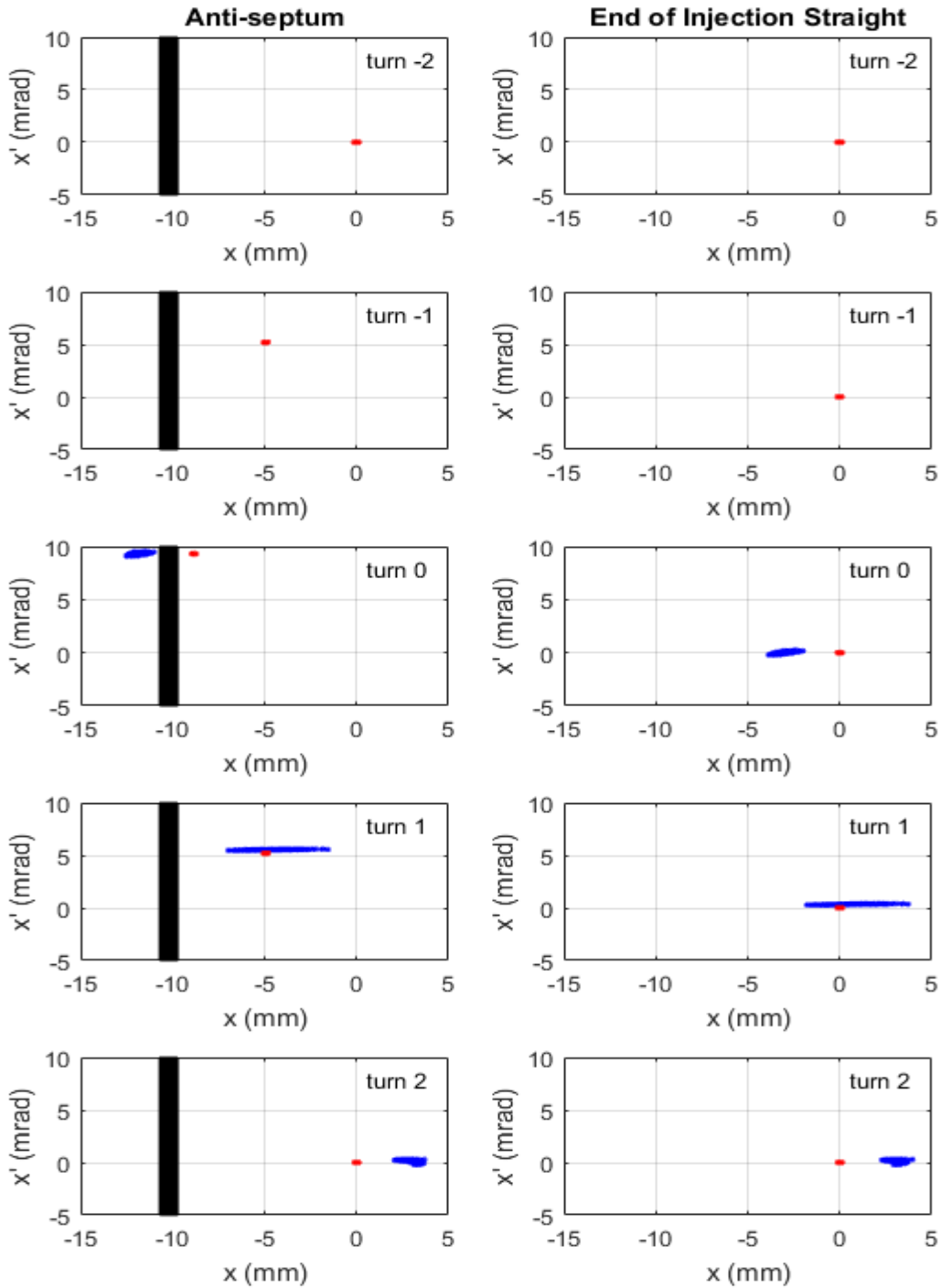
Figure 2-71 : Phase space diagram illustrating the injection process during the firing of the injection kickers (turns -2 to 2). The stored beam is shown in red, the injected beam is in blue, and the anti-septum plate is shown as a vertical black line. The particle coordinates at the exit of the anti-septum kicker magnet are plotted in the left-hand column, and the coordinates at the exit of the injection straight are in the right-hand column.

The displacements of the main and anti-septum plates from the stored beam centreline have been chosen to be as small as possible, without reducing the physical acceptance of the ring which is determined by the 10 mm radius vacuum vessel in the arc sections. After scaling with the respective beta-functions, this leaves the anti-septum plate at an offset of 9.2 mm from the centreline. In turn, this displacement sets the amplitude of the closed orbit bump and hence the required kicker bend angles defined in Table 2-25 and the displacement of the main septum magnet.

2.3.5.3. Initial Commissioning

It is envisaged that during early commissioning the transfer line and storage ring pulsed magnets will be configured to allow on-axis injection. This can be achieved by steering the beam in the transfer line to exit the main septum magnet with a larger angle and increasing the bend angle of the final kicker magnet to compensate. The injected beam will then exit the injection straight on-axis and travel through the centre of all subsequent magnets and diagnostic equipment. This has the advantage of greatly simplifying the initial commissioning of storage ring components, such as setting all bending and corrector magnet fields to achieve first turns, coping with a reduced, un-optimised dynamic aperture, and for calibrating the BPM centres to the adjacent quadrupoles. Once sufficient charge can be captured in the ring on a single-shot basis and basic tune and chromaticity corrections have been completed, the injection pulsed magnets can be re-configured for off-axis accumulation.

2.3.5.4. Top-up Operation

As with Diamond, the new storage ring will be operated in top-up mode to keep the stored beam current constant and to enable user experiments to continue uninterrupted. An important consideration arising from this mode is the residual disturbance given to the stored beam during the injection process. This can have a number of sources, including leakage of the main septum field, timing and amplitude of the kicker magnet pulses, and uniformity of the kicker vessel coating. All of these aspects will receive close attention during the design and construction phases. In the event that any residual disturbance is significant for users, experience at Diamond and elsewhere has demonstrated that countermeasures can be taken to compensate for this kick, including fine-tuning of the individual kicker pulse waveforms, rolling the pulsed magnets [13], using a multi-bunch feedback or installing additional compensation kickers into the ring [14]. Top-up timing signals will continue to be distributed to all beamlines for gating purposes.

Aside from these measures, further changes to the baseline injection scheme remain under consideration. The first of these is to see whether the four-kicker bump and anti-septum magnet can be replaced with a thick/thin main septum magnet plus nonlinear kicker arrangement. The feasibility of this depends upon the acceptable vertical aperture of the nonlinear kicker magnet ceramic chamber and hence the horizontal position of the peak magnetic field, as this determines how close the injected beam can be brought to the stored beam. Another way to minimise the total beam disturbance during top-up is to increase the amount of charge injected per shot. One way to do this would be to accumulate beam in the booster first and only transfer into the storage ring on the final shot (see Section 2.13). Alternatively, multi-bunch injection directly from the linac could be used, with an increased charge per shot. Raising the injection energy of the booster is also being considered as a way to improve transfer efficiency.

2.3.5.5. Injected Beam Properties

Simulations of the storage ring dynamic aperture under realistic field and alignment tolerances imply that the injected electrons must be within ~3-4 mm displacement from the reference closed orbit, and that ~0.5-1% energy acceptance is available at this amplitude for synchrotron oscillations. Assuming the first ~2 mm of this dynamic aperture is allocated for the stored beam size and anti-septum plate thickness (plus beam-jitter and alignment tolerances), this leaves only ~1-2 mm at most for the injected beam.

Shown in Figure 2-72 is a plot of the injected beam size (full width) as a function of booster emittance for several representative values of horizontal beta function. The emittance of the existing booster synchrotron has been highlighted as a dashed black line. The optimal value of β_x at the exit of the transfer line that minimises the required storage ring acceptance can be calculated based upon the size and separation of the stored and injected beams, along with β_x at the storage ring injection point [15]. If β_x is too large, the injected beam size is also large, leaving part of the beam outside the dynamic aperture. If it is too small, then the divergence of the injected beam will be too large, again making it difficult to capture.
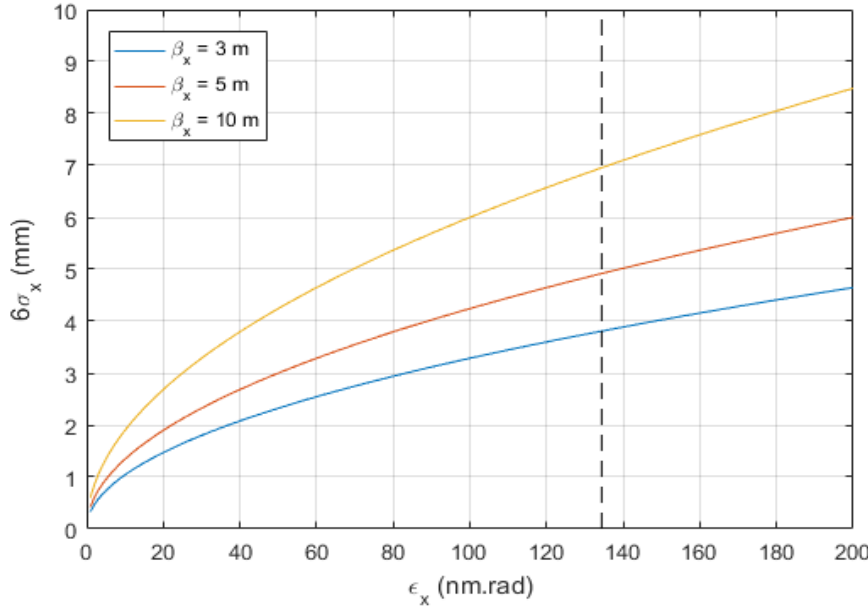
Figure 2-72 : Injected beam size as a function of booster emittance for several representative values of beta function. The emittance of the existing booster at 3 GeV has been highlighted as a dashed vertical line.

From Figure 2-72, it is clear that the extracted beam emittance from the existing booster is too large to be compatible with the new storage ring, even at the present maximum energy of 3 GeV. If high injection efficiency into the storage ring is to be maintained, a booster emittance in the range 10-30 nm is required. A similar analysis can be carried out on the bunch length. In this case, a momentum compaction factor of 1.2×10^{-4}, synchrotron frequency of ~1500 Hz and a total energy acceptance of ~0.5-1% at 4 mm offset for the storage ring implies that the RMS bunch length for the injected beam should be less than ~20-40 ps. Again, the existing value of 99 ps at 0.9 MV is too large to allow high injection efficiency into the new storage ring.

In light of these requirements, and the need to extract at 3.5 GeV instead of 3 GeV, the existing booster synchrotron will be replaced with a new, low emittance design to reduce both the transverse and longitudinal dimensions of the injected beam. A description of the new booster is given in Section 2.13, along with a summary of the extracted bunch parameters and simulated booster performance. Under this assumption, the scheme outlined here in combination with the established dynamic aperture is sufficient to ensure injection efficiency approaching 100%.

References

[1]   Y. Cai, "Ultimate Storage Ring based on Fourth-order Geometric Achromats," *Phys. Rev. ST Accel. Beams,* vol. 15, no. 054002, 2012.

[2]   R. Dimper, H. Reichert, P. Raimondi, L. S. Ortiz, F. Sette and J. Susini, "The Orange Book: ESRF Upgrade Programme Phase II (2015-2022)," 2015.

[3]   T. Atkinson, et al., "Development of a Non-linear Kicker System to Facilitate a New Injection Scheme for the BESSY II Storage Ring", in *IPAC'11*, San Sebastian, Spain, 2011.

[4]   D. Shuman et al., "Stray Field Reduction of ALS Eddy Current Septum Magnets", in *PAC'05*, Knoxville, Tennessee, 2005.

[5]   C. Gough and M. Aiba, "Top-up Injection with Anti-septum," in *IPAC'17*, Copenhagen, Denmark, 2017.

[6]   C. Gough, "Development of Injection Elements for SLS 2.0," in *2nd Topical Workshop on Injection and Injection Systems*, PSI, Switzerland, 2019.

[7]   M. Aiba, "Longitudinal Injection Scheme using Short Pulse Kicker for Small Aperture Electron Storage Rings," *Phys. Rev. ST Accel. Beams,* vol. 18, no. 020701, 2015.

[8]   M.-A. Tordeux, "Longitudinal Injection into Low-Emittance Ring, a Novel Scheme for Soleil Upgrade," in *Topical Workshop on Injection and Injection Systems*, Berlin, Germany, 2017.

[9]   C. Steier, "Progress of the R&D Towards a Diffration Limited Upgrade of the Advanced Light Source," in *IPAC'15*, Richmond, USA, 2015.

[10]   M. Borland, "On-axis Swap-out Injection," in *Workshop on Accelerator R&D for Ultimate Storage Rings*, Beijing, China, 2012.

[11]   C. Pappas, "Kicker Systems for the ALS Upgrade," in *Topical Workshop on Injection and Injection Systems*, Berlin, Germany, 2017.

[12]   A. Streun, "SLS-2 Conceptual Design Report," 2017.

[13]   K. Fukami, "Beam-Based Alignment of Injection Bump Magnets using Remote Controlled Tilt Adjustment System at Spring-8," *Nucl. Inst. Meth. A,* no. 694, pp. 1-5, 2012.

[14]   C. Mitsuda, "The Fast Kicker Correction System for Transparent Top-up Injection at Spring-8," in *Topical Workshop on Injection and Injection Systems*, Berlin, Germany, 2017.

[15]   A. Streun, "SLS Booster-to-Ring Transferline Optics for Optimum Injection Efficiency," SLS-TME-TA-2002-0193, 2005.

2.4. Magnets

This chapter presents the conceptual designs for the longitudinal gradient dipoles (DL), transverse gradient dipoles (DQ), quadrupoles, sextupoles, octupoles and corrector magnets which are required in the Diamond-II 3.5 GeV storage ring lattice with parameters as shown in Table 2-13.

The lattice design relies on the use of strong focusing quadrupoles with gradients up to 85 T/m and dipole quadrupole (DQ) magnets with gradients up to 33 T/m. These magnets require a very small bore aperture to achieve the design field (12 mm inscribed radius in the case of the quadrupoles and sextupoles). The magnet cross section and length have been also driven by a complex engineering integration, considering clashes with the photon extraction pipe, adjacent magnets and other lattice elements such as flanges, gate valves, vacuum pumps, absorbers, BPMs. The location of magnets in one arc is shown in Figure 2-124. They are accommodated on two 7 m long girders separated by the mid-straight section. The distance between magnetic elements has been made as small as reasonably practicable, 7.5 cm iron-to-iron, which has meant that coil overhang has had to minimised in all electromagnets.

2.4.1. Longitudinal Gradient Dipole (DL)

The design of the Diamond-II lattice requires a dipole field which varies longitudinally along the beam trajectory. The Accelerator Physics model of the field of the DL magnet is shown in Figure 2-73. There are four similar DL magnets per cell with exactly the same longitudinal distribution of magnetic field, except the field variation is reversed.
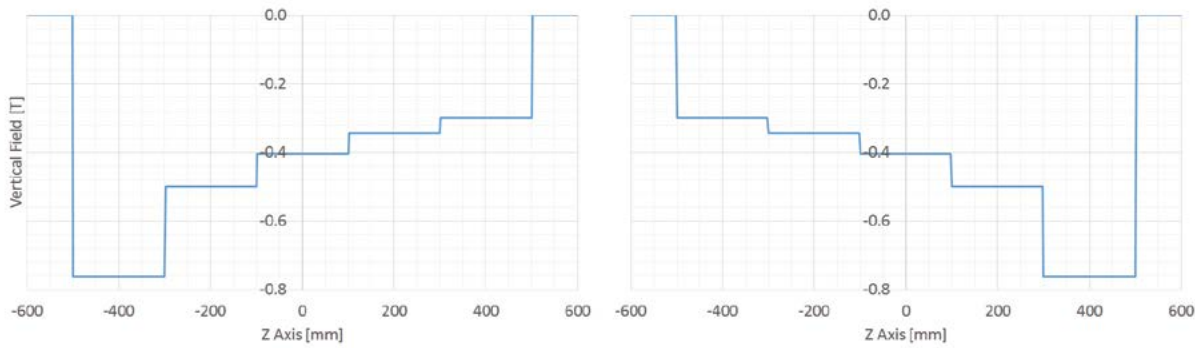
Figure 2-73 : Accelerator Physics model for the required step-like dipole field along the trajectory, left: first and third DLs in a cell, right: second and fourth DLs in a cell.

Conceptually this magnet can be either an electromagnet or permanent magnet (PM). In order to save space and power, we have chosen a PM design following positive experience at ESRF [1]. Each DL magnet consists of 5 modules, 200 mm long. Each module has its own PM blocks to generate the required magnetic flux, pole tip shape to produce the required magnetic field and, return yoke to close the magnetic flux and avoid flux leaking from a module to the adjacent ones. Magnetic and thermal shunts are used to tune the field to the nominal values. For simplicity of design the pole shape is the same for all modules.

2.4.1.1. DL Magnet Design Parameters

The DL cross-section is shown in Figure 2-74. The design parameters are shown in the Table 2-26.
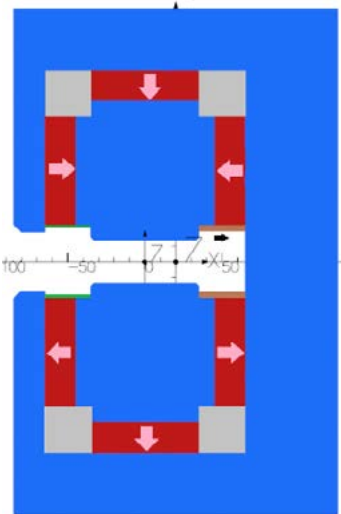
Figure 2-74 : DL magnet cross-section, blue: iron, red: PM blocks with magnetisation vector direction, grey: Aluminium spacer, brown: thermal shunt, green: magnetic shunt.

Table 2-26 : DL magnet design parameters.

Parameter	Value	Unit	Parameter	Value	Unit
Field	-0.299340	T	Yoke Material	Low carbon steel	-
	-0.344580		PM Material	Sm_2Co_{17}	-
	-0.403421		PM Dimensions (x, y, z)	(63,83)x20x20	mm
	-0.498745		PM Max Field	1.10	T
	-0.762594		PM Mass per Magnet	~35	kg
Integrated Field	-0.461736	Tm	Total yoke Mass	~350 (5x70)	kg
Half Gap	13	mm	Good Field Region	±10	mm
Pole Width	55	mm	(GFR)		
Magnet Length	999	mm	ΔB/B within GFR	< 5E-04	-

2.4.1.2. 2D and 3D Field Analysis

Magnet design has been carried out using the 3D static magnetic solver (TOSCA) of the Dassault Systèmes OPERA software[*]. The magnet structure is designed to ease manufacturing while minimising the number of PM blocks needed for each module. The OPERA model has been fully parametrised to allow it to be optimised, maintaining the spatial and magnetic constraints relative to the longitudinal gap between poles and yokes, the size of iron piece in both sides of PM blocks touching either pole or yoke, and the longitudinal arrangement of PM blocks (especially distance to the yoke end, see Figure 2-75 and Figure 2-76).

---

[*] https://operafea.com/magnet-design-software/
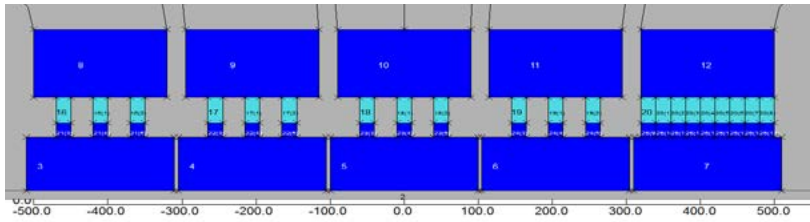
Figure 2-75 : 2D model of the DL magnet.
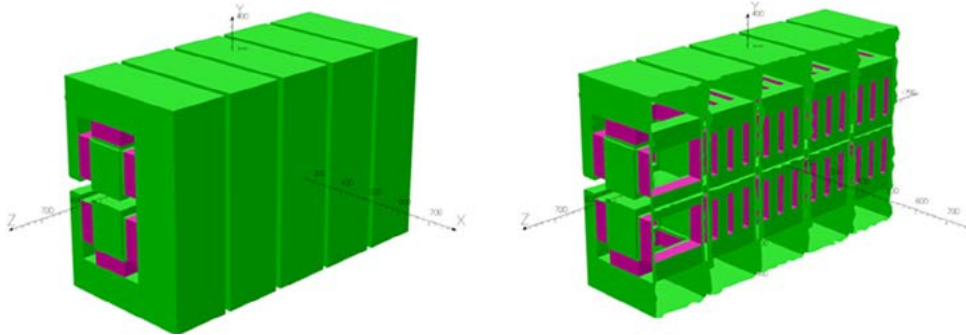
Figure 2-76 : 3D model of the DL magnet with PM block (magenta); left: full model, right: full model with cut plane to show layout of the PM blocks.

The magnetic performance of the PM blocks should be the same from magnet to magnet and also from module to module, but in reality there are some unavoidable differences in the production of PM blocks, including physical and magnetic properties. We have therefore chosen only two sizes of PM block to be used for the DL magnets: 96 larger blocks (83x20x20) and 48 smaller blocks (63x20x20); this enables us to measure and sort the PM blocks more consistently during the manufacturing process. The magnetic simulation results for the uncorrected field and corrected field after calculating proper magnetic shunt pieces are shown in Figure 2-77.
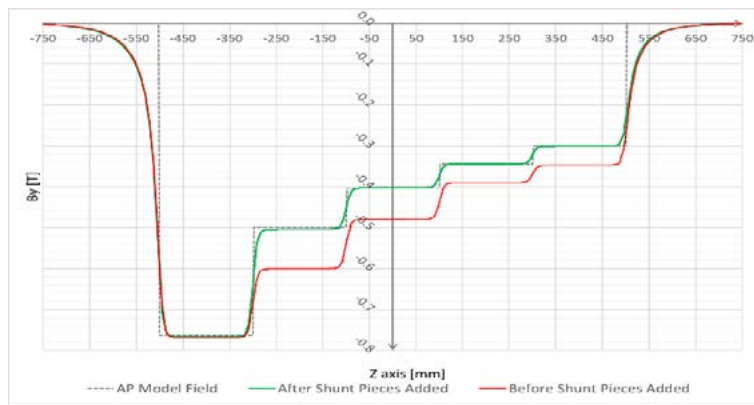
Figure 2-77 : DL field along the Z axis, ideal (black) and before (red) and after (green) adding magnetic shunts.

Shunt pieces are used to partially shortcut the field of the PM blocks in order to tune the field in the magnet gap. These shunts are simple iron pieces which are added to the open side of the magnet, see Figure 2-78.
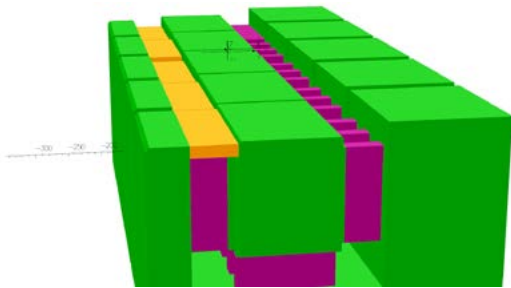
Figure 2-78 : Magnetic shunt pieces in yellow shown for half magnet. After the optimisation of the shunt pieces of the magnet, the integrated multipole components evaluated perpendicular to the particle trajectory at a reference radius of 10 mm, normalised to the dipole field, are shown in Table 2-27.

Table 2-27 : DL magnet normalised multipoles (r=10 mm) in the centre of the magnet and integrated along the Z axis.

Component / n	2	3	5	7	9
Central Multipoles [%]	0.00	-0.01	-0.01	-0.01	0.00
Integrated Multipoles [%]	0.02	-0.01	-0.03	0.00	0.00

2.4.2. Transverse Gradient Dipole (DQ)

The lattice design for Diamond-II requires a relatively high gradient combined function dipole magnet (33 T/m in a 0.7 T dipole). For such a high gradient the conventional dipole geometry with inclined profile cannot be used. Two design options were initially considered based on an offset curved quadrupole or a conventional combined function dipole magnet with two auxiliary poles increasing the gradient up to the required value. For simplicity of manufacturing process and reducing power consumption, the latter model has been chosen. The DQ curved magnet is similar to the one that has been produced for the ESRF-EBS upgrade project [1].

2.4.2.1. DQ Magnet Design Parameters

The design parameters for the DQ are shown in Table 2-28. The magnet consists of two main poles, two auxiliary poles and two sets of coils, the magnet cross-section is shown in Figure 2-79. The magnet yoke can be made of either laminated or solid iron. Since a high level of magnetic field is expected in the yoke, the yoke material will be high permeable low carbon steel in order to reduce both the magnet power and size.

Table 2-28 : DQ magnet design parameters.

Parameter	Value	Unit	Parameter	Value	Unit
Field	0.7	T	Curvature Radius	16421	mm
Gradient	-33	T/m	Yoke Material	Low carbon steel	-
Half Gap at 0.7 T	~14.2	mm	Total Yoke Mass	~1150	kg
Int. B	0.607	T m	Good Field Region (GFR)	±10	mm
Int. G	28.6	T	ΔB/B within GFR	5E-04	-
Iron Length	867	mm	ΔG/G within GFR	1E-03	-

2.4.2.2. Pole and Yoke Geometry

The DQ magnet has been designed to produce a constant dipole and quadrupole magnetic field along the particle trajectory by means of a curved profile, the magnet however will be straight, only the pole profile will be curved.
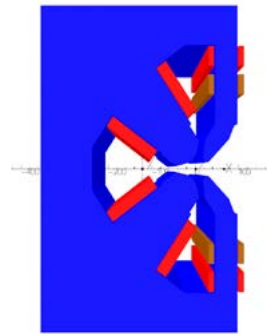
Figure 2-79 : DQ magnet, blue: iron, red: main coils (48+8), brown: trim coils.

A straight pole profile would result in a varying magnetic field along the trajectory as shown in Figure 2-80 where the black line shows the magnetic field profile along the particle trajectory in a straight magnet while the red line shows the magnetic field along the particle trajectory for the same magnet but the pole profile is curved.
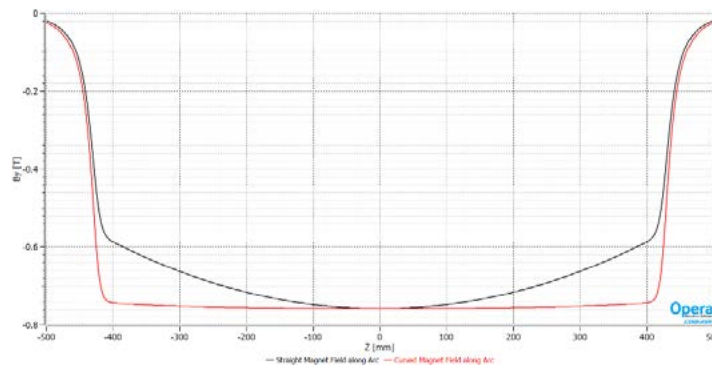
Figure 2-80 : Effect of DQ magnet geometry on the dipole field variation along the electron trajectory.

The pole tip profile is shown in Figure 2-81. The centre of magnet where the field is 0.7 Tesla is indicated.
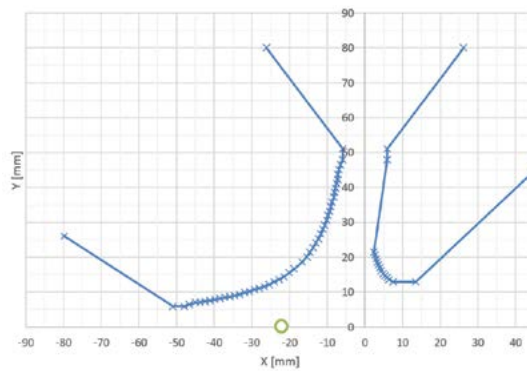
Figure 2-81 : DQ pole tip configuration. The green circle marks the magnet centre.

2.4.2.3. 2D and 3D Field Analysis

Both 2D and 3D simulations have been carried out using the OPERA software. In the 2D model, the DQ has a 2-fold symmetry, therefore only a half geometry is sufficient to model the behaviour of the magnetic field as shown in Figures 2-82 and 2-83.
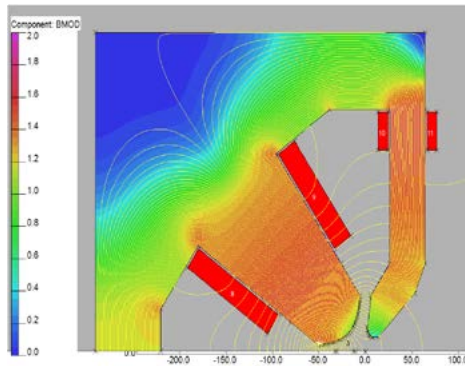
Figure 2-82 : DQ magnet 2D model, magnetic field inside the yoke is kept below 1.8 T.
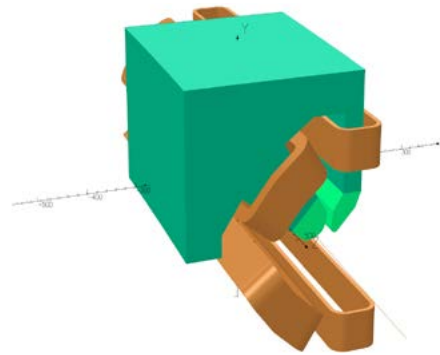
Figure 2-83 : DQ magnet 3D model and particle trajectory.

Having analysed the field in 3D along the particle trajectory, the magnet centre needs to be redefined to get the required integrated dipole and quadrupole fields. The integrated field and gradient values evaluated perpendicular to the particle are shown in Table 2-29.

Table 2-29 : DQ magnet field analysis for shifted centre.

Component	Centre Field $[T/m^{n-1}]$	Integrated Field $[T/m^{n-1}.m]$	L_{eff} [m]
Dipole (n=1)	-0.6936	-0.607	0.875
Quadrupole (n=2)	32.96	28.6	0.868

The dipole and quadrupole field distributions along the particle trajectory are shown in Figure 2-84 and the higher multipole errors are shown in Table 2-30.

Table 2-30 : Normalised multipoles (r=10 mm) in the centre of the magnet and integrated along the particle trajectory for DQ magnet.

n	3	4	5	6
Central Multipoles [%]	0.04	0.03	0.02	0.00
Integrated Multipoles [%]	-0.04	0.09	0.03	0.00
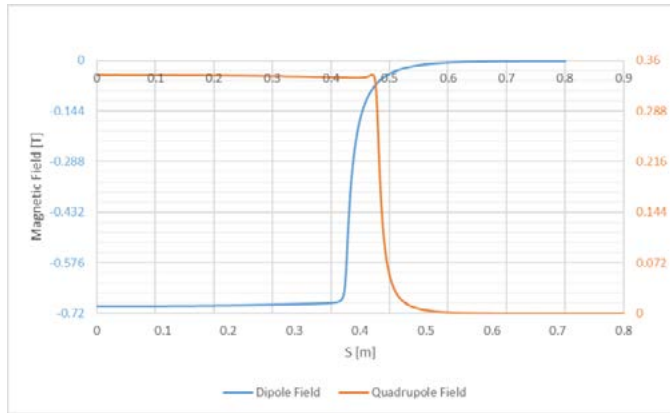
Figure 2-84 : DQ magnet dipole and quadrupole field components along the particle trajectory.

The excitation curves for the integrated components are shown in Figure 2-85, the saturation for integrated and central gradient are 5.5% and 4% respectively at the highest nominal current (i.e. I=178.3 A) and increases to a maximum of 14% at 120% of nominal current. The saturation for integrated and central dipole field is 5% and 4% respectively.
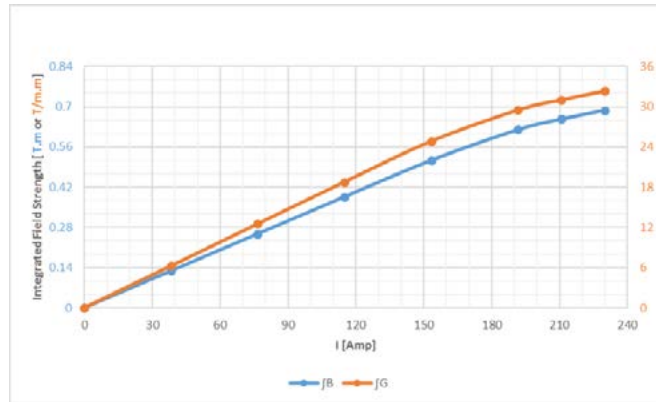
Figure 2-85 : Integrated field and gradient along the particle trajectory as a function of currents for DQ magnet.

2.4.2.4. Quadrupole Component Tunability

The DQ magnet has two sets of coils: the main coils and trim coils. The main coils are responsible for the generating the dipole field with the designed gradient component. The trim coils are added to the magnet to provide independent gradient tunability within a range of -17% to 7% of the nominal value in combination with a change of the main coil current within the range -4% to 2% of the nominal current (i.e. I=178.3 A), see Figure 2-86. The total Ampere-turns in the trim coils required to sweep this range varies within the range of +4000 to -5200 Ampere-turns. Choosing a trim coil with 600 turns, the current needed varies between +6.7 A to -8.7 A.
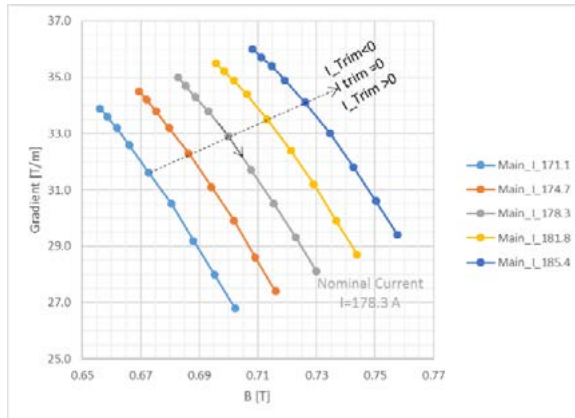
Figure 2-86 : DQ magnet field-gradient phase space diagram.

2.4.2.5. Coil Design: Power Supply and Cooling

The main goal for designing the coil is to keep the water flow speed below 2.5 m/sec while the water pressure drop is fixed at 6 bar. The power and cooling parameters are given in Table 2-31.

Table 2-31 : The DQ magnet power and cooling parameters.

Parameter	Value	Unit	Parameter	Value	Unit
Main coil turns	48	-	cooling circuits	2	-
Aux. coil turns	8	-	Temperature rise	8	°C
current	178.3	A	Water flow rate per magnet	276	litre/hour
current density	3.42	A/mm²	Water flow speed	1.4	m/sec
Conductor size	9x9	mm	Pressure drop per magnet (max)	6	bar
Cooling hole diameter	6	mm			
Total Conductor length	235	m	Trim coil turns	600	-
Total Magnet resistance	81	mΩ	Trim coil conductor size	1.5x1.5	mm
Voltage per magnet	14.4	V	Trim coil current (max)	8	A
Total power per magnet	2.56	kW			

2.4.3. Quadrupole

The lattice design for Diamond-II requires very high gradient quadrupole magnets (G~85 T/m). For designing such a high gradient magnet the inscribed radius has been chosen to be as small as possible (r=12 mm) which helps to lower the magnet power consumption and decrease the pole tip field. There are two general options to achieve such a high gradient:

- Conventional hyperbolic profile with special high permeable material (e.g. Permendur) for the pole tips
- Segmented profile with standard yoke iron at the pole tips.

To avoid complexity during the manufacturing process, the second option has been chosen.

2.4.3.1. Quadrupole Magnet Design Parameters

The design parameters of the quadrupole magnet are shown in Table 2-32 and the proposed quadrupole cross-section is shown in Figure 2-87. The design has been carried out using an optimisation algorithm which starts from a hyperbolic profile and displaces specific points on the hyperbola to minimise the multipole components, while keeping the inscribed radius equal to 12 mm or more and the vertical pole-to-pole separation equal to 10 mm or more. The resulting pole shape after optimisation is shown in Figure 2-88.

The yoke material will be low carbon steel with a relatively high permeability as the magnet is running very close to the saturation with a field inside the yoke of 1.7 T. The top and bottom magnet parts are installed on aluminium pieces which are machined to match the photon extraction pipe designs.

Table 2-32 : Quadrupole magnet design parameters.

Parameter	Value	Unit
G (Max)	85	T/m
Inscribed Radius	12	mm
Length(s)	(105, 150, 185, 250, 360)	mm
Yoke Material	Low carbon steel	-
Good Field Region	±10	mm
ΔG/G at GFR	1E-03	-
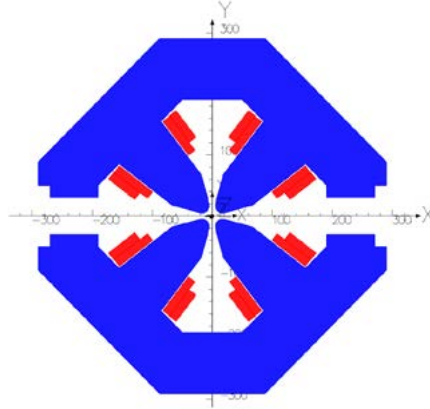
Figure 2-87 : Quadrupole magnet, blue: iron, red: coils.
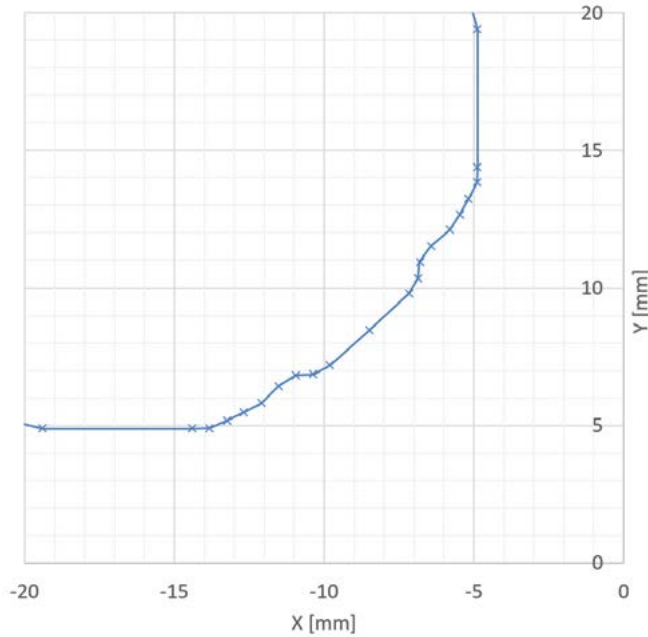
Figure 2-88 : Quadrupole pole tip configuration.

2.4.3.2. 2D and 3D Field Analysis

The design started with a 2D model of the magnet with a realistic coil cross-section, see Figure 2-89. Once the field quality was achieved, the 2D model was used to build the 3D model. In the 3D model some modifications are needed to reach the required field quality, by means of the end chamfers. The optimised end chamfer is 2 mm deep at an angle of 53° to the magnet pole, see Figure 2-90.
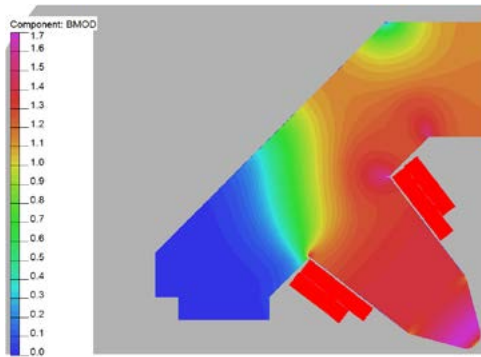
Figure 2-89 : 2D model of the quadrupole; the magnetic field inside the yoke is kept below 1.7 T.
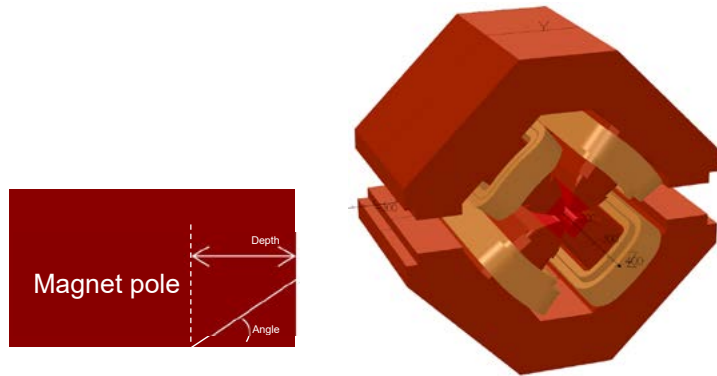
Figure 2-90 : 3D model of the quadrupole and end chamfer details.

The integrated multipoles are shown in Table 2-33. Given the quadrupole symmetry, the only expected multipoles are related to 12-pole, 20-pole and so on, while the 8-pole, 16-pole, and 24-pole are due to the saturation in the yoke.

Table 2-33 : Normalised multipoles (r=10 mm) in the centre of the magnet and integrated over its length.

n	4	5	6	7	8	9	10
Central Multipoles [%]	-0.01	0	-0.02	0	0.01	0	-0.04
Integrated Multipoles [%]	0.01	0	-0.01	0	0.02	0	-0.04

The central and integrated gradient of the quadrupole magnet as a function of excitation are shown in Figure 2-91. The saturation at the highest nominal current is about 2% increasing to a maximum of 12% at 120% of the nominal current.
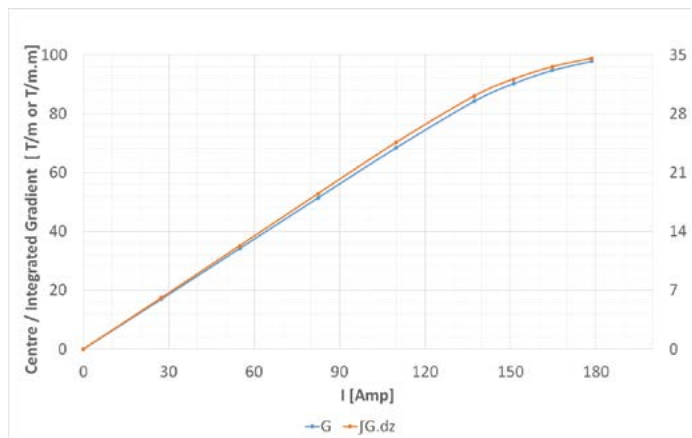
Figure 2-91 : Central and integrated gradient as a function of current.

The effective length of the magnet at different currents is shown in Figure 2-92. As the iron starts saturating, the ends of magnet become less permeable and then the overall length of the magnet is reduced. Such an effect can explain why the 12-pole is current dependent, since, at high current, the end chamfers lose their effectiveness in eliminating the systematic integrated multipole errors.
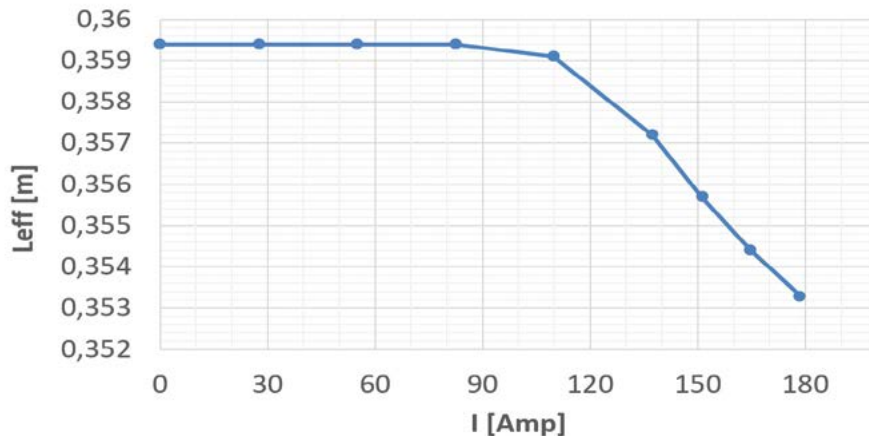
Figure 2-92 : The magnetic length of the quadrupole as a function of current.

2.4.3.3. Coil Design: Power Supply and Cooling

The quadrupole coil is designed to keep the pressure drop fixed at 6 bar with a water flow speed not exceeding to 2.5 m/sec. Furthermore, the current should be kept below 200 Ampere to match power supply design requirements. The coil parameters are shown in Table 2-34.

Table 2-34 : The quadrupole magnet power and cooling parameters.

Parameter	Value	Unit	Parameter	Value	Unit
Main coil turns	36	-	Voltage per magnet	9.1	V
current	140	A	Total power per magnet	1.27	kW
current density	3.312	A/mm^2	cooling circuits	4	-
Conductor size	7x7	mm	Temperature rise	7	°C
Cooling hole diameter	3	mm	Water flow rate per magnet	160	litre/hour
Total Conductor length	160	m	Water flow speed	1.6	m/sec
Total Magnet resistance	66	mΩ	Pressure drop per magnet (max)	6	bar

2.4.4. Sextupole

The lattice design for Diamond-II requires relatively high gradient sextupole magnets (S~3800 T/m^2). The sextupole should also provide three different corrector field components, B_x, B_y, and skew quadrupole (SQ). The dipole corrections are required to be part of the fast orbit feedback.

2.4.4.1. Sextupole Magnet Design Parameters

The magnet design parameters are shown in Table 2-35. For reducing the power consumption of the magnet and the pole tip field, the inscribed radius has been chosen to be as small as possible, within the given mechanical engineering requirements. Two different inscribed radii and yoke shapes have been chosen (See Figure 2-93 and Figure 2-94).

Since the sextupole magnet is also required to provide fast dipole correctors in the horizontal and vertical planes, the yoke material is chosen to reduce the eddy current effects inside the yoke, due to fast changing magnetic fields. The yoke will therefore be made of silicon steel laminations with 0.5 mm thickness.

Table 2-35 : Sextupole magnet design parameters.

Parameter	Value	Unit
S (Max)	3800, 2800	T/m^2
Inscribed Radius	12, 15	mm
Length	(100, 140)	mm
Yoke Material	Silicon Steel	-
Yoke structure	Laminated	-
Good Field Region	±10	mm
ΔS/S at GFR	<1E-02	-
B$_x$ Corrector Field (max)	116	mT
B$_y$ Corrector Field (max)	116	mT
SQ Corrector Gradient	-1.0	T/m
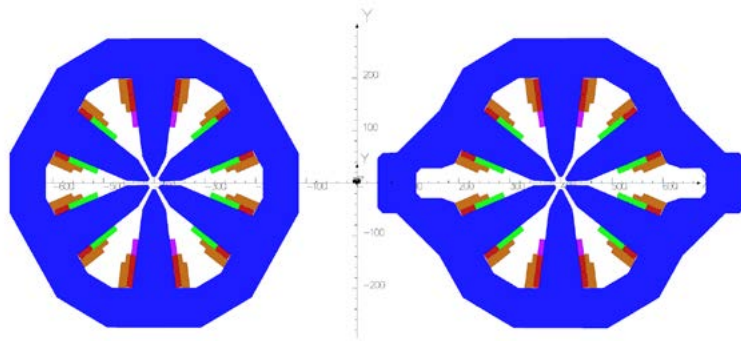
Figure 2-93 : Sextupole magnet types, blue: iron, brown: main coils, red: vertical field trim coils, green: horizontal field trim coils, purple: skew quadruple trim coils.

2.4.4.2. 2D and 3D Field Analysis

The magnet design has been carried out using OPERA software. The pole profile is a simple parabola at a given radius, truncated to provide sufficient pole-to-pole separation and shimmed to achieve required field quality. The flat pieces have been added at the pole truncation point to make a parallel gap between poles and avoid sharp corners in the pole tip area. Two different sextupole cross-sections with different inscribed radii were chosen. The magnet assembly is however exactly the same in both cases.
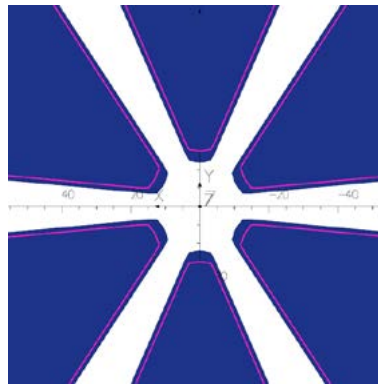
Figure 2-94 : Sextupole pole profile for different radii dark blue: r=12 mm and red line: r=15 mm.

The 2D model of the sextupole magnet is shown in Figure 2-95, the yoke size has been chosen as wide as possible allowing the corrector field components to remain linear with current at high sextupole strength. In order to achieve this, the field inside the yoke is kept below 1.4 Tesla which maintains a high relative permeability (>3000). The trim coils are fitted inside the main coils to reduce the coil size and the overall coil overhang. The 3D model is shown in Figure 2-96.
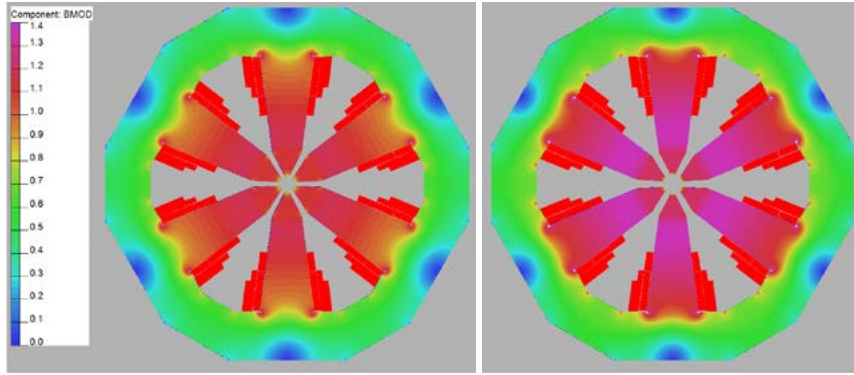
Figure 2-95 : 2D model of the sextupole; left: r=12, right: r=15 mm (correctors off).
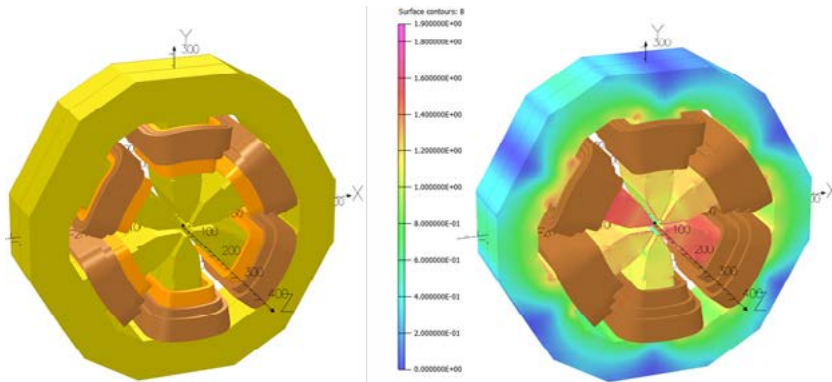
Figure 2-96 : Left - 3D model of the sextupole; brown - main coils, orange - trim coils; Right - field distribution with all correctors powered.

The integrated multipoles are shown in Table 2-36. Because of the sextupole symmetry the only expected multipoles are related to 18-pole, 30-pole etc. The multipole components when all correctors are powered are shown in Table 2-37.

Table 2-36 : Normalised central and integrated multipoles (r=10 mm) in the sextupole magnet with correctors off.

n	9	15
Central Multipoles [%]	-0.56	-0.63
Integrated Multipoles [%]	-0.74	-0.53

Table 2-37 : Normalised central and integrated multipoles (r=10 mm) in the sextupole magnet with correctors on.

	n	1	2	3	4	5	6	7	8	9	10	11
Bx	a_n/a_1 [%]	100	-8.74	-0.02	5.21	-35.05	-0.01	4.1	-0.16	-0.02	-0.13	1.87
	$\int a_n.dz/ \int a_1.dz$ [%]	100	-7.58	-0.06	4.25	-28.74	0	3.07	-0.11	0.03	-0.13	1.52
By	b_n/b_1 [%]	100	0.82	-	0.47	34.96	-0.03	4.12	0	-1.9	-0.01	-1.85
	$\int b_n.dz / \int b_1.dz$ [%]	100	0.79	-	0.43	28.69	-0.01	3.02	0.01	-1.87	-0.02	-1.53

The central gradient and integrated gradient of the sextupole magnet as a function of excitation are shown in Figure 2-97. It shows that there is relatively little saturation. As a result there is also very little change of magnetic length with excitation.
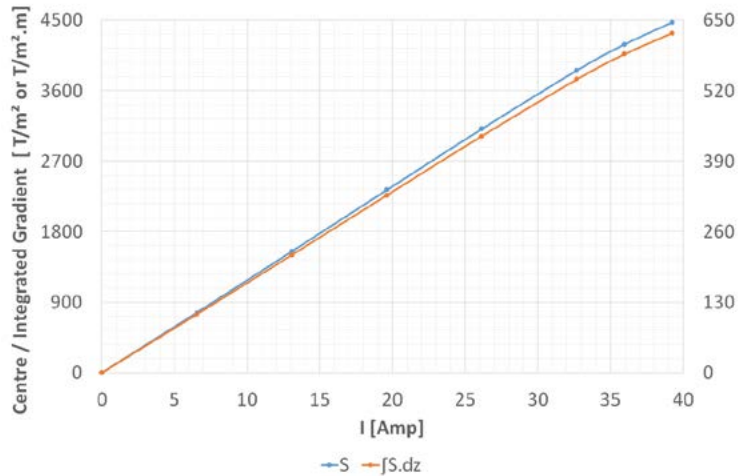
Figure 2-97 : Central and integrated gradient of the sextupole as a function of current.

2.4.4.3. Coil Design: Power Supply and Cooling

The sextupole coil design goal is to keep the current below 50 Amperes to match the current power supply designs, also the water flow speed is kept below 2.5 m/sec, and coil overhang should be less than 40 mm. The power and cooling parameters are shown in Table 2-38.

Table 2-38 : The sextupole magnet power and cooling parameters for two different radii (12 mm, 15 mm).

Parameter	Value	Unit	Parameter	Value	Unit
Main coil turns	56	-	Cooling circuits	6	-
Current	(33, 48)	A	Temperature rise	(2, 4)	°C
Current density	(2.5, 3.7)	A/mm^2	Water flow rate per magnet	100	litre/hour
Conductor size	4x4	mm	Water flow speed	1.5	m/sec
Cooling hole diameter	2	mm	Pressure drop per magnet(max)	6	bar
Total Conductor length	150	m	By Trim coil turns	(150,300)	-
Total Magnet resistance	210	mΩ	Bx Trim coil turns	300	-
Voltage per magnet	(6.8, 10.1)	V	SQ Trim coil turns	150	
Total power per magnet	(230, 490)	W	Trim coil conductor size	2X2	mm
			Trim coil current (max)	4.5	A

Fitting the trim coils inside of the main coils (see Figure 2-98) allows reaching the bending radius criteria (R >3x conductor size) with reduced coil overhang (i.e. the trim coils will fill the required gap generated between the main coil and the yoke to achieve the hollow conductor minimum bend radius criterion).
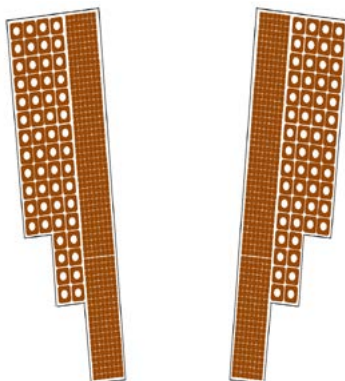
Figure 2-98 : Coil layout for sextupole magnet (overall width is 37.5 mm).

2.4.5. Octupole

The lattice design for Diamond-II requires octupole magnets with moderate gradient of 1.1E+05 T/m^3. Conceptually this magnet can be designed with a size as small as 150x150 mm (pole tip radius r=12 mm), but to make it easier to manufacture and to guarantee a sufficient mechanical strength and rigidity, the magnet size has been chosen 190x190 mm.

2.4.5.1. Octupole Magnet Design Parameters

The design parameters of the octupole are shown in Table 2-39. The proposed magnet cross-section is shown in the Figure 2-99.

The octupole magnet is a DC magnet which works at a fixed current. The magnet size is larger than magnetically required, therefore a material with moderate permeability is suitable for the yoke.

Table 2-39 : Octupole magnet design parameters.

Parameter	Value	Unit
Octupole Strength	110300	T/m^3
Inscribed radius	12	mm
Iron Length	90	mm
Yoke Material	Low carbon steel	-
Good Field Region	±10	mm
ΔB/B at GFR	<5E-02	-
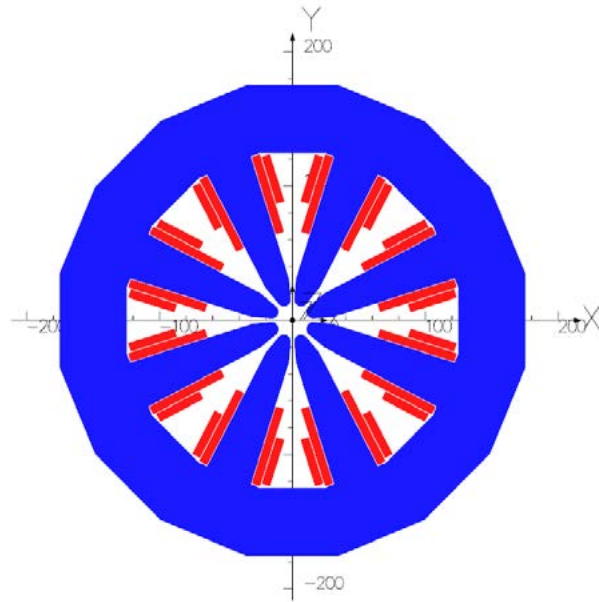
Figure 2-99 : Octupole magnet, blue: iron, red: coils, overall size of 190x190 mm.

2.4.5.2. 2D and 3D Field Analysis

The magnet design has been carried out using OPERA software. The pole profile is determined by the relation $(x^3y - xy^3) = r^4/4$, which has been truncated to provide sufficient pole to pole gap. Flat pieces have been added at the pole truncation point to make a parallel gap between poles and avoid sharp corners in the pole tip area.

The 2D and 3D models of the octupole magnet are shown in Figure 2-100 and Figure 2-101 respectively, the yoke size has been chosen sufficiently large to have enough space for fitting coils.
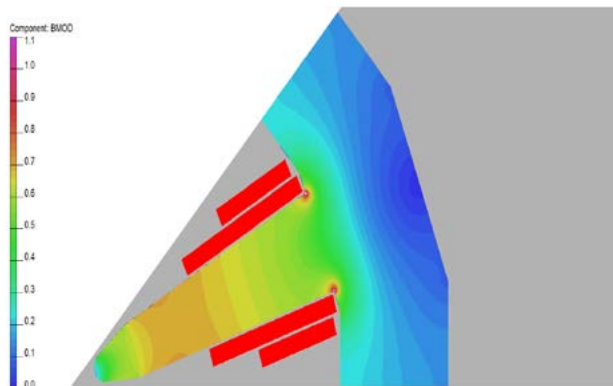
Figure 2-100 : 2D model of the octupole magnet; the magnetic field inside the yoke is relatively low.
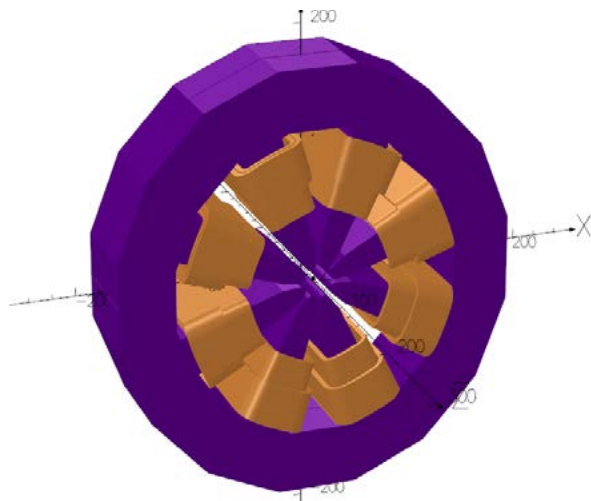
Figure 2-101 : 3D model of the octupole magnet.

The integrated multipoles are shown in Table 2-40. Because of the octupole symmetry the only expected multipoles are 24-pole, 40-pole etc., while the 12-pole, 44-pole are due to end effects.

Table 2-40 : Normalised central and integrated multipoles (r=10 mm) in the octupole magnet.

Component / n	6	12	20	22	28
Central Multipoles [%]	0	-0.04	-0.02	0	0.00
Integrated Multipoles [%]	-0.01	-0.13	0.00	-0.01	-0.01

The central and integrated octupole strengths as a function of current are shown in Figure 2-102. There is little saturation and as a result there is also no appreciable variation of magnetic length with excitation.
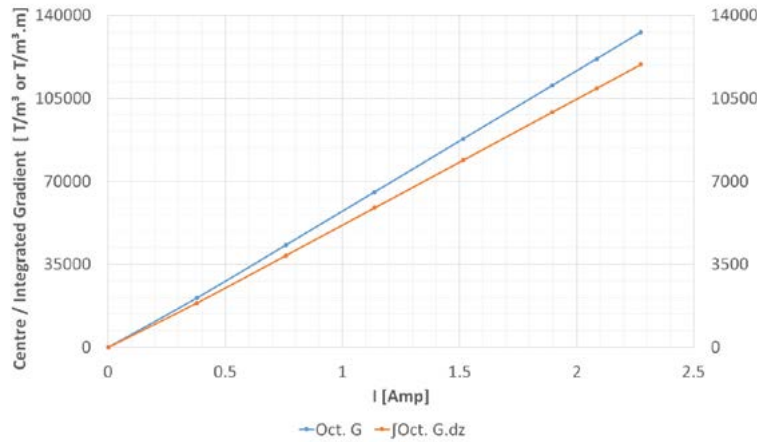
Figure 2-102 : Central and integrated octupole strength as a function of current.

2.4.5.3. Coil Design: Power Supply and Cooling

The octupole can be air cooled, therefore there is no cooling channel through the conductor. In this case the current density is kept below 1 A/mm². The coil is made of simple insulated copper wire with rectangular cross-section. The magnet power parameters are shown in Table 2-41.

Table 2-41 : The octupole magnet power parameters.

Parameter	Value	Unit	Parameter	Value	Unit
Main coil turns	256	-	Total conductor length	700	m
Current	1.85	A	Total magnet resistance	5.7	Ω
Current density	0.823	A/mm²	Voltage per magnet	10.555	V
Conductor size	1.5x1.5	mm	Total power per magnet	19.5	W

2.4.6. Correctors

The Diamond-II lattice requires 12 discrete corrector magnets with vertical and horizontal field components. The design parameters are shown in Table 2-42.

Table 2-42 : Corrector magnet design parameters.

Parameter	Value	Unit
Horizontal deflection	1	mrad
Vertical deflection	1	mrad
Gap (V, H)	(29,59)	mm
Iron length	80	mm
Yoke material	Low carbon steel	-

Regarding the design parameters, the required magnet aperture should be a rectangular shape (i.e. 29x59 mm), the possible magnet cross-sections are shown in the Figure 2-103.
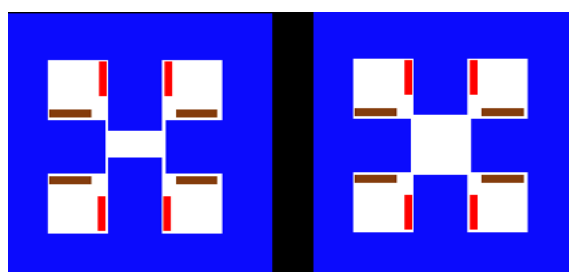
Figure 2-103 : Corrector magnet with rectangular (left) and square (right) aperture; blue - iron, red - vertical field coils, brown - horizontal field coils.

For the rectangular aperture the field quality is poor and for the square aperture the power needed is increased, which exceeds to the maximum power supply current. The proposed solution is to separate the B_x and B_y components longitudinally (See Figure 2-104). This introduces the flexibility of optimising each component independently to satisfy both field quality and power consumption requirements.
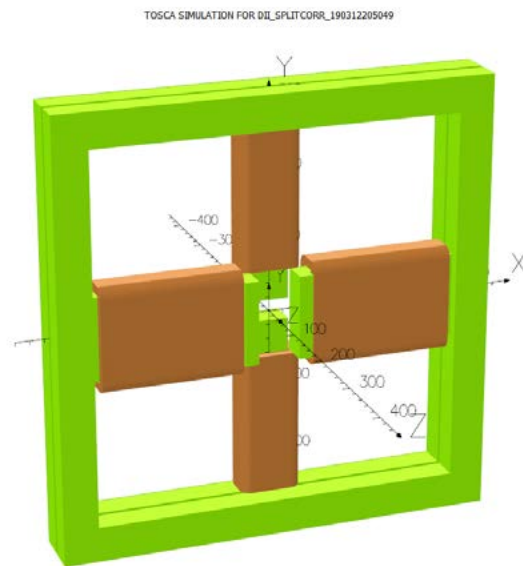
Figure 2-104 : Split corrector magnet with rectangular aperture.

2.4.6.1. 3D Field Analysis

The corrector magnet design has been carried out using OPERA software. The 3D model of the corrector magnet is shown in Figure 2-105, in this model the horizontal and vertical gaps between poles are (59, 29) mm respectively which produces the required integrated field and deflection angle in both planes (maximum deflection angle of 1.0 mrad).
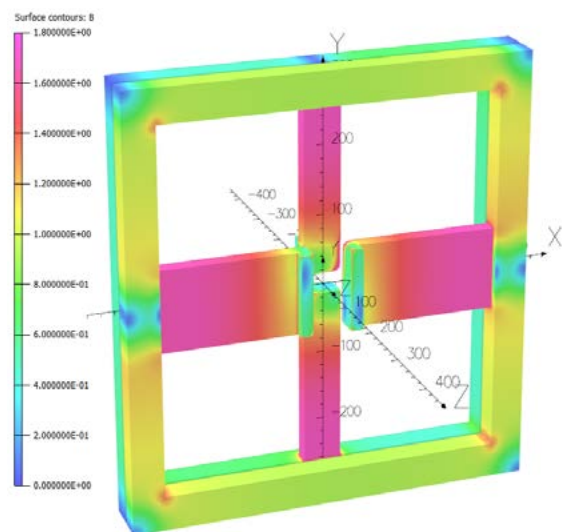
Figure 2-105 : 3D model of the split corrector magnet; the magnetic field is kept below 1.8 T in the yoke.

The field profile along the beam axis is shown in Figure 2-106, corresponding to 1 mrad deflection in each plane. The multipole errors in this case are shown in Table 2-43 and are much better than the single magnet case.
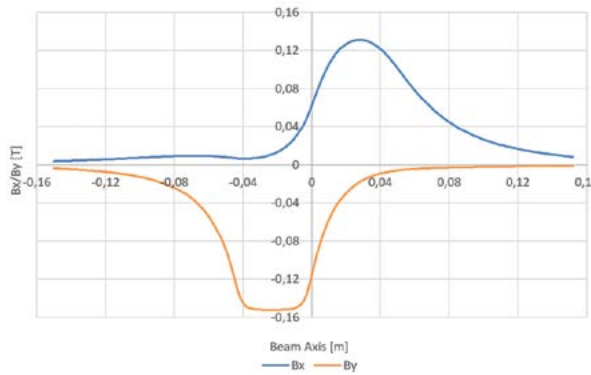
Figure 2-106 : Corrector magnet field components along the Z axis.

Table 2-43 : Normalised central and integrated multipoles (r=10 mm) for horizontal and vertical field components in the corrector magnet.

n		3	5	7
Horizontal Field (B$_x$)	Central Multipoles [%]	3.9	-0.1	0.0
	Integrated Multipoles [%]	5.8	0.2	0.0
Vertical Field (B$_y$)	Central Multipoles [%]	-0.9	-0.2	0.0
	Integrated Multipoles [%]	-2.0	-0.2	0.0

2.4.6.2. Coil Design: Power Supply Parameters

The main goal for coil design is to minimise the coil overhang. The corrector magnet power parameters are shown in Table 2-44.

Table 2-44 : The Corrector magnet power parameters.

Parameter	Bx	By	Unit
Number of turns	900	600	-
Current	4.6	3.9	-
Current density	1.6	0.9	A/mm^2
Conductor size	1x2.9	1x4.3	mm
Total conductor length	1010	462	m
Total magnet resistance	6.2	1.9	Ω
Total magnet voltage	28.9	7.6	V
Total power per magnet	134	30	W

2.4.7. Magnetic Measurements and Alignment

2.4.7.1. DL Magnet Measurement and Alignment

The magnetic measurement of this type of magnet includes measuring the field for every single module using either a Hall Probe Bench (HPB) or a Stretched Wire Bench (SWB), then relating its outer fiducials to the magnetic axis then aligning them in the module to reach the desired integrated field along the particle trajectory (See Figure 2-107). For doing this type of alignment it is important to know the field profile along the particle trajectory from the 3D model for every single module individually.
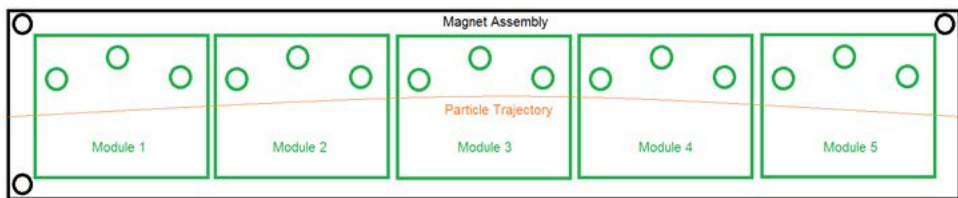
Figure 2-107 : DL magnet assembly outer fiducials; circles - tooling holes defining local coordinates systems).

Having aligned all modules, the DL magnetic field integral can be cross checked using the SWB. Thereafter the DL magnet alignment on the girders is carried out using a laser tracker which puts the magnet assembly fiducials on their predefined nominal locations on the girder coordinates system.

2.4.7.2. DQ Magnet Measurement and Alignment

The DQ magnet is a curved combined function magnet which needs to be measured magnetically using a HPB. Once the field map is produced then the particle trajectory is calculated and fiducialised with respect to the outer mechanical fiducials (i.e. tooling holes on the top of magnet structure).

Having defined the relationship between tooling holes and particle trajectory, the magnet can be installed on the girder using a laser tracker which puts the magnet mechanical fiducials on their predefined nominal locations on the girder coordinates system.

2.4.7.3. Multipole Magnet Measurement and Alignment

Every multipole magnet should be measured magnetically using a SWB or a Rotating Coil Bench (RCB) to determine the magnet centre coordinates (i.e. C_x and C_y), the magnetic axis direction (i.e. A_x, A_y, and A_z), and the roll angle which is the rotation angle of the horizontal plane. Once the magnet centre and axis have been measured, the magnet will be fiducialised with respect to the mechanical fiducials (tooling holes on the top of magnet) using either a laser tracker or a Faro Arm.

Having defined the relationship between the magnet axis and centre and mechanical fiducials, the magnet can be installed on the girder using a laser tracker which puts the magnet fiducials on their predefined nominal locations on the girder coordinates system.

For the multipole magnets, there is a possibility of doing the in-situ alignment on the girder using a SWB. This procedure is more precise than the alignment with using laser tracker but needs to be included in the design of the girders. In fact the girder must accommodate the bench towers at both ends of each straight section to align a string of magnets installed on this straight line. Although this method is very precise (~10 µm), it can be very time consuming. Also the interference between stretched wire movement and other equipment on the girder can affect the accuracy of the alignment.

References

[1]   C. Benabderrahmane et al., Proc. IPAC 2018, Vancouver, Canada, WEPMK009, p. 2648.

2.5. Vacuum

2.5.1. Introduction

2.5.1.1. Requirements

The vacuum system for the Diamond-II storage ring has to fulfil a number of different performance requirements. These are summarised in Table 2-45.

Table 2-45 : Diamond-II storage ring vacuum system requirements.

Parameter	Specification
Vacuum performance	Gas lifetime should be in excess of 10 hours at 300 mA after 100 Ah of beam conditioning. This is taken to mean an average pressure of 10^{-9} mbar or better around the storage ring at 300 mA after 100 Ah of beam conditioning.
Machine impedance	Geometric and resistive wall effects on the machine impedance should be controlled. Geometric effects are minimised by minimising steps, gaps and cross-section changes and by shielding RF bellows. Resistive wall effects are material dependent and can be affected by base material, coating material(s) and surface morphology, e.g. roughness.
Electron beam stay clear	Defines the minimum aperture for the vessel interior space so as not to reduce the lifetime.
Magnet compatibility	The vessel external size and shape must allow enough space for the magnet poles, coils and yokes with an allowance, where required, for mechanical decoupling and in-situ bakeout heaters/insulation. Vessel materials must not affect the magnetic field applied to the beam by the magnets (both AC and DC). In-situ bakeout must not produce excessive temperatures in nearby magnets. Vessel movements, e.g. due to heating and cooling during operations, must not move the magnets by a significant amount.
Photon extraction	It must be possible to extract the useful photon beams from bending magnets and insertion devices.
Heat load management	Synchrotron radiation power loading on the vessel wall from bending magnets and insertion devices must be handled adequately by the vessel materials and cooling features.
Operations	The final vacuum system must operate reliably, be maintainable and be provided with vacuum monitoring to verify the correct functioning and to give early warning of any problems. Energy efficiency of the active systems should be considered in the design.

2.5.1.2. Proposed Solution

A vacuum system design is proposed here which fulfils all of the above requirements. The main features are:

- Extensive use of Non-Evaporable Getter (NEG) coatings to provide distributed pumping, supplemented by discrete sputter ion pumps.
- In-situ bakeout and NEG coating activation.
- Main construction materials copper and stainless steel.
- Combination of discrete and distributed photon absorbers.

2.5.2. Reference Projects

Many aspects of the proposed Diamond-II vacuum system build on experience from the Double-Double-Bend Achromat (DDBA) upgrade [1], which was installed in Diamond Cell 2 in 2016. The DDBA vacuum system is mechanically similar to the proposed system for Diamond-II. The main difference is the addition of NEG coating for Diamond-II compared with the uncoated vessels for DDBA. The vacuum performance of uncoated vessels for DDBA, while adequate for one cell, would not be adequate to achieve the target for a complete storage ring. Experience from the Diamond vacuum system build and user operation [2], [3] was also taken into account.

Experience and design reports from other facilities were also considered in developing the proposed design, including SOLEIL [4], Max-IV [5], SLS-2 [6], ESRF-EBS [7] and APS-U [8].

2.5.3. Vacuum Pumping Scheme

The dense magnetic lattice and narrow beam tubes (typically 20 mm internal diameter) mean that the vacuum system is strongly conductance limited with little space for discrete vacuum pumps. This leads naturally to a design with distributed pumping which, in the proposed design, is provided by a Non-Evaporable Getter (NEG) coating, a technology which has successfully been used extensively on a number of accelerator projects [9]–[11] In addition to local surface pumping, NEG coatings provide much-reduced gas loads from surface outgassing compared to uncoated vessels [12].

An alternative design approach, which could avoid NEG coating, would be to widen out the vessels to incorporate an antechamber to increase the gas flow conductance to the nearest discrete pump and/or to incorporate other kinds of distributed pumping such as NEG strips. This has been rejected in favour of simple circular vessels with NEG coating where possible due to lack of space and due to the convenience and high performance of the NEG coating. In some areas, the vessel does have to be widened out in any case to allow the photon heat load to be handled and/or for photon beam extraction.

NEG coating alone is not sufficient to pump the complete vacuum system, as non-active gases such as noble gases and methane are not pumped, and also saturation occurs at a low gas load [13]. Additional pumping is therefore provided by discrete sputter ion pumps near regions of high gas load such as high flux photon absorbers. Representative pumping calculations are presented in the following Sections.

A combination of distributed and discrete photon absorbers is used to handle dipole radiation, which is generally the same in every cell, plus insertion device radiation which varies from cell to cell. Further details of heat load management can be found in Section 2.6.

2.5.4. Pumping Calculations

In this first iteration of the pumping scheme, a simple tubular vessel with 20 mm internal diameter centred about the electron beam path is considered. The only radiation considered is the output from the six dipoles per cell; radiation from insertion devices, chicane magnets, quadrupoles and higher order magnets is ignored. Cell 5 is arbitrarily taken as the reference cell for this study. Radiation from the final dipole in cell 4 is included in the calculation as some of its light hits the wall near the beginning of cell 5. In this simplified first design study, there is no photon beam extraction; all of the synchrotron radiation is handled within the storage ring.

In addition to pumping from the NEG coating, small discrete sputter ion pumps of 20 l/s are applied at the downstream end of each of the six dipoles, near where the maximum photon flux hits the vessel walls. 1000 l/s of sputter ion pumps and some additional gas loads are also applied in each of the straights (both the existing long straight and the new mid-cell straight) to simulate an in-vacuum undulator or cryogenic permanent magnet undulator (CPMU) in these locations. The total applied ion pump speed in the cell is therefore 2120 l/s.

The basic layout of cell 5 is shown in Figure 2-108. The upstream (LM) and downstream (MS) girder sections are shown in more detail in Figure 2-109 and Figure 2-110.
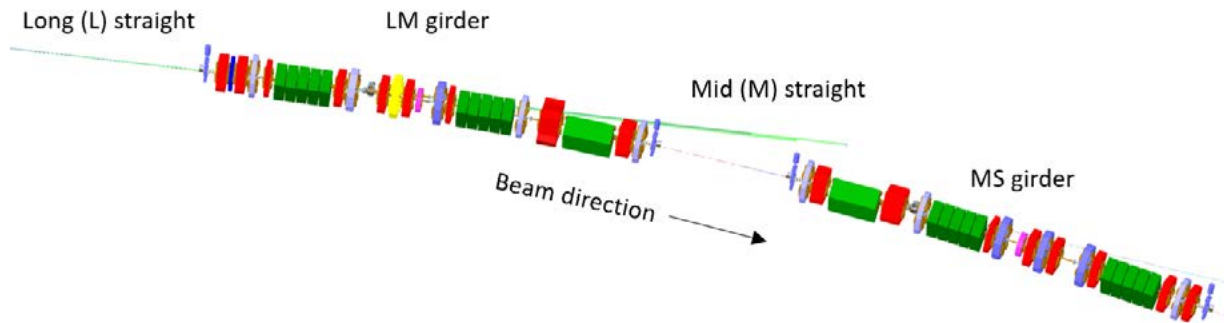
Figure 2-108 : Basic layout of cell 5, showing the magnet locations; green - dipole bending magnets, red - quadrupoles, yellow - sextupoles. The long straight, LM girder, mid straight and MS girder are identified.
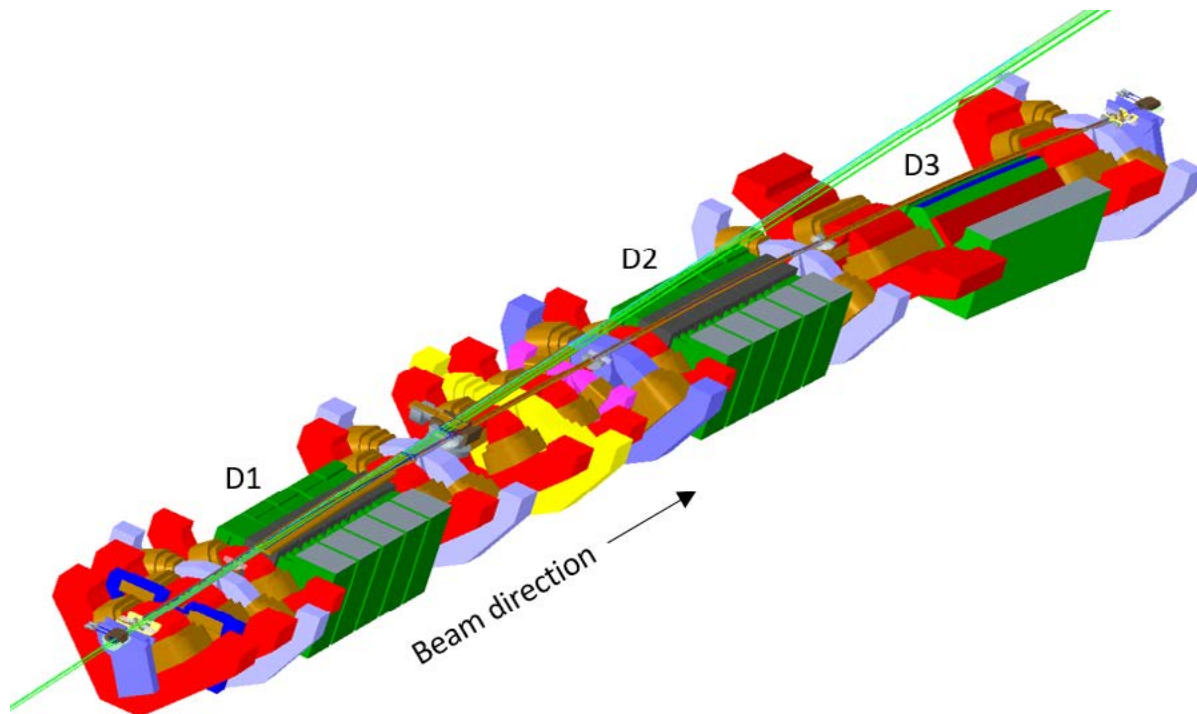
Figure 2-109 : Layout of cell 5 LM girder, identifying the three dipole magnets D1 – D3.
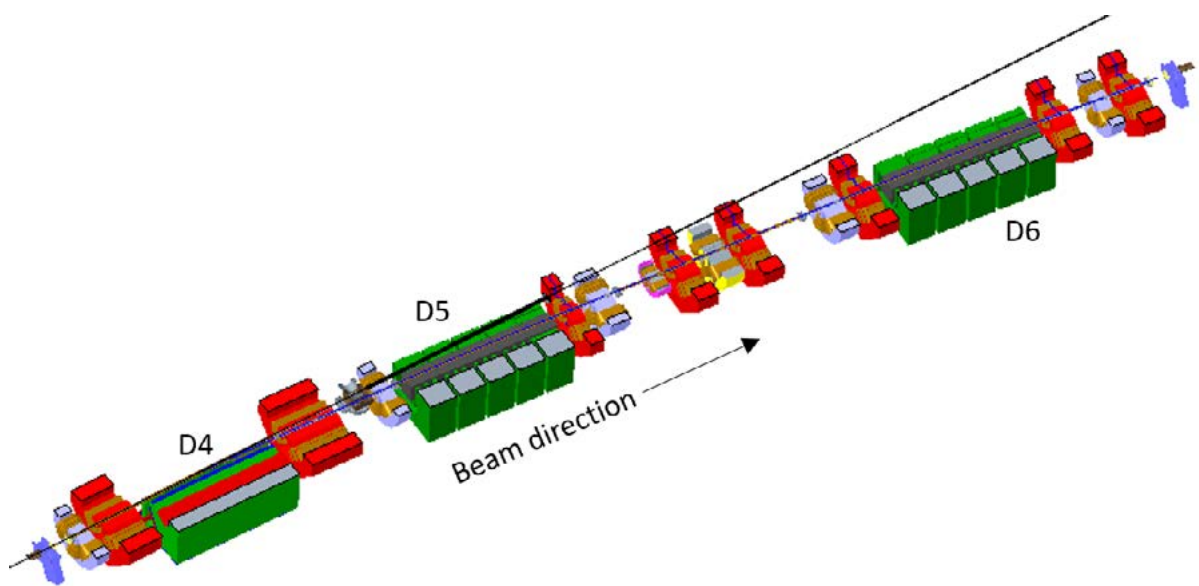
Figure 2-110 : Layout of cell 5 MS girder, identifying the three dipole magnets D4 – D6.

The vacuum simulation was carried out for three different vessel wall materials:

a. Plain copper/stainless-steel

b. Fully-activated NEG coating

c. CO-saturated NEG coating

This enables a direct comparison between a non-NEG-coated design (a) and a NEG-coated design (b). The saturated NEG coating calculation (c) was included so that the low-outgassing and pumping effects of the NEG coating can be understood separately and to investigate what kind of performance deterioration can be expected in case of coating saturation during operation.

Published values for photon-stimulated-desorption (PSD) yield and sticking probability for the NEG coating were used [14]. A conservative, lower value of 0.1 was used for the sticking probability for CO and CO_2 on NEG, rather than the published value of 0.5 for a freshly activated coating, to allow for some degree of saturation.

Partial reactivation of the NEG coating by synchrotron radiation amounting to approximately 2×10^{-5} new adsorption sites created per incident photon, has been reported [14]. This will tend to prevent the CO-saturated NEG coating losing all its pumping speed in the presence of synchrotron radiation; however, this process has not been well studied to date and therefore has not been taken into account in the current simulations.

The thermal outgassing rate and PSD yield for stainless steel / copper have been taken from experience using previous calculations at Diamond [3]. Plain copper is assumed to have identical vacuum properties to plain stainless-steel.

The thermal outgassing rates from the NEG coating for all gases are very low, difficult to measure and consequently not well known. The actual values are not critical to the design and have been taken as 0.1% of the corresponding values for plain copper/stainless steel.

The thermal outgassing rate and PSD yield for the CO-saturated NEG coating are taken to be the same as for the activated NEG coating while the sticking probabilities for all gases in the CO-saturated is case are set to zero.

These parameters are summarised in Table 2-46. The assumed PSD yield vs photon dose curves for NEG and Copper/ Stainless Steel are plotted in Figure 2-111.

Table 2-46 : Values used for thermal outgassing rate (Q), Sticking probability (s) and initial PSD yield for the four gases and three materials in this study.

Material	Cu/StSt	Activated NEG	Saturated NEG
Q H_2 (mbar.l/s/sqcm)	1.0×10^{-11}	1.0×10^{-14}	1.0×10^{-14}
Q CH_4 (mbar.l/s/sqcm)	1.0×10^{-13}	1.0×10^{-16}	1.0×10^{-16}
Q CO (mbar.l/s/sqcm)	1.0×10^{-12}	1.0×10^{-15}	1.0×10^{-15}
Q CO_2 (mbar.l/s/sqcm)	1.0×10^{-13}	1.0×10^{-16}	1.0×10^{-16}
s H_2	0	7.0×10^{-3}	0
s CH_4	0	0	0
s CO	0	0.1	0
s CO_2	0	0.1	0
Initial PSD yield H_2 (molecule/photon)	1.0×10^{-2}	1.5×10^{-5}	1.5×10^{-5}
Initial PSD yield CH_4 (molecule/photon)	2.0×10^{-4}	2×10^{-7}	2×10^{-7}
Initial PSD yield CO (molecule/photon)	5.0×10^{-3}	$< 1 \times 10^{-5}$	$< 1 \times 10^{-5}$
Initial PSD yield CO_2 (molecule/photon)	2.0×10^{-3}	$< 2 \times 10^{-6}$	$< 2 \times 10^{-6}$
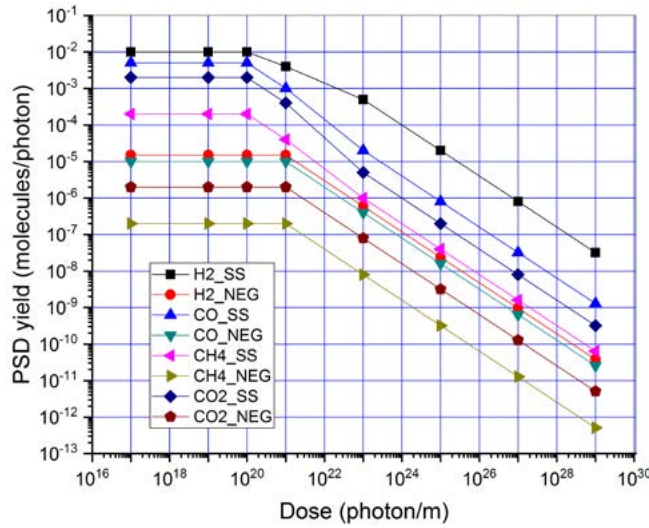
Figure 2-111 : Plot of values used for the PSD yield vs photon dose for the four gases for stainless steel / copper and NEG.

Figure 2-112 shows the result of geometric ray tracing the synchrotron radiation from the dipole magnets with a 20 mm inside diameter circular vessel, to show where the generated photons land on the vessel wall, downstream of the source points. The vessel axis is assumed to follow the beam path, i.e. it is curved in the dipole magnets. The received photon flux on the wall is important as this determines where photon-stimulated gas desorption occurs.
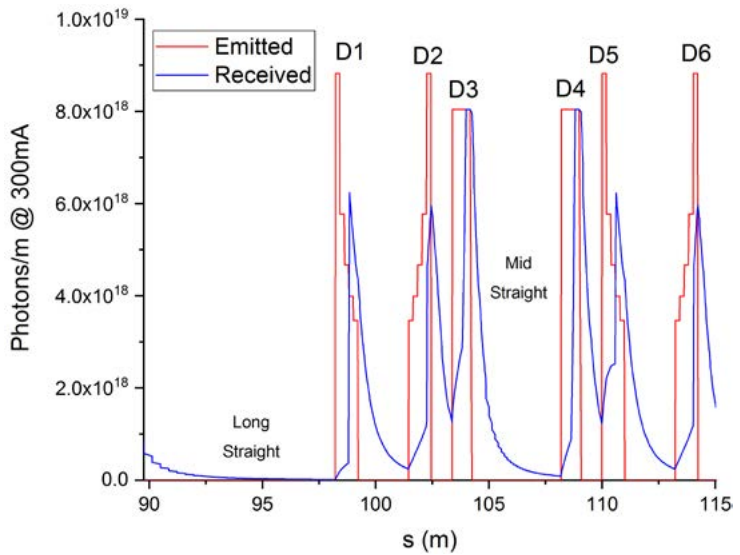
Figure 2-112 : Photon flux for all photon energies per unit length at 300 mA emitted from the six dipoles in one cell and received at the vessel wall for a 20 mm internal diameter vessel. Only primary incident flux is considered, i.e. no scattering or re-emission from the walls.

In the next stage of the simulation, the received photon flux on the walls is combined with the wall material properties (thermal outgassing rate, photon-stimulated desorption yield, sticking probability), the gas flow properties of the vessel and any discrete pumps to calculate the pressure profile along the tube. This calculation was repeated for the four main gases (H_2, CO, CH_4 and CO_2) and for beam conditioning doses in the range from 10^{-5} to 10^4 Ah. The photon desorption yield is taken to vary with beam dose according to Figure 2-111. Sticking probability and thermal outgassing rate are assumed to be beam dose invariant. The calculation was carried out using the Diamond in-house PressureProfile code [15].

For each beam conditioning dose, the Z^2-weighted sum of the pressure from the four main gases is then calculated to obtain the CO-equivalent pressure which is relevant for calculating beam lifetime [16].

Figure 2-113, Figure 2-114 and Figure 2-115 show the calculated pressure vs distance for the three different wall materials. In each case the four main gases are plotted at two beam conditions: (i) no beam and (ii) 300 mA beam after 100 Ah.

Figure 2-116 shows the CO-equivalent pressure vs distance for the three different wall materials for the same two beam conditions.

Figure 2-117 shows the mean CO-equivalent pressure in the whole cell at 300 mA beam current for each wall material, plotted against beam conditioning dose. The vacuum performance differences between the three different vessel wall materials are very clear. For uncoated stainless-steel or copper vessels, the target mean pressure of 10^{-9} mbar is not achieved even after a beam conditioning dose of 10,000 Ah, which represents nearly 7 years of operation at 300 mA with 5000 operating hours per year. Without NEG coating or some other distributed pumping scheme, a very different vacuum design would be required, for example wider vessels to increase the gas flow conductance and/or more discrete pumps.

With the fully-activated NEG coating, the target pressure is achieved after a beam conditioning dose of only 6 Ah: this comfortably meets the 100 Ah conditioning dose target. In reality this is probably somewhat over optimistic as beam scattering, reflection and re-emission and the effect of uncoated areas have been neglected. It has also been implicitly assumed that all photon absorbers are NEG coated. Furthermore, it is likely that the NEG coating would show some degree of saturation in areas near sources of high gas loads and would be less efficient in these places. It should also be noted that the initial ramp up of the beam current to 300 mA after the upgrade would be done slowly to allow beam conditioning of other parts of the accelerator and beamlines and for thermal monitoring.

Interestingly, the fully saturated NEG coating, which is taken to have the same outgassing properties as the activated NEG coating but zero wall pumping, is predicted to have less than one order of magnitude higher pressure than for the fully activated case. So partial saturation in some areas may not have a serious effect on the vacuum system performance.
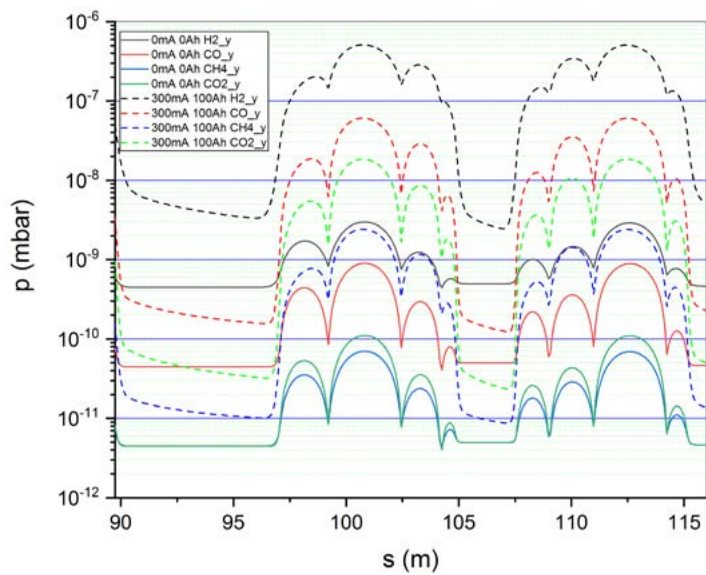
Figure 2-113 : Calculated partial pressures vs distance for copper/stainless steel uncoated vessels with zero beam current and with 300 mA after 100 Ah beam conditioning.
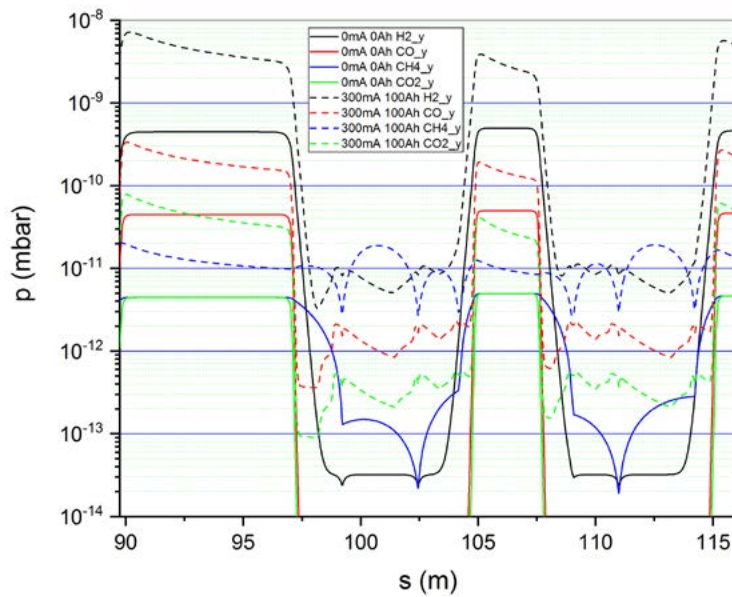
Figure 2-114 : Calculated partial pressures vs distance for activated NEG-coated vessels with zero beam current and with 300 mA after 100 Ah beam conditioning.
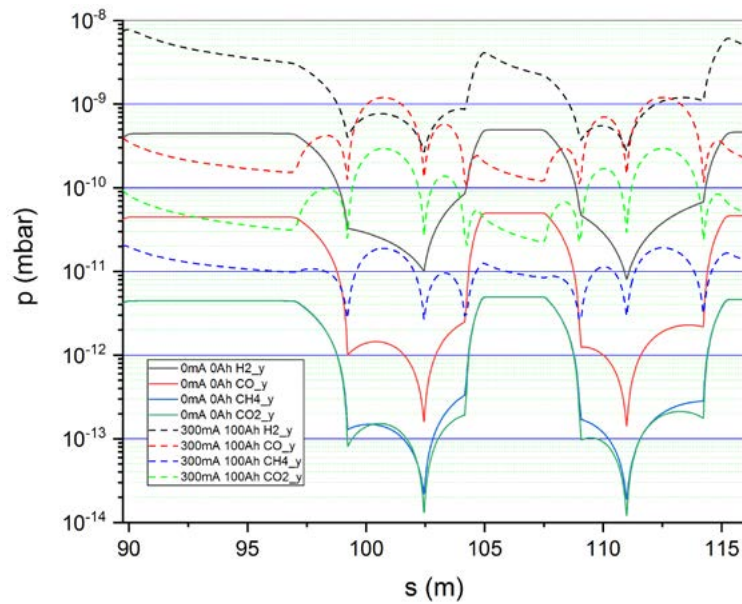
Figure 2-115 : Calculated partial pressures vs distance for saturated NEG-coated vessels with zero beam current and with 300 mA after 100 Ah beam conditioning.
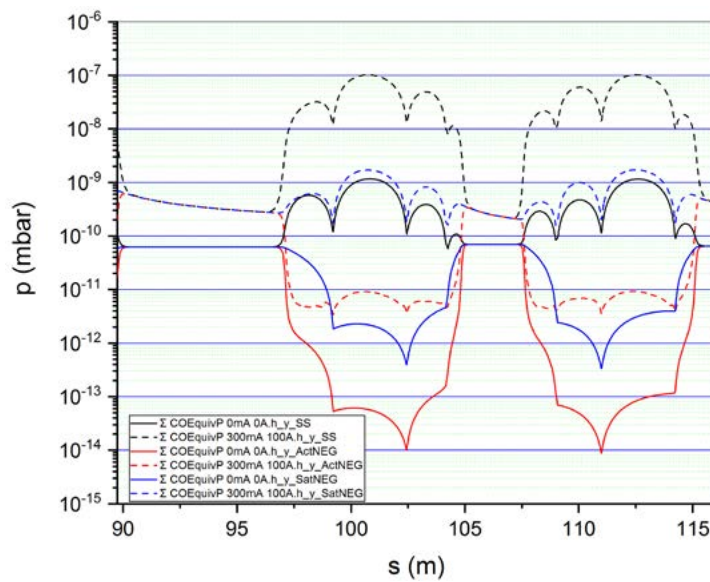
Figure 2-116 : Calculated CO-equivalent pressure vs distance for uncoated stainless-steel / copper, activated NEG coating and saturated NEG coating with no beam and with 300 mA beam after 100 A.h of beam conditioning.
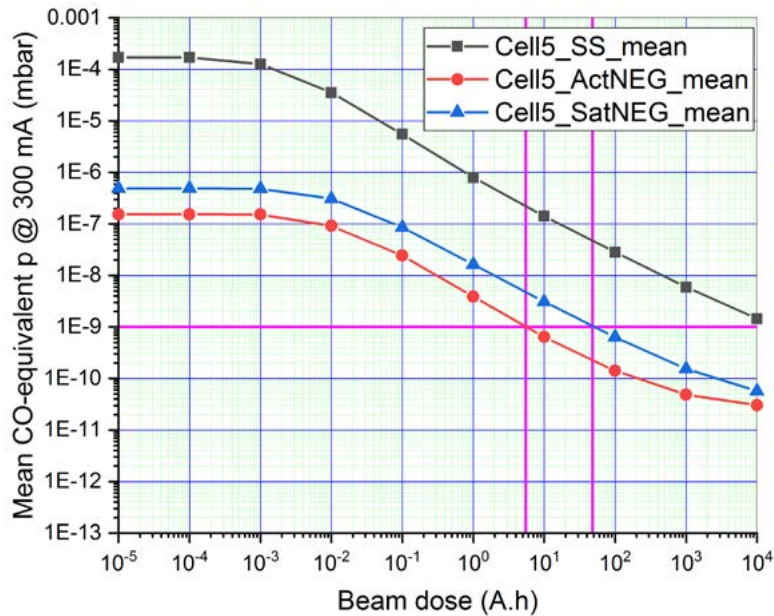
Figure 2-117 : Mean CO-equivalent pressure at 300 mA calculated for a whole cell vs beam conditioning dose for the three different vessel wall materials.

2.5.5. Vacuum Design – Next Steps

As noted above, these preliminary simulations are valid only for a simplified geometry. More detailed calculations will be carried out as the detailed design progresses. In addition to 1D calculations using the Pressure Profile program, full 3D simulations will be carried out using a Monte-Carlo molecular-flow approach [17] and/or the method of angular coefficients [18]. Refinements to the existing calculations will include:

• Discrete pump locations which fully respect the available space.

• Use of the actual engineering vessel geometry including antechambers and crotch absorbers where these are needed for photon beam extraction and heat load management.

• Consideration of all of the different types of insertion device which may be fitted in the straights as these have very different photon output characteristics and vacuum interfaces. Generally, each straight should incorporate sufficient pumping to handle its own gas load for all gases, as the NEG coating in the adjacent sections cannot handle this additional gas load.

• Addition of the photon beam extraction legs which connect to the front ends.

• Consideration of the time for initial beam conditioning following installation. The beam current will need to be increased slowly to prevent the pressure increasing above a safe level (normally taken to be around 10^{-6} mbar).

• Inclusion of a proper photon scattering model in the calculation. Surfaces which are not directly illuminated by the primary photon beam will be bathed in a background of low intensity radiation. Such surfaces condition more slowly than directly illuminated surface and can significantly affect the long-term beam conditioning behaviour [3]. This is partially taken into account in the Pressure Profile model which assumes the radiation is evenly distributed around the circumference of the vacuum vessel.

2.5.6. Vacuum Vessels and Components

2.5.6.1. Materials and Construction

Vessels are generally circular with 22 mm outside diameter, 1 mm wall thickness and 20 mm inside diameter. The smallest magnet pole inscribed diameter is 24 mm; the proposed vessel size allows for 1 mm clearance between the vessel and the magnet poles, which is adequate to install a thin in-situ bakeout system.

In some areas, it is necessary to vary from this cross-section in order to extract the photon beams, to provide adequate gas flow conductance to the nearest pump or to deal with the photon beam heat load. This requires, for example, an "antechamber" or extended "keyhole" cross-section in the dipole 1 and dipole 4 vessels with an associated crotch absorber downstream. Further details of photon beam extraction geometry can be found in Section 2.6.

Vessel material will be mainly copper alloy due to its favourable combination of mechanical, magnetic and thermal properties and its availability and manufacturability. Silver-loaded OFS copper alloy, as used on DDBA, is preferred due to its higher strength. Stainless steel will be used in areas where a lower electrical conductivity is needed, e.g. in the region of fast corrector magnets. 316LN material is preferred for its higher strength and low magnetic permeability and was the material of choice for Diamond. Aluminium will also be considered in some areas due to the ease of manufacture of complex sections. NEG-coated extruded aluminium insertion device vessels up to 6 m long are already in use on Diamond and are performing well. Aluminium does have some disadvantages compared with copper / stainless-steel, such as higher thermal expansion coefficient and lower radiation shielding power. It also requires bimetallic conversion joints to connect to standard stainless-steel vacuum flanges. All three materials are compatible with NEG coating. Many of the vessels will use a combination of materials to reduce the number of flange joints, using bonding techniques such as TIG welding and vacuum brazing, as the material requirements vary from place to place.

Additive manufacturing processes, such as electroforming and 3D printing, are rapidly developing technologies and may also be useful for manufacture of some of the vacuum vessels and components.

The vessels in each cell will be made identical as far as possible, with few variants, for economies of scale, efficiency of design and manufacture and reduced spares inventory. For beam impedance reasons, abrupt cross-section changes and gaps will be avoided.

Vessel support and alignment concepts are presented in Section 2.6.1.3.
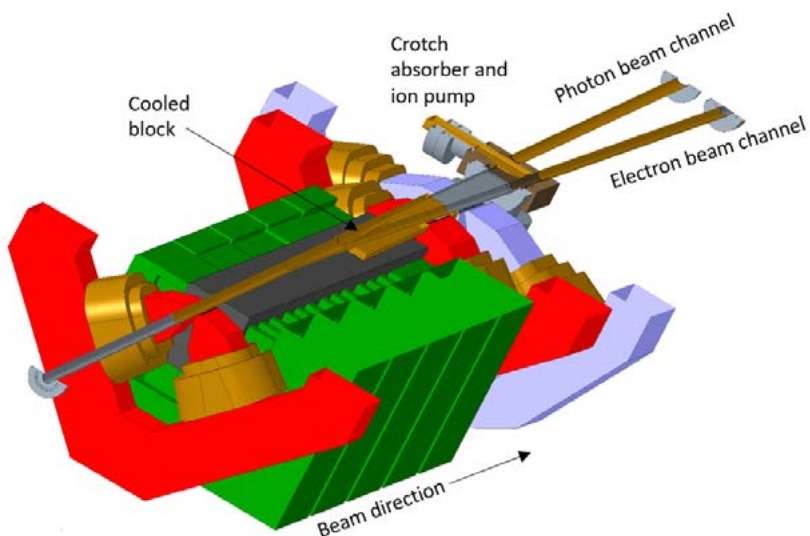
Figure 2-118 : Concept for dipole vessel showing separation of electron and photon beam channels. Different vessel materials are indicated – copper (brown) and stainless steel (grey).

Figure 2-118 shows a concept for the dipole vessel and crotch with separation of electron beam channel and photon beam channel and downstream crotch absorber and pump. Figure 2-119 shows in more detail the proposed crotch vessel and absorber concept, which is very similar to that used on DDBA. The vessel body is made of copper and is water cooled as is

the crotch absorber body. The crotch absorber shown here is vacuum brazed to a stainless-steel flange; however use of a copper-chromium-zirconium alloy is also being investigated which would enable the absorber and flange to be made in one piece.
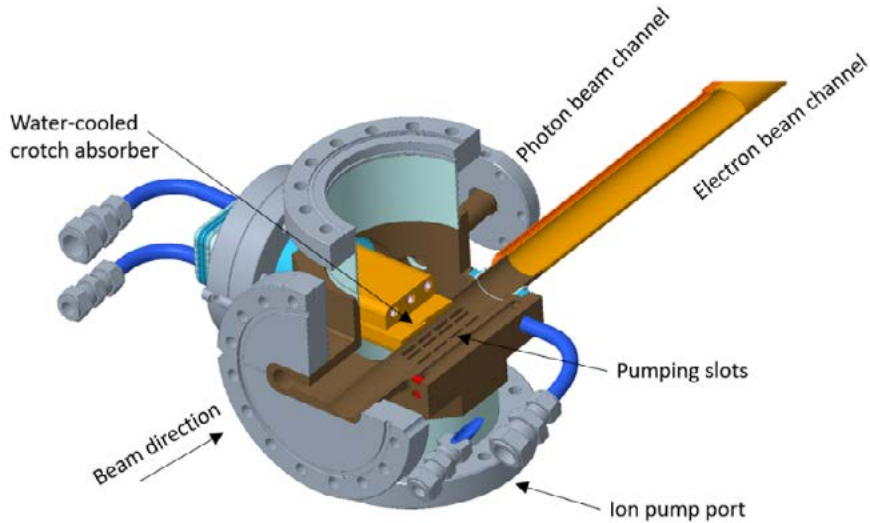
Figure 2-119 : Concept for crotch vessel and absorber.

Figure 2-120 shows the LM girder identifying areas of copper and stainless steel. Copper is the default material; stainless steel is used in the region of AC magnets.
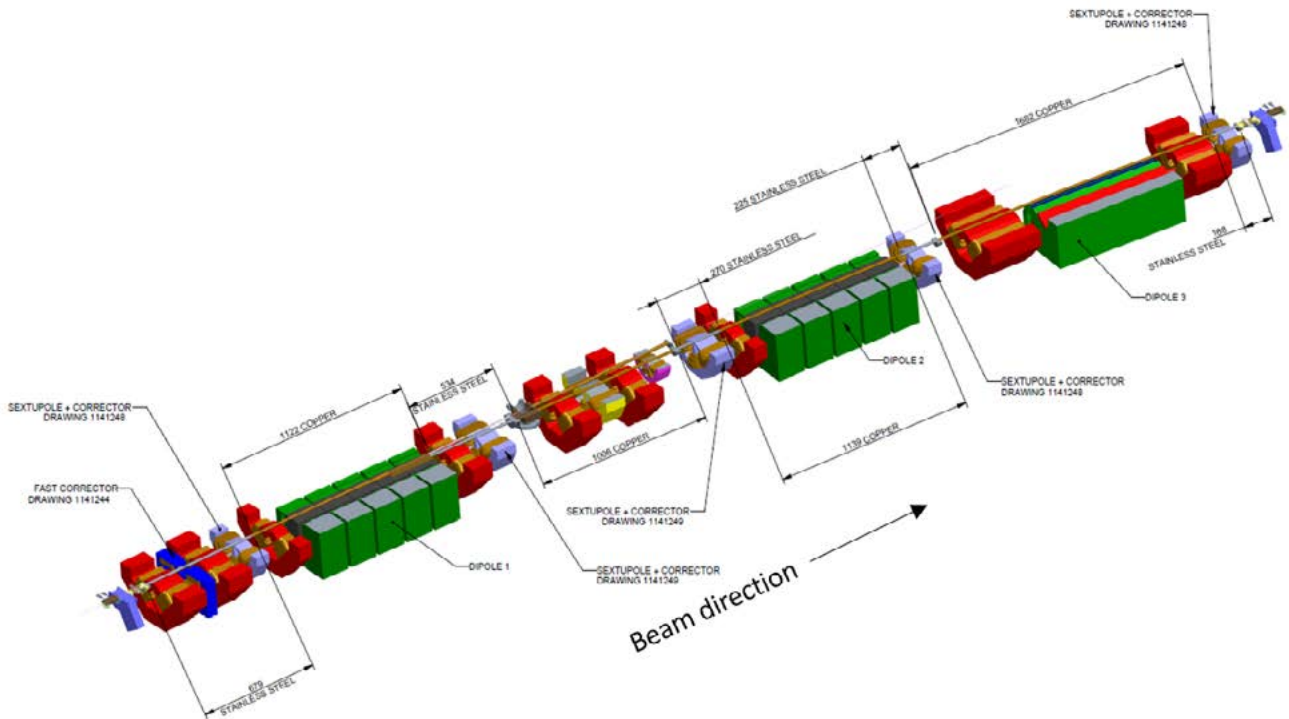
Figure 2-120 : LM girder layout showing areas of copper (brown) and stainless steel (grey).

2.5.6.2. NEG Coating

Non-evaporable getter (NEG) coating is an established technology [13] which is critical to the proposed vacuum system design. A thin (typically 1 micron thick) coating of a reactive metal alloy (most commonly Ti-Zr-V) is applied to the interior vessel surface which, after thermal activation, provides greatly improved vacuum surface properties compared with the substrate (base) material. The improvements are threefold:

1. The coating acts as a barrier layer to reduce thermal outgassing from the substrate.

2. The coating has much lower photon-stimulated desorption compared with the substrate.

3. The coating provides wall pumping for active gases: most gases, apart from hydrocarbons and inert gases, are pumped by the coating to a greater or lesser extent.

These favourable properties are generally only achieved after thermal activation of the NEG coating. For the Ti-Zr-V alloy the minimum activation temperature is around 180°C. A range of different alloys has been investigated; the ternary alloy Ti-Zr-Hf-V could be particularly interesting due to its lower activation temperature [19]. Once vented or exposed to active gases, a further thermal activation cycle is needed to fully recover the favourable vacuum properties. This has a strong influence on the sequence for vacuum system assembly and installation and on procedures for vacuum maintenance and interventions.

NEG coating has been successfully applied to a range of metal substrates including copper, stainless-steel and aluminium. The coating is usually applied by DC magnetron sputtering in a low-pressure inert gas environment. Obtaining an even, well-adherent coating on complex geometries can require significant process development.

NEG coating has been successfully used at many synchrotrons, including some extruded aluminium insertion device vessels at Diamond. Use of NEG coating is increasing as vacuum systems become narrower and increasingly conductance limited. NEG coating allows rapid initial beam conditioning and establishment of acceptable vacuum conditions. SOLEIL [4] and Max-IV [5] stand out as making extensive use of NEG coatings.

NEG coatings provide a high local pumping speed for active gases, but generally the capacity is low before saturation [13]. In general, it is necessary to provide additional forms of pumping such as ion pumps near high gas load sources, such as uncoated absorbers hit by synchrotron radiation.

Some studies [14] have reported that synchrotron radiation activation of a saturated NEG coating can recover some of its pumping speed but, at this stage, the design should not rely on this. It is possible that minor planned interventions could be carried out using inert gas purging, e.g. ultra-high-purity neon, to avoid a NEG reactivation bakeout [20]. However, at this stage, it is considered that in-situ bakeout is an important feature to provide and so will be designed in. With in-situ bakeout, in the absence of gross contamination, a 24-hour bakeout and activation cycle is all that is needed to recover the NEG coating properties after a major intervention or an accidental venting. Without in-situ bakeout, a swap out of the vacuum section or even the whole girder is needed, which is a much greater undertaking. Downsides of in-situ bakeout are the vessel thermal expansion during bakeout which may require additional RF shielded bellows and the need to ensure that nearby magnet poles and other components do not become too hot during bakeout.

When depositing a NEG coating there are many factors which can be fine tuned depending on the deposition conditions. As well as the thickness and elemental composition, the morphology can also be varied between dense and columnar, which have rather different properties [21]. It is even possible to deposit multiple layers with different properties [22] although this may not be practical for large production runs.

NEG coating also has an effect on surface resistivity and hence on machine impedance [23]. The coating thickness and morphology will need to be optimised to balance the RF and vacuum properties.

It should be noted that NEG coatings have proven reliable and effective. However there can be problems if all parameters and conditions of substrate preparation, coating deposition, handling and operations and contaminants are not carefully controlled. These problems can include peeling / delamination and poisoning [24].

2.5.6.3. Flanges

Demountable flange joints are needed to enable the vessels and components to be manufactured, tested, NEG coated and handled in reasonable lengths. They also enable individual vessels and components to be replaced if required. Due to lack of available space, such flange joints will be minimised.

There are two main functions of the flanges:

1.   To provide a reliable, mechanically robust vacuum seal.

2.   To provide RF continuity for flange joints along the electron beam path.

Other requirements to be fulfilled include resistance to thermal cycling, resistance to radiation, ease of assembly and alignment in poorly accessible locations, small separation distance for breaking and making the joint, compatibility with different vessel materials and different cross-sections and ease of inspection for correct assembly. For these and other reasons, all-metal seals are required. Some joint designs are more tolerant of synchrotron radiation heating which can be asymmetric (one-sided) and may require upstream shadowing features.

A number of different flange and seal designs have been used successfully on different accelerator projects. Table 2-47 lists some of the RF flange types currently under consideration for Diamond-II. Final selection will require further testing and evaluation. They fall into two main classes: one class where the vacuum seal and RF continuity are made by the same gasket (e.g. Flat seal and MO seal) and one class where the vacuum seal and RF continuity are made by two different features (Helicoflex® seal and CF flange with RF insert).

Table 2-47 : Some of the RF flange types currently under consideration for Diamond-II.

Flange type	Comments
MO seal [25]	Variants in use at a number of different facilities. Specially shaped copper gasket makes vacuum seal and RF continuity.
Flat seal [26]	Thin etched aluminium gasket with sealing ridge makes vacuum seal and RF continuity. Flat flange faces. Originally developed by the VAT company but now also available from third party sources.
Helicoflex® seal [27]	Spring energised C ring makes vacuum seal. Internal flange spigot or land closes RF gap.
CF flange with RF insert [7]	Standard CF gasket makes vacuum seal. Insert makes RF continuity. A number of variants have been used some with spring inserts and some with elastoplastically-deformed metal insert.

Diamond used a CF flange with a spigot to close-up the gap around the electron beam channel. This is considered sub-optimal for Diamond-II due to the gap non-reproducibility experienced on Diamond. DDBA used Helicoflex® seals with internal "land" to close up the RF gap. These have proven reliable, however the required surface finish of the flange deal groove proved to be difficult to achieve with a milling operation which restricted vessel manufacturing options.

Where RF continuity is not required, standard 316LN CF stainless-steel flanges will be used with silver-plated copper gaskets as on Diamond. In areas of poor accessibility, clamp flanges rather than conventional bolts and/or special tooling may be needed.

2.5.6.4. BPMs

Beam Position Monitor (BPM) stations will be provided at the required locations for monitoring the electron beam position. The basic concept and proposed pick-up button configuration for these is described in Section 2.7.

2.5.6.5. RF Shielded Bellows

RF shielded bellows are needed to accommodate thermal expansion caused by in-situ bakeout and due to beam heating during operation. They are also needed to allow for manufacturing and alignment tolerances and to achieve flange separation for assembly and maintenance. One disadvantage of using aluminium for vacuum vessels is its higher thermal expansion coefficient compared with copper or stainless-steel, which requires a greater range of movement in the bellows and vessel supports during in-situ bakeout (see Section 2.6).

The proposal is to use a variation of the RF bellows used successfully both on Diamond and on DDBA (see Figure 2-121 and Figure 2-122). Other designs will also be considered.
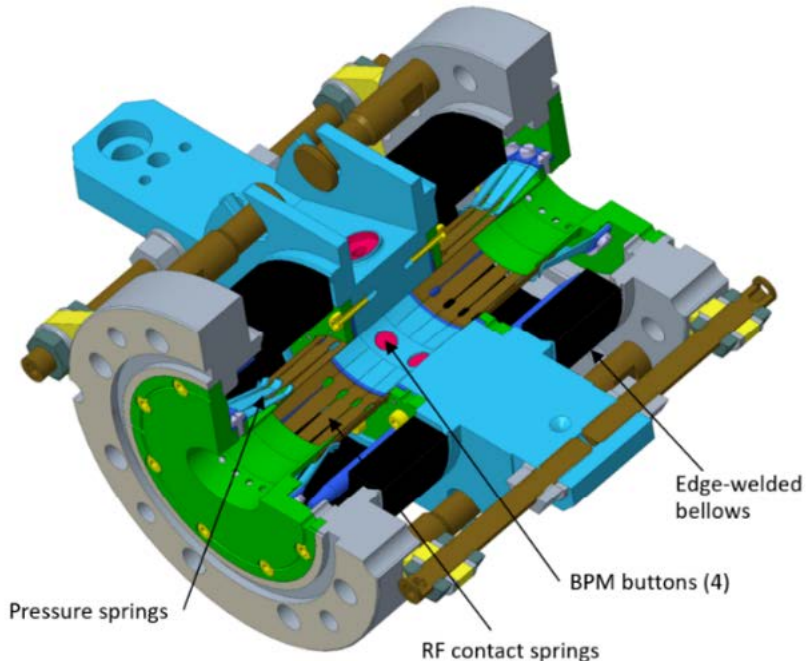
Figure 2-121 : Concept for RF-shielded bellows, in this case a double bellows unit with central beam position monitor station.
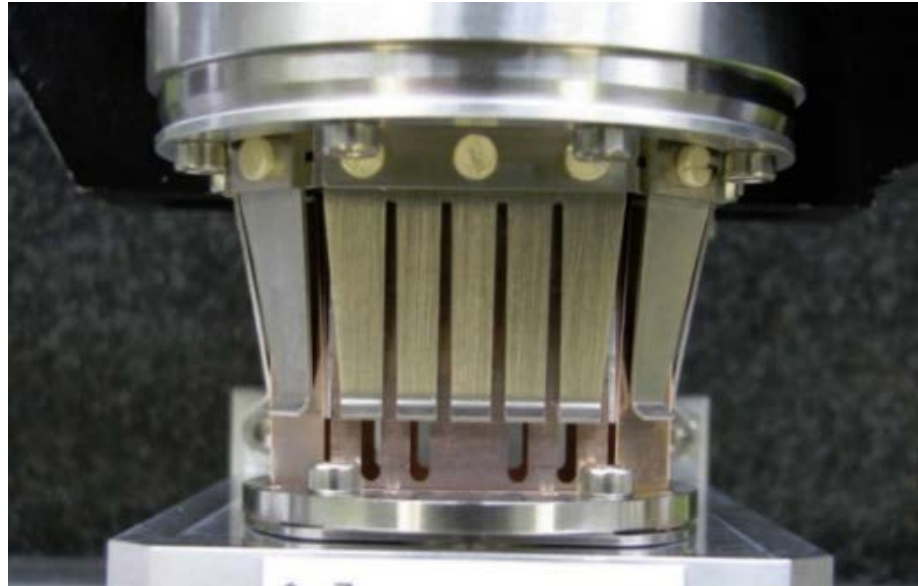
Figure 2-122 : Internals of RF-shielded bellows used on DDBA.

2.5.6.6. Valves

An RF-shielded gate valve will be fitted at each end of each girder. A non-shielded gate valve will be fitted to each beam extraction port making a total of 3 gate valves per girder. This enables each girder vacuum section to be installed and connected to adjacent vacuum sections without breaking the vacuum, thus avoiding re-baking and re-activation of the NEG coating on installation.

All of the gate valves will be pneumatically actuated and connected to the machine protection system (MPS). They will be commercially available customised standard gate valves similar to those used on DDBA. Additional all-metal manual valves DN40 and DN63 will be fitted for installation and maintenance.

2.5.6.7. Photon Absorbers

The proposed photon absorber configuration is described in Section 2.6. Consideration will be given to NEG coating of the absorber surfaces to reduce photon stimulated desorption and the consequent vacuum outgassing.

2.5.6.8. Bakeout system

The vessels will be provided with in-situ bakeout capability, to be used for initial installation and for system recovery after a major vacuum intervention or other vacuum incident. It is expected this will reduce the recovery time after such an event from several weeks without in-situ bakeout to several days with in-situ bakeout.

The proposed bakeout system is similar to that developed and implemented successfully on DDBA. Figure 2-123 shows a DDBA vessel prepared for bakeout with fitted thin film Kapton heater and the PLC-based bakeout control system which was developed for DDBA.

Figure 2-123 : Left - DDBA vessel with thin film Kapton heater applied; Right - PLC-based bakeout controller developed for DDBA.

The bakeout system will be capable of achieving at least 180°C, which is the required activation temperature with the currently commercially-available NEG technology. Different types of commercially-available heaters are appropriate for different areas, selected from thin film Kapton heaters, coaxial sheathed heaters and heated jackets, and it is expected than a mix of different heater types will be used, as on DDBA. As the heaters will be permanently fitted, the possibility of radiation damage has to be considered.

The heaters, together with a suitable air gap or thermal insulation, will be incorporated into the 1 mm clearance between the vessel and the magnet poles. This will be done in such a way that it does not preclude supporting the vessels off the magnets in a thermally-isolated manner. Excessive heating of the magnet poles and other nearby components has to be avoided and allowance has to be made for thermal expansion.

2.5.7. Build Sequence

The vacuum system build will take place using the same general scheme which was used for the DDBA project. As there are three gate valves on each girder to the adjacent vacuum systems (two straights and one front end / dummy front end), the girder vacuum vessels can be installed without venting. It is assumed each half arc is supported on a single girder, i.e. two girders per cell. All of the magnets are assumed to be splittable except the dipoles which can be retracted sideways.

The main build steps are:

1. Assemble and align magnets on girder.
2. Split / retract magnets.
3. Assemble vacuum vessels and in-situ bakeout system on girder on the magnet lower sections.
4. Vessel alignment, pump down and leak test.
5. Reassemble magnet tops.
6. Bakeout, degas instrumentation, NEG activation and maintain under vacuum.
7. Move into position in the storage ring.
8. Make vacuum connections to the adjacent vacuum sections, pump these down and bake if necessary.
9. Only open the gate valves to the adjacent vacuum sections once clean ultra-high vacuum conditions have been achieved and verified in these adjacent sections.
10. In case of an unplanned venting of the girder vacuum vessels it will be necessary to re-bake and reactive the NEG coating in-situ which can be done using the installed bakeout system. For planned interventions, it may be possible to avoid thermal reactivation by carrying out the work in an ultra-pure neon atmosphere.

2.5.8. Vacuum Controls and Interlocks

Each standard storage ring cell is divided into four vacuum sections by RF gate valves. Each of these vacuum sections will be fitted with vacuum pressure gauge sets for monitoring the vacuum conditions and to provide interlock signals. Two gauge sets per vacuum section are foreseen for redundancy. Each gauge set will consist of a cold cathode gauge and Pirani gauge. Pressure data will be fed to the Machine Protection System (MPS) and will also be visible in real time and archived for retrospective analysis.

Residual Gas Analysers (RGAs) are useful tools to investigate vacuum issues such as leaks, contamination and pressure spikes as well as trending gas composition over time. However, they are quite costly and do need regular maintenance and service so a practical balance has to be struck on their numbers. The current plan is to have one RGA per cell installed and running at any one time; additional RGAs can be installed where needed for closer monitoring of problem areas. Manual all-metal right-angle valves with dedicated side pumping ports will be fitted in each straight and near each crotch vessel. In this way, RGAs can be added, removed and replaced without venting the vacuum section. The RGAs will run on a private high-capacity network, which can be accessed by EPICS, allowing for long-term data archiving and retrieval as well as real-time viewing.

Vessel temperature monitoring is important to identify any hot spots which could indicate beam mis-steers or excessive RF heating. Temperature sensors will be fitted to flanges and other critical points; their data will be fed to the MPS and will also be viewable in real time and archived for retrospective analysis.

References

[1] R. Bartolini *et al.*, "Double-double bend achromat cell upgrade at the Diamond Light Source: From design to commissioning," *Phys. Rev. Accel. Beams*, vol. 21, no. 5, p. 050701, 2018.

[2] M. Cox and B. Boussier, "Commissioning of the Diamond Light Source storage ring vacuum system," *J. Phys. Conf. Ser.*, vol. 100, no. 9, p. 092011, Mar. 2008.

[3] O. Malyshev and M. Cox, "Design modelling and measured performance of the vacuum system of the Diamond Light Source storage ring," *Vacuum*, vol. 86, p. 1692, 2012.

[4] J.-M. Filhol *et al.*, "Operation and Performance Upgrade of the SOLEIL Storage Ring," in *IPAC 2010 - Proceedings of the First International Particle Accelerator Conference*, 2010.

[5] E. Al-Dmour et al., "The status of the vacuum systems of the MAX IV laboratory," in *IPAC 2013 - Proceedings of the 4th International Particle Accelerator Conference*, 2013.

[6] "SLS-2 Conceptual Design Report," *PSI Bericht 17-03 December 21 2017*, 2017.

[7] "ESRF Upgrade Programme Phase II (2015-2022) Technical Design Study," p. 190, 2014.

[8] "Advanced Photon Source Upgrade Project Preliminary Design Report," *APSU-2.01-RPT-002 Argonne Natl. Lab. Sept 2017*, 2017.

[9] P. F. Tavares et al., "The Max IV storage ring project," *J. Synchrotron Radiat.*, vol. 21, no. 5, p. 862, 2014.

[10] M. Hahn, "Operational experience and relation to deposition process for NEG-coated chambers installed on the ESRF electron storage ring," *Vacuum*, vol. 81, no. 6, p. 759, 2007.

[11] C. Herbeaux, N. Béchu, and J. Filhol, "Vacuum conditioning of the SOLEIL storage ring with extensive use of NEG coating," *EPAC 08 - Proc. 11th Eur. Part. Accel. Conf.*, 2008.

[12] P. Chiggiato and R. Kersevan, "Synchrotron radiation-induced desorption from a NEG-coated vacuum chamber," *Vacuum*, vol. 60, p. 67, 2002.

[13] C. Benvenuti *et al.*, "Vacuum properties of TiZrV non-evaporable getter films," *Vacuum*, vol. 60, p. 57, 2002.

[14] V. V. Anashin *et al.*, "Comparative study of photodesorption from TiZrV coated and uncoated stainless steel vacuum chambers," *Vacuum*, vol. 75, p. 155, 2004.

[15] B. F. Macdonald, S. Bryan, H. S. Shiers, and M. P. Cox, "Storage ring vacuum system pressure modelling at Diamond," *Vacuum*, vol. 84, p. 283, 2009.

[16] A. Wrulich, "Single beam lifetime," *Cern Accel. Sch. Finl. 94-01*, vol. 1, pp. 409–435, 1994.

[17] R. Kersevan and J.-L. Pons, "Introduction to MOLFLOW+: New graphical processing unit-based Monte Carlo code for simulating molecular flows and for calculating angular coefficients in the compute unified device architecture environment," *J. Vac. Sci. Technol. A Vacuum, Surfaces, Film.*, vol. 27, no. 4, p. 1017, 2009.

[18] J.-L. Kersevan, R.; Pons, "Analytical and numerical tools for vacuum systems," *Cern Accel. Sch. Vac. Accel. Platja d'Aro, Cern.*, pp. 285–312, 2007.

[19] O. B. Malyshev, R. Valizadeh, and A. N. Hannah, "Pumping properties of Ti-Zr-Hf-V non-evaporable getter coating," *Vacuum*, vol. 100, p. 26, 2014.

[20] G. Lanza et al., "The LHC experimental beam pipe neon venting, pumping and conditioning," in *IPAC 2011 - Proceedings of the 2nd International Particle Accelerator Conference*, 2011.

[21] O. B. Malyshev et al., "Effect of coating morphology on the electron stimulated desorption from Ti-Zr-Hf-V nonevaporable-getter-coated stainless steel," *Vacuum*, vol. 86, p. 2035, 2012.

[22] O. B. Malyshev, R. Valizadeh, and A. N. Hannah, "Pumping and electron-stimulated desorption properties of a dual-layer nonevaporable getter," *J. Vac. Sci. Technol. A Vacuum, Surfaces, Film.*, vol. 34, p. 061602, 2016.

[23] R. Nagaoka, "Study of Resistive-wall Effects on SOLEIL," *EPAC 04 - Proc. 9th Eur. Part. Accel. Conf.*, 2004.

[24] S. Calatroni *et al.*, "NEG thin film coating development for the MAX IV vacuum system," *IPAC 2013 - Proc. 4th Int. Part. Accel. Conf.*, 2013.

[25] Y. Suetsugu, M. Shirai, and J. M. Ohtsuka, "Application of stainless-steeel, copper-alloy and aluminum-alloy MO (Matsumoto-Ohtsuka)-type flanges to accelerator beam pipes," *IPAC 2010 - Proc. 1st Int. Part. Accel. Conf.*, 2010.

[26] G. Heidenreich, L. Schulz, and P. Wiegand, "Vacuum system for the Swiss Light Source," *EPAC 98 - Proc. 6th Eur. Part. Accel. Conf.*, 1998.

[27] "Technetics Group." [Online]. Available: www.technetics.com.

2.6. Mechanical Engineering

2.6.1. Machine Integration

2.6.1.2. Layout
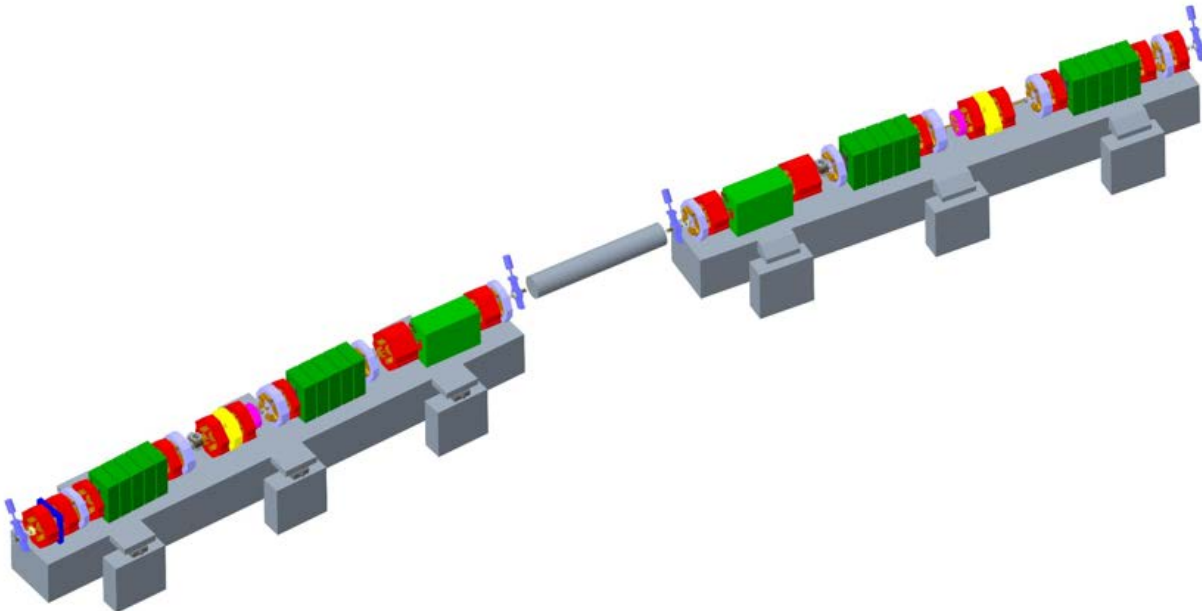
Figure 2-124 : *Diamond-II assembly of vessels, magnets and girders for a typical cell showing mid-cell straight; green=dipole, red=quadrupole, yellow=sextupole, blue=corrector, violet=combined sextupole and corrector, magenta= octupole.*

It is proposed to mount the magnets and vessels on two girders per cell, one either side of the mid-cell straight (see Figure 2-124). The lattice configuration requires four different girder configurations for different locations:

* LM - long straight to mid-straight (6 in total).
* SM - standard straight to mid-straight (18 in total).
* ML - mid-straight to long straight (6 in total.
* MS - mid-straight to standard straight (18 in total).

2.6.1.2. Magnets

To meet the accuracy requirements for each magnet type we will use a shimming system similar to that developed for the DDBA project in that for each magnet the elevation, pitch and roll will be set using four shims machined to the correct thickness in conjunction with the use of magnetic measurement system. The yaw, lateral and longitudinal locations will be set in a similar manner using three shims referenced against dowels located in the girder surface. The lesson learnt from DDBA is that it will be necessary to analyse the interaction between these lateral shims and the dowels to ensure that displacement of the reference surfaces is insignificant.

The stiffness of the magnet supports will be maximised to limit the amplification factor of ground-induced vibration.

The field of the dipole magnets will be measured and each magnet will be individually shimmed to correctly vertically orientate the dipole field before mounting on its girder. For vessel assembly/removal and for in-situ bake-out each dipole will require a system of lateral displacement or complete removal to avoid overheating of the permanent magnets.

All multipole magnets will have an inscribed pole tip diameter of 24 mm apart from the specific locations downstream of dipoles 1 and 4 where the reduced magnetic field requirement permits the sextupoles to have an increased inscribed pole tip diameter of 30 mm to facilitate photon beam extraction.

2.6.1.3. Vessels

The same build philosophy will be used for Diamond-II vessel integration as was used for the initial build, as described in Section 2.5.7. Individual vacuum vessels will be built up on supporting girders. The support of the vessels needs to satisfy three constraints:

1. The supports must be capable of positioning the vessels with sufficient accuracy with respect to the magnet centres and beam stay-clear envelope.
2. The supports must allow guided thermal expansion to take place during operation and bake-out.
3. They should not amplify ground vibration.

Previously a system of fixed support points and flexible support points was adopted. The fixed points were located at the crotch vessels where the photon beam trajectory departs from the electron beam. These points contain the first aperture presented to the photon beam in the form of vessel walls of the photon exit leg of the crotch vessel. In order to avoid uncontrolled illumination of the vessel walls it is important to have these as fixed points. All other supports were stiff laterally and vertically, but flexible axially. By this means the vessel could be accurately located with respect to the magnet pole tips, but have the flexibility to expand axially. This system will be retained for Diamond-II but the means by which this is achieved will be reviewed.

To cater for thermal expansion of the vessels over a temperature range of 160°C during bake-out requires the inclusion of vacuum and RF-compatible bellows in the vessel assembly. Over the expected temperature range, the expansion will be 2.7 mm/m for copper and stainless steel vessels and 3.7 mm/m for aluminium alloy vessels. Bellows units similar to those developed for the DDBA design will be acceptable but latest developments in designs will be reviewed during the detailed design phase.

The reduced space between magnets in Diamond-II inevitably reduces the space available for vessel supports. In addition, the smaller vessel diameter required to fit within the magnets means that it becomes more flexible, which increases the challenge of accurately positioning it. In Diamond the girder top surface was the reference plane for supporting the vessels; for the Diamond-II design it is intended to use the magnet yoke or pole pieces as the reference surfaces for vessel support as the forces necessary to retain a significantly more flexible vessel reduce sufficiently to values which are unlikely to result in significant magnet pole displacements.

2.6.1.4. Girder Positioning

The determining factors for the choice of alignment strategy are: static magnet positional requirements, magnet stability requirements (vibration), magnet reposition frequency, magnet string build & installation time and cost of the solution. The axes that define magnet and girder motion relative to the electron orbit are illustrated in Figure 2-125.
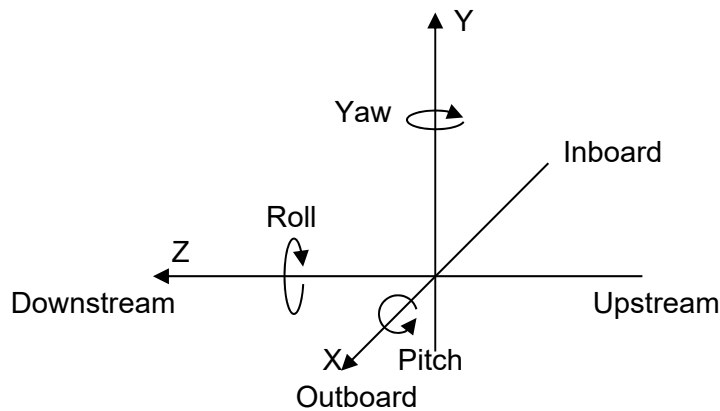
Figure 2-125 : Magnet and Girder Axes.

Table 2-14 defines the positional requirements for magnet and girder alignment. Magnets will be aligned to the girders prior to installation as outlined in Section 2.4.7. The possibility of in-situ alignment of the magnets on the girder will be considered during the detailed design phase. The required girder misalignment and roll RMS tolerances of 150 μm and 150 μrad with a 2σ cut-off are within the measurement accuracy of the laser tracker to be used during installation.

The current proposal is that girders will be positioned using wedge jacks which have been successfully used and tested by the ESRF as part of the EBS upgrade project [1] and which allow for small incremental movement whilst achieving a high joint stiffness. A system of these wedge jacks is able to adjust the girder by a smaller increment than can be measured using the laser tracker which strongly suggests the girder alignment tolerance can be achieved. Due to the large size and mass of the girder, an arrangement of wedge jacks that over constrains the girder (i.e. more than 3 vertical jacks) will be used to meet the required system stiffness. Six wedge jacks could be used in the Y direction, two would be used in the X direction and adjustment screws would be used for the Z direction. To allow for Yaw and motion in the X direction a similar arrangement to that used on the ESRF-EBS girders is proposed. This arrangement allows for the Y jacks to slide and rotate.

As the system is over-constrained, deflection of the girder from the wedge jacks is a possibility that must be considered. As part of the proposed solution, the motion of each wedge jack would be measured by means of a linear encoder and the wedge jacks would be manually adjusted. This allows for calculation of over-constraint and measurement due to the increased torque needed to adjust the jacks when deflection occurs. This solution can be adapted to motorisation if required.

Further investigations will be made in the detailed design stage into the best arrangement for the wedge jacks. FEA modal analysis combined with topological optimisation will be used to determine the feasibility of a system with fewer wedge jacks to meet the 50 Hz natural frequency target. Additionally, the APS-U 6 DOF semi-kinematic system will be assessed [2]. This arrangement of 6 adjusters is also used by MAX IV, who have a very stable beam [3].

2.6.1.5. Vibration

To meet the stability requirement for the magnets the natural frequencies of the girder system, including the magnets, should not overlap peaks in the known ground and cultural spectra. A recent measurement showing the vertical and horizontal ground displacement is shown in Figures 2-126 and 2-127. The measurements were taken in the same location at two different time periods (mid-day and mid-night) and in the worst case show a total RMS motion between 0 and 100 Hz of 21.7 nm vertical and 14.7 nm horizontal.
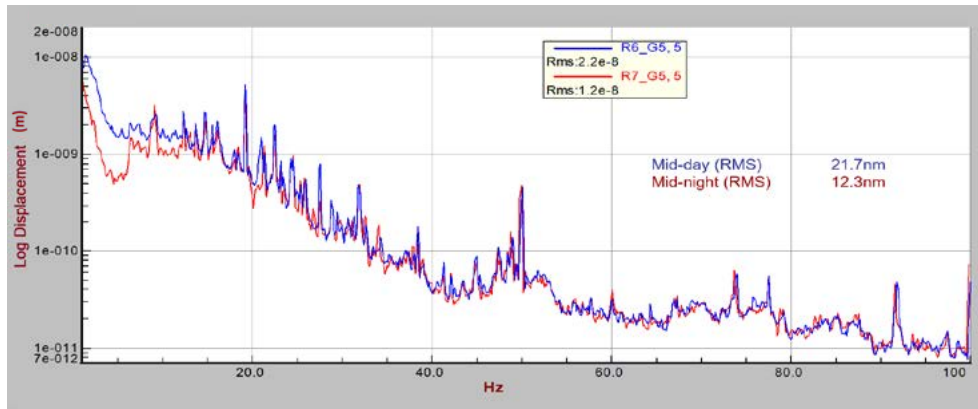
Figure 2-126 : Average vertical displacement of the storage ring slab.
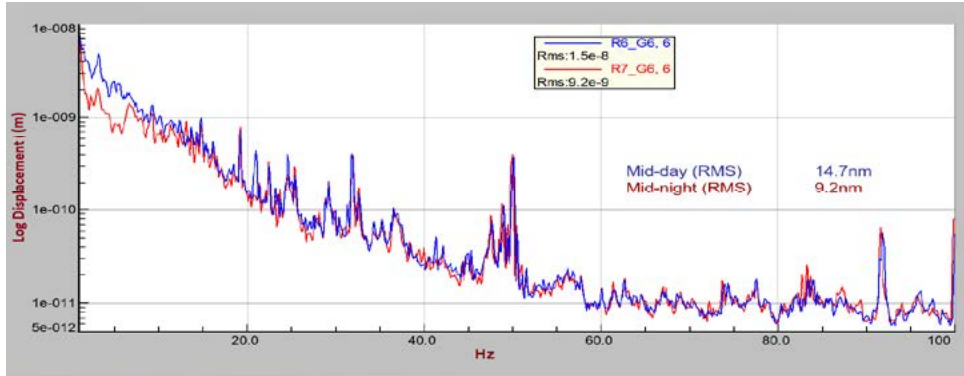
Figure 2-127 : Average horizontal displacement of the storage ring slab.

Based on the above, a target for the first natural frequency of the girder system should be above 50 Hz. Initial modal analyses indicate that an arrangement of six Airloc 414-KSKC wedge jacks for vertical positioning combined with a further two wedge jacks for horizontal positioning could be a suitable solution. Further optimisation of the girder is needed to meet the high stiffness and low weight required to achieve a first natural frequency of the system above 50 Hz.

2.6.1.6. Mechanical Services

Two cooling water circuits currently supply the Storage Ring with demineralised water for cooling copper and stainless steel components and filtered raw water for cooling aluminium and aluminium alloy components. Copper-based and aluminium-based components have to be on different water circuits due to their differing electrode potentials, which would otherwise cause galvanic corrosion. Demineralised water is required to cool components that require close control of the chemical and physical composition such as magnets and vacuum vessels.

The present flow capacity of the demineralised water circuit is nominally 480 litres per minute to each of the 24 existing storage ring cells. The flow requirements for Diamond-II will be of the order of 240 litres per minute and therefore well within the system's capacity so no upgrade is envisaged.

The aluminium circuit is capable of delivering 42 litres per minute to each of the 24 storage ring cells, although the system is currently set to deliver a maximum of 24 litres per minute. More aluminium alloy components may be included in the Diamond-II design, however as the circuit is presently operating at 57% of its capacity an upgrade to this system will not be necessary.

The girder reconfiguration for Diamond-II will require more components to be supplied with cooling water from the first service trench in each cell, therefore the pipe bores at this point will have to be increased in every cell, requiring the pipework to be replaced in these locations.

For the existing storage ring girders the cooling water is distributed to the magnets and vessels via stainless steel pipework manifolds mounted on each girder. Turbulence in this system contributes significantly to undesirable vibration of the magnets. For Diamond-II the water will be distributed via floor mounted pipework manifolds with flexible connections to the individual magnets and vessels on each storage ring girder. By adopting this change and minimising water velocities, this vibration source should reduce significantly. To improve access to the girders the manifolds will be located on the ratchet wall side of the girder, as they were for DDBA, but be located below the girder top surface to avoid obstructing access, which was a lesson learnt from DDBA. Flexible hoses will be used to make the final connection to the individual components with connection points below the mid plane to minimise the degradation effects of hard X-rays and bremsstrahlung radiation.

For the existing storage ring, water flow balancing between the various sets of components was achieved using orifice plates. However, these abrupt changes in the bore of the pipework have proved to be a significant source of vibration. It is therefore a design goal for Diamond-II that the pressure drop across the various parallel circuits is made the same, 6 bars, by choosing appropriate pipe sizes. For example, the water cooling flows through all of the magnets have been matched to give the same pressure drop as described in Section 2.4.

As regards compressed air, the number of air-actuated components is not expected to increase significantly for the upgraded machine and therefore the compressed air supply capacity is sufficient.

2.6.2. Storage Ring Photon Power Handling

2.6.2.1. Radiation

The majority of the dipole light produced is absorbed in the storage ring by water cooled absorbers distributed along the vessel walls on the horizontal mid-plane. The storage ring photon absorbers for Diamond were manufactured from copper or aluminium alloy. The dipole power produced by the Diamond-II maximum field of the longitudinal gradient dipole (DL) magnets will be similar to that of the Diamond dipole magnets in terms of angular power density (Table 2-48), therefore similar designs and materials to those developed for the Diamond may be used.

A further comparison may be made by considering the power density received at the vessel wall immediately downstream of the first Dipole magnet for each lattice configuration (Figure 2-128 illustrates the geometry). Thanks to the larger bending radius and hence smaller angle of incidence, the surface power densities in the Diamond-II dipole vessels (as well as for DDBA) are significantly less than in Diamond. It is therefore expected that the material types and absorber designs used for Diamond will be compatible with the demands of Diamond-II.
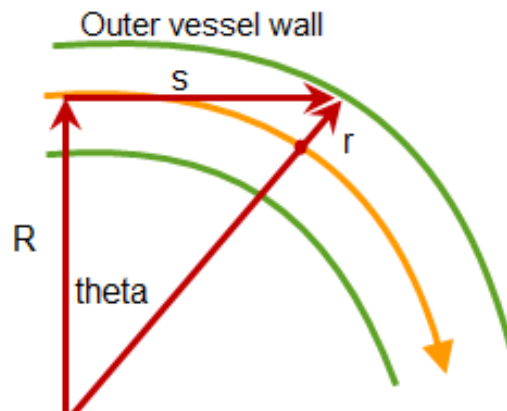
Figure 2-128 : Dipole radiation incident on the dipole vessel outer wall.

Table 2-48 : Comparison of dipole radiation angular and surface power densities on the dipole vessel outer wall at 300 mA.

Lattice	Field (T)	R(m)	r(m)	s(m)	Θ(rad)	Vertically integrated angular power density (W mrad⁻¹)	Peak angular power density (W mrad⁻²)	Vertically integrated surface power density (W mm⁻¹)	Peak surface power density (W mm⁻²)
Diamond	1.4	7.17	0.0400	0.76	0.106	48	184	6.67	33.93
Diamond DDBA	0.8	12.50	0.0135	0.58	0.046	27	105	2.18	14.49
Diamond-II DL (max)	0.76	15.35	0.0100	0.55	0.036	41	186	2.69	21.78

2.6.2.2. Photon Extraction

The ability of the vessel configuration to extract the portions of the photon fan required by each beamline through the available apertures has been assessed. The most demanding has been determined to be the output from the I05 Helical Undulator, which produces the widest photon fan. The interaction between Insertion Device photons and the vacuum vessel wall is a more significant factor for Diamond-II compared with the current storage ring vessels due to the reduced vessel aperture and the higher electron energy. Figure 2-129 shows the layout of the area which follows a long straight, such as I05.
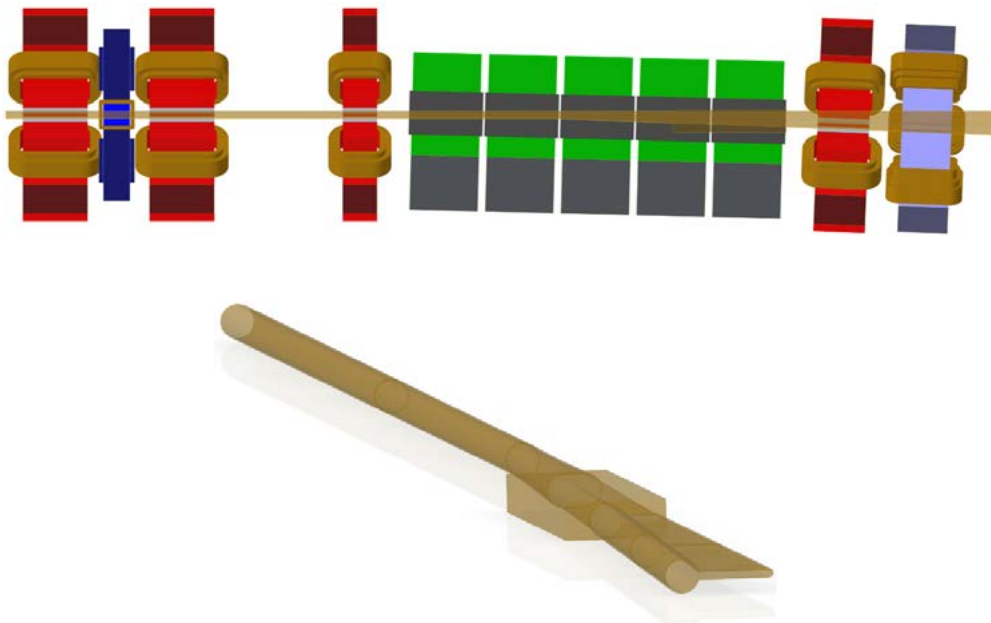
Figure 2-129 : I05 Crotch Vessel Layout and Vessel.

In Diamond the vessels are sufficiently large that the photons could project into the Front End absorbers without any interaction with the walls of the vessels forming the main storage ring. For Diamond-II this is no longer the case.

Two procedures for assessing the thermal stresses in the vessel walls and absorbers have been assessed. Synrad [4] can be used to project dipole and wiggler power distributions. Power densities can then be mapped onto the vessels and absorbers in ANSYS to produce temperature and stress values. COMSOL [5] multi-physics modelling can be used to project all source power distributions, if used in conjunction with planar power density maps from the Synchrotron Radiation Workshop (SRW) application [6] or similar. In addition, COMSOL has the potential to produce power densities, temperature

and stress results. Both procedures are being tested and compared with a view to formalising the process for the detailed design. Initial analysis of I05 using COMSOL has determined the projected total powers and power densities shown in Table 2-49 while Figure 2-130 shows the light projection onto the vessel in each case.

Table 2-49 : Projected total powers and power densities on the vessel downstream of the I05 helical undulator in three different polarisation modes.

Polarisation	Total heat load on Crotch Vessel (W)	Peak power density on Crotch Vessel (W/mm²)
Circular	1933	1.42
Vertical	1724	5.43
Horizontal	43	0.073
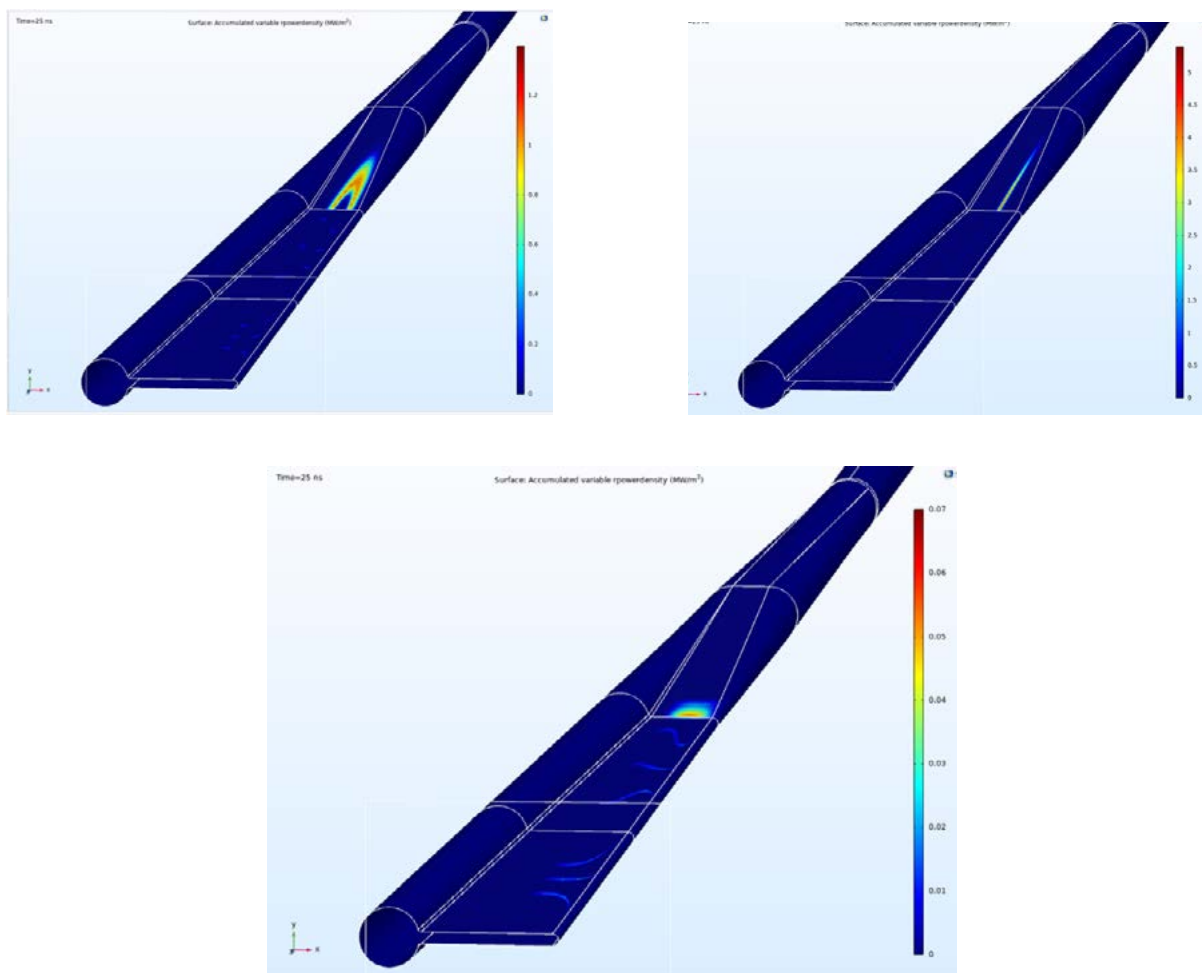
Figure 2-130 : Projection of radiation from the I05 helical undulator in various polarisation modes: upper left - circular, upper right – vertical, lower – horizontal.

In the circular and horizontal polarisations, it is clear that the only segment of the vessel that interacts with the photon beam is within the dipole. This section of vessel which is around 300mm long will experience a larger amount of power per unit length than the DDBA vessel which in its worst case was subject to 1.2 kW over a 300mm length. However, as the new vessel is situated inside a dipole, there is ample space to route cooling channels. Furthermore, the cross-section of the vessel provides a large surface area for the light to interact with.

The dipole and crotch vessels providing light for Beamlines I09 and I13 will have to be unique to storage ring cells 09 and 13. The requirement to maintain the existing canting angles of 0.741 mrad and 2.28mrad respectively, coupled with second angles of 1.3 mrad and 4.0 mrad for beam separation will require designs unique to those cells.

A number of other insertion device straight sections have canting magnets, as shown in Table 2-50. The current aim is to retain these angles in Diamond-II in order to minimise the amount of re-alignment required. However, this may result in further dipole and crotch vessel configurations to cater for the differing photon trajectories and an assessment will be required to test commonality between differing angles.

Table 2-50 : Groups of beamlines with canted angle (second angle shown where there is a second ID which will be retained in Diamond-II); +=away from machine centre.

Straight number(s)	First Canting Angle (mrad)	Second canting angle (mrad)
2, 3, 4	+0.25	
7, 11, 19, 24	+1.5	
9	-0.741	+1.3
13	-2.28	+4.0
20	+0.8	

The ability to extract canted photon beams from the Diamond-II magnetic lattice without being obstructed by the magnet poles, coils or yokes will also have to be investigated to ensure compatibility with the magnet designs.

2.6.2.3. Location of Storage Ring Photon Absorbers

As mentioned in Section 2.6.2.2, the periphery of the photon beam from a low energy helical undulator will interact with the a 20 mm bore storage ring vessel after travelling approximately 5 m, which would correspond to the location of the first dipole vessel. Restricting apertures will have to be introduced into the dipole vessel to shadow the vessel walls downstream in the crotch and photon extraction leg up to the Front End. The dipole magnet surrounding the dipole vessel will only permit apertures to be inserted from the outboard side. There may well be the need for more than one aperture to remove successively smaller, but more intense portions of the photon fan. The crotch of the bifurcation between exiting photons and the continuation of the orbiting electrons will require a mask or 'crotch absorber' since this region will be impacted by approximately 300 W of dipole radiation from the first longitudinal gradient dipole magnet, with a peak power density of 186 W/mrad^{-2} (see Table 2-48).

Photons from the dipole magnets will impact with the vessel walls along their entire lengths and the absorbed energy must be removed by water cooling, but as illustrated in Table 2-48, the incident dipole power will be significantly less for Diamond-II.

For in-situ bake-out the water from any cooled feature should be capable of being completely drained. However, complete draining of the water-cooled circuits may be impossible to guarantee, therefore a venting system must be included to avoid over pressurisation during bake-out due to the formation of steam.

2.6.2.4. Outline Storage Ring Absorber Design

The distributed absorbers running along the length of the circular vessels will have a nominal bore of 3 mm based on the DDBA design. Although the majority of the vessel will only be illuminated on the outboard side by dipole light, cooling both sides is desirable to maintain dimensional stability.

Inevitably, there will be regions of the vessel that cannot be directly cooled such as BPM blocks and flanged joints. A methodology will have to be developed during the detailed design phase of how to shadow these areas from direct illumination. The two main candidate methods are to include raised features on the internal tube profile, as employed on DDBA, or to include an outboard antechamber with a finger absorber protruding slightly into the main beam vessel.

In the DDBA design, the second dipole vessel was a curved tube as there was no exiting photon tube. In Diamond-II, there is a proposal to adopt this design for dipole vessels 2, 3, 5 and 6 which correspondingly have no exiting photon tube. This proposed solution will be reviewed during the detailed design phase.

The majority of the discrete absorbers will be made out of oxygen-free electrolytic copper (C10100) unless the power density requires the higher strength alloys of copper. Aluminium or aluminium alloy absorbers may be used for relatively low power regions. Generally distributed absorber cooling channels will match the vessel material, which may be copper, aluminium alloy or stainless steel.

There is an opportunity to utilise emerging additive manufacturing techniques to form discrete absorbers and vessels, which would give the advantage of conforming cooling channels that would boost the effectiveness of the cooling. This will be examined during the detailed design phase.

The cooling water velocities in the original design for Diamond were calculated to maximise the heat transfer coefficient at the boundary layer between the cooled component and the cooling water without exceeding the available pressure drop. This resulted in a water system with high fluid velocities that is noisy and contributes significantly to vibration of the girder mounted magnets and vessels above 400 Hz, which is beyond the correction capability of the fast orbit feedback system. For Diamond-II this philosophy will change to one where the heat absorbing components are designed to operate with lower heat transfer coefficients. This was successfully incorporated into the design of the DDBA cell and will be repeated in the design of Diamond-II, the reduction in cooling water velocity will reduce the heat transfer coefficient as illustrated in Figure 2-131 for a typical application.
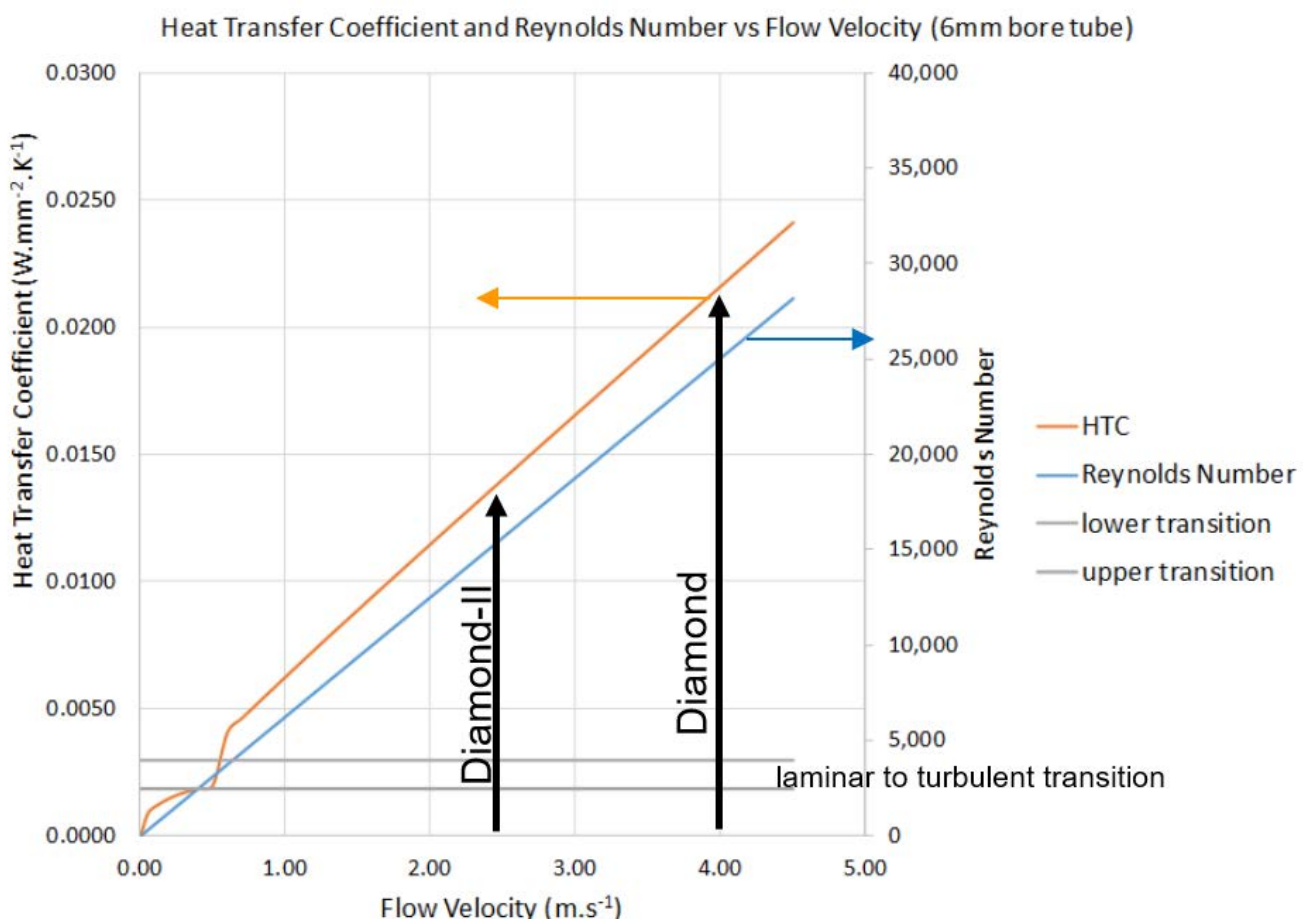
Figure 2-131 : Comparison of target cooling water velocities between Diamond and Diamond-II.

References

[1]   F. Cianciosi *et al.*, "The Girder System for the new ESRF Storage Ring," *MEDSI Proc.*, pp. 147–151, 2016.

[2]   "Advanced Photon Source Upgrade Project Preliminary Design Report Chapter 4 : Accelerator Upgrade," 2017.

[3]   B Jensen, "MAX_IV_Stability_Task_Force_Update," Beijing, 2017.

[4]   R. Kersevan, "SYNRAD, a Monte Carlo synchrotron radiation ray-tracing program," in *IPAC Proceedings*, 1993.

[5]   Comsol, "Comsol Multiphysics," *User Guid.*, 2012.

[6]   O. Chubar and P. Elleaume, "Accurate and efficient computation of Synchrotron Radiation in the near field region," *EPAC Proc.*, pp. 1177–1179, 1998.

2.7. Diagnostics and Feedbacks

2.7.1. Overall Requirements

Diamond-II will rely on state-of-the-art diagnostics and active feedback to an even larger degree than Diamond does. The optics specification will directly be reflected in tighter specifications for some diagnostics. On top of the reduction in beam size, we anticipate that faster data acquisition will require beam stability to higher frequencies, thus the increase in both frequency range and reduction in fractional beam size, shown in Table 2-51.

Table 2-51 : Some parameters relevant to diagnostics in Diamond and Diamond-II.

Parameter	Diamond (2019)	Diamond-II
Emittance H/V	2700 pm / 8 pm	160 pm / 8 pm
BPM block aperture H/V	80 mm / 22 mm	20 mm round
Number of BPMs	175	252
Beam size at source H/V (standard straight)	123 µm / 3.5 µm	30 µm / 4 µm
Orbit stability relative	10% of H/V size to 100 Hz	3% of H/V size to 1000 Hz
Orbit stability absolute (centre of standard straight)	12 µm / 0.35 µm	0.9 µm / 0.12 µm

2.7.1.1. Tasks to be Completed During the Detailed Design Phase

- In Diamond, the TMBF kicker structures, DCCT, Pinger magnet and TMBF pickup BPM are all located in straight 23 upstream and downstream of an in-vacuum ID. Since standard straights are shorter in Diamond-II, some of these items will need to be moved into other straights.

- The cross-section of the Diamond-II vacuum vessel is much smaller. As a consequence the physical designs of all diagnostics devices will need to be adapted.

- Any diagnostics for the new booster and booster to storage ring transfer line will need to be defined and specified. No particularly challenging demands are expected.

- There is currently too little detail available to make a statement in which shape the optical diagnostics in the storage ring can remain. Diamond uses visible light Time Correlated Single Photon Counting (TCSPC) for high dynamic range fill pattern monitoring, and a streak camera for longitudinal bunch profile assessment [1]. If it is feasible to retain visible light output and floor space for the cabin, these systems will be retained. In case this is not possible, TCSPC can be done with X-ray photons as well (already in practice in Diamond), and other options for longitudinal bunch profile measurement need to be evaluated.

- All ID front-ends with Tungsten vane XBPMs [2], [3] will need to be checked for compatibility with the new beam parameters. There are currently over 30 devices installed in 17 front-ends. In some cases, it will be necessary to procure new XBPMs for the additional mid-straights into which some devices are moved.

- Bending magnet front-ends will require modifications to their XPBMs as well, as they are changing into three-pole wigglers or IDs in mid straights.

2.7.2. Emittance Monitoring

The emittance monitoring deployed for Diamond-II should:

- provide measurements of the horizontal and vertical emittances $\varepsilon_{x,y}$ and energy spread σ_E of the electron beam in the storage ring

- consist of at least two transverse beam size monitors, which are located at positions in the storage ring with different lattice parameters, specifically dispersion

- operate at an acquisition rate and robustness suitable for continuous feedback systems

- ideally be distributed around the ring to provide global monitoring of the transverse profile of the electron beam.

2.7.2.1. Beam Profile Measurement and Emittance Calculation

Absolute beam profile measurement are planned using X-ray pinhole cameras, following good experience in Diamond [4]–[6]. In practice, an image of the beam has also proven useful in cross checking other instruments, like TMBF or orbit stability.

In order to calculate the emittance and energy spread of the electron beam, the measured beam sizes are combined with knowledge of the lattice parameters as:

$$\begin{bmatrix} \sigma_{x_1}^2 \\ \sigma_{x_2}^2 \\ \sigma_{y_1}^2 \\ \sigma_{y_2}^2 \end{bmatrix} = \begin{bmatrix} \beta_{x_1} & 0 & \eta_{x_1}^2 \\ \beta_{x_2} & 0 & \eta_{x_2}^2 \\ 0 & \beta_{y_1} & \eta_{y_1}^2 \\ 0 & \beta_{y_2} & \eta_{y_2}^2 \end{bmatrix} \begin{bmatrix} \varepsilon_x \\ \varepsilon_y \\ \sigma_E \end{bmatrix}$$

where $\sigma_{x_{1,2}}$ and $\sigma_{y_{1,2}}$ denote the measured horizontal and vertical beam sizes, $\beta_{x_{1,2}}$ and $\beta_{y_{1,2}}$ denote the beta functions and $\eta_{x_{1,2}}$ and $\eta_{y_{1,2}}$ denote the measured dispersion values at locations 1 and 2.

2.7.2.2. Source Selection

Each cell in Diamond-II includes 6 dipoles and a mid-straight. Dipoles 1 and 4, and a potential 3 pole wiggler (3PW) located on a mid-straight, are viable source points for SR extraction. The 3PW is included as a comparison, and data for an exemplary device with peak field of 1.8 T is used in calculations.

Using XOP 2.4 [7], the SR emission from each source type has been simulated under circumstances resembling the Diamond-II pinhole cameras as a first estimate. In the simulation, a small angle of 0.25 mrad (1 mm width at 4 m distance from source) illuminated an aluminium exit window to air. The pinhole array and X-ray imager were placed in air for ease of maintenance. Propagation of X-rays through 1mm aluminium window and 9-12 m of air hardens the X-rays to peak at 19-23 keV. Power density spectra for each case are calculated and displayed in Figure 2-132. These show that peak power from D1 and D4 of Diamond-II is approximately half that of the Diamond bending magnet, whilst the 3PW provides approximately a factor 6.5 greater peak power.

Table 2-52 : Source point properties, beam size contributions and available power.

Parameter	DLS-I: BM	D1: Long	D1: Standard	D4	Mid Straight 3PW
β_x [m]	0.84	1.43	1.46	0.27	2.4
β_y [m]	20.34	18.97	13.46	16.13	1.15
η_x [m]	14.44	0	0.1	6.4	24.6
ε_x [pm]	3200	150			
ε_y [pm]	8	8			
σ_E [%]	0.107	0.078			
H beam size from emittance [µm]	51.8	14.6	14.8	6.4	19.0
H beam size from energy spread [µm]	15.4	0	0.1	5	19.2
Total H beam size [µm]	54	14.6	14.8	8	27
V beam size from emittance [µm]	12.8	12.3	10.4	11.4	3
Available power in 250 µrad [mW]	70	31	31	24	264
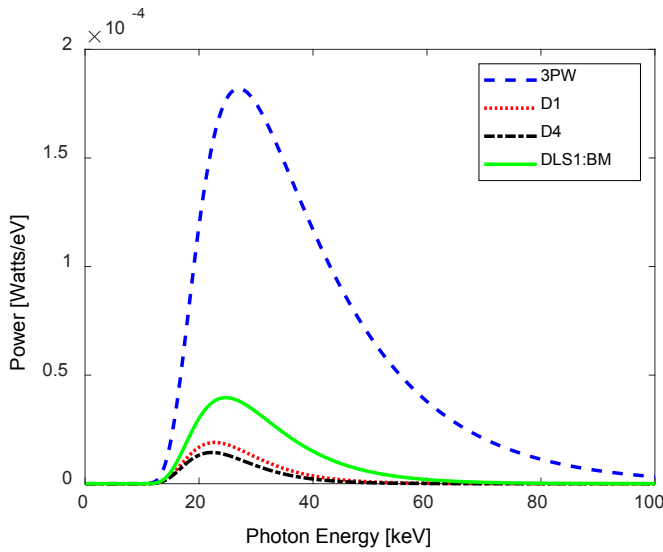
Figure 2-132 : Comparison of the transmitted spectral power distribution through a 1 mm aluminium window and 10m of air for dipoles 1, 4, 3PW and a Diamond bending magnet.

The properties for each source point are shown in Table 2-52. It is observed that:

- the most suitable source for emittance measurement is D1 from both long and standard straights because the energy spread contribution to the total horizontal beam size is negligible
- in addition to D1, the most suitable source for energy spread measurement would be the 3PW on the mid-straight due to the larger dispersion
- the D4 source point would also be suitable for both emittance and energy spread measurements in addition to X-ray pinhole cameras on D1 due to large dispersion in comparison to the horizontal beta function, but with a more challenging horizontal beam size.

2.7.2.3. Tasks to be completed during the detailed design phase

- Decide on the sources to use and design the dipole/crotch vessels accordingly.
- Decide whether a common vessel design suitable for all locations is possible.
- Decide on the number of X-ray pinhole cameras to be installed, and on the details of beam extraction to air.
- Choose pinhole size, method of fabrication, suitable support and actuation.
- Choose scintillation screen, lens, camera, readout and processing.

2.7.3. Fast Orbit Feedback

In Diamond-II, Fast Orbit Feedback (FOFB) is required to operate to higher frequencies compared to Diamond, which achieved a closed loop 0 dB crossover frequency of 140 Hz:

- Beamline applications are using increasingly shorter exposure times (Eiger detectors have frames rates > 1 kHz [8], fast scanning is performed at > 1 kHz [9], [10]), and start to resolve the beam motion at higher frequencies > 100 Hz.
- Noise from cooling water has been identified as a contributor to orbit motion between 100-500 Hz. While increased efforts will be put into the design of Diamond-II water cooling, it remains to be to be seen how much this can be improved while maintaining the necessary heat dissipation from vacuum vessels and magnets.
- The slope of the closed frequency response below crossover is determined fundamentally, so an increase of crossover frequency is necessary to improve suppression at lower frequencies, where a large amount of excitation is found originating from the floor and potentially water cooling.

For Diamond-II, we are targeting a crossover frequency of 1 kHz. Comparative closed loop frequency responses simulated using a single input single output Integrated Model Controller [11] are displayed in Figure 2-133 (left). We are aware that to reach this performance the frequency response and latency of all components in the feedback loop (beam position monitor, communication network, feedback processor, power convertor, corrector magnet and vacuum vessel) need to be budgeted and monitored during design, prototyping and production.
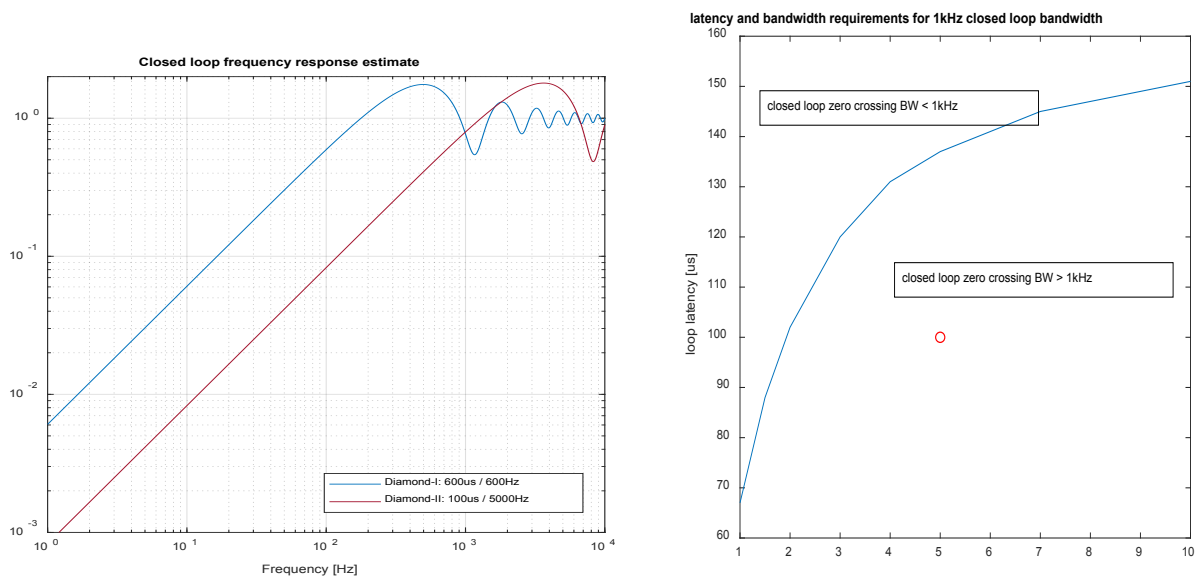
Figure 2-133 : Simulated closed loop frequency response estimates (left), simulated latency and bandwidth requirements (right).

We have established through measurements in the past that a first order low pass filter with latency is a useful approximate model of the complete system of all components in the feedback loop. We have also simulated what deviations from our target 100 μs latency and 5000 Hz first order low pass filter are acceptable to maintain the overall 1000 Hz crossover frequency target for the closed loop frequency response (see Figure 2-133 (right)).

Diamond-II will require an increased number of BPMs (252 versus 168 in the original Diamond), and the aspiration to decrease the latency in the feedback loop necessitates a higher rate of data exchange. This Fast Acquisition (FA) data stream is required to speed up from approximately 10 kHz to 100 kHz to reduce the systematic latency associated with the low pass filter (or averaging) in the production of this data stream. This provides the main motivation for the development of new BPM processing electronics. Equally, power convertors for the corrector magnets will need a decrease in latency.

2.7.3.1. Beam Position Monitor Pickups

Diamond-II will use standard blocks of four buttons in 45 degree orientation. At this moment we could base any analysis only on conceptual layouts which will have to evolve into realistic designs with features to handle synchrotron radiation and include bellows.

The conceptual designs have been investigated with an implementation of the Boundary Element Method [12], [13] and 3D electromagnet simulations using GdfidL [14], [15] that have both been used previously for the DDBA buttons and button blocks. Both simulations have been confirmed by measurements as far as possible, and we thus have good confidence in these simulations. Details of the buttons and blocks are shown in Table 2-53 and Figure 2-134.

The boundary element simulations calculate the 2D electric field distribution for a range of X/Y offsets of the beam inside the aperture, making the assumption that an electrostatic simulation is sufficient for the geometric response mapping and calculation of intercepted wall current flows. The high speed of the 2D simulation allows maps of 100s of beam positions to be created. These show a pincushion distortion typical of the Δ/Σ calculation of the position from the individual button signals. It is planned to remove this distortion as far as possible inside the processing electronics using polynomial expressions.

On the other hand, GdfidL simulations estimate 3D electromagnetic interactions with the simulated passing of a short pulse of charged beam. Most importantly, the longitudinal wake loss factor is calculated, and related losses in materials are accounted for. This is very useful for minimising the heating of button feedthroughs [16], [17], which otherwise leads to undesired deformations of the blocks or even damage. However, a fine 3D mesh is required to adequately model the structure, which in consequence demands a small simulation time step. A single simulation still takes a number of hours, so does not lend itself to creating maps of many beam positions. For the future, comparative simulations of some offset beams are planned. GdfidL further calculates wake potential and wake impedance (Figure 2-135) which show that the first resonance of the button is at ~12 GHz. At this frequency, the spectrum of the 5 mm length Gaussian bunch used for simulation has already decayed to 25% of its peak power density.

Table 2-53 : Button block simulation input parameters and results.

Input parameters	Value
Button diameter	6 mm
Button thickness	4 mm
Button gap	300 μm
Vessel inner diameter	20 mm
Further button detail	316L casing, Molybdenum button
Bunch length	5 mm or 16.6 ps
GdfidL mesh, time step	100 μm, 170 fs
Boundary Element Simulation results	
Button capacitance	2.33 pF
Geometrical scale factor	7.3 mm
Power per button from beam at centre @300 mA	72 μW or -11.4 dBm
Noise power of 20dB NF receiver in 0-10 kHz	-114 dBm
Estimated noise limited resolution in 0-10 kHz	27 nm
GdfidL results	
Longitudinal wake loss factor (whole block)	2.0 mV/pC
Total power loss for 300 mA / 686 b	1.7 W
Fractional power lost into button	18%
Fractional power lost into block	65%
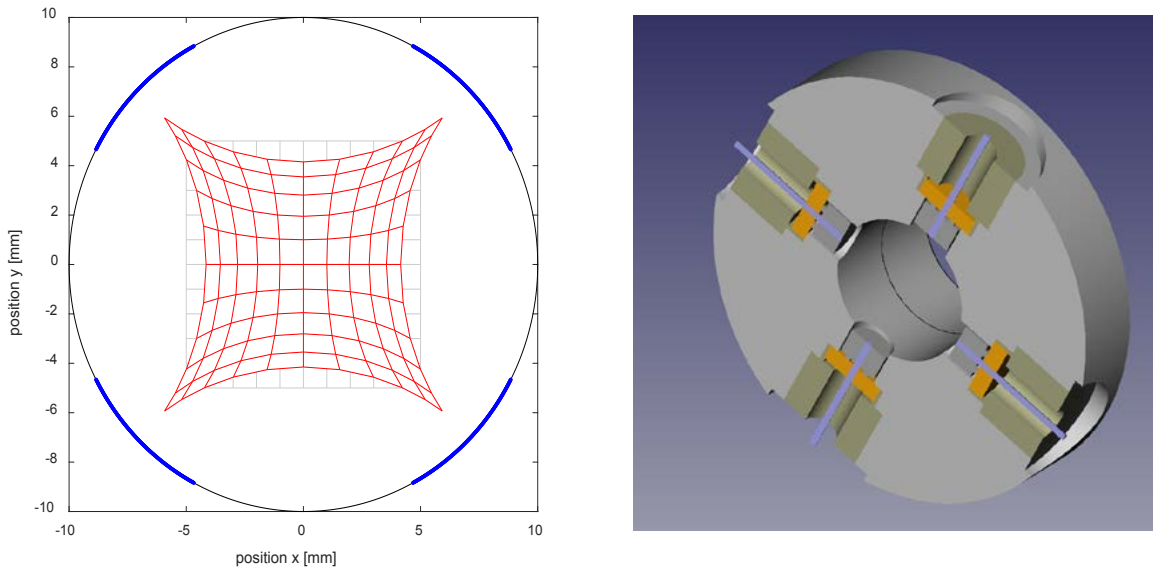
Figure 2-134 : BEM simulation of button geometry (left), 3D model of GdfidL simulation (right).
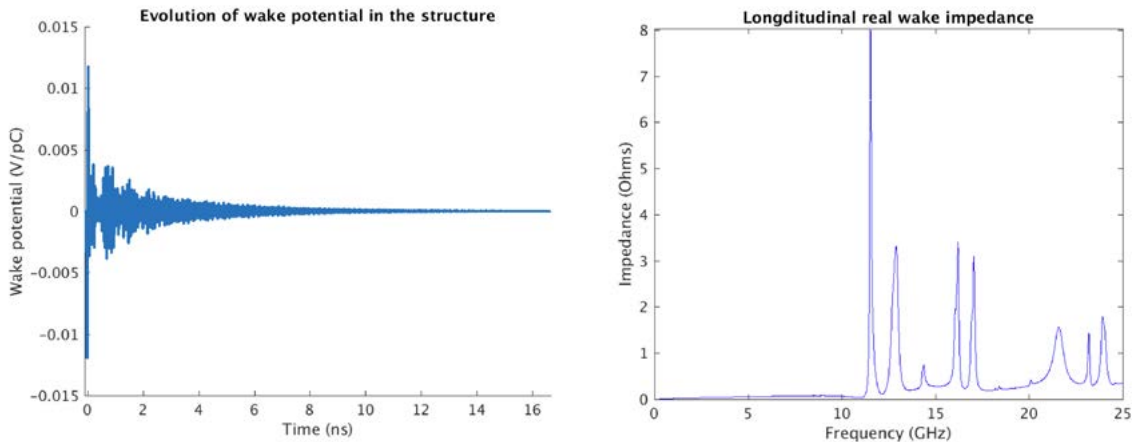
Figure 2-135 : GdfidL simulated wake potential (left) and wake impedance (right).

2.7.3.2. Beam Position Monitor Electronics

Diamond used commercial BPM processing electronics, which realised multiplex switching for the first time in BPMs [18]. While this concept has seen huge success in the past 15 years and benefitted Diamond as well as other light sources tremendously, it has some limitations:

- The switching frequency of GaAs switches is limited to a single digit kHz for this application [19]. Higher rate FA data would be full of switching harmonics.
- In the future, there is likely to be a higher demand for turn-by-turn data with orbit feedback running, which is not compatible with multiplex switching for channel normalisation [20].
- The switching process happens at the input of the BPM electronics, typically located after up to 30 m of cabling. It has been established that significant variations of signal can be introduced due to environmental influences like relative humidity [21], observations at DLS have independently shown the same effect. The impact is at least one order of magnitude larger than the position stability of the processing electronics.

These limitations can be overcome by an alternative electronic stabilisation approach, namely injection of a pilot tone. This approach which has been previously proposed for the BPMs of SLS [22] and NSLS-II [23], but ultimately not put into permanent operation. More recently it found positive experience at Elettra [24], Spring-8 [25] and ALS, the main difference in the success being the identification that ceramic filters work much better than surface acoustic wave filters with a pilot tone placed about ~1 MHz from the bunch frequency.

For Diamond-II, we foresee analogue frontends (AFE) with signal conditioning (pilot tone injection, pre-amplification and programmable attenuation) in the tunnel, followed by ADC sampling and Digital Signal Processing (DSP) in the Control and Instrumentation Area (CIA). This approach would mitigate any drift in the cables to the CIAs and limit the controlled cabling to the short distance from the BPM pickup to the AFE. The AFE will contain no highly integrated electronics and will be mounted in a place where the risk of radiation damage is minimised.

For the calculation of the limiting resolution from noise in the 0-10 kHz band (see Table 2-53) we have assumed a receiver noise figure of 20 dB. This number is a conservative estimate, since another advantage of placing the AFE in the tunnel is an improvement of the noise figure due to moving the long cables behind the AFE. The LMR-240 type cables used in DLS have around 6 dB attenuation at 500 MHz.

ADC sampling can conveniently be implemented on FPGA Mezzanine Cards (FMC), which can be mounted on Advanced µTCA Cards (AMC) with FPGA. On these the DSP processing will be implemented. Already today, there is a selection of ADC FMCs as well as FPGA AMCs from a range of suppliers available, and in future this situation is likely to improve, which should provide a strategy against obsolescence and allow targeted improvements were necessary. This approach will also provide a reduction of the space requirements from half a 19-inch rack for 7 BPMs in Diamond towards 2U in µTCA technology for 10-12 BPMs in Diamond-II.

The accelerator community has adopted µTCA technology widely [26]–[28], and it is reasonable to suppose that it will become a successor to VME. Furthermore, µTCA crates can be purchased with redundant power supplies and monitoring features for temperature and fan speed, which will improve the long term reliability and availability.

With respect to the FA data rate, we are aiming at near 100 kHz, most likely $f_{rev}/5$ or $f_{rev}/6$, which gives headroom for a broad low pass filter for the FA data stream, resulting in minimised latency. For instance a finite impulse response low pass filter with 20 kHz pass band and good suppression at 50 kHz and above would produce a latency of 15 μs.

We have already begun to evaluate two solutions of ADC/FPGA in combination with an AFE for pilot tone injection, provided through a collaboration with Elettra. To this end, we use in-house effort to provide firmware/software required for evaluation, which will also later be used as a foundation for our operational firmware/software. Our strategy for Diamond-II is to design/manufacture our own frontend, while we will procure ADCs, FPGA carriers and μTCA crates from existing commercial sources.

2.7.3.3. Orbit Feedback Controller

In Diamond, the FA data produced by 173 BPMs flows through a complex topology best described as a 2D torus of 4 by 6 nodes of 7-9 BPMs each. In Diamond-II FA data will be concentrated within each cell in the μTCA crate, and a single uplink will send the data to a central controller. The controller will compute the corrector vector from the orbit vector and then re-distribute the corrector data to the cells through individual links. This double star topology provides the lowest latency solution to true global orbit feedback.

We plan to implement the FOFB controller using a COTS AMC card, which provides 24 fibre inputs/outputs, a large FPGA as well as 2 powerful DSPs, and we have begun evaluation of this component. We will implement a controller capable of running feedback with 252 BPMs and 252 corrector magnets in 2 planes. We are also exploring the use of model predictive control to handle situations with different dynamics of some correctors adequately. With regards to latency, we are confident that all transfers and calculations from BPMs to controller to corrector power supply can be completed within 30 μs. We will also ensure that there are available channels to input X-ray beam position monitor data into the orbit feedback controller. The location of the monitor can be chosen in the future to correct the beam position at the most relevant point along a beamline (see Section 3.5).

2.7.3.4. Fast Corrector Power Supplies Dynamics

Diamond-II will require newly developed power supplies specified for high bandwidth and low latency. Taking the APS-U fast power supplies as guidance, we are confident that is possible to implement 10 kHz, 3 dB lower pass frequency for small signal frequency response [29], [30]. We have equipped ourselves with the relevant instrumentation and methods to quickly evaluate the frequency response of prototypes or commercial offerings. More details are given in Section 2.10.1.8.

2.7.3.5. Corrector Magnet Dynamics

We plan to use mainly additional windings on sextupole magnets (see Section 2.4.4) and a small number of dedicated corrector magnets (see Section 2.4.6). The material chosen for these magnets is M270-50, and we measured the frequency response of a small dedicated corrector magnet produced from this material which showed that the magnet dynamics are flat in both amplitude and phase up to 100 kHz.

2.7.3.6. Vacuum Vessel Dynamics

The dynamics of a magnetic field passing through a conductive vessel can be calculated analytically from the eddy currents flowing in the material [31]. While the ultimate detail of the chamber is still under consideration, we have already decided to put stainless steel vessels inside all corrector and sextupole magnets, which are used as correctors. With an assumed 20 mm ID round tube with 1 mm wall thickness, a stainless steel tube will provide a 3 dB bandwidth of 10 kHz, while a copper tube of same dimensions would only provide a low pass at 260 Hz.

2.7.3.7. Tasks to be Completed During the Detailed Design Phase

- Conduct a 'button pickup workshop' with other accelerator institutes and representatives of manufacturers.
- Select a small subset of manufacturers and advance to prototypes, which will be evaluated on the bench and installed in Diamond.
- Design button block solutions (potentially involving shielded bellows) and identify reliable manufacturers.
- Investigate options for BPM analogue frontends.

- Complete evaluation of ADC and FPGA boards for BPM processing.
- Provide a prototype new BPM with comparable output data streams.
- Complete evaluation of central FOFB processor.
- Evaluate prototype fast corrector power supplies.
- Monitor magnet development and vessel choice, test dynamics on prototypes.

2.7.4. Multibunch Feedback

Multibunch Feedback (MBF) is likely to become more relevant due to higher resistive wall impedance or ion instabilities during initial conditioning. We also regard MBF as an 'insurance policy' to mitigate a range of effects, from deviations from predicted strength of collective effects [32] to initially higher vacuum pressures. For Diamond-II, MBF thus becomes a requirement from the start, and must be implemented with reliability for permanent operation in mind.

The original Diamond MBF used a commercial Libera Bunch-by-Bunch processor. The firmware/software was originally provided by the ESRF and has subsequently been adapted and developed over 10 years at DLS. In 2017, the MBF processor hardware was renewed and extended to the longitudinal dimension [33]. The new system is based on COTS µTCA and FMC components, and the results have been shared and implemented at ESRF, Elettra, and BESSY-II to increase the user base.

MBF has evolved beyond bunch-by-bunch control, it offers per bunch manipulation and investigation techniques. At DLS we use it in operation for transverse MBF and betatron tune measurement (including tune feedback) [34] . On top of that we use MBF for synchrotron tune measurement, longitudinal MBF, bunch cleaning and excitation for resonant spin depolarisation.

The new MBF system is expected to be moved into Diamond-II with as little as possible adjustments, so will only be reviewed briefly here.

2.7.4.1. Bunch by Bunch Beam Position Monitor Pickups and Low Level RF Frontend

For the pickup, we are using a standard BPM button pickup. We are expecting to be able to find space for an extra pickup to this purpose in Diamond-II. The pickup signals will be combined in RF hybrids, fed to the CIA, and processed there at 1.5 GHz in a commercial RF frontend to baseband X/Y/S signals.

2.7.4.2. Multibunch Feedback Processor

These baseband signals are digitised by 500 MS/s ADC on a FMC module, then processed on Virtex-7 onboard of commercial AMC and finally converted back to analogue via 500 MS/s DAC onboard of the earlier FMC. The processor runs in-house developed firmware and software.

2.7.4.3. Power Amplifiers

We have upgraded to new transverse power amplifiers that cover 10 kHz-250 MHz with good amplitude and phase flatness. The low start frequency is of particular importance to provide good feedback for transverse coupled bunch mode -1, which is typically driven by resistive wall impedance. We are using a single amplifier per axis followed by a power hybrid to drive the kicker striplines in differential mode. This 180º-splitter also protects the amplifier from the common mode pickup signal collected by the striplines from the beam.

In the longitudinal plane we have currently 4 amplifiers driving the four input ports into the kicker cavity. These provide a total of 100 W in the 1.75-2.0 GHz bandwidth of the cavity but could be upgraded at relatively low cost should that be required.

2.7.4.4. Transverse and Longitudinal Kicker Structures

The transverse kicker structure are currently a copy of the SLS design [35]. A new design of these transverse structures will be required to suit the new round chamber. A round chamber may make the same design feasible for both horizontal kickers and vertical kicker structures. Care will be taken to reduce the dissipation of RF power in the structure we have experienced with the existing structure under some conditions. Evolved understanding and simulation capabilities will be used to this end.

The longitudinal kicker structure was installed in 2017. While it is not currently required for operation in Diamond, it is currently still unclear if it will be required for Diamond-II. If this is the case, then the structure will need to be evolved to fit the new smaller beam pipe.

2.7.4.5. Tasks to be Completed During the Detailed Design Phase

• Design new transverse and potentially new longitudinal kicker structures.

2.7.5. Beam Loss Monitoring

We expect to need improved Beam Loss Monitoring facilities during the commissioning and operation of Diamond-II due to smaller apertures (both physical and dynamic). In principle, we could re-use the existing PIN-diode based loss counters, which have proven useful to determine an overall background distribution. We have 180 of these monitors in a reasonably small and robust enclosure. To continue their use we would likely have to upgrade the readout counters to a modern standard, as the current VME based readout solution maybe be retired for Diamond-II.

However, the PIN-diode base system has a number of limitations:

• The pickup devices are reasonably small, but given the tight packing density on our girders we may find it challenging to place the devices close to the beam pipe. When placed further away, the count rate diminishes quickly.

• Since PIN-diodes produce countable events (the existing system produces ~1 event/s from natural background and electronic noise or 10-10000 events/s in the storage ring during operation at 300 mA), they fail to represent instantaneous events like beam loss or injection losses correctly, since the sensor is not integrating.

• Both these shortcomings are addressed with scintillator/PMT sensors and fast analogue readout, as available in commercial solutions developed for the ESRF-EBS. We have already 5 of these 'fast BLM' systems in Diamond and gathered successful data with these, for instance assess the loss rate near our septum during injection. The sensors of these systems require less than 3 cm longitudinal space so can be fitted much more freely, and the readout electronics are fully integrated electronics including EPICS level integration. This allows quick movements into 'hot spots' for investigations. For Diamond-II we aim to increase the number from currently 5 systems (20 sensors) to 24 systems (96 sensors) to have fast beam loss monitoring in every cell.

References

[1]   C. Thomas and G. Rehm, "Time Domain Measurements at Diamond," in *Proc. of DIPAC*, 2007.

[2]   C. Bloomer and G. Rehm, "Real-time Calculation of Scale Factors of X-ray Beam Position Monitors During User Operation," in *Proc. of IBIC*, 2012, pp. 79–82.

[3]   C. Bloomer, J. Brandao-Neto, G. Rehm, and C. Thomas, "Dual Beam X-ray Beam Position Monitor," in *Proc. of DIPAC*, 2009, pp. 4–6.

[4]   C. Thomas, G. Rehm, I. Martin, and R. Bartolini, "X-ray pinhole camera resolution and emittance measurement," *Phys. Rev. Spec. Top. - Accel. Beams*, vol. 13, no. 2, p. 022805, Feb. 2010.

[5]   L. M. Bobb, A. F. D. Morgan, G. Rehm, and D. L. Source, "Performance Evaluation of Molybdenum Blades in an X-Ray Pinhole Camera," in *IBIC*, 2016.

[6]   I. P. S. Martin *et al.*, "Reconstruction of Electron Bunch Motion During CSR Burts Using Synchronised Diagnostics," in *Proc. of IPAC*, 2015, pp. 5–8.

[7]   M. Sánchez del Río and R. J. Dejus, "XOP v2.4: recent developments of the x-ray optics software toolkit," 2011, vol. 8141, p. 814115.

[8]   "Eiger Detector Specification - Dectris Website." [Online]. Available: https://www.dectris.com/products/eiger/eiger2-x-for-synchrotron/specification. [Accessed: 25-Feb-2019].

[9]   M. D. de Jonge, C. G. Ryan, and C. J. Jacobsen, "X-ray nanoprobes and diffraction-limited storage rings: opportunities and challenges of fluorescence tomography of biological specimens," *J. Synchrotron Radiat.*, vol. 21, no. Pt 5, pp. 1031–47, Sep. 2014.

[10]   U. Boesenberg *et al.*, "Fast X-ray microfluorescence imaging with submicrometer-resolution integrating a Maia detector at beamline P06 at PETRA III," *J. Synchrotron Radiat.*, vol. 23, no. 6, pp. 1550–1560, Nov. 2016.

[11]   S. Duncan, "The design of a fast orbit beam stabilisation system for the Diamond Synchrotron," 2007.

[12]   A. Olmos, F. Pérez, and G. Rehm, "MATLAB code for BPM button geometry computation," in *Proc. of DIPAC*, 2007, pp. 186–188.

[13]   F. Marcellini, M. Serio, and M. Zobov, "Daphne Broadband Button Electrodes," 1996.

[14]   R. Bartolini *et al.*, "Double-double bend achromat cell upgrade at the Diamond Light Source: From design to commissioning," *Phys. Rev. Accel. Beams*, vol. 21, no. 5, p. 050701, May 2018.

[15]   W. Bruns, "GdfidL: A Finite Difference Program with Reduced Memory and CPU Usage," in *Particle Accelerator Conference*, 1997, pp. 2651--2653.

[16] R. Nagaoka and K. L. F. Bane, "Collective effects in a diffraction-limited storage ring.," *J. Synchrotron Radiat.*, vol. 21, no. Pt 5, pp. 937–60, Sep. 2014.

[17] A. F. D. Morgan and G. Rehm, "Considerations and Improved Workflow for Simulation of Dissipated Power From Wake Losses," in *Proc. of IBIC*, 2015, pp. 202–205.

[18] U. Mavrič, "Innovative RF Design Unites Benefits of Multiplexed and Multi-Channel System," in *AIP Conference Proceedings*, 2004, vol. 732, no. 1, pp. 373–378.

[19] T. Fujita, S. Sasaki, M. Shoji, T. Takashima, and J. Spring-, "A Problem in RF Switches of Multiplexing BPM System," in *DIPAC 2005*, 2005, pp. 217–219.

[20] B. Podobedov *et al.*, "Single Micron Single-Bunch Turn-By-Turn BPM Resolution Achieved at NSLS-II," in *IPAC*, 2016.

[21] T. Fujita, H. Dewa, M. Masaki, S. Matsubara, S. Sasaki, and S. Takano, "Long-Term Stabilty of the Beam Position Monitors at SPRING-8," in *IBIC*, 2015.

[22] M. Dehler, A. Jaggi, P. Pollet, T. Schilcher, V. Schlott, and R. Ursic, "New Digital BPM System for the Swiss Light Source," in *DIPAC*, 1999.

[23] O. Singh *et al.*, "NSLS-II BPM and Fast Orbit Feedback System," in *IBIC*, 2013, pp. 316–318.

[24] G. Brajnik, S. Bassanese, G. Cautero, S. Cleva, and R. De Monte, "Integration of a Pilot-Tone Based BPM System Within the Global Orbit Feedback Environment of Elettra," in *IBIC*, 2018.

[25] H. Maesaka, H. Dewa, T. Fujita, M. Masaki, and S. Takano, "Development Status of a Stable BPM System for the SPring-8 Upgrade," in *IBIC*, 2016.

[26] H. Schlarb, T. Walter, K. Rehlich, and F. Ludwig, "Novel Crate Standard MTCA.4 for Industry and Research," in *IPAC*, 2013.

[27] D. O. Tavares *et al.*, "Development of an Open-Source Hardware Platform for SIRIUS BPM and Orbit Feedback," in *Proceedings of ICALEPCS 2013*, 2013, pp. 1036–1039.

[28] T. Walter, M. Fenner, K. Kull, and H. Schlarb, "MicroTCA Technology Lab At DESY: Start-Up Phase Summary," in *IPAC*, 2017.

[29] B. M. Song and J. Wang, "Mathematical Modeling and Analysis of a wide Bandwidth Bipolar Power Supply for the Fast Correctors in the APS Upgrade Controller," in *IPAC*, 2015, pp. 2–4.

[30] J. Wang, G. Sprau, I. Abid, and R. Keane, "Preliminary Designs and Test Results of Bipolar Power Supplies for APS Upgrade Storage Ring," in *IPAC*, 2018, pp. 2381–2384.

[31] B. Podobedov, L. Ecker, D. Harder, G. Rakowsky, and N. York, "Eddy Current Shielding by Electrically Thick Vacuum Chambers," in *Proceedings of PAC*, 2009, pp. 3398–3400.

[32] V. Smaluk, "Impedance computations and beam-based measurements: A problem of discrepancy," *Nucl. Instruments Methods Phys. Res. Sect. A Accel. Spectrometers, Detect. Assoc. Equip.*, vol. 888, pp. 22–30, Apr. 2018.

[33] M. G. Abbott, G. Rehm, and I. S. Uzun, "A New Transverse and Longitudinal Bunch By Bunch Feedback Processor," *ICALEPCS*, 2017.

[34] M. T. Heron *et al.*, "Feed-forward and feedback schemes applied to the Diamond Light Source storage ring," in *Proc. of IPAC*, 2014, pp. 1757–1759.

[35] M. Dehler, "Kicker Design for the Elettra / SLS Longitudinal Multi-Bunch Feedback," in *EPAC*, 2002, pp. 2070–2072.

2.8. Front Ends

2.8.1. Introduction

The existing Front Ends are compatible with a storage ring operating at 3 GeV and a maximum electron beam current of 500 mA. The compatibility of these Front Ends to continue to operate with a storage ring operating at 3.5 GeV and 300 mA is one of the main considerations determining the extent of changes required. The second main consideration are changes in photon beam exit trajectories brought about by the new magnetic lattice of the storage ring. Currently there are 31 Front Ends, as listed in Table 2-54.

Table 2-54 : List of Diamond Front Ends.

Source	Location
Single Insertion Devices	I02, K02, I03, I05, I06, I07, I08, I10, I11, K11, I12, I14, I15, I16, I18, I19, I21, I22, I23, I24
Two angled Insertion Devices	I04 and I04-1, I09-1 and I09-2, I13-1 and I13-2, I20-1 and I20-2
Bending Magnets	B07, B16, B18, B21, B22, B23, B24

2.8.2. Front End Changes Needed for Diamond-II

The major changes associated with the Front Ends fall into seven categories:

1. Three new Front Ends in new locations where existing beamlines are being re-located.
2. Realignment and upgrading of existing Front Ends K02 and K11 which are aligned to insertion devices located in mid-straights created by the DDBA and DIAD projects.
3. Realignment and possibly upgrading of Front Ends on all existing Bending Magnet beamlines.
4. Changes resulting from the shift of source point.
5. Changes in exit apertures due to the different photon beam properties.
6. Changes of photon beam radiation power densities that have implications for the beam power handling components.
7. Changes in the heat transfer coefficient to the cooling water due to the requirement to reduce water velocities and hence reduce excessive turbulence as a source of vibration.

The required changes identified are as follows:

*   Twenty-four Front Ends will require an additional module to match the new termination point of the crotch vessel, including modified versions for K02 and K11.
*   Three of the Beamlines with shared occupancy will require relocation and hence new Front Ends (I04-1, I20-2 and B07-1).
*   Ten Front Ends will require detailed assessments for the configuration of the wall penetration shielding with respect to the exiting photon beam. Retaining canting angles for those Front Ends associated with the Insertion Devices listed in Table 2-50 will still require repositioned chicane magnets resulting in lateral offsets in the photon trajectory.
*   One Front End (K11) will require the modification of the ratchet wall penetration.
*   The seven current Bending Magnet Front Ends will require either complete renewal or major reconfiguration, including the wall penetration shielding.
*   It is estimated that ten ID Front Ends will require new photon exit apertures.

2.8.3. Outline Design of Critical Components

The reconfigured magnetic lattice has moved the first dipole magnet approximately 7 metres further upstream compared with the current location. This is the region where the photon beam separates from the electron beam and is the start of the Front End. This change means that all of the existing Insertion Device Front Ends will require a 'Module Zero' which makes up the space between the existing entry to the Front End and the new entry point. This will consist in its simplest form of a round tube of sufficient diameter to avoid illumination by the photon beam. If avoidance of the photon beam is not a practical proposition, then cooling channels will be added to the design.

Table 2-55 : Critical components of a Front End.

Component	Function
Isolating Gate Valve	To provide vacuum isolation between the Front End and the Storage Ring.
First Aperture	To remove the part of the dipole light that is not coincident with required photon beam.
Fast Valve	In the event of loss of vacuum in the Front End, to slow the propagation of the resulting pressure wave back into the storage ring.
Absorber	To block all of the photon energy when not required by the Beamline.
Beam Splitter	Where a single Front End serves two Beamlines, this component defines the two apertures.
Custom Aperture/Slits	Limit the size of photon beam to that required by the Beamline.
Twin Port Shutter	A pair of metal blocks of sufficient density to block all radiation exiting to the Beamline when set in position. This is part of the Personnel Safety System.

Assessments will be carried out for all of the beam absorbing components listed in Table 2-55 to determine whether they can be retained or not. To date a major assessment has been made to determine whether the Absorber and Custom Apertures can withstand the additional heat load of Diamond-II (see next Section).

2.8.4. Front End Radiation Power Handling

The assessment criteria have been set with photon radiation power densities calculated at 3.5 GeV, 330 mA (300 mA + 10%) and a cooling heat transfer coefficient based on 75% of the current water velocity values of the existing front end. The value of 75% is based on the results of ongoing development work to reduce the water velocities in the existing storage ring for the reasons discussed in Section 2.6.2.4. Among all Diamond insertion devices, a CPMU insertion device produces photon radiation with the highest normal peak power density around 83 kW/mrad^2 and a high total power around 9.5 kW; a SCW insertion device produces photon radiation with highest total power around 50.1 kW and a high peak density around 51.8 kW/mrad^2.

Finite Element Analysis (FEA) has been carried out using ANSYS to determine if the Front End beam power-handling components can withstand the additional heat load in Diamond-II. Priority was given to the absorbers of CPMU front ends and beam facing components of SCW front ends. Table 2-56 below lists the FEA results to date. A complete analysis will be made during the detailed design phase.

Table 2-56 : Existing Front End compatibility with Diamond-II at 3.5 GeV, 330 mA, with 75% of current water flow.

Front End	Component	Material	Insertion Device	Total Power (kW)	Normal Incidence Peak Power Density (kW/mrad^2)	FEA Result
I03	Absorber	OFHC	CPMU	9.5	83.2	Pass
I12	1st Aperture	OFHC	I12 SCW	50.1	51.8	Pass
	Absorber	OFHC				Pass
	Slits	OFHC				Pass
I13	Beam Splitter	OFHC	I13-2	5.5	55.8	Fail
	Absorber	OFHC	I13-1	6.5	62.0	Fail
I15	1st Aperture	OFHC	I15 SCW	43.2	43.5	Pass
	Absorber	GLIDCOP/ AL15LOX				Pass
	Beam Splitter	GLIDCOP/ AL15LOX				Fail
I14	Absorber	OFHC	CPMU	9.5	83.2	Pass
I24	Absorber	OFHC	CPMU	9.5	83.2	Pass

Components failing the FEA assessment will need to be replaced. Further studies of the remaining life of front end absorbers due to thermo-mechanically induced fatigue are also necessary in the detailed design phase. The fatigue life of the absorbers will need to be established for the high heat load of Diamond-II beam power. A survey of Diamond phase I front end absorbers shows that the absorbers experienced an average of 320, and maximum of 500, thermal cycles per year. Therefore, a minimum 15000 cycles to 'failure' threshold or equivalently a 30 year life assuming every thermal cycle occurs at maximum power could be used as a conservative basis.

2.9. Radio Frequency System

2.9.1. RF Parameters

The optimal RF frequency for a synchrotron light source is determined by a combination of desired beam parameters (for example bunch to bunch distance, bunch length and RF aperture) and the availability of technology at the selected frequency (high power amplifiers and accelerating cavities). The size of a cavity scales with RF wavelength, and so spatial restrictions lead to a practical lower frequency limit of tens of megahertz. Dissipation of power from the cavity walls limits the upper frequency of a CW normal conducting cavity to approximately 800 MHz [1], and superconducting cavities may operate up to several gigahertz before surface losses begin to adversely affect performance [2].

A first parameter to consider when selecting a frequency in the allowed range is the voltage required to maintain a defined RF aperture, δ_{RF}, which is a function of energy loss, U, rotation frequency, f_0, momentum compaction factor, a, RF frequency f_{RF}, beam energy, E and a dimensionless factor, F:

$$\delta_{RF} = \frac{U f_0}{\pi \alpha f_{RF} E} F$$

F is a function of the overvoltage, q:

$$F = 2\left(\sqrt{q^2 - 1} - \arccos\left(\frac{1}{q}\right) \right)$$

with

$$q = \frac{e_0 V_0}{U}$$

where e_0 is the electronic charge.

For the Diamond-II parameters, the RF aperture scales with total voltage, V_{total}, as shown in Figure 2-136 for bare lattice losses and in Figure 2-137 including insertion device losses. Three nominal frequencies in the range of interest are shown.
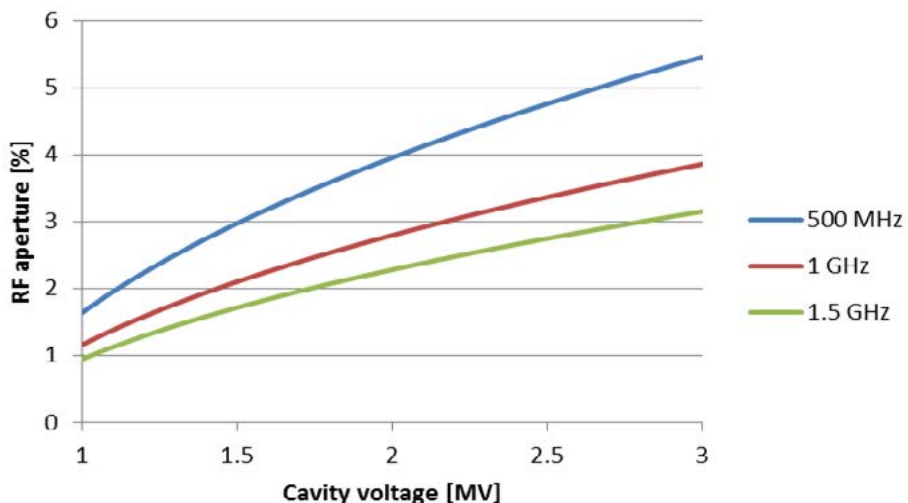
Figure 2-136 : RF aperture as a function of voltage for the bare lattice.
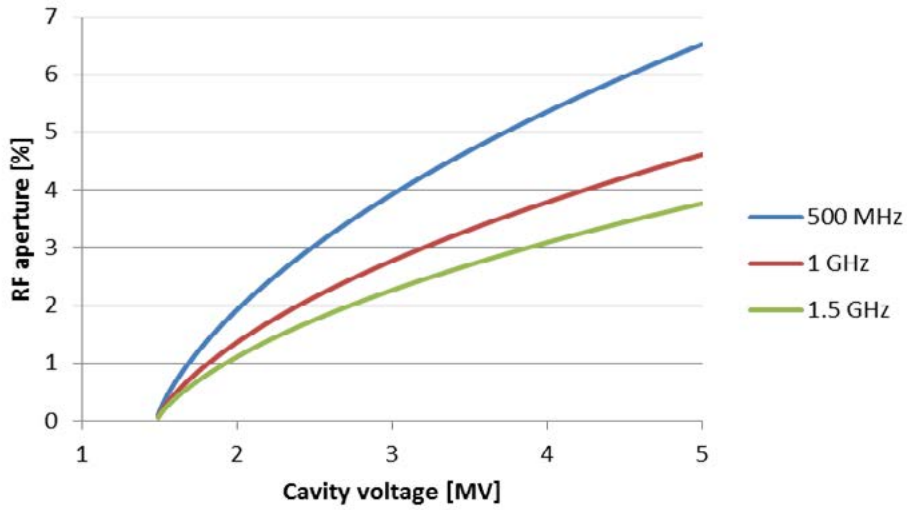
Figure 2-137 : RF aperture as a function of voltage including ID losses.
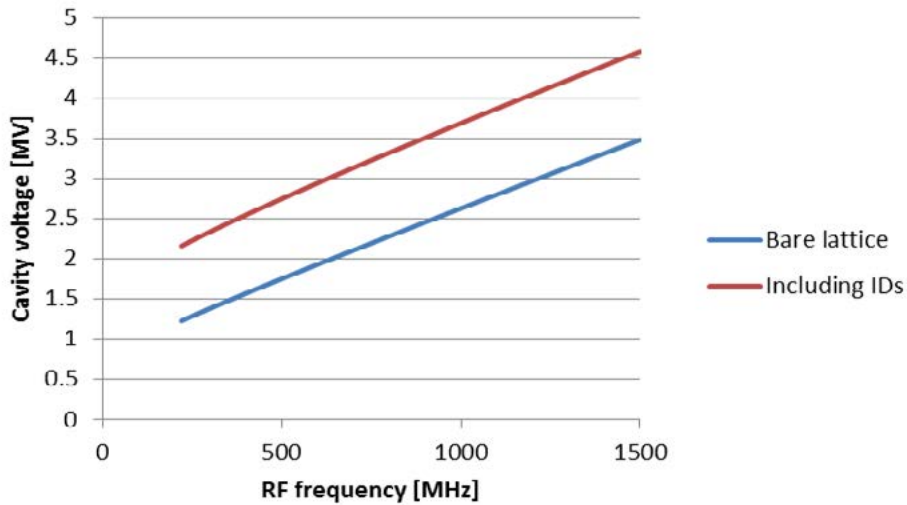
Figure 2-138 : Voltage required to maintain 3.5% RF aperture with and without ID losses.

The Voltage, V_{req}, required to maintain a momentum aperture of 3.5% is shown in Figure 2-138 for an RF frequency range of 100 MHz to 1.5 GHz with bare lattice losses and also for full ID losses. As can be seen, the Voltage is minimised at the lower end of the frequency range.

For a storage ring with RF acceptance as large as transverse acceptance the Touschek lifetime scales with RF frequency as:

$$\tau_t \propto \sqrt{\frac{1}{1+\dfrac{C}{f_{RF}}}}$$

where C is derived from the machine parameters:

$$C = \frac{f_0 U}{\alpha E \delta_{RF}^2}$$

The relative Touschek lifetime across the range of frequencies is shown in Figure 2-139, showing that the lifetime starts to fall off at low RF frequency.
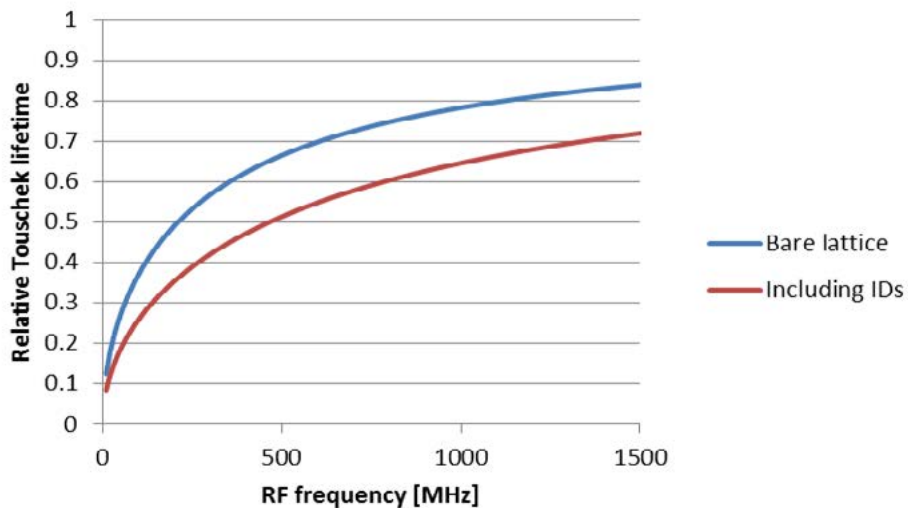
Figure 2-139 : Relative Touschek lifetime with and without ID losses.

Minimisation of the required voltage leads to lower RF frequency, but the loss of lifetime limits the minimum value to several hundred Megahertz and so an operating frequency of 500 MHz has been chosen. Other advantages of this frequency are the existence of more than one design of 500 MHz cavity and the availability of several different RF amplifiers at this frequency. The choice of the same frequency as Diamond also enables the use of much of the same infrastructure and instrumentation.

2.9.2. Precise Operating Frequency

In order to reduce the cost of Diamond-II, components from Diamond should be reused as far as possible. Retention of the 500 MHz RF frequency allows much of the infrastructure to be used in Diamond-II, but the high quality factor and consequent narrow bandwidth of several items places constraints on the exact RF frequency:

1. The existing CESR-B superconducting cavities in the storage ring have an unloaded quality factor Q_0 in excess of 1×10^9 with some tuning of the fundamental frequency possible by deformation of the cell geometry.

2. Normal conducting cavities in the storage ring, of the EU HOM-damped cavity design, have $Q_0 = 33,000$ and can be tuned with a tuning plunger.

3. Normal conducting five cell PETRA-type cavities in the booster have $Q_0 = 29,000$ and can be tuned with a tuning plunger.

4. Linac 5.2 m S-band structures of the DESY II design have $Q_0 = 14,000$ and have no fast tuning mechanism.

All normal conducting structures, including the linac, can be further tuned by a change of water temperature in the regulating circuit. All amplifiers, whether klystron, IOT or solid state, have a much broader bandwidth than the resonant structures and do not limit the operational frequency. The narrow bandwidth and limitations to tuning of the different structures lead to the restrictions on precise operating frequency shown in Table 2-57.

Table 2-57 : Tuning ranges of Diamond RF cavities and structures.

Device	Minimum frequency	Maximum frequency	Notes
SR superconducting cavities	499.5 MHz	499.8 MHz	Upper limit may be possibly raised by further distortion, but risk of damage is high. Lower frequency may be extended by a smaller amount with further risk
SR normal conducting cavities	499.3 MHz	500.1 MHz	Minor further tuning is possible by changing water temperature
Booster cavities	499.5 MHz	500.0 MHz	
Linac structures	499.6 MHz	499.9 MHz	Tuning by water temperature only

The storage ring circumference is defined by the lattice, and the selected harmonic number of 934 leads to a machine RF frequency of 499.499 MHz. This frequency is on the limit of operation of the superconducting cavities but within the tuning range of the normal conducting cavities in the storage ring. Operating the booster cavities and linac at elevated temperatures, slightly above Diamond operating temperature in the booster and at approximately 60°C for the linac structures, would enable these Diamond devices to be reused in Diamond-II.

2.9.3. Cavities

The total voltage requirement at 500 MHz calculated according to Section 2.9.1 above is 2.7 MV with all insertion devices. Diamond currently has four superconducting CESR-B 500 MHz cavities, each demonstrated to operate with a different safe voltage, above which they become susceptible to cavity fast vacuum trips; these operating voltages are given in Table 2-58.

Table 2-58 : Proven safe operating voltages for Diamond's CESR B cavities.

Cavity	Safe operating voltage
A	1.1 MV
B	1.2 MV
C	1.4 MV
D	0.8 MV

Three CESR-B cavities would therefore be required to make up the total voltage requirement in Diamond-II. The current RF straight can accommodate three CESR-B cavities but the shorter Diamond-II straight can only take two cavities, as shown in Figure 2-140.

As there is no second RF straight the only possible location for a third CESR-B cavity is in a 2.9 m mid-cell straight; installation here would however involve compromise of the taper gradient around the cavity and so a fully superconducting storage ring RF system as used in the original Diamond design is not attractive.
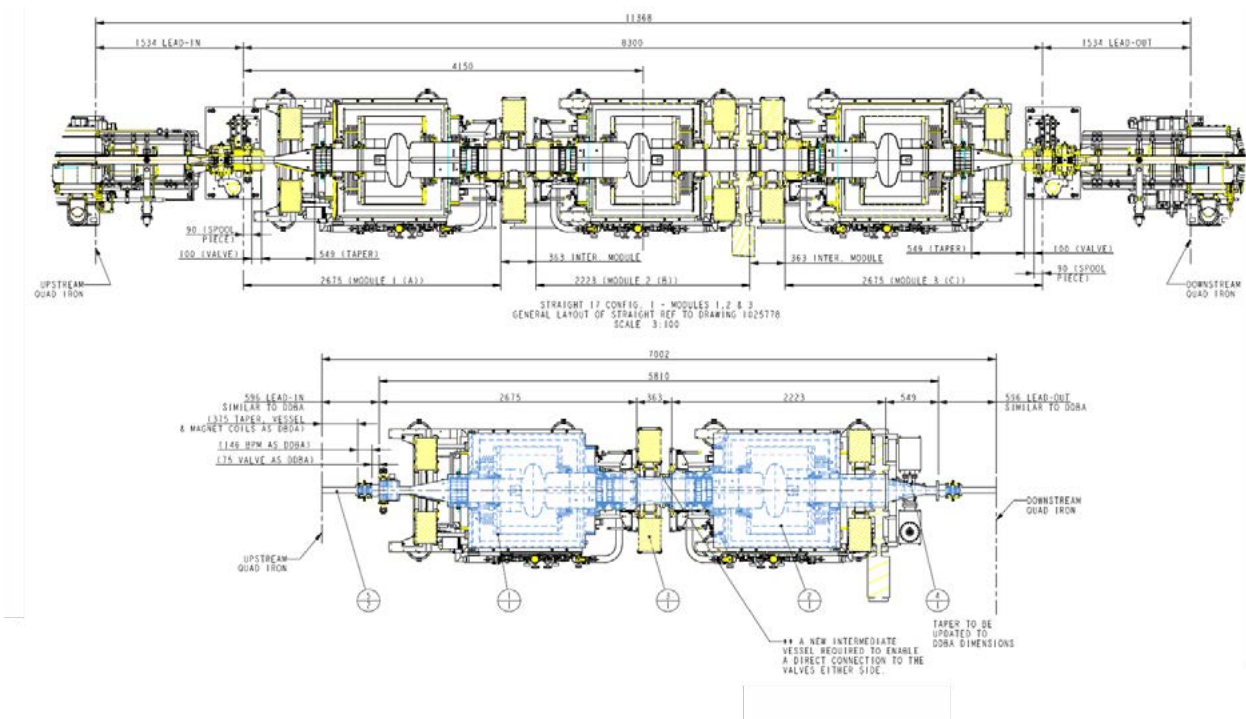
Figure 2-140 : Diamond RF straight (above) and Diamond-II RF straight (below).

Although superconducting cavities are routinely supporting beam in Diamond, two cavity vacuum leaks in the past five years have resulted in significant machine down-time and reduced-current operation, with repair proving to be prolonged and expensive. Normal conducting cavities have several advantages over superconducting cavities in terms of maintenance and repair in that:

- they are immediately available for access without a slow warmup and removal of cryostat,
- repairs to a damaged cavity can be carried out without a cleanroom, and
- no chemical surface treatment is required before the cavity is reintroduced into the ring.

It is cost effective to run the multiple cryostats needed for superconducting cavity operation from a single cryogenic plant, but this plant then becomes a single point of failure for the entire RF system. Use of normal conducting cavities eliminates this risk.

Because of the risk to machine continuity posed by a superconducting cavity failure, in recent years Diamond has installed two EU HOM-damped cavities of the BESSY design [3]. These cavities are also installed at ALBA [4] and have a nominal maximum voltage of 700 kV but are operated conservatively at operating voltages up to 450 kV [5] to ensure long-term reliability. A comparison of selected parameters of the two cavities is given in Table 2-59. These parameters are broadly representative of the performance of other superconducting and normal conducting cavities used in synchrotron light sources, for example the superconducting KEKB cavities [6], also used in the Taiwan Photon Source [7] and the normal conducting ELETTRA- type cavities used at ELETTRA [8] and Anka [9].

Table 2-59 : Fundamental parameters of CESR-B and EU HOM-damped cavities.

Parameter	CESR-B cavity	EU HOM-damped cavity
Flange-to-flange length	At least 2.2 m	0.5 m
Reliable operating voltage	0.8 MV to 1.4 MV	Up to 450 kV
Power handling capability	300 kW	120 kW

Measurements of beam excitation by higher order modes in the Diamond storage ring have shown that the EU HOM-damped cavities are indeed very well damped and so installation of normal conducting cavities is not expected to trigger instabilities in the ring. Should multiple cavities have a measurable effect, instabilities can be damped with multibunch feedback systems of type already installed at Diamond [10]. For the above reasons, the choice has therefore been made to adopt the EU HOM-damped normal conducting cavities for Diamond-II.

The total power that must be delivered to a 300 mA storage ring beam current with a full complement of insertion devices is 460 kW. For a normal conducting cavity, the generator power P_g needed to support a given field V_c at a beam current I_b is given by [11] where R_L is the shunt impedance, β the cavity coupling factor, ψ the cavity tuning angle and φ the synchronous phase.

$$P_g = \frac{V_c^2}{R_L} \frac{\beta+1}{8\beta} \left[\left(1 + \frac{2R_L I_b}{V_c} \cos(\phi) \right)^2 + \left(\tan(\psi) + \frac{2R_L I_b}{V_c} \sin(\phi) \right)^2 \right]$$

The free parameters above can be optimised to calculate the minimum generator power required for a given total voltage, beam current and beam power. Working parameters and optimal coupling values are given in Table 2-60 for multiple cavities of the EU HOM-damped design.

Table 2-60 : Working parameters required for multiple normal conducting cavities.

Parameter	6	7	8	9
Optimal cavity coupling	3.8	4.3	4.7	5.2
Individual cavity voltage	450 kV	386 kV	338 kV	300 kV
Generator power per cavity	104 kW	85 kW	73 kW	63 kW
Power dissipated per cavity	27 kW	20 kW	15 kW	12 kW
Power dissipated in all cavities	164 kW	140 kW	123 kW	109 kW

The use of six cavities results in individual cavity voltages at the maximum acceptable value; increasing the number of cavities reduces voltage and dissipated power. The total power lost in the cavity walls is comparable to that required for the helium compressor for an equivalent superconducting RF system. The exact number of cavities will follow from an analysis of capital and running costs, but eight is a reasonable number. For eight cavities operating with maximum ID losses $\beta = 4.7$ allows operation at 300 mA with critical coupling, as can be seen in Figure 2-141.
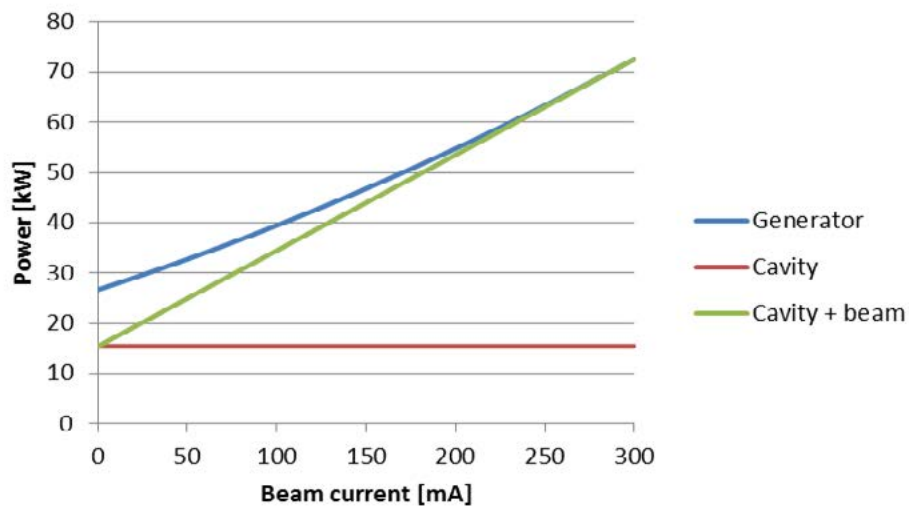
Figure 2-141 : Generator, cavity and beam powers with 8 EU HOM-damped cavities.

Use of eight cavities at conservative voltage and power levels also provides some protection against cavity voltage faults, as seven cavities can be run harder in the event of one cavity failure [12]. This option is not possible with a small number of superconducting cavities as power and voltage coupled to the failed superconducting cavity cannot be replaced by the remaining devices; this would be the case even with a single superconducting cavity in a hybrid arrangement.

In summary, both the physical restrictions and the long-term risk to operations rule out the use of a complete superconducting storage ring RF, whereas the simple design of the normal conducting cavities offers advantages in terms of maintenance and reparability. HOMs are well-damped in the normal conducting cavity chosen and power loss in the resistive cavity walls is comparable with that on the cryogenic plant, leading to a conceptual design of eight normal conducting EU HOM-damped cavities in the storage ring.

2.9.4. Physical Layout

Eight EU HOM-damped cavities can be accommodated in the Diamond-II ring using the full RF straight and two of the mid-section straights. The layout of the RF straight is shown in Figure 2-142, with pumps installed between each cavity and a taper at either end of the multiple cavity assembly. The front end leading from the previous straight can be threaded between the limbs of the cavities with minor adjustments to the support structures.
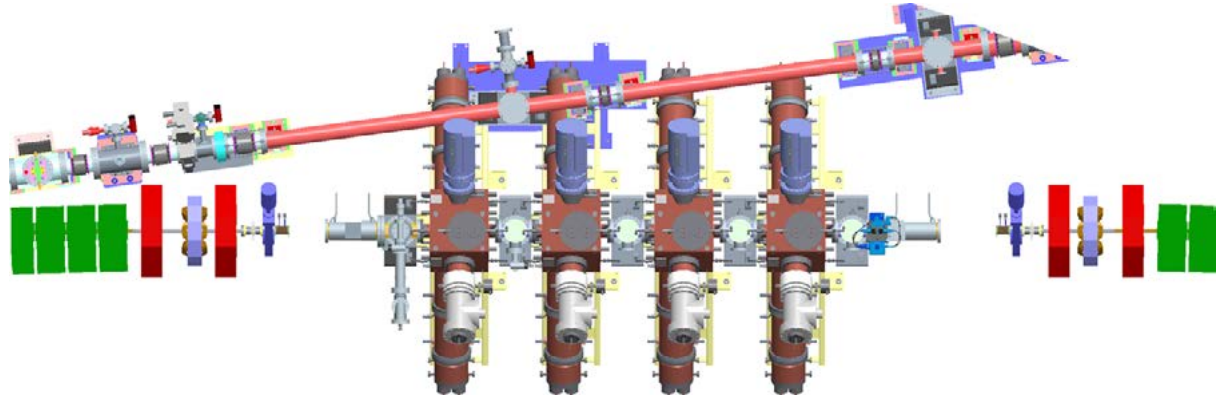
Figure 2-142 : Four EU HOM-damped cavities in the RF straight.

The mid-section straight arrangement is shown in Figure 2-143, again with space for cavities, vacuum components and tapers and the requirement for some redesign of the front-end supports.
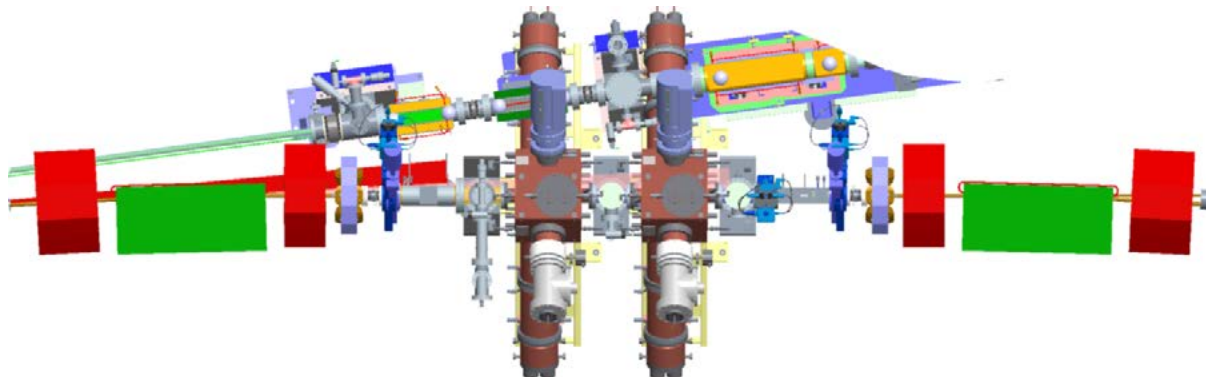
Figure 2-143 : Two EU HOM-damped cavities in a mid-section straight.

2.9.5. Amplifiers

Many different designs of high power amplifier exist at 500 MHz, based on both vacuum tube and LDMOS transistor technology. Figure 2-144 displays high power vacuum tubes currently on the market [13], showing that a 500 MHz solution can be achieved with IOT or klystron designs. Klystrons have the advantage of high gain, meaning that fewer tubes and ancillary devices are needed, whereas IOTs are more efficient and operate at lower voltages, making them easier to work with.

The Diamond experience with vacuum tube amplifiers is that infrequent tube arcs are inevitable, but linking multiple IOTs with a single power supply removes any advantages of tube redundancy that multiple IOTs may have over a single klystron. If each IOT were powered by an individual power supply the initial capital costs would be higher, but the tolerance to tube faults would be a significant advantage over klystrons.
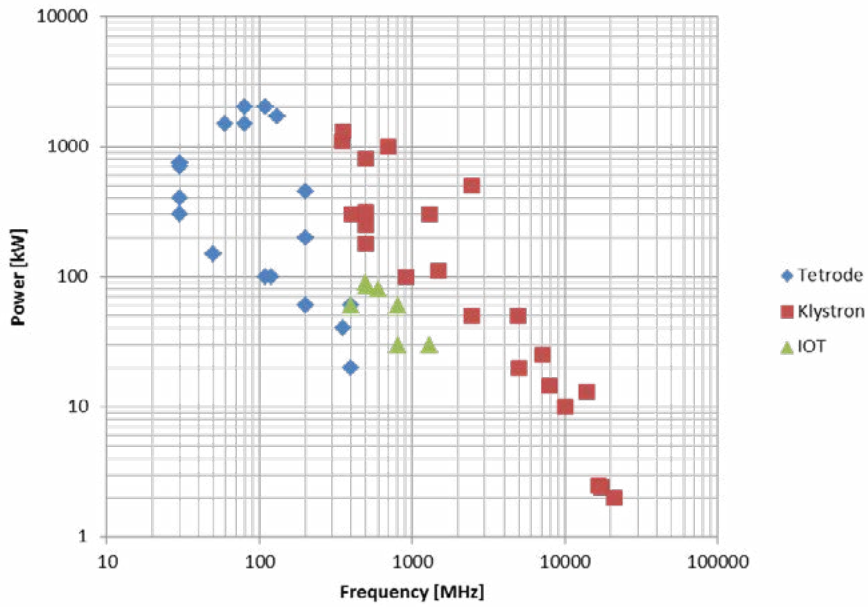
Figure 2-144 : Commercially available high power CW vacuum tubes.

Further fault redundancy can be gained by using a very large number of RF power transistors, arranged such that failure of one transistor module does not stop operation of the combined amplifier. Several high power transistors are available on the market, Figure 2-145 shows power from single chips against a nominal frequency [13]. It should be noted here that transistor bandwidth is very broad and so a choice of chips is available at 500 MHz.
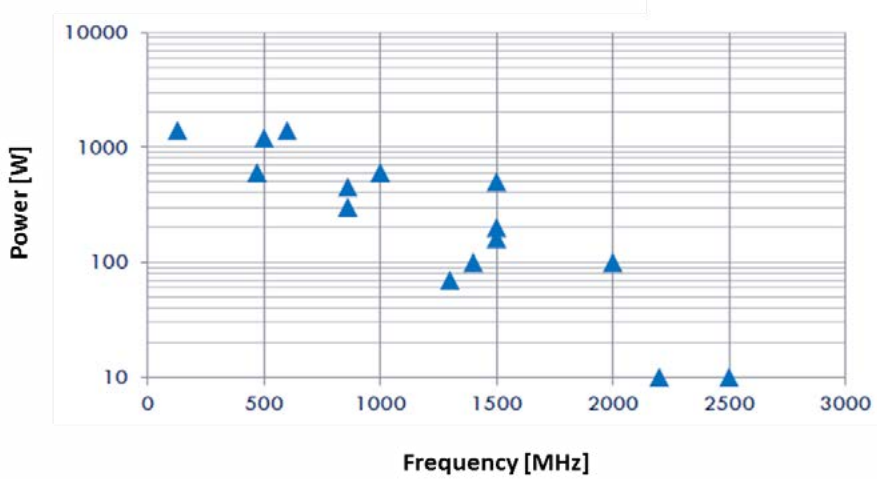
Figure 2-145 : Commercially available high power RF transistors.

Solid state amplifiers offer advantages over vacuum tube amplifiers in their extreme modularity and resulting high redundancy, and are also easier to work with, as they generally operate at tens of volts rather than the tens of kilovolts or more required for vacuum tubes. The absence of a high voltage power supply removes the risk of high voltage breakdown in the amplifier, and also means that no PWM switching circuit is required to maintain the tube voltage, resulting in a cleaner output spectrum from the solid state amplifier.

Several recent light sources have been designed to operate with solid state amplifiers, such as Soleil [14] or Sesame [15], and several other light sources have been upgraded to replace tubes with transistors, for example ESRF [16] and BESSY [17]. All report positive results.

Solid state amplifiers are available from multiple vendors, Diamond has recently installed two solid state amplifiers from Ampegon [18] operating at 80 kW and 60 kW consisting of 64 and 48 output power modules combined in a single cavity combiner. This allows a compact arrangement of modules, controls and 50 V power supplies in a single rack, shown in Figure 2-146.

Figure 2-146 : High power solid state amplifier schematic.

Each power module is identical, and includes two Ampleon BLF578 50 V LDMOS power transistors operating at a nominal power of 850 W. Each power transistor is in line with its own circulator to protect against reflected power. This design ensures redundancy of amplifiers, and continuity of operation has been demonstrated by removing a module while the amplifier is running at full power.

Redundancy arising from modularity, purity of spectrum, ease of operation and security of supply as IOT broadcast transmitters are replaced by solid state devices has led to the selection of 500 MHz solid state amplifiers based on LDMOS power transistors for Diamond-II.

EU HOM-damped cavities installed to date in Diamond have a maximum power handling rating of 120 kW cavity. This power can be supplied by two amplifiers of the design shown in Figure 2-146, which could be combined with a simple hybrid combiner. The high power level of the combined amplifiers requires transmission line to be constructed from either 9 3/16 inch coaxial line or WR1800 rectangular waveguide, both of which are available from a number of suppliers.

RF amplifier and cavity control has been maintained in Diamond by analogue LLRF loops, but increasingly in recent years digital LLRF control has been adopted by particle accelerator laboratories [19][20]. The use of a digital LLRF control system rather than an analogue system offers the great advantage of being flexible and reconfigurable solely via software, allowing the LLRF to be updated as demands change [21]. A digital system can also be constructed with built-in diagnostics and post-mortem capabilities in order to rapidly diagnose faults and consequently reduce machine downtime. Following the adoption of the MicroTCA standard for LLRF at XFEL [22], a community of accelerators using this technology has rapidly grown [23], and Diamond has recently incorporated a digital system based on that developed at Alba and in also used at Max IV [24]. This design of digital LLRF is suitable for use in Diamond-II.

2.9.6. Higher Harmonic Cavity

Higher harmonic cavities are necessary in Diamond-II to minimise storage ring component heating, alleviate collective instabilities and maximise beam lifetime [25]. Harmonic cavities have been used in many synchrotron light sources [26] [27][28][29] and are well understood; one or more cavities are introduced to the storage ring near the nth harmonic of the fundamental RF frequency to flatten the profile around the synchronous phase and stretch the individual bunches. The optimal flat potential case may be achieved if the first and second derivatives of the RF waveform are set to zero with the relative voltage and phase of the higher harmonic cavity, k_{fp} and φ_{hfp} given by [30] [31]:

$$k_{fp} = \sqrt{\frac{1}{n^2} - \frac{1}{n^2 - 1}\left(\frac{U}{e_0 V_{rf}}\right)^2}$$

$$\tan\left(n\phi_{hfp}\right) = -\frac{\dfrac{nU}{e_0 V_{rf}}}{\sqrt{\left(n^2 - 1\right)^2 - \left(n^2 \dfrac{U}{e_0 V_{rf}}\right)^2}}$$

where V_{rf} is the amplitude of the fundamental RF frequency.

Many designs of higher harmonic cavity are in operation, powered or passive, normal conducting or superconducting; examples from six laboratories are presented in Table 2-61.

Table 2-61 : Examples of higher harmonic RF cavities.

Cavity Parameters	NSLS II	BESSY II	ELETTRA/SLS	Max IV	APS-U
Superconducting or normal conducting	SC	NC	SC	NC	SC
Active or passive	passive	passive	passive	passive	passive
Cells	2	4 x 1 cell	2	3 x 1 cell	1
Frequency	1.5 GHz	1.5 GHz	1.5 GHz	300 MHz	1.4 GHz
Typical voltage	860 kV	400 kV	600 kV	170 kV	900 kV

All superconducting higher harmonic cavities to date operate in the passive mode, although coupling ports are available in the structures and so they can in principle be used in the active mode. An active normal conducting cavity was also used at the NSLS VUV ring [32].

A suitable cavity for Diamond-II would be a third harmonic cavity at 1.5 GHz. A full comparison of advantages and disadvantages of the different types is needed before final selection is made, but some fundamental points of the types so far used may be summarised in Table 2-62 [32]

Table 2-62 : Comparison of different higher harmonic cavity designs.

	Passive normal conducting	**Active normal conducting**	**Passive superconducting**
Advantages	Simple	Allows operation at optimal voltage and phase for any beam current	Passive operation down to low currents Less sensitive to gaps in filling pattern Less sensitive to Robinson instability as bandwidth is small and detune is close to 90°
Disadvantages	Optimal operation only at one beam current Gap in fill pattern induces strong voltage and phase modulation which reduces effectiveness Operation well into the Robinson unstable slope	RF amplifier required Gap in fill pattern induces strong voltage and phase modulation which reduces effectiveness Operation well into the Robinson unstable slope	Cryogenic system required Narrow bandwidth means cavity is harder to control

If a normal conducting RF system is used for the fundamental cavities in Diamond-II, then the existing cryogenic plant may be used for a passive superconducting higher harmonic cavity. Both the NSLS II design and CEA "Super-3HC" design (used at ELETTRA and SLS) are suitable and so the effects of a higher harmonic cavity can be demonstrated using the parameters of one of these cavities, in this case the Super-3HC cavity.

Instantaneous bunch current I as a function of time t can be calculated from the RF profile using an iteratively derived bunch form factor F_c. For an RF field generated by the fundamental cavity alone, I is shown in Figure 2-147. In this case, peak current is 28 A, assuming a full fill in the storage ring. Phase and voltage are distorted somewhat by transient fields arising from gaps in the fill pattern, but this effect is much less for a superconducting higher harmonic cavity than for a normal conducting cavity, as noted in Table 2-62.
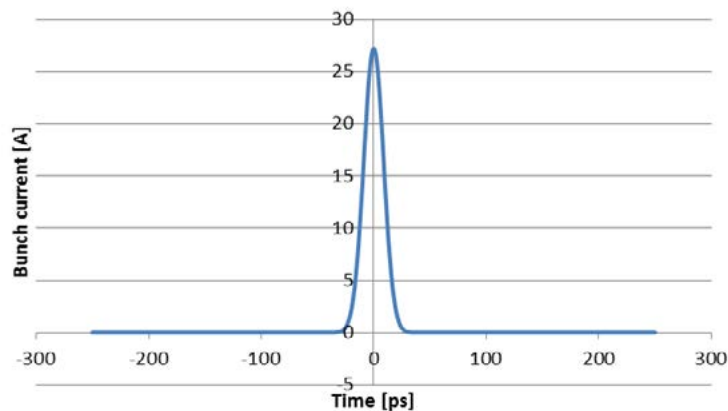
Figure 2-147 : Instantaneous bunch current for 300 mA operation at 500 MHz.

Addition of a third harmonic cavity with an amplitude and phase equal to the flat potential case above can be used to reduce this instantaneous peak current and to stretch the bunch. With a passive cavity, amplitude and phase can be controlled by detuning the resonant frequency of the cavity. With a Super-3HC cavity and Diamond-II operating conditions, a detune of 48.5 kHz satisfies the flat potential conditions and gives the field shown in Figure 2-148.
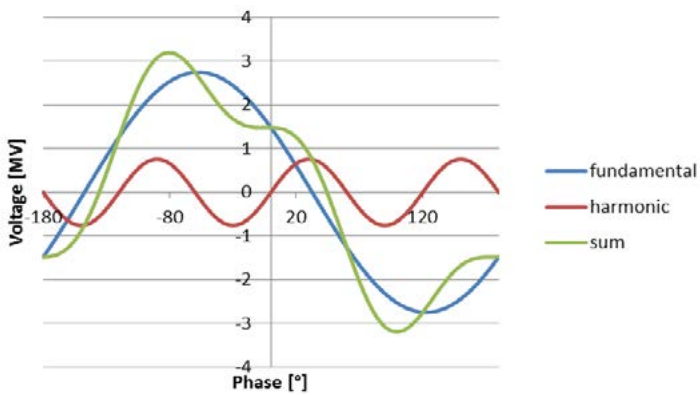
Figure 2-148 : Fundamental, higher harmonic and summed RF for a Super-3HC cavity detune of 48 kHz.

The bunch profile is then effectively flattened, as seen in Figure 2-149.
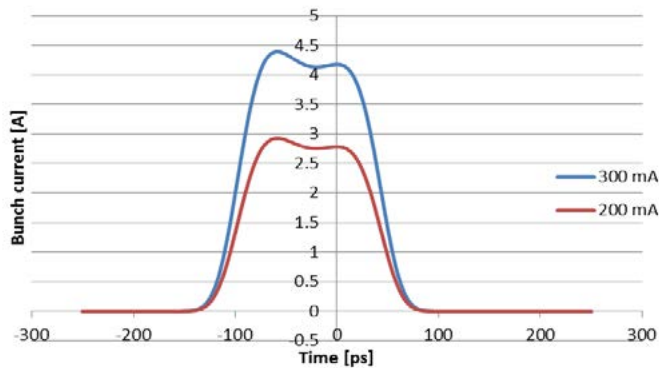
Figure 2-149 : Bunch profile for a Super-3HC cavity detune of 48 kHz at 300 mA and 32 kHz at 200 mA.

Similar analysis shows that the bunch profile can be effectively flattened with a passive superconducting cavity at much lower currents than possible with a normal conducting cavity, for example a detune of 32 kHz is sufficient to flatten a bunch in a storage ring uniformly filled to 200 mA. This bunch shape is also shown in Figure 2-149 This flexibility of operation, together with the availability of cryogenic infrastructure from Diamond, leads to the selection of a superconducting passive third harmonic cavity for Diamond-II. The third harmonic cavity can be located in a mid-section straight in the vicinity of the cryogenic plant.

2.9.7. Summary of the Design

There is no clear advantage to moving away from the Diamond frequency of 500 MHz and so the Diamond-II RF system will operate at this frequency, with a precise value of 499.499 MHz determined by the lattice and the storage ring harmonic number. The continued use of EU HOM-damped normal conducting cavities recently introduced in Diamond will ensure machine continuity and rapid repair, and eight cavities will be used to reduce cavity voltage and power for reliable long-term operation. Solid state amplifiers with redundant power amplifier modules will be used to guarantee fault tolerance, and a digital LLRF system will allow modification and improvement of control loops as required. A passive superconducting third harmonic cavity will be used, supported by the Diamond cryogenic plant.

References

[1] M. Abo-Bakr, E. Weihreter, G. Wustefeld, EPAC 2000, Vienna.

[2] P. Schmuser, Superconductivity in High Energy Particle Accelerators, Prog. Part. Nucl. Phys. 49 (2002) issue 1.

[3] F. Marhauser and E. Weihreter, EPAC 2004, Lucerne.

[4] F. Perez et al., EPAC 2006, Edinburgh.

[5] J. Ocampo, ESLS-RF 2017, Krakow.

[6] Y. Morita, IPAC 2010, Kyoto.

[7] C-H. Lo et al., SRF 2014, Paris.

[8] A. Fabris et al., EPAC 1998, Stockholm.

[9] M. Bocciai et al., EPAC 1998, Stockholm.

[10] A. F. D. Morgan et al., IPAC 2017, Copenhagen.

[11] T. Schilcher, PhD thesis, University of Hamburg, March 1998.

[12] A. Salom et al., IPAC 2017, Copenhagen.

[13] E. Montesinos, LLRF 2017, Barcelona.

[14] P. Marchand et al., IPAC 2011, San Sebastian.

[15] D. Foudeh et al., IPAC 2017, Copenhagen.

[16] J. Jacob et al., IPAC 2011 San Sebastian.

[17] W. Anders et al., IPAC 2017, Copenhagen.

[18] B. Fritsche, CWRF 2018, Hsinchu.

[19] S. Simrock, Linac 2004, Luebeck.

[20] D. Teytelman, PAC 2003, Portland.

[21] M. E. Angoletta, EPAC 2006, Edinburgh.

[22] J. Branlard, MIXDES 2013, Gdynia.

[23] T. Walter, ICALEPCS 2017, Barcelona.

[24] A. Salom et al, IPAC 2017, Copenhagen.

[25] A. Hofmann and S. Myers, CERN-ISR-TH-RF/80-26, 1980.

[26] R. Biscardi, S. L. Kramer, and G. Ramirez, NIM. A 366, 26 (1995).

[27] M. Georgsson, Å. Andersson, and M. Eriksson, Nucl. Instrum. Methods Phys. Res., Sect. A 416, 465 (1998).

[28] G. Penco and M. Svandrlik, Phys. Rev. ST Accel. Beams 9, 044401 (2006).

[29] M. Pedrozzi et al, LINAC 2004, Luebeck.

[30] J. M. Byrd and M. Georgsson, Phys. Rev. STAccel. Beams 4, 030701 (2001).

[31] P. F. Tavares et al, Phys. Rev. ST Accel. Beams 17, 064401 (2014).

[32] R. Onken, ESLS-RF 2018, Paris.

2.10. Storage Ring Power Supplies

The new Diamond II storage ring lattice requires a substantial increase in the number of power supplies compared to the existing lattice (from 962 to 1476). This challenges the power supply specification on two fronts:

- Reliability, as the overall power supply systems should be the cause of no more than five machine trips per year.
- Space, as the power supplies are located in control/instrumentation areas (CIAs), additional rack space is limited and extending the CIAs is challenging due to physical constraints in the technical services area.

2.10.1. Storage Ring

2.10.1.1. Typical Requirements for One Sector

The storage ring is divided into 24 sectors, each with a set of power supplies that are replicated on the six-fold symmetry. The number of power supplies per cell is outlined in Table 2-63.

Table 2-63 : Number of power supplies per cell.

Magnet type	No. per CIA†	Power Supply type
Transverse gradient dipoles (DQ)	2	1Q 200A, 20V
Transverse gradient dipole trim	2	1Q 50A, 20V
Quadrupoles	16(17)	1Q 200A, 20V
Sextupoles	10	1Q 50A, 5V
Octupoles	2	1Q 5A, 25V
H/V correctors	20(22)	4Q 5A, 20V
Skew quad	6	4Q 5A, 20V

† - numbers in brackets refer to long straights.

2.10.1.2. Key Elements for Magnet Power Supplies

Diamond already implements discrete control for each quadrupole and sextupole power supply, so architectural changes to the power supply system are not required. All existing power supplies use a standardised digital power supply controller integrated with 'standard' power modules. This design philosophy will be carried forward for Diamond-II.

To achieve the required reliability, n+1 redundant designs will be used, as in Diamond. This applies to control power or housekeeping power supplies, bulk DC power and in the output power converters. This technique is a proven method used in industry for high availability systems (e.g. telecoms and data centres). For single quadrant applications rated between 25A and 200A, Diamond has a proven 1Q 50A power module design, which can be paralleled up to provide n+1 capability. These will be used on the DQ, quadrupole and sextupole magnet power supplies.

2.10.1.3. Transverse Gradient Dipoles (DQ)

The re-use of the existing single dipole power supply was investigated, but the complexity of being able to trim the dipole and quadrupole fields increased the number of power supplies required per device, so reducing the overall system reliability. As a result, each DQ magnet will be supplied by two power supplies which allows for discrete control of the dipole and quadrupole field components. The main DQ magnet coil will be powered by a single unipolar 200 A power supply.

2.10.1.4. Transverse Gradient Dipole Trim

For the transverse gradient dipole trim magnets, a 50 A unipolar power supply is required. These power supplies shall use the same DC link as used for the main DQ winding. The power supplies will use the standard 50 A modules as detailed above. To allow full flexibility of the dipole trim magnet function, polarity reversal switches will be added to the output of the power supplies. Both the main and trim dipole magnet power supplies will be located within the same rack cabinet.

2.10.1.5. Quadrupole Power Supplies

The existing quadrupole (10 channels) and sextupole (7 channels) power supply will be upgraded and modified to exclusively power the 17 quadrupoles for the new lattice. The original 50 A power modules for the quadrupole power supplies were designed for a 30 year life span. These have proven to be extremely reliable. So, pending a review of the modules for any possible aging effects, they will be refurbished and reused. Where additional power modules will be needed, these will be of the newer Diamond designed 50 A power module.

The changes that will be required are:

- Upgrade of the DC link supplies from two transformer rectifiers to an n+1 redundant telecoms rectifier. This will save at least one rack position in the CIAs and reduce the coupling of mains borne disturbances onto the magnet current.
- The existing sextupole power supplies will be removed from the suite of cabinets to allow for the additional seven 200 A quadrupole power supplies.

2.10.1.6. Sextupole Power Supplies

For the 10 sextupole power supplies two new rack cabinets will be required. The DC link will be derived from a commercial off-the-shelf n+1 low voltage power supply. The DC link will be used to supply the Diamond designed 50 A power module in an n+1 configuration. These shall be contained within the cabinets.

2.10.1.7. Octupole and Skew Quadrupole Power Supplies

For the octupole and skew quadrupole power supplies, the proven 4Q 5 A, 20 V power supply will be reused. All the power supplies for the octupoles and skew quadrupoles will be assembled into one rack cabinet.

2.10.1.8. Horizontal and Vertical Correctors

The fast orbit feedback system in Diamond-II demands reduced latency and increased bandwidth compared to the existing system. The existing corrector power supply has been optimised to its design limits to a point where no further gains can be made. The power supply is quite large at 3U, 28HP. As over 500 corrector power supplies will be required for Diamond-II, a new design with the following criteria is required:

- Form factor: 9U MicroTCA crate, each corrector occupying 1-2 mid-size AMC/RTM* slot.
- Small signal bandwidth of 3 kHz, ±1 mA.
- ±20 V, ±5 A power from RTM*.
- Between 12 - 16 power supplies per MicroTCA crate, based on two channels per card.

AMC – Advanced Mezzanine Card / RTM – Rear Transition Module

The corrector power supplies will not use a the same digital controller as the DC power supplies, nor will it have the same high stability of the DC supplies, as the power supplies will be continuously adjusted by the orbit feedback system.

2.10.2. Insertion Device Power Supplies

2.10.2.1. Trim Power Supplies

Each insertion device requires vertical and horizontal trim power supplies. Insertion devices installed in standard or long straights will reuse the existing trim power supplies. For the additional mid-straight insertion devices, new trim power supplies will be installed. These extra power supplies will be the same type as used on existing Diamond insertion device trim magnets.

2.10.2.2. Chicane Power Supplies

Where the insertion device is canted with respect to the nominal beam path, three bump chicane magnets are added. There are currently two types of power supply, depending on the rating of the chicane magnets, a high current version 100 A, 30 V or a low current version 5 A, 20 V. The high current version uses the same power supply architecture as the sextupole power supplies, while the 5A version is the same as the ID trim power supplies.

2.10.2.13. Superconducting Wigglers

Both the I12 and I15 superconducting wigglers will keep their existing power supplies.

2.10.2.4. Physical Space Requirements

Estimates for the space required for the power supplies are detailed in Table 2-64. This confirms that the additional power supplies can be accommodated within the existing limits of the control and instrumentation areas.

Table 2-64 : Space requirements for the storage ring power supplies.

Magnet	Magnets	Power Supplies	No per CIA	Per sub-rack	Sub racks	Racks
DQ Magnet Main	48	48	4	1	4	0.75
DQ Trim	48	48	4	2	1	0.25
Quadrupoles	396	396	17	1	17	5
Sextupoles	288	288	10	2	5	2
Octupoles	48	48	2	2	1	0.5
Correctors	252	504	22	12	2	1
Skew quad	144	144	6	3	2	0.5
Totals	1224	1476	61	15	33	10

2.10.3. General Performance Criteria

The general performance of the power supplies is shown in Table 2-65. As the corrector power supplies are within the fast orbit feedback system, the stability and precision has been relaxed.

Table 2-65 : General performance criteria of the storage ring power supplies.

Magnet Type	Bandwidth Hz	Max Current Ripple/noise	Stability 100s - 8h	Stability 8h – 6m	Absolute Precision	Resolution
Dipoles (DQ)	DC	±10 ppm ‡	±10 ppm	±50 ppm	±50 ppm	3.81 ppm
Quadrupoles	DC	±10 ppm ‡	±10 ppm	±50 ppm	±50 ppm	3.81 ppm
Sextupoles	DC	±10 ppm ‡	±10 ppm	±50 ppm	±50 ppm	3.81 ppm
Octupoles	DC	±10 ppm ‡	±10 ppm	±50 ppm	±50 ppm	3.81 ppm
Correctors	7 kHz	±10 ppm ‡	±1000 ppm	±1000 ppm	±1000 ppm	3.81 ppm
Skew quad & ID Trim	DC	±10 ppm ‡	±10 ppm	±50 ppm	±50 ppm	3.81 ppm

‡ - For Sextupole and corrector power supplies maximum current ripple shall be maintained over a bandwidth of 50 kHz. For other power supplies, 1 kHz will suffice.

2.10.4. Power Supply Controller

The power supply controller currently used on Diamond's power supplies was originally sourced from the Paul Scherrer Institute (PSI). With its standardised interface, diagnostics and software development kit, it has brought many advantages. This strategy also relieved the power supply manufacturers of the risk and burden of supplying a control system that matched Diamond's specification. However, the PSI design and the associated software support tools are now obsolete, and so a replacement digital power supply controller is currently in development. The performance of this new power supply control system in terms of pulse width modulator resolution and ADC performance is expected to be an improvement on the existing PSI controller. This control system will be used on all DC power supplies for Diamond-II. Each controller is equipped with a Toradex Colibri Computer module, which provides the Epics server for device. The interface to the control system shall be via a standard Ethernet over UTP.

2.11. Electrical Engineering

2.11.1. Cabling and Connector Strategy

Storage Ring

There are several options for cabling in Diamond-II. Initially, it was thought that the Front End (FE) and Insertion Device (ID) cables would be left in-situ, while all other cables would be removed. This has the benefit of saving time at the end of the cabling scheme, as the FE and ID cables would not need re-terminating. However, given that some FE components may not stay in the same place, some of the existing cables may not be long enough. Even if cables are long enough, the time taken to identify and separate circuits would easily negate any time saving. Additionally, there is a danger that cables will be damaged as they rub against objects and each other during extraction; Figure 2-150 shows typical cable routing/grouping. Taking these and several other factors into consideration, the current thinking is that all cables should be removed from the tunnel.

Removing all cables from the vault has the following advantages:

- Improved safety by being able to give clear instructions to contract staff in the removal of circuits.

- Having the tunnel clear of all cables will make other works easier – especially if FE components have to be changed or moved.

- Radiation damage to cables does occur over time; some of the cables have been in the tunnel for 15 years, so replacement would be the safe option.

Figure 2-150 : Storage Ring CIA showing underfloor cable containment.

The PSS system was to remain unchanged but this is under review: a safety PLC based system with 2/3 voting could be the preferred solution. This may necessitate a distributed I/O system - leading to changes in wiring methods. While the PSS cable system has its own containment and the search routes could stay the same, the change in technology (and components used) could mean significant wiring changes – especially in the vault. Therefore, the removal of the PSS wiring is currently assumed.

A further assumption was that the 4-tier containment would remain in the vault; it is a robust and proven solution (see Figure 2-151). However, given the changes to the layout of the girders, it is very unlikely that the various entry/exit junctions would be in the correct place and would require some major rework. Over the course of some 10 years of operations, it has been determined that there would be a real benefit in having a cable containment system which could also be used as a walkway or access platform. This will be looked at in more detail during the design of the cable containment system.

Figure 2-151 : Storage Ring Vault showing current cable containment.

Booster

Before we go in to the 'dark period', the new booster synchrotron will be partly installed. This work will be done during shutdown periods and the new booster will be constructed while the original is in-situ and operational. This upgrade will of course require new cables, cable containment and new racks - as well as at least one new CIA. The new booster will sit on the centre line of the vault; the current containment system is on the inside of the booster ring (see Figure 2-152) which lends itself to easy access to components. The containment for the new booster could also be on the inside, but a firm decision has not yet been taken.

Figure 2-152 : Booster Vault showing the cable containment inboard of the booster ring.

An investigation is underway, to determine the spare capacity of the existing cable ducts between the CIAs and the booster vault. If that capacity is not sufficient, new ducts will be required. This could be a necessity anyway due to the position of the current duct apertures in the booster vault (being on the inside of the booster ring.

The connector strategy for both the storage ring and booster synchrotron is straight forward; we will continue to use connectors which adhere to EMC standards (metal bodied and which will allow the 360° termination of a screen). A large percentage of Diamond's cables are terminated using UTO and D-Type connectors; these have proven robust and easy to terminate in the field. The pins for these connectors should be of the machined and crimped type. Most, if not all of the technical teams at Diamond are set up with the correct tooling to use these types and are happy to continue doing so.

Soldered connections are acceptable if the equipment comes with a particular type (Lemo for example), or if a very small cable/wire is required (although this generally tends to be the case with beamline end-stations rather than the accelerators).

2.11.2. Racks and CIAs

Storage Ring

There are generally between 11-15 racks per cell in the storage ring - not including power supplies (which will account for nine racks per CIA.). There is an argument that while it may be possible to reuse the racks as fitted, terminals and wiring would need replacing. It is perfectly reasonable to assume that these deteriorate with operational time.

The level of work required to refit the racks will also depend on the technology used within it. Each department will make the decision of what technology they will use (e.g. Vacuum group could be using later versions of gauge/pump controllers). Certainly, the use of distributed I/O could mean less wiring in any rack.

To maximise the use of space in the CIAs, some of the racks will be consolidated. In recent years, some of the FE and ID racks were converted from two racks into one. In fact, with some of the Beamlines swapping from a bending magnet to an ID, there is a necessity to consolidate the racks where possible. Figure 2-153 shows a comparison of the current CIA for cell 4 with what it will probably be for Diamond-II. Consolidation does make the racks harder to work on both in construction and for future modification (generally due to lack of space); the design of these racks will have to address this issue.

It is clear we cannot refit all of these during the dark period. We therefore anticipate the use of external contactors, who will build up the racks to our specifications. This is a necessary expense due to the time constraints; however, not all racks in the CIA will need to be refitted – or indeed refitted during the dark period. As an example, the Network rack generally has no internal wiring; all cables are field cables, so this could be modified as necessary in–situ. Initially, we should budget for 20-30% of the racks to be refitted in-house, either before or during the dark period.

Booster

The new booster will be built while the existing one is operational, so currently there is not enough room in the existing CIAs to house the racks for the new booster. Initial thoughts pointed towards having four new CIAs constructed. Once the new booster is up and running, the old booster could be removed and the original CIAs used for storage. A more recent idea is that the existing CIAs could be utilised where possible; some racks are not entirely populated and there are spare rack positions in booster CIAs (see Figure 2-154). If required, a further CIA could be constructed in what is currently the Vacuum storage area. An investigation is underway to determine exactly how many new racks can be accommodated in each CIA and if any systems can be consolidated into fewer racks.
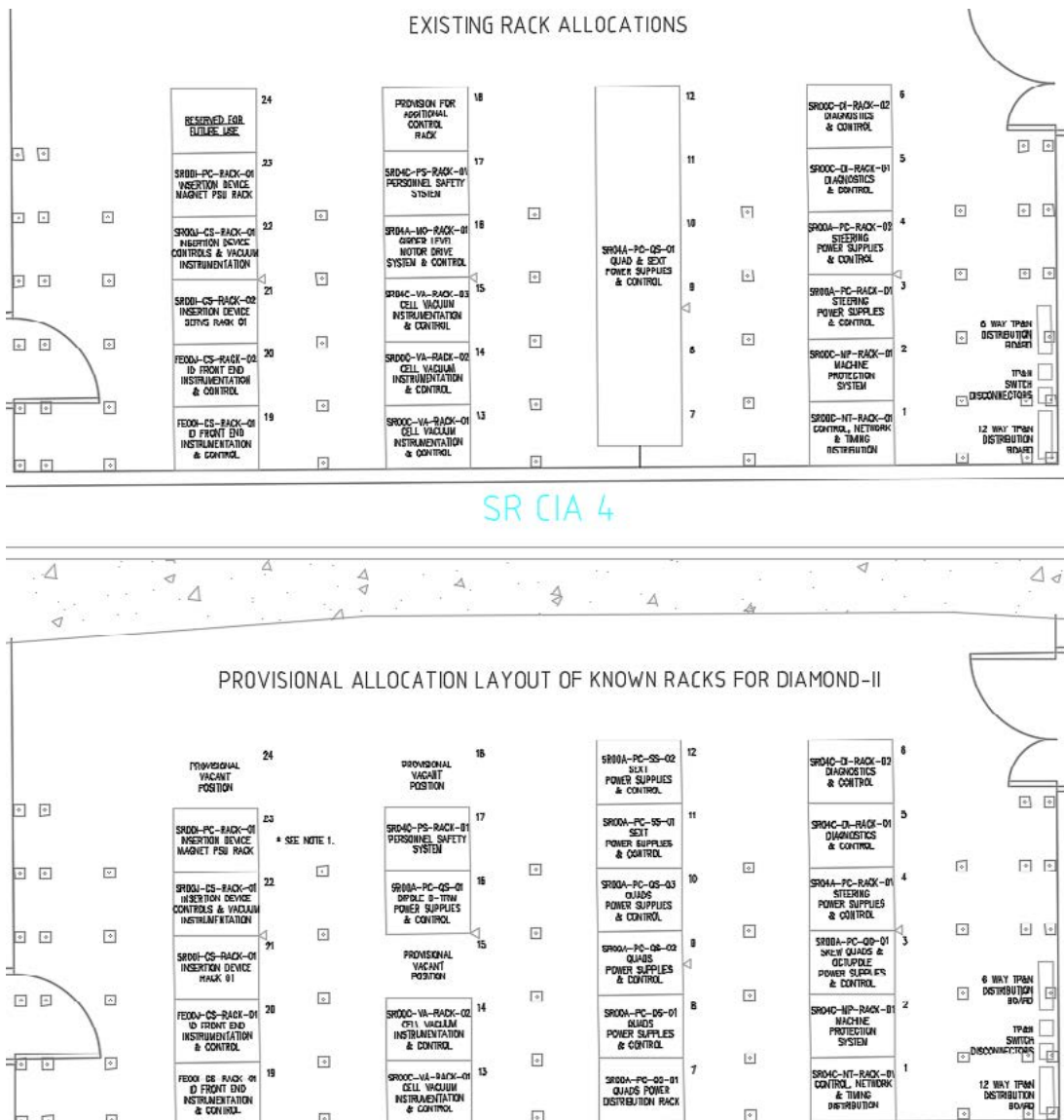
Figure 2-153 : SR CIA 4 rack allocation comparing Diamond and Diamond-II.

Figure 2-154 : Booster CIAs 1 & 2 showing spare rack positions.

2.12. Controls & Interlocks

2.12.1. Introduction

The Diamond control systems were built with equipment purchased from 2004 to 2007. There are known reliability issues that are a function of age. Assuming Diamond-II will be commissioned around 2026 it means any equipment carried over to Diamond-II will be around 20 years old. If we retain existing equipment for the life of Diamond-II operation we will be reliant on 35 year old equipment. This does not seem wise and we will therefore look to upgrade the majority of the controls systems.

There are major functional areas that the control systems support. Some of these are the support of technical sub-systems providing a customer style relationship. There are others where we provide a critical sub-system in its own right. The controls group is also responsible for the overarching tools that provide interfaces to operations, including EPICS interfaces, data browsers, archiving, file-systems, software tools and middle-layer software.

2.12.2. Overall Approach

We will continue to use EPICS as our SCADA system. EPICS V3 is our current version. We will consider a move to EPICS V7 during the TDR.

We will retain the use of the Primary network for SCADA control and a Secondary network for distributed instrumentation. We will add a further independent network for the programming of Safety and machine protection PLC devices.

The Diamond-II lattice has a significantly increased requirement for power supplies (see Section 2.10). In order to accommodate the extra racks in the existing Control and Instrumentation Area (CIA) rooms without expanding them, we will make use of recent developments in control system components to reduce the number of racks taken by Front End and Insertion Device control systems where practical.

Primary control systems are to be based around two technologies, Ethercat interfaces for lower performance requirements and μTCA for high performance requirements. Motion control systems will be based around the Delta Tau Brick controller or equivalent. Where practical VME systems will be phased out as the use of newer technologies will provide the same or better performance in a smaller form factor and reduced power consumption. This will allow us to manage the age of the installed equipment and also reduce the number of racks required.

Ethercat based Linux PCs will be used as the EPICS IOC Server in most cases. Where necessary serial communications will be interfaced using a local terminal server. EPICS IOCs will be primarily implemented as 'softIOCs' running on Ethercat Linux PCs or on other rack-mounted PCs. As a part of the TDR we will consider where we might want to place processing nodes and also consider the applicability of running EPICs IOCs on virtualised machines.

All distributed Ethernet devices will be interfaced by an EPICS softIOC and managed on an instrumentation network isolating the components from the global network.

During the TDR we will look to ensure that development is complete or largely complete before the commencement of the Diamond-II installation shutdown (the dark-period). This will include the updating of systems during the years leading up to the shutdown.

We also plan to complete a user interface review and a system reliability review as a part of the TDR.

2.12.3. Personnel Safety Systems

The personnel safety systems will be updated to a PLC based system, which may be a two-out-of-three system depending upon further research. This would be a significant development and deployment project and will be explored further in the TDR.

2.12.4. Machine Protection Systems

The slow protection system will be implemented in a PLC using remote I/O to support the distributed nature of the controls racks in the CIA and remote I/O will be deployed in the ring for the acquisition of non-critical signals.

The fast protection system will be based on an FPGA design that is the subject of a current design and development project.

2.12.5. Diagnostics Systems

The following components will be interfaced via a Beckhoff Ethercat based system or via direct Ethernet interfaces connected to a local instrumentation network:

- Beam-loss monitors.
- BPM Length encoders.
- Beam current monitor.
- Ethernet cameras.
- General low-bandwidth signal monitoring (temperatures, analogue & digital signals)

Collimators will be controlled via Delta-Tau Geobrick motion controllers.

Beam Position Monitor (BPM) electronics are based on an analogue front-end with an FPGA based system. There will be a development project in conjunction with the Diagnostics Group to develop the signal processing FPGA software, as described in more detail in Section 2.7.3.

2.12.6. Vacuum

The vacuum systems for Diamond-II will be significantly different to the current configuration. To manage this we plan to build new racks to support the new booster systems and the new storage ring. We plan to base the design on the proven technologies used in the storage ring DDBA upgrade.

We plan to integrate PLC protection systems across a number of sub-systems within the CIA to reduce cabling and to improve reliability.

The computing components will provide an interface to all gauge controllers and pump controllers, to the PLC and to the Ethercat I/O components. We will ensure that all instrumentation is connected to a local network, isolating it from the main networking infrastructure.

The in-situ bake-out equipment will consist of a PLC performing warm-up and cool-down processes and monitor for over-heating and temperature imbalances. This system design will be based on the proven system used for the storage ring DDBA upgrade.

2.12.7. Power Supplies

The power supply systems for Diamond-II will be significantly different to the current configuration. To manage this we plan to build new racks to support the new booster systems and the new storage ring. The new Diamond Power Supply Controller will be used in the booster and the storage ring.

A new booster machine will be built and will require a standard set of interfaces to be available. The Diamond Power Supply Controller will be used as a single standard interface and control device for all power supply/magnet types.

The Diamond-II Fast Orbit Feedback (FOFB) system is discussed below and in Sections 2.7 and 2.10. However, it is recognised that a separate µTCA based power supply controller and inverter module will be developed.

A common EPICS interface will be developed to support both types of power supply controller.

Pulsed power supplies will be operated using the Diamond Power Supply Controller and the standard computing infrastructure will apply. See Section 2.10 for further details.

2.12.8. Insertion Devices

The insertion device development program for Diamond-II is as follows:

- Undertake a motion control system development program.
- Support the design, build and development of upgraded and new insertion devices.

As discussed earlier, there are a number of factors that influence the design of the insertion device control system including the age of installed equipment, the use of more modern control components and the pressures on space in the Control and Instrumentation Areas (CIAs). This is a sensible opportunity to consider the next generation of control systems for insertion devices.

The system will be based on an Ethercat PC running the EPICS IOC and communicating over a local instrumentation network to the motion controller and other local devices.

2.12.9. Front Ends

The Front-End (FE) development program for Diamond-II is as follows:

- Undertake an electromechanical and control system review program.
- Support the move and recommissioning of beamline FEs for Diamond-II.
- Support the design, build and development of bending magnet beamlines conversion to insertion devices beamlines.

The system will be based on an Ethercat PC running the EPICS IOC and communicating over a local instrumentation network to the motion controller and other local devices.

2.12.10. Girder Alignment System

The requirements for the motion system are defined in Section 2.6.1.4 This outlines usage and motion requirements in terms of range of motion, resolution, accuracy and repeatability. From experience it is clear that we need a system that is mechanically constrained so that it cannot damage the components on or around it (the bellows, for instance).

We will install additional instrumentation permanently on each girder to give an accurate measurement of girder position that is archived via EPICs:

- Permanent pitch and roll inclinometers.
- A method of measuring the absolute position of the girder referenced with absolute linear sensors to ground.
- Vibration analysis sensing.

We will build a purely mechanical alignment system. We will investigate the option that the design could be upgraded to full automation should the need arise. This will be done during the TDR. Any automated system should not significantly impact on the immunity to vibration. Any subsequent development of a control system will be based on an Ethercat PC running the EPICS IOC and communicating over a local instrumentation network to the motion controller and other local devices.

2.12.11. Radio Frequency

As described in Section 2.9, all cavities will be driven by Solid State Amplifiers and controlled via Digital LLRF systems. There will also be requirements for Vacuum, MPS and PSS interfaces. Further interfaces to ancillary systems will be required. Control systems to support these devices will be developed.

Other controls requirements will be met by the development of a control system will be based on an Ethercat PC running the EPICS IOC and communicating over a local instrumentation network to the motion controller and other local devices.

2.12.12. Fast Orbit Feedback

A new μTCA based Fast Orbit Feed-Back (FOFB) power supply architecture will be developed to give a high level of integration between the beam position measurement systems (BPMs and associated front-end electronics) and the corrector power supplies. There will be a centralised FOFB computation node that will calculate the corrections for each

corrector. The corrections will be distributed via a fibre communication network. It may be possible to re-use the existing fibres; otherwise new fibres will need to be installed.

Low latency signal processing will be required. We will provide a fast archiver mechanism.

It is recommended that the FOFB system will be tested on the existing booster and will then be available to be deployed in the storage ring. This will be considered further in the TDR.

FOFB is discussed further in Sections 2.7 and 2.10.

2.12.13. High level Applications

The Diamond High Level Applications provide the following:
- software tools to support the use of EPICS
- databases to support machine operation and configuration management
- a number of machine related operational tools
- low frequency feed forward / feedback controllers.

A review of the High Level Applications suite of tools will commence as a part of the TDR.

2.12.14. Timing

The Harmonic Number for Diamond-II is 934. Unfortunately there are only two factors of 934, namely 2 and 467. This leads us to the conclusion that we need to develop an updated timing system.

Any changes to the timing system will have an impact across the machine and the beamlines. We need to ensure that the system we develop will support operation of beamline systems and components.

There is a technical risk with this approach that we will need to evaluate during the TDR and attempt to minimise.

The system can be considered as consisting of an Event Generator (EVG) and multiple Event Receivers (EVRs). We would plan to design the units as being able to fulfil both roles. There is an interface to some specialist timing electronic systems that the EVG will need to interface to.

We would plan to rely on NTP time distribution to support EPICS timing across the accelerators and beamline systems. EVRs would only be deployed where it is necessary to provide highly accurate timing signals.

2.12.15. Computing Infrastructure

The current computing and networking infrastructure is considered adequate to support Diamond-II. However there will inevitably be some component updates as the lifetime of Servers is of the order of 5 years and for network switches it is 10 years. We will also add a third isolated network that is dedicated to support the access and programming of Personnel Safety and Machine Protection PLCs.

2.12.16. Building Management System Interface

The Diamond Facilities BMS are currently interfaced to the EPICS SCADA system via a number of servers implementing a BACnet gateway between the two domains. This system works well, however we plan to implement a larger number of servers to segregate the interfaces to a finer degree. This is to improve our ability to manage the impact of changes to the gateways as they arise. We plan to complete the improvements to the BMS interfaces ahead of the Diamond-II installation shutdown.

2.13. New Booster Synchrotron

2.13.1. Introduction

As detailed in Section 2.3.5, maintaining high injection efficiency into the Diamond-II storage ring will require a reduction in both the emittance and pulse length of the electron bunches extracted from the injector. A lower emittance and careful optics matching will ensure the fresh electron bunches can be brought within the smaller dynamic aperture of the new ring, and shorter bunch lengths minimise the energy deviations experienced by particles at the head and tail of the bunches during synchrotron oscillations, leading to higher injection efficiency.

The optimal way of achieving the required level of emittance reduction is to replace the existing booster synchrotron with a new, low emittance design. By doing so, the increase in extracted beam energy from 3 GeV to 3.5 GeV can also be taken into account from the beginning of the design process. The main features of the new booster lattice are described in the following sections, alongside a summary of the predicted performance and an outline of the installation and commissioning strategy.

2.13.2. Booster Lattice

Similar to the existing ring, the new booster synchrotron will have a racetrack structure consisting of two arc sections and two long straights. Each arc section is built from 14 identical unit cells, with each unit cell containing one dipole, two families of quadrupoles and two families of sextupoles. A systematic study investigating all aspects of the design found that this number of unit cells was optimal, achieving the necessary reduction in emittance whilst maintaining a large dynamic aperture, low energy spread, and keeping the total number of magnets low. The horizontal cell tune was selected to minimise the emittance of the ring and to keep the phase advance and beta functions within reasonable bounds. The vertical cell tune was chosen in order to minimise the natural vertical chromaticity. As part of the design process, the locations and lengths of each magnet were treated as variables to be optimised.

At the ends of each arc section are two matching cells. These cells act as dispersion suppressors, and each contain a half-length dipole and a short drift space to leave the long straights dispersion-free. At the outer edges of the matching cells are quadrupole triplets that are used to control the phase advance across the long straights. The two long straight sections will be used to house the injection and extraction elements respectively. RF cavities and diagnostic components will be distributed either in the remaining space in the long straights, or alternatively placed in the short straight sections in the four matching cells.

A comparison of the main existing and new booster parameters is given in Table 2-66 below, and a summary of the magnet requirements is given in Table 2-67. A plot showing the Twiss parameters for one super-period is shown in Figure 2-155.

Table 2-66 : Comparison of Main Parameters for the Existing and New Booster Lattices.

Parameter	Unit	Existing Booster	New Booster
Energy Range	GeV	0.1 to 3.0	0.1 to 3.5
Final Emittance	nm	134.4	13.9
Circumference	m	158.4	170.5
Betatron Tunes	-	[7.18, 4.27]	[13.17, 4.37]
Natural Chromaticity	-	[-9.7, -6.3]	[-25.7, -10.1]
Final Energy Spread	-	7.3×10^{-4}	10.5×10^{-4}
Peak Energy Loss per Turn	MeV	0.58	1.64
Mom. Compact. Factor	-	25.2×10^{-3}	2.77×10^{-3}
Natural Bunch Length	ps	99.3	41.1
Peak RF voltage	MV	0.9	2.0
RF acceptance	%	0.24	0.58
Damping Times (τ_x, τ_y, τ_s)	ms	[5.46, 5.47, 2.74]	[2.43, 2.43, 1.22]
Repetition Rate	Hz	5	5

Table 2-67 : Summary of Magnet Parameters for the Existing and New Lattices.

Unit Cell Dipole Magnets	Unit	Existing Booster	New Booster
Number	-	36	28
Length	m	2.16	1.70
Bend Radius	m	12.4	8.1
Peak Field	T	0.81	1.44
Matching Cell Dipole Magnets			
Number	-	-	4
Length	m	-	0.85
Bend Radius	m	-	8.1
Peak Field	T	-	1.44
Quadrupole Magnets			
Number	-	44	132
Length	m	0.34	0.30
Peak Gradient	T/m	14.1	26.8
Sextupole Magnets			
Number	-	28	90
Length	m	0.16	0.15
Peak Strength	T/m	40.8	282.3
Corrector Magnets (H/V)			
Number	-	22/22	34/34
Design	-	Separate function	Sextupole windings
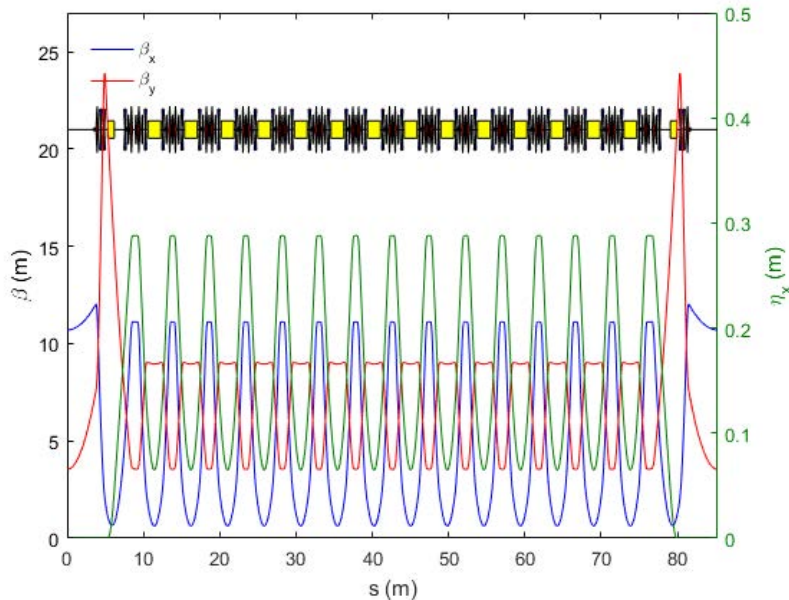
Figure 2-155 : Beta functions and dispersion for one super-period of the new booster synchrotron lattice.

2.13.3. Injection and Extraction

In order to minimise the number of shots fired into the storage ring during each top-up cycle, the option to carry out all accumulation in the booster is currently being explored. This would entail firing many consecutive shots into the booster, and only extracting beam once sufficient charge has been accumulated. As such, there would only be one top-up shot per cycle into the storage ring, greatly reducing any adverse impact from the storage ring pulsed magnets on the users' experiments. If this scheme is to be achieved, the booster injection scheme must be off-axis, and the available dynamic and physical aperture must be sufficiently large to accommodate both stored and injected beams. In addition, injection into the booster occurs at the final linac energy of 100 MeV, implying that radiation damping will be negligible. Should accumulation into the booster prove to be impractical, an alternative would be to increase the charge from the gun directly and inject multi-bunch shots straight from the linac. The downside to this approach is the loss of flexibility in tailoring the filling patterns, and a limit to the maximum charge per shot that can be produced (single or multi-bunch).

The baseline assumption is that off-axis injection into the booster can be achieved with three fast kicker magnets and a single septum magnet. The septum magnet will be used to steer the electron beam from the exit of the linac-to-booster transfer line and place it parallel to the reference trajectory in the booster. The three kicker magnets will bump the reference orbit in the booster towards the septum plate, thereby producing a transitory reduction in the separation of stored and injected beams. The field in the kicker magnets must drop to zero in a sufficiently short period to prevent the injected beam from colliding with the septum plate on subsequent revolutions. In order to accommodate both single and multi-bunch beams from the linac, the kicker pulse waveform should be flat-top, with rise/fall times consistent with the ring circumference and the maximum length of the multi-bunch train. The peak strength of the kicker magnets will also have sufficient contingency such that it remains possible to place the injected beam on-axis, should the need arise.

Extraction from the booster will be single-turn in order to kick the whole beam out of the booster in one block. This should be possible using one fast kicker magnet and one septum magnet. As with the injection pulsed magnets, the extraction kicker waveform should have a flat-top consistent with the multi-bunch filling pattern, and the rise time should be fast enough to reach peak field during the gap in the filling pattern. The fall time for this magnet is not critical. Given the moderate increase of the extraction energy to 3.5 GeV, the possibility to re-use existing extraction magnets will be the subject of further investigations.

The precise details of all the injection and extraction pulsed magnets will be developed in parallel with the engineering design.

2.13.4. Lattice Performance

In order to enable off-axis injection and accumulation, the physical and dynamic acceptances must be large enough in the horizontal plane to accommodate both the injected and stored beams at 100 MeV, plus room for the septum plate and contingency for closed orbit and alignment errors. The beam stay clear in the vertical plane is dictated by the injected beam size (plus contingency). Alongside a reduction in the extracted beam emittance, a significant aspect of the lattice design was to provide this wide dynamic aperture with field gradients low enough to be practical with the large magnet bore radius.
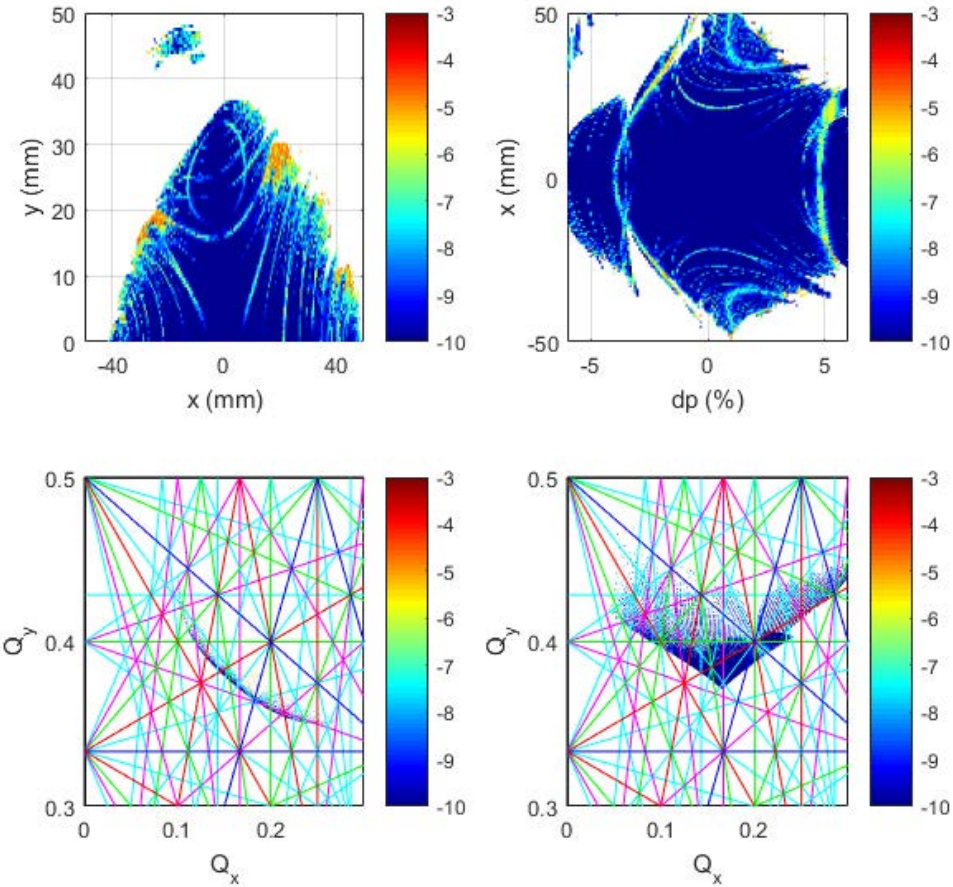
Figure 2-156 : Dynamic Aperture (top row) and frequency maps (bottom row) for the new booster synchrotron. The left hand column shows on-momentum particles in the x/y plane, and the right hand column shows the off-momentum dependence as a function of horizontal position.

Figure 2-156 shows the on and off-momentum dynamic apertures and associated frequency maps for the ideal lattice. The edge of the dynamic aperture is limited to -41 mm / +48 mm for on-momentum particles. However, compared to the normalised emittance of the injected beam from the linac of ~100 mm.mrad, this should be more than sufficient to capture the injected beam. The momentum aperture of the bare lattice is restricted to -3.3% / +4.0% by a strong skew-sextupole resonance, considerably larger than both the linear RF acceptance at extraction and the energy spread of the beam from the linac (~0.2%, [1]).

Closed orbit distortions in the booster are less critical than in the storage ring. However, to ensure robust, reliable performance, 34 horizontal correctors, 34 vertical correctors and 34 BPMs have been included in the design. This includes one of each element per unit cell, with additional BPMs and correctors in the matching cells at each end of the long straight sections. In this preliminary design, it has been assumed that the correctors will be integrated into the sextupole magnets; however, this decision may be revisited as the design progresses.

The robustness of the design has been tested by applying random alignment and field errors according to the values given in Table 2-68. The closed orbit distortions before and after orbit correction, beta-beat after tune correction, and final on-momentum dynamic apertures after orbit, tune and chromaticity correction over 50 error seeds are shown in Figure 2-157, Figure 2-158 and Figure 2-159 respectively. From these simulations, the performance of the ring is clearly sufficient to withstand realistic magnet construction and installation tolerances.

Table 2-68: RMS Alignment and Field Errors used for Booster Magnets.

Element	x/y displacement (μm)	Tilt (μrad)	Strength Error
Dipole	30	200	1×10^{-3}
Quadrupole	30	200	3×10^{-3}
Sextupole	30	200	5×10^{-3}
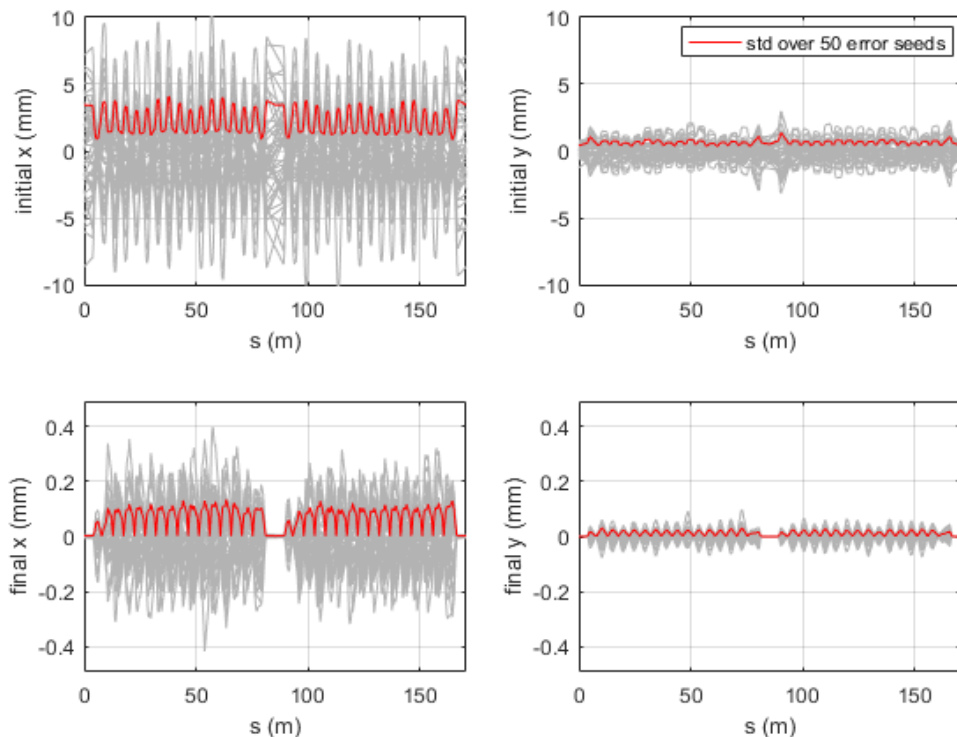
Figure 2-157 : Closed orbit distortions over 50 error seeds before (top) and after (bottom) orbit correction.
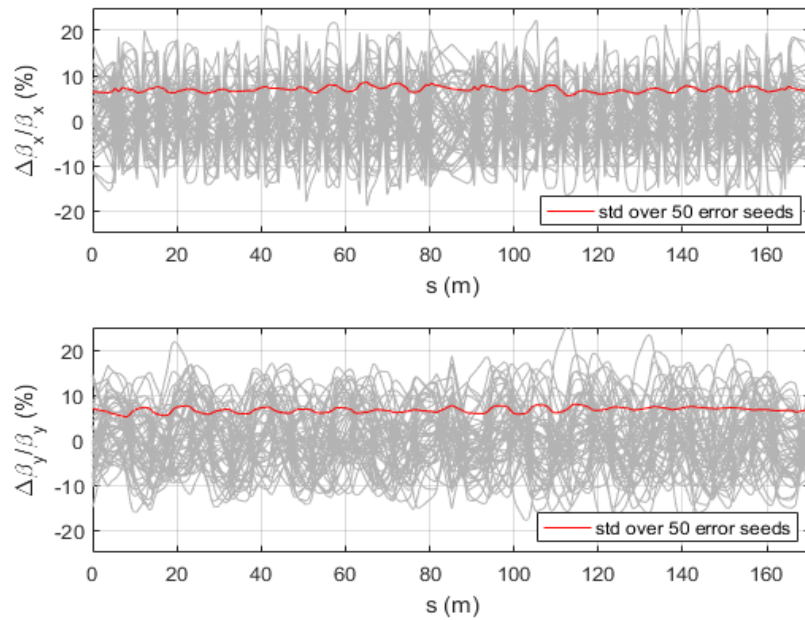
Figure 2-158 : Horizontal (top) and vertical (bottom) beta-beat after tune correction only over 50 error seeds.
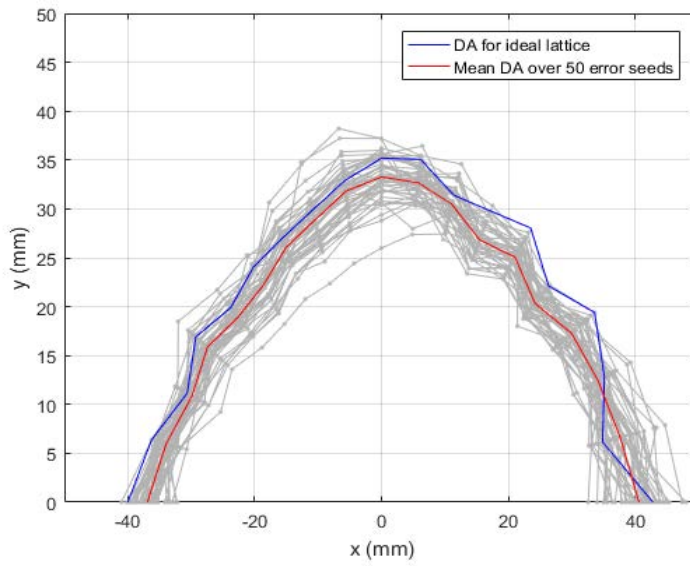
Figure 2-159 : Dynamic aperture over 50 error seeds after orbit, tune and chromaticity correction.

2.13.5. Implementation of the New Booster

The arc radius of the new booster was selected to allow it to be installed around the outside edge of the existing ring, as shown in Figure 2-160. This is possible because the booster vault is relatively wide, in excess of 4.0 m. The precise geometry and engineering design of the new ring will be developed alongside that of the storage ring, ensuring the circumference of the new ring is consistent with the final RF frequency. The decision to locate the new booster as close as possible to the existing ring was taken so that changes to the transfer lines are minimised and that access from the outer edge is maintained.
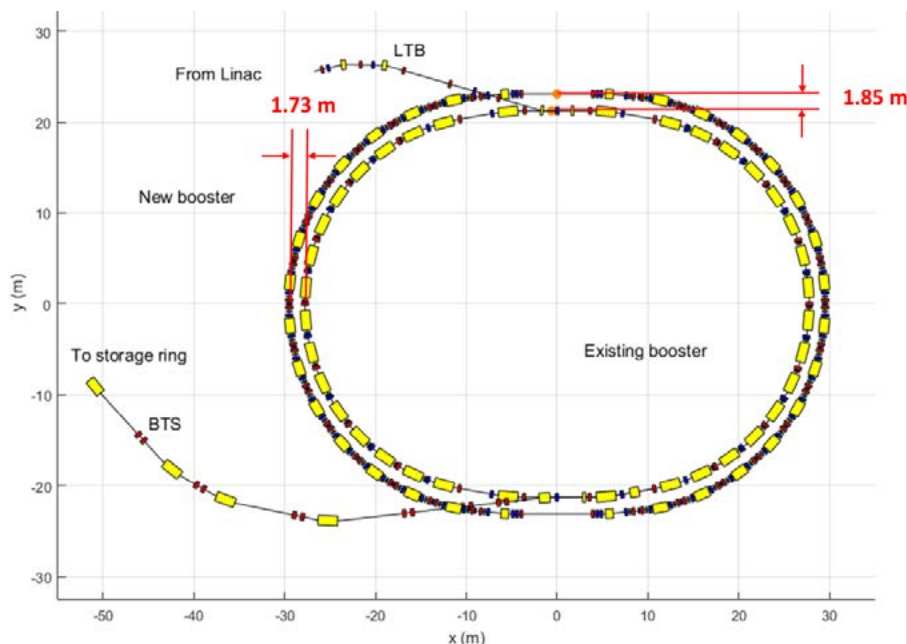
Figure 2-160 : Location of upgraded booster synchrotron. The new ring can be installed close to, but on the outer edge of the existing booster. The linac-to booster and booster-to-storage ring transfer lines will be modified to match the new injection and extraction points.

It is currently assumed that ~80% of the new booster will be installed during the standard shutdowns in a two year period preceding the main shutdown. This would allow completion of the booster installation and its commissioning to be carried out in parallel to the replacement of the storage ring, and before storage ring commissioning so that the total shutdown period is not extended. The existing ring will be left in place to be removed at a later date.

The booster has cast in-situ walls and roof with no crane cover. In addition to the personnel entry labyrinths the booster has two "break down" walls made up of concrete blocks. One or both of these will be modified to install a moveable concrete wall that can be opened and closed easily on air pads or moved on rails hydraulically.

The new booster build will be based on preassembled, pre- aligned and functionally tested girders with vacuum vessels already on the girder and under vacuum (approx. 36) delivered to site ready to install, as was successfully implemented for the existing booster construction. The existing two PETRA-type 5-cell cavities will be re-used on the new booster.

A consequence of a parallel build of the new booster while the old one is operational will be the need for additional Control and Instrumentation Areas (CIAs) for electronic systems and power supplies, with suitable cable runs from them. Since there is a large amount of free rack space in existing Booster CIAs 2 and 3, the current plan is to construct one new Booster CIA of twice the normal length in a location adjacent to the linac exit door and booster gate 3, an area presently used for storage. Unused CIA space once booster 1 is decommissioned will be repurposed for spares storage.

Cooling water for the existing booster has sufficient capacity for the new booster but distribution will differ and will be designed to make use of existing routing in the vault while keeping the existing booster operational.

2.13.6. Future Studies

Whilst the proposed design for the new booster meets the requirements, there are a number of further developments or changes which remain under consideration. The first of these is to see whether a single injection kicker magnet could be used to accumulate beam rather than by creating a closed bump for the stored beam with three kicker magnets. Using this configuration, the oscillations are shared by both stored and injected beams, and so the overall dynamic aperture requirements may be smaller.

Another possibility to improve the total transfer efficiency for the system is to raise the injection energy from 100 MeV to 200 MeV. This would help to improve both the initial injection efficiency from the linac into the booster, and to reduce any losses for any beam that may already be in the booster. This could be achieved using the existing linac structures by installing SLED cavities [2].

The final change which is being considered is to see if a re-design of the booster arc sections using combined-function magnets is beneficial. The primary question which this work seeks to address is whether the final electron bunch parameters can be maintained, whilst using a design with reduced peak field in the dipole magnets and a reduction in the total number of magnets.

References

[1] C. Christou and V. Kempson, "Commissioning of the Diamond Pre-Injector Linac," in *Proceedings of EPAC'06*, Edinburgh, Scotland, 2006.

[2] Z.D. Farkas, H.A. Hogg, G.A. Loew, P.B.Wilson, "SLED: A Method of Doubling SLAC's Energy", SLAC-PUB-1453, 1974.

3. Critical Upgrade Projects and Developments

3.1. Beamlines

In order to take advantage of the increased brightness, coherence and higher X-ray energy offered by Diamond-II, all beamlines will need to make improvements to their optics, detectors, instrumentation and software. A significant number of these can be catered for by the resources from the ongoing upgrade programme, a substantial capital uplift from our funders from FY 18/19 to ensure Diamond's facilities continue to be competitive. One of the main advantages of the proposed Diamond-II lattice is that it introduces new mid-straights (see Section 2.1) which enables bending magnet beamlines to remain competitive, and in fact in many cases gain capability through having their source replaced from a bending magnet to an insertion device as described in Section 2.2. However, the new lattice gives a different source point and the new sources have different characteristics, so in many cases the present optical arrangements will not work in Diamond-II and substantial upgrades are required. In addition, due to the shortened straights in Diamond-II, beamlines that are currently on a side branch are not compatible and will need to be relocated. Table 3-1 lists the existing beamlines which will require major and critical changes.

Table 3-1 : The beamlines which will require major and critical change (see Table 1-1 for beamline characteristics).

Beamline	New Position	Critical Major Modifications
I04-1	K04	Relocation
I20-EDE	K14	Relocation
B07-1	K08	Relocation, but reusing current endstation
B07-2		New front end and removing M1. Some other optics replacements would be required. An optics hutch may be required
B16		New optics throughout and extra shielding
B18		New optics throughout and extra shielding
B21		Some new optics and extra shielding
B22		New front end and optics
B23		New front end and optics
B24		New front end, new M1 and other mirrors

Two beamlines on long straights (I09 and I13) will also need substantial changes to the optics in order to accommodate the removal of the mini-beta magnets, and two recent beamlines (VMXm and DIAD) will need substantial realignment. Table 3-2 lists those and the remaining beamlines where critical changes are required. Note that only major changes of the sources, front-end optics and shielding are listed: ALL beamlines will need substantial upgrades to be completed as part of the ongoing upgrade programme, in order to deliver the new capabilities listed in the Diamond-II science case.

Table 3-2 : Beamlines where critical changes are required (see Table 1-1 for beamline characteristics).

Beamline	Critical Modifications
VMXi	Upgrades completed as part of ongoing upgrade programme
VMXm	New position of beam, realigning equipment, hutch changes
I03	New filters and window
I04	New filters and window
I05	New ID to reduce heatload, otherwise new M1
I06	Improved cooling for M1. And possible replacement of M3, M6 optics?
I07	Upgrades completed as part of ongoing upgrade programme
I08	New grating and diagnostics
I09	New mirrors SM1 and HM3
I10	Improved cooling for M1. May need new gratings
I11	Upgrades completed as part of ongoing upgrade programme
DIAD (K11)	New optics and realignment
I12	Upgrade to primary heat filters. Increased shielding for hutches
I13 Imaging	New CRL's, new optics
I13 Coherence	New CRL's, new optics
I14	Improved cooling and performance on primary mirror system
I15	Heatload needs mitigating, new filters and increased shielding for hutches
I15-1	Heatload needs mitigating, new filters.
I16	Upgrades completed as part of ongoing upgrade programme
I18	Upgrades completed as part of ongoing upgrade programme
I19	Shielding improvements and upgrades completed as part of ongoing upgrade programme
I20-Scanning	New M1 and M2
I21	Heatload can be mitigated by new ID.
I22	Upgrades completed as part of ongoing upgrade programme
I23	Upgrades completed as part of ongoing upgrade programme
I24	New filters and shielding improvements

3.2. Optics and Metrology

The Diamond-II source brings opportunities and challenges for beamline optics. Since the optics for every beamline have been individually optimised, this optimisation must be repeated for the new source. The source upgrade will also allow upgrade of beamline optics to match evolving needs and emerging opportunities in areas such as nano probe, high spatial resolution, higher energy-bandwidth, maximum transverse coherence or combinations of any of these chosen by the user. Important outcomes of the Diamond-II upgrade will be the possibility of using nano focusing optics to achieve sub-micron focused beam spots (down to ~30 nm) on a greater variety of beamlines and the delivery of X-ray beams to the sample with greatly increased lateral coherence.

To take advantage of the new source and for the experiments to stay at the forefront of research, every beamline should be reassessed from the source to detector. For instance, it is likely that almost all Double Crystal Monochromators (DCMs) will have to be replaced, some even before the Diamond-II upgrade. For some beamlines, horizontally deflecting DCMs may be more appropriate to increase the beam stability.

At a time when facilities worldwide are poised to start upgrades, and when there are only a few qualified suppliers of X-ray optics, it is mission critical that Diamond has the correct infrastructure and expertise in place (Figure 3-1). The key investment will be in a fabrication facility for developing multilayer optics and finishing mirrors without which, it will be difficult to keep Diamond at the forefront of SR science.
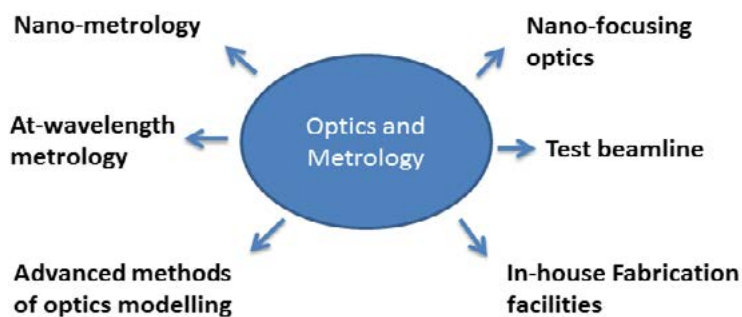
Figure 3-1 : Main activities in Optics and Metrology at Diamond.

The integration of manufacturing, metrology and testing is key to the optics development [1-7] when reaching nanometre precision. Whilst we have built over the years a state-of-the-art metrology lab [8] and X-ray testing facility [9], we do not directly control the manufacturing stage. We plan to improve this situation by establishing in-house multilayer (ML) optics fabrication facilities. ML optics (ML coated curved mirrors and Multilayer Laue Lenses) are the only X-ray optics that have demonstrated sub-10nm focusing for hard X-rays. As Diamond aspires to produce such beams on Diamond-II for the benefit of UK scientists pursuing science at the nano-scale, it is crucial for Diamond to have reliable access to such a facility.

Several beamlines on Diamond-II will require ultra-high quality X-ray optics that are ~ 2-5 times lower in figure error than the present day X-ray optics. This would require enhancing the capabilities of our in-house metrology facilities so that X-ray optics of ~50 nrad rms slope error can be reliably measured and characterised.

When installed on a beamline, it is not possible to perform conventional metrology and one has to use at-wavelength metrology (i.e. using X-rays) [10-11]. Diamond has extensive experience in developing and using these methods that will be used for real time in-situ characterisation of optics on beamlines. Measurements will be combined with simulations to allow the development of procedures for fast, automatic optics alignment and for compensation for drift and beam vibrations.

Exploitation of Diamond-II for nano-focusing, for coherence preservation and high-resolution gratings requires figure errors on mirrors less than 1 nm. This is only possible via deterministic polishing, for example ion beam figuring (IBF). These techniques ideally require at-wavelength optimisation. There are only a few suppliers of the most technologically demanding optics and this represents a serious risk to cost and time. A prototype IBF system has been designed and developed at Diamond. This system will be enhanced and upgraded to keep the X-ray optics competitive on Diamond-II.

X-ray crystal monochromators will also require development to cope with the high heat loads and to minimise wavefront

distortion. Wavefront distortion may be caused by the imperfect polishing of the diffracting surface and existing strain in the diffracting surface. An in-house silicon cutting and polishing facility would be used for achieving the required surface finish.

With the predicted demand for upgrading existing beamlines, facilities for cost-efficient refurbishing and upgrading existing optics for higher performance are proposed.

References

1. L. Alianelli, D. Laundy, S. Alcock, J. Sutter, and K. Sawhney, Development of Hard X-ray Focusing Optics at Diamond Light Source, *Synchrotron Radiation News,* **29**, 3 (2016).

2. K. Sawhney, D. Laundy, V. Dhamgaye and I. Pape, Compensation of X-ray mirror shape-errors using refractive optics, *Appl. Phys. Lett.,* **109**, 051904 (2016).

3. D. Laundy, K. Sawhney, I. Nistea, S. G. Alcock, I. Pape, J. Sutter, L. Alianelli, and G. Evans, Development of a multi-lane X-ray mirror providing variable beam sizes, *Rev. Sci. Instrum.,* **87**, 051802 (2016).

4. M. Hand, H. Wang, F. Maccherozzi, M. Apollonio, J. Zhu, S. Dhesi and K. Sawhney, Quantitative investigation of linear arbitrary polarization in an APPLE-II undulator, *J. Synchrotron Rad.* 25, 378 (2018).

5. S. G. Alcock, I. Nistea, R. Signorato, R. Owen, D. Axford, J. Sutter, A. Foster and K. Sawhney, Dynamic adaptive X-ray optics, Part II. High-speed piezoelectric bimorph deformable Kirkpatrick-Baez mirrors for rapid variation of the 2D size and shape of X-ray beams, *J. Synchrotron Rad.* **26**, 45 (2019).

6. L. Alianelli, M. S. del Rio, O. J. Fox, and K. Korwin-Mikke, Aberration-free short focal length x-ray lenses, *Opt. Lett.,* **40**, 5586 (2015).

7. X. Yang, H. Wang, M. Hand, K. Sawhney, B. Kaulich, I. V. Kozhevnikov, Q. Huang, and Z. Wang, Design of a multilayer-based collimated plane-grating monochromator for tender X-ray range, *J. Synchrotron Rad.,* **24**, 168 (2017).

8. S. G. Alcock, I. Nistea, and K. Sawhney, Nano-metrology: The art of measuring X-ray mirrors with slope errors <100 nrad, *Rev. Sci. Instrum.,* **87**, 051902 (2016).

9. K. Sawhney, I. Dolbnya, M. K. Tiwari, L. Alianelli, S. Scott, G. Preece, U. Pedersen and R. Walton, A Test Beamline on Diamond Light Source, *AIP Conference Proceedings – Tenth International Conference on Synchrotron Radiation Instrumentation, Australia,* **CP1234**, 381 (2010).

10. K. Sawhney, H. Wang, J. Sutter, S. Alcock, and S. Berujon, At-wavelength Metrology of X-ray Optics at Diamond Light Source, *Synchrotron Radiation News,* **26**, 17-22 (2013).

11. H. Wang, Y. Kashyap, and K. Sawhney, Hard-X-Ray Directional Dark-Field Imaging Using the Speckle Scanning Technique, *Phys. Rev. Lett.,* **114**, 103901 (2015).

3.3. Detectors

The increase in brightness of Diamond-II and the improvements in the optical layout of several beamlines will lead to a considerable increase in photon flux, in some cases two or more orders of magnitude. The current generation of detectors is not able to cope with the sheer number of photons. In order to take full advantage of the investment in the machine and optics, Diamond is developing a strategy for the Diamond-II project that includes a vigorous R&D effort in detectors to be pursued collaboratively with STFC and with other partners in Europe and worldwide.

A few major areas of development for Diamond-II can be identified: detectors for X-ray diffraction (crystallography and imaging), detectors for X-ray spectroscopy, area detectors for soft X-rays, and electron detectors and photon counting detectors.

3.3.1. Detectors for X-ray Diffraction Imaging and Crystallography

There are more than 16 photon counting detectors, 4 flat panels, and 1 CMOS-based detector in operation on beamlines at Diamond currently. The increase in photon flux will have a big impact in crystallography and diffraction imaging beamlines which currently use photon counting area detectors. In some cases, for example pink-beam ptychography, the increase of coherent photon flux at the sample position will be more than two orders of magnitude when all upgrades are considered together (machine emittance, new ID, optics). The detectors will no longer be capable of discriminating the arrival of individual photons. This will dictate a shift in technology from photon counting area detectors to "integrating" area detectors which work by accumulating the charge generated by X-rays, followed by a read-out at the end of the integration period.

The development of integrating area detectors with characteristics suitable for Diamond-II requires considerable R&D effort. This can be pursued with STFC which has significant expertise in this area gained through the development of

the so-called Large Pixel Detector (LPD), for MHz frame rate imaging at the European XFEL. A proposal has recently been submitted to the European Union's ATRACT Initiative from STFC, Diamond, and EU-XFEL to conduct a preliminary study of an integrating read-out ASIC with pixel size smaller than 100 microns and frame rate exceeding 100,000 fps (required since the current LPD detector has large pixel sizes). Diamond-II will require scaled-up full large area systems based on this technology, but will also require the use of sensors other than silicon (for instance CdZnTe sensors) for applications at high photon energy. STFC has here again a vast experience in the characterisation and use of such sensors. We will also follow the development of integrating detectors at PSI (JUNGFRAU, developed for SwissFEL), and work closely with PSI and other European partners such as the ESRF and DESY through LEAPS (League of European Accelerator-based Photon Sources) initiatives.

3.3.2. Detectors for X-ray Spectroscopy

There are currently 3 multichannel Ge systems and 17 silicon drift detector (SSD) systems in operation at Diamond. It has been recognized for a long time that the throughput of these detectors is one of the major limiting factors for XAFS and elemental mapping experiments. I20 is currently severely limited by the detector and work has already started at Diamond (in collaboration with Soleil) to improve multi-element Ge detectors, with the aim to increase the throughput per unit area by an order of magnitude with respect to the current generation of detector systems. With Diamond-II, certain spectroscopy beamlines such as B18, which is also limited by the detector, will upgrade to a three-pole wiggler with commensurate flux improvements. The detector development initiated in this area will need to be expanded to deliver very large multi-elements systems in the years to come, with the aim to produce a step change for Diamond-II spectroscopy beamlines.

Other developments that should be considered in this area include Silicon Drift Detector (SDD) arrays to enhance the efficiency and throughput of fluorescence detectors for elemental mapping on beamlines such as I14 or I18. A drastic improvement in count rate capabilities could be obtained by exploiting monolithic arrays of SDDs, if efficient pulse processor solutions can be found. To this end, there is an opportunity to develop further the recent technology of the Xpress 4 processor system developed at Diamond/STFC in order to process the signals from monolithic arrays of SDD and produce the gain in throughput required for Diamond-II.

3.3.3. Area Detectors for Soft X-rays

There are currently 5 Soft X-ray cameras in operation, but diffraction and microscopy in the soft X-ray regime is an area severely limited by the detectors currently in use, mainly back-thinned and back-illuminated CCD cameras. The low frame rate capabilities of this class of imagers is the limiting factor (either for fast scanning or dynamic experiments) for magnetism beamlines such as I06 and I10, as well as scanning and coherent diffraction imaging beamlines such as B24, I08 and J08. Exploiting the recent progress in scientific CMOS chips is of paramount importance for these beamlines, as the brightness will increase by a factor between 5 and 10 in the soft X-ray energy range. The detector group at Diamond joined a few years ago the Percival collaboration, led by DESY, which targets the development of a soft X-ray camera based on CMOS imaging sensors for FLASH FEL and enables acquisition of images at frame rates up to 360 fps. Further developments of CMOS sensor targeted specifically for synchrotron needs will be needed to exploit fully the specific time structure of synchrotron radiation.

3.3.4. Electron Detectors and Photon Counting Detectors

Direct electron detectors have played a pivotal role in the success of cryoEM and are in the process of being integrated to X-ray driven electron microscopes such as the I06 XPEEM facility at Diamond, where a Medipix3 read-out chip bonded to a silicon sensor is currently being commissioned. The first tests highlighted the dramatic increase in speed and noise performance of this imager with respect to the previous detector (from one frame per second to 1800 frames per second). Further improvements in speed and fields of view will be possible by exploiting the forthcoming Timepix4 read-out chip developed by CERN. The 4-side buttability and larger format of Timepix4 enable a larger sensitive area than the current system. The time stamp capabilities of Timepix4 would also enable the observation of high-speed processes similarly to what can be done with a time resolved detector such as Tristan (Diamond), currently being developed for X-rays. With Tristan we are currently aiming at a time resolution of 1 microsecond for time-resolved crystallography but have also demonstrated that Timepix3 can effectively separate the photon events coming from the isolated electron bunches (<10 ns). This system could also be used for electron microscopes to offer vast improvements when applied to high energy microscopes by enabling the implementation of centroiding algorithms with the consequent enhancement of spatial resolution.

3.4. Sample Environment Developments

The transformation in throughput and science output with Diamond-II can only be delivered if the necessary sample preparation and handling tools are provided to the user community in parallel. Integrated specialised facilities co-located at Diamond, the Research Complex at Harwell (RCaH), the Rosalind Franklin Institute (RFI) and Harwell partners such as the Catalysis Hub, the Faraday Institution and the XFEL Hub will provide a supportive environment for implementing challenging sample preparation and new *operando* environments when coupled with world class expertise. New experimental methods and advanced sample environments lie at the core of much of the biological and materials science research carried out at Diamond. Most complex biological systems and multi-component physical science materials rely on the need for sophisticated instrumentation to measure complementary properties of a system simultaneously, the resultant data reporting on the *exact same system*, often referred to as *operando.*

Most beamlines have seen an upsurge in exotic combined experiments being proposed and accepted, where the users are bringing devices that are ever more complicated to the beamline. This will only continue and in order to get the best out of the Diamond-II upgrade, an engineering approach is required to develop advanced environments that is commensurate with the improvements in focusing, brightness and speed of data collection. Critical to the success of this new breed of experiments is integration of the sample environment into data collection where multiple parameters can be explored simultaneously. A way forward to handle the range of environments and sample delivery methods could be the development and exploitation of collaborative robots (so called cobots) that can be adapted readily with multiple end effectors and taught the tasks in hand by scientists and users enabling rapid development of experimental envelopes and automation, the MX group (which has been at the forefront of robot usage at Diamond and elsewhere) are investigating these, but such tools will have a much broader impact across Diamond.

Establishment of a Sample Environment Development Group/Lab would allow Diamond to place strategic emphasis on the development of new technologies, including robotics, automation, motion and thermal stability, for ultimately more coherent experimentation. This facility would also benefit our Industrial activities to allow more challenging in-situ experiments to be accommodated.

3.5. Photon Diagnostics

The ultimate goal of Diamond-II is to deliver stable photon beams to the sample points in beamlines. To this end, a definition of the required stability is needed at the outset of the design process. Typical specifications might be the acceptable deviation in beam position or angle, in beam size or in beam intensity, expressed either as peak-peak or RMS. There might be also other parameters of particular importance to the individual beamline. For each parameter where stability is important, a relevant reference point and a tolerance around this reference must be defined. It is also important to define the time scales over which the parameter is expected to remain within the given tolerance, or where necessary provide several tolerance values for different time scales [1].

Photon diagnostics are the instruments used in measuring these properties. Initially, these instruments are essential in the commissioning and alignment of the beamline. Beyond displaying the current state, measurements are typically recorded over long periods and analysis allows an assessment of stability. Furthermore, where this analysis highlights instabilities or drifts to the detriment of the ultimate experiment, feedback loops can be implemented if applicable actuators can be identified. However, this 'step-by-step' approach to feedback building can create several challenges:

1. If the diagnostics instruments are coordinated by the individual beamlines with initial alignment primarily in mind, they are unlikely to make good inputs to permanent feedback loops. In practice, availability, reliability, quality as well as readout speed and latency frequently become limiting factors.

2. Equally, the late selection of potential actuators often creates limitations in a feedback loop that would have been comparability trivial design choices at an earlier stage.

3. Finally, the variety of different instruments used for the same purpose creates overhead for controls integration and often limits closure of the feedback loops to high level layers. Again, this often leads to a deterioration in the performance of the feedback due to excessive latency [2].

Owing to the smaller source size, improvements of monochromators and optics, as well as the increasing speed of data acquisition of detectors [3]–[5], requirements for stability of the photon beam will increase dramatically. As a consequence, photon diagnostics become ever more important, and will evolve from a commissioning tool to an essential operating component. These are required with high reliability and integrity, certainly when integrated in feedback loops.

Today, designers of beamlines aim to meet or exceed the stated stability requirements. However, owing to external factors like floor stability, air temperature variation or heat load variations it is sometimes challenging to achieve a system intrinsically stable within the durations important for the beamline. The angular changes of the beam on optics which will cause noticeable deviation to beamlines have now shrunk to 30-50 nrad. Such small deflections are generated by a variety of effects on a range of time scales, from liquid cooling in optical elements to sagging of components.

In the future, as part of an integrated beamline design process estimates will be made of the intrinsic beam stability that can be achieved. Next, the capacity to read the relevant parameters will be added to further monitor and ultimately achieve the required stability using active feedback. This feedback does not need to be available on 'day one' of the beamline, however it is essential that it is considered at the design stage and is not added as an afterthought. As part of this process, the timescales over which active feedback should operate in order to complement the intrinsic mechanical stability must be carefully evaluated.

The recently completed beamline VMXm at DLS might serve as an example [6], [7]; it employs single-crystal diamond X-ray beam position monitors [8] along the beamline which are used as alignment targets during commissioning and included in active feedback. This technology has also significant potential for further development, by moving from metallised flat partitioning to full 3D laser written structures inside a diamond substrate, thus enabling an advance from quadrants to many pixels [9]. In the end, this may allow concurrent visualisation of the transverse intensity distribution of micron sized X-ray beams.

VMXm is also one of the first beamlines to contain low latency feedback from monochromatic beam position sensors to actuators like DCM crystals and mirrors. Ultimately, however, the bandwidth of any physical movements is limited, so we will keep the option of steering the X-ray beam directly by sending electron beam offset demands back to the central orbit controller. This would realise a much more agile corrector, as in this case the electron beam would be moved inside the ID creating the X-rays for the beamline in questions (see also Section 2.7.3).

References

[1]   G. Rehm, "Achieving and measuring sub-micrometer beam stability at 3rd generation light sources," J. Phys. Conf. Ser., vol. 425, no. PART 4, 2013.

[2]   C. Bloomer et al., "Using DCM pitch modulation and feedback to improve long term X-ray beam stability," in Journal of Physics: Conference Series, 2013, vol. 425, no. 4, p. 042010.

[3]   M. Basham et al., "Software Mapping Project with Nanopositioning Capabilities," Synchrotron Radiat. News, vol. 31, no. 5, pp. 21–26, Sep. 2018.

[4]   M. D. de Jonge, C. G. Ryan, and C. J. Jacobsen, "X-ray nanoprobes and diffraction-limited storage rings: opportunities and challenges of fluorescence tomography of biological specimens." J. Synchrotron Radiat., vol. 21, no. Pt 5, pp. 1031–47, Sep. 2014.

[5]   U. Boesenberg et al., "Fast X-ray microfluorescence imaging with submicrometer-resolution integrating a Maia detector at beamline P06 at PETRA III," J. Synchrotron Radiat., vol. 23, no. 6, pp. 1550–1560, Nov. 2016.

[6]   J. Trincao et al., "VMXm: a new sub-micron beamline for macromolecular crystallography at Diamond Light Source," Acta Crystallogr. Sect. A Found. Adv., vol. 71, no. a1, pp. s191–s191, Aug. 2015.

[7]   "Where no synchrotron has gone before": Diamond Light Source." [Online]. Available: https://www.scitecheuropa.eu/diamond-light-source-synchotron/90914/. [Accessed: 11-Mar-2019].

[8]   C. Bloomer, G. Rehm, and I. P. Dolbnya, "An experimental evaluation of monochromatic x-ray beam position monitors at diamond light source," in AIP Conference Proceedings, 2016, vol. 1741.

[9]   C. Bloomer, G. Rehm, P. Salter, and M. Newton, "A single crystal CVD diamond x-ray beam diagnostic with embedded graphitic wire electrodes," 2019, p. 060058.

3.6. Data Management and Computation

3.6.1. Diamond-II Data Management and Computation

The scientific output from Diamond-II will critically depend on effective data management (acquisition, storage, accessibility, metadata) and computation (online/real-time analysis, post beam-time analysis).

There is an ongoing programme of investment in data management and computation to ensure that Diamond remains competitive, driven by continued advances in beamline hardware and software. However, Diamond-II will deliver more than an order of magnitude increase in brightness and coherence to most beamlines. From experience with the enhancement of the current beamlines we can model the effect of such a step change in capability on the data throughput, and the increased demand for storage and computation. This experience underpins our assessment of critical additional resources required to take advantage of the scientific opportunities presented by Diamond-II.

3.6.2. Data Management and Computation Requirements

Data rates have been increasing at Diamond more quickly than IT advances (i.e. outstripping Moore's Law). The large majority of the data produced currently comes from the imaging and macromolecular crystallography beamlines, which have benefitted from several generations of detector developments and experiment automation. To take scientific advantage of the step change in beam properties with Diamond-II will require new detector technologies on all of these beamlines, and may enable a number of other beamlines to move to this data-rich regime.

Initial considerations for detectors on Diamond-II, based on those currently developed for FELs, or in development, give raw data rates of terabytes per second. Such data rates will make acquisition and analysis very challenging and require new solutions such as first-line analysis and Machine Learning to be able to effectively analyse the data.

Alongside this, scientific techniques are becoming more complex and multimodal, requiring more sophisticated data acquisition/management and analysis processes to make them effective. Reconstruction algorithms are increasingly complex, for example in tomography and ptychography. New algorithms and close to real-time analysis tools will be needed to enable users to quickly assess experiments, and where already available to maintain users' ability to take away scientific results rather than simply data.

Finally, synchrotron sources increasingly support new and inexperienced users, requiring greater simplicity of experiment operation and the complexity to be hidden in the facility software. There is also a trend towards automation, mail-in services and remote use of instruments in specific disciplines. Already over half of Diamond MX access is remote, and an increasing proportion entirely automated. These developments mean that the step change in throughput in Diamond-II can be used more efficiently but will demand new imaginative software and hardware solutions.

At this time, an outline model for computation and software might be:
- Pre-experiment modelling performed in a cloud-based computing environment.
- Web-based control of experiments, for both passive and interactive experiment control and appropriate access points for intervention from real-time intelligent/informed experiment processing.
- All beamlines to have full and rich metadata and metadata catalogues, with fast access to historical data to combine experiments or inform experimental design.
- Experiment-appropriate models for on-the-fly data reduction will be used for all beamlines (and rules will be developed to ensure only useful data will be stored).
- Experiment design - in some instances be enabled to intelligently modify strategies on the fly.
- Data capture will be initially to local 'data buckets' with parallel on-the-fly first cut analysis and display, which will likely benefit from novel approaches to real-time data analysis, e.g. hardware accelerated data analysis.
- Near real-time analysis will be performed on local instances of the data.
- Post-processing analysis will be performed in a cloud-based computing environment.

A review of what data actually means for each experiment type should be undertaken in preparation for Diamond II in a similar manner to the approach taken for the extremely high data rates expected at LCLS-II [1]. Proof-of-principle implementations will be part of the longer-term programme of upgrades to the machine, beamlines and other infrastructure and will require additional staff, new hardware and software solutions.

3.6.3. Critical Developments in Data Management and Computation

Examples where critical developments will be transformational are outlined below.

Real-time Diffraction Data Processing

Since the first Diamond MX beamlines opened the technique has been transformed by developments in detectors, optics, software, especially data processing pipelines, and automation. Diamond-II will bring additional brightness which will require new detectors to exploit the scientific potential more fully. Present state of the art Eiger detectors have a frame rate of a little over 130 fps for a 16 M pixel detector. Integrating detectors such as the Jungfrau, designed initially for XFEL, are likely to be adopted by synchrotrons and, for the same pixel count can already achieve and order of magnitude higher framerate, with 2.4 kHz anticipated [2]. It is reasonable to expect a further factor of 5 increase in data rates in the years before Diamond-II becomes operational which, allowing for duty-cycle and compression could realistically result in data rates of ~10's petabytes per week. The current model of store-and-process of the data stream is not practical at such data rates, and so a new real-time in-memory processing architecture will have to be developed to process the raw diffraction data as it comes out of the detector. The initial application is macromolecular crystallography, but other high throughput techniques will require similar approaches.

Imaging Techniques

Present day imaging techniques create challenging data volumes, enabling diverse science:

- Initiatives in neuroscience like the Human Brain project [3] aim to advance understanding by building atlases of the brain. To understand neuronal circuits a longstanding goal has been to image 1 mm^3 of brain tissue with nm resolution which would lead to up to 10^{18} voxels in processed data alone (>100 petabytes).

- Security concerns and the need to maintain critical legacy systems has led to several projects worldwide aimed at reverse engineering both new and obsolete integrated circuits. Demonstrations of small volume imaging have been achieved but longer term goals requiring imaging of full size integrated circuit (cm^2) with nanoscale resolution leading to petabyte data volumes.

- Optimising metal casting and additive manufacturing are areas of intense study and require time resolved studies at the time scales of critical processes. High frame rate, long time duration experiments now routinely produce 100's of terabytes and demand for higher rates/increased information content (multi-detector or multi-modal) is growing.

- In energy research, imaging of storage and generation systems such as batteries and fuel cells over time during *operando* conditions will be crucial for developing better understanding of such complex architectures and to provide underpinning science to prevent failures and extend lifetimes. This will often be in combination with simultaneous diffraction experiments to probe structural changes in the individual phases and lead to terabytes of data to store and process.

The increase in brightness and coherence of Diamond-II, will enable significant steps towards these goals through faster acquisition, improved transverse coherence and higher contrast, leading to more data. Increased coherence, especially at higher photon energies, will increase the power of ptychography and tomo-ptychography imaging techniques. Both are computationally and data intensive, increasing demands on compute, storage and network infrastructure.

To manage these challenges in preparation for Diamond-II will require significant development of tools along the data flow of imaging techniques. These will include control of sample position to enable adaptive acquisition schemes (e.g. sparse sampling or optimised trajectories), and high data rate transfer from detectors to storage. The latter will need advances in data compression algorithms to minimise the impact on networks and storage. To effectively manage the experiment through real-time tomogram visualisation or ptychography visualisation will require near real-time reconstruction and streaming.

Advanced Data Analysis

Processing and analysis tools are an essential component in converting large data sets into scientific knowledge. For Diamond-II, we will work with the respective communities to identify new needs and opportunities, prioritise them, and work out strategies (including partnerships etc) to deliver improved tools. Some initiatives are already beginning through the Ada Lovelace Centre within STFC, but they will need to be scaled-up and focused on the needs of Diamond-II. Where appropriate, partnerships will extend to other facilities and beyond the UK user community.

An exciting emerging opportunity for data-rich science is Machine Learning. This is currently undergoing a revolution driven by advanced tools and readily available compute power. However, specific tools and processes need to be developed to integrate with science techniques, and data acquisition and analysis processes.

The processes of engagement, prioritisation, planning and pilot projects will need to run alongside other aspects of the longer-term programme of upgrades to the machine, beamlines and other infrastructure, if we are to deliver tools of immediate value when Diamond-II launches.

3.6.4. Data Catalogue and Archive

Diamond provides a catalogue and archive of all data taken from experiments during the life of the facility. As of February 2019 this holds 17 Petabytes of data and is expected to grow to ~70 petabytes by 2025. The technology of the current catalogue and archive will not accommodate the volume of data produced and changes in working practices envisaged by the move to Diamond-II. A new data catalogue and archive will have to be developed to support data volumes of 100's petabytes together with on-line rich meta-data to enable meaningful queries of data. The data catalogue and archive will form the basis of data analysis services, whereby datasets may be selected for interactive processing or processing using analysis pipelines in a cloud-based compute resource. The Experiment Data Management Policy will open up opportunities for data analysis and data mining through techniques such as Machine Learning from communities far beyond those originally conducting the experiment.

3.6.5. Computation Infrastructure

Diamond currently operates data centres of 500 kW combined capacity, providing around 5000 x86 cores of compute resource, 130 GPUs and 16 PB of high-performance storage. The network provides 1 Gb and 10 Gb Ethernet connections to detectors and workstations and 40 Gb Ethernet to the highest rate detectors. InfiniBand is used within the data centres and is being deployed to beamlines. A rolling programme of investment in the computation infrastructure will continue, however increases in data rates and volumes for Diamond-II will require a step change in the compute infrastructure.

It is expected that for Diamond-II computing and data management will be provisioned through a combination of in-house resource and external resource. The latter will be through initiatives such as STFC IRIS [4] and from commercial cloud providers and will be key to providing post-visit data processing services. For the first level storage and compute and real-time visualisation and analysis of data, compute and storage for data-heavy experiments would continue to be most effectively delivered on-site.

For Diamond-II a new data centre will be necessary with an anticipated capacity of ~3 MW. The network fabric from the data centre to the beamlines will be upgraded as will connections off-site. The new data centre would be fitted out with an initial deployment of compute and storage and filled by a rolling programme to meet demand.

References

[1] https://portal.slac.stanford.edu/sites/lcls_public/Documents/LCLSDataAnalysisStrategy.pdf.

[2] https://www.psi.ch/detectors/jungfrau.

[3] https://www.humanbrain project.eu/en/.

[4] https://www.iris.ac.uk/.

4. Implementation

4.1. Machine project schedule

4.1.1. Outline Project Schedule

4.1.1.1. Introduction

The outline project schedule (Figure 4-1) sets down the main tasks between the approval of the CDR (assumed to be June 2019) and the resumption of the full range on user operations in October 2026. The Gantt chart shows the major tasks and the important milestones. The major tasks are: Reference Design, Diamond-II Assembly Building, Storage Ring and Booster.

4.1.1.2. Reference Design

The Reference Design task will take place during the two-year period in which the TDR is being developed. In some cases, e.g. the girders, it is expected that a full detailed design will be produced by DLS staff during this time, and in others, e.g. vacuum vessels, it is expected that reference designs and procurement specifications will be produced by DLS staff to be included in calls for tender.

4.1.1.3. Diamond-II Assembly Building

The Diamond-II Assembly Building will host the building of the Storage Ring girders. It is considered that this building must be ready for the assembly of the prototype vacuum vessels and prototype girders at the end of December 2022. In order to achieve that, and allowing for reasonable time contingency, it may be necessary to start the design of the new building as early as January 2020.

4.1.1.4. Storage Ring

The detailed design of the Storage Ring will follow the completion of the TDR, and it is expected to last two years. The procurement for all Storage Ring components will start following the green light to start the execution of the project, marked by the milestone in December 2021. It is intended to build a prototype cell, that is two girders and two ID make-up assemblies. The prototype build will take place in the new Diamond-II Assembly Building, which will allow the equipment and processes to be fully tested, including girder and rack commissioning, bake-out, alignment and magnetic measurement. This will last nine months and precede the main girders build, which will last one year.

The installation is expected to start in April 2025 and last for one year. The outline project schedule shows a six-month contingency period between the completion of the procurement and girders build tasks and the start of the installation. An outline shutdown schedule is described below. The primary source of estimated durations is the 2016 Shutdown 4 planning schedule in which the DDBA components were installed in Cell 2.

The six-month commissioning task will start at the end of the installation task, and it is expected to comprise two parts: firstly commissioning of the Machine alone for three months, and then continuing for three months together with commissioning of the beamlines.

4.1.1.5. New Booster

For the New Booster it is proposed that the installation will be largely completed during shutdowns in advance of the Dark Period. It is also assumed that the Booster magnets will be procured from a single manufacturer who will provide the detailed design, followed by a production series of complete girder assemblies, as was done successfully for Diamond. In order for the Booster to be at least 80% installed in advance of the shutdown, with 6 months contingency, requires that a call for tender is opened as soon as the TDR is complete, i.e. April 2021.

4.1.2. Outline Shutdown Schedule

4.1.2.1. Introduction

The outline shutdown schedule (Figure 4-2) covers the period from the start of the Install stage and the start of beamline commissioning, a total period of roughly one year.

The shutdown schedule comprises seven overlapping stages: Completion of Installation of Diamond-II Booster Ring, Dismantle Diamond Storage Ring, Diamond-II Storage Ring Preparation, Install Diamond-II Storage Ring, Systems Commissioning, Booster Commissioning, Machine Commissioning and Beamline Commissioning. The estimates for the duration of work in the special straights, including the RF straight and the injection straight will be added as the schedule is developed.

4.1.2.2. Completion of Installation of Diamond-II Booster Ring

It is intended to complete approximately 80% of the Booster Ring installation in advance of the Dark Period. The remainder will be installed at the start of the shutdown and the stage will also include any modified Linac components, as well as the BTS. The stage is shown with a duration of six months; this relatively relaxed timescale is intended to reduce resource conflicts with the Storage Ring work.

4.1.2.3. Dismantle Diamond Storage Ring

The dismantling and removal of the current storage ring is expected to take about three months. The work will be done by opening the roof on two cells at a time, at opposite sides of the storage ring in order to minimise crane over-fly stopping work in a cell. Each cell will take about one week using two working shifts per weekday. This will require up to four separate teams from each group, with a team typically comprising three people. After one cell's roof is closed following dismantling and removal, the clockwise adjacent cell's roof will be opened.

4.1.2.4. Diamond-II Storage Ring Cell Preparation

The preparation work primarily comprises old cables removal, floor preparation and mechanical services installation (Part 1 - flow panels). This work will start in each cell after the roof has been replaced following the dismantling and removal of the Diamond components. Each cell is expected to take about 20 working days and the entire preparation work is expected to take about 6 months. Unlike the dismantling and removal work, it is anticipated the cell preparation work will be done during normal working hours.

4.1.2.5. Install Diamond-II Storage Ring

The work in each cell will start after the preparation work in that cell has finished. The outline schedule uses an estimate of 17.5 normal working days for install the girders and straights (and connection to the existing front ends). This is then followed by the installation of mechanical services (water and air), estimated at 5 days. The total duration is estimated at 10 months.

4.1.2.6. Systems Commissioning

Systems commissioning includes everything necessary to bring individual systems into operation, prior to beam commissioning, including controls and interlock testing. This will be carried out on a progressive cell-by-cell basis, commencing as soon as installation work in a given cell has been completed. A total of 25 working days has been allocated for each cell.

4.1.2.7. Booster Commissioning

Once the Booster has been completely installed and its systems commissioned, it is expected that commissioning the Booster with beam will start and continue for three months, so that it is ready well in advance of the commissioning of the Storage Ring with beam.
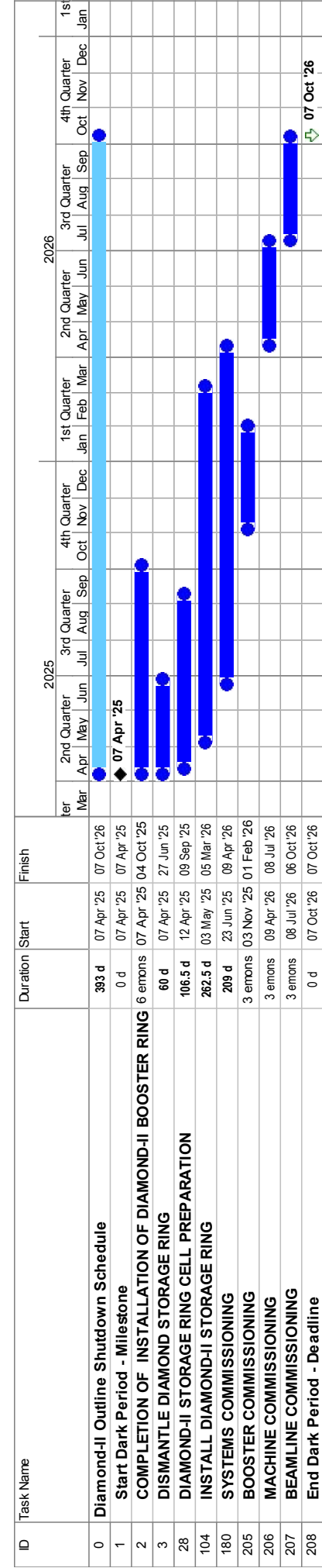
4.1.2.8. Machine & Beamline Commissioning

Beam commissioning will initially be dedicated to the machine for an estimated period of 3 months, until minimum performance targets have been met, at which point the remaining time will be shared between further machine commissioning, vacuum conditioning and beamline commissioning.

Figure 4-1 : Outline Machine Project Schedule.

ID	Task Name	Duration	Start	Finish
0	**D-II Machine Outline Project Schedule**	**1888 d**	**13 Jun '19**	**07 Oct '26**
1	CDR Approval - Milestone	0 d	13 Jun '19	13 Jun '19
2	REFERENCE DESIGN	21 emons	13 Jun '19	04 Mar '21
3	Project Approval - Milestone	0 d	31 Dec '21	31 Dec '21
4	**DIAMOND-II ASSEMBLY BUILDING**	**632 d**	**06 Jan '20**	**24 Jun '22**
5	DIAMOND-I ASSEMBLY BUILDING DESIGN	12 emons	06 Jan '20	31 Dec '20
6	DIAMOND-I ASSEMBLY BUILDING PROCURE	6 emons	31 Dec '20	29 Jun '21
7	DIAMOND-I ASSEMBLY BUILDING BUILD	12 emons	29 Jun '21	24 Jun '22
8	Diamond-II Building Complete - Milestone	0 d	31 Dec '22	31 Dec '22
9	Start of Dark Period - Milestone	0 d	07 Apr '25	07 Apr '25
10	**STORAGE RING**	**1618 d**	**06 Jul '20**	**29 Sep '26**
11	STORAGE RING DETAILED DESIGN	33 emons	06 Jul '20	23 Mar '23
12	STORAGE RING PROCUREMENT	33 emons	03 Jan '22	19 Sep '24
13	STORAGE RING PROTOTYPE COMPONENTS BUILD	9 emons	02 Jan '23	29 Sep '23
14	STORAGE RING GIRDERS BUILD	12 emons	01 Oct '23	25 Sep '24
15	STORAGE RING INSTALL	12 emons	07 Apr '25	02 Apr '26
16	STORAGE RING COMMISSIONING	6 emons	02 Apr '26	29 Sep '26
17	**BOOSTER**	**1282 d**	**04 Mar '21**	**01 Feb '26**
18	BOOSTER TENDER & SELECTION	3 emons	04 Mar '21	02 Jun '21
19	BOOSTER DESIGN & MANUFACTURE	24 emons	02 Jun '21	23 May '23
20	PARTIAL BOOSTER INSTALL	24 emons	24 Nov '22	13 Nov '24
21	PARTIAL BOOSTER SYSTEMS COMMISSIONING	16.67 emons	19 Nov '23	02 Apr '25
22	BOOSTER INSTALLATION COMPLETION & SYSTEMS COMMISSIONING	6 emons	07 Apr '25	04 Oct '25
23	BOOSTER COMMISSIONING	3 emons	03 Nov '25	01 Feb '26
24	User Beam Resumes - Milestone	0 d	07 Oct '26	07 Oct '26

Figure 4-2 : Outline Shutdown Schedule.

ID	Task Name	Duration	Start	Finish
0	**Diamond-II Outline Shutdown Schedule**	**393 d**	**07 Apr '25**	**07 Oct '26**
1	**Start Dark Period - Milestone**	**0 d**	**07 Apr '25**	**07 Apr '25**
2	**COMPLETION OF INSTALLATION OF DIAMOND-II BOOSTER RING**	6 emons	07 Apr '25	04 Oct '25
3	**DISMANTLE DIAMOND STORAGE RING**	**60 d**	**07 Apr '25**	**27 Jun '25**
28	**DIAMOND-II STORAGE RING CELL PREPARATION**	**106.5 d**	**12 Apr '25**	**09 Sep '25**
104	**INSTALL DIAMOND-II STORAGE RING**	**262.5 d**	**03 May '25**	**05 Mar '26**
180	**SYSTEMS COMMISSIONING**	**209 d**	**23 Jun '25**	**09 Apr '26**
205	BOOSTER COMMISSIONING	3 emons	03 Nov '25	01 Feb '26
206	MACHINE COMMISSIONING	3 emons	09 Apr '26	08 Jul '26
207	BEAMLINE COMMISSIONING	3 emons	08 Jul '26	06 Oct '26
208	**End Dark Period - Deadline**	0 d	07 Oct '26	07 Oct '26

4.2. Logistics

4.2.1. Overview

The over-arching principle for the logistics of Diamond-II is that the 'dark period', the length of time that the Users are without light, must be as short as possible.

Considering this principle against many years' experience of variable and extended lead-times from suppliers on other projects drives a conclusion that as much equipment as possible for Diamond-II must be procured, assembled and tested before the long shutdown starts. In particular, all of the storage ring sub-assemblies (girders) must be pre-built and in store ready for installation before the shutdown commences. For the new Booster, pre-assembled girders will be installed in the Booster tunnel during Diamond shutdowns over a period of 2 years before the dark period.

4.2.2. Support Buildings for Storage and Preparation

4.2.2.1.Storage Ring Girders

Based on experience with the successful DDBA project which replaced one DBA cell of Diamond with a 4 bend Double-DBA, it is anticipated that the 24 cell Diamond-II storage ring will comprise 48 girder structures of approximately 7.5 m in length. A minimum area of 1 m * 10 m would be required per girder to allow access for lifting as well as temporary pumping, which would lead to a storage space of approximately 500 m^2.

The girder lengths add up to 360 m, which leaves 130 m of other vessel assemblies to complete the storage ring and 70 m of IDs which will be stored separately. Given similar packing density, then storing these other vessel assemblies will require a further 200 m^2.

Storing completed girders and vessel assemblies therefore requires 700 m^2. This space could be provided in temporary buildings on the site or by renting suitable storage space off-site (noting that the ESRF successfully stored built girders 25 km from their site). A cost benefit analysis of the two approaches will be carried out.

Vessel vacuum processing, magnet alignment and girder assembly tasks required 500 m^2 for Diamond in assembly building R79. However, for Diamond-II with longer girders, capacity to build two storage ring cells simultaneously and given the more exacting magnet alignment tasks, an estimate of 1250 m^2 is proposed based on the ESRF assembly building and a layout is shown in Figure 4-3.

Of course, components need to be delivered and stored before processing and assembly. To a first approximation, the same areas will be required again to receive and store vessels and magnets for the storage ring. Hence, 800 m^2 for all the vessels and 500 m^2 for storage ring magnets, 500 m^2 for the bare girders. Other components such as stands, pumps, gauges, etc, could easily add up to a further 200 m^2 so in total 2000 m^2 is estimated. However, girder assembly will commence as soon as there are enough components to allow it so the total 'goods in' space required will reduce to fit with supplier delivery schedules. Components can also be stacked in boxes to reduce the square area required. ESRF experience suggests that packing box size and load carrying capacity should be specified in the tender specification so that components from different suppliers can be easily stacked. If these combined factors were 35% then 700 m^2 will be required for storage ring components 'goods in' inspection and store prior to assembly. This space would be required on-site.
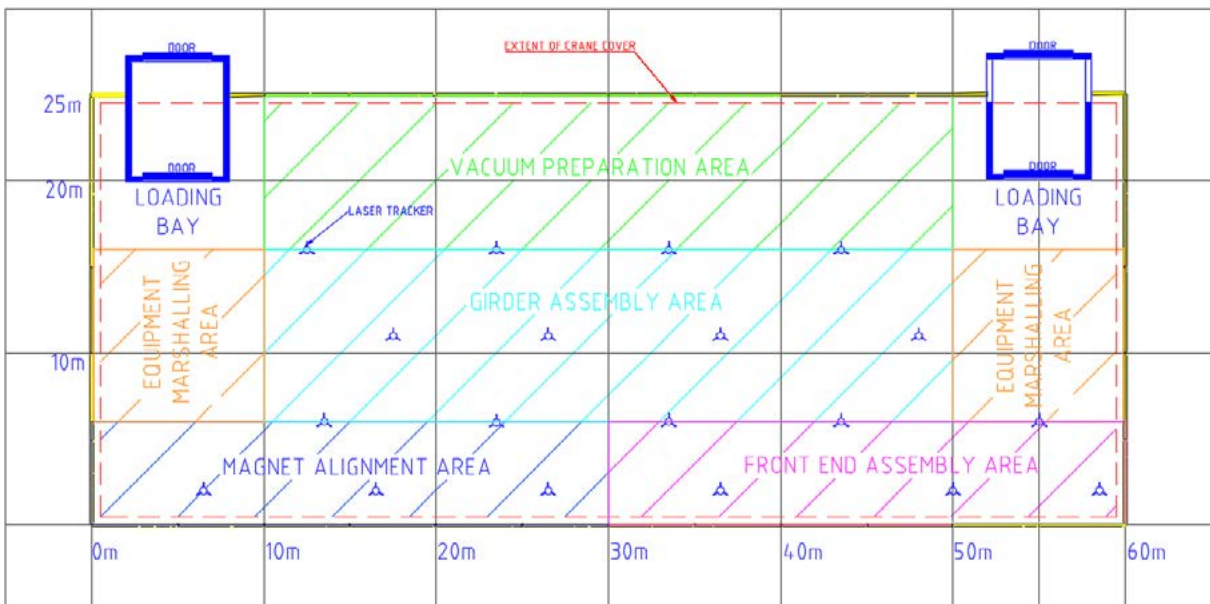
Figure 4-3 : Diamond-II Assembly Building Layout.

4.2.2.2. Storage Ring Control Racks and Magnet Power Supply Racks

The storage ring control system and magnet power supplies will also need significant space to allow new racks to be built before the shutdown. The current 24 Control and Instrumentation Areas (CIAs) devoted to the storage ring are each 5 m x 10 m and so add up to 1200 m^2 in total. There are typically 24 racks per CIA and it is expected there will be a mixed economy of some racks modified in-situ such as for Front Ends and Insertion Devices (IDs), some racks unmodified such as PSS and others completely rebuilt such as magnet power supplies. Given this approach, the same area of 1200 m^2 should be sufficient to manage goods in, assembly and test as well as final storage. Industry is well equipped and able to build control racks to a Diamond design and specification and as much of this work should be sub-contracted as possible to reduce the staff effort and storage space at Diamond.

4.2.2.3. Front Ends

The vast majority of ID front ends will stay in-situ whilst Diamond is removed and Diamond-II installed around them. Initial analysis confirms that the majority of existing absorbers and shutters are suitable for use in Diamond-II. If any absorbers are to be changed then this can be done during preceding Diamond shutdowns. All the cables and will be stripped out and replaced as part of Diamond-II.

The Bending Magnet (BM) front ends will need more significant modification as these beamlines are changing from a BM source to an ID source as well as a shift in source position of some 200 mm and 15 mrad. Front ends are currently built and tested at the supplier and then re-built, baked and aligned at Diamond before installation. Allowing sufficient space for say 6 front ends to be assembled at once will require 20 m x 25 m = 500 m^2 of quality, clean and temperature controlled space but as it is highly likely that they will be delivered in a phased way, two at a time, hence a front end assembly and test area will reduce to 200 m^2.

4.2.2.4. Insertion Devices

The majority of the IDs will stay in-situ in the tunnel; these are mainly in-vacuum devices, plus the two superconducting wigglers. With suitable protection to each ID new girders for Diamond-II can be installed either side of the existing IDs.

Approximately ten Insertion devices will be removed either because they can no longer be physically accommodated or a change in parameters is needed, or both. Storage space for 10 IDs is estimated at 100 m^2.

The new mid-straights will require a range of new IDs and will require cabling and plumbing to suit as well as CIA rack installations. These services can be supplied through the existing girder 2 trench as shown in the case of DDBA.

R79 girder build area (500 m²) and ID area (300 m²) could be devoted to ID goods in, inspection, assembly clean, build, test and storage of complete IDs.

Consideration will be given on how to supply LN2 to the new mid-straight positions where CPMUs will be installed.

4.2.2.5. Booster

A new booster will be installed in the existing tunnel alongside the existing ring over a number of Diamond- shutdowns commencing up to 2 years before the dark period. The temporary buildings could be used to store Booster components and girders before the Storage Ring components require the space. Pipework, cables and control racks would be installed as well, connections made and low level commissioning carried out on fluid flow and electrical polarity, etc. There are a number of rack positions available in existing CIAs and one further CIA will be constructed. The new booster could then be partially commissioned without beam as an 80% complete ring before the Diamond-II storage ring shutdown starts. It is not planned to inject into the Diamond storage ring because of the complexity of rearranging Linac to Booster (LTB) and Booster to Storage Ring (BTS) transfer lines. Once the dark period commences, the LTB and BTS transfer lines can be connected and the ring completed, allowing commissioning with beam to commence. The new booster can be fully commissioned in the early months of the dark period whilst the storage ring is being removed which allows very good use of RF and Accelerator Physics teams.

4.2.2.6. Beamlines

Since it is planned to construct up to 3 replacement beamlines before the dark period, in addition to the significant modifications for many beamlines that will need to be prepared in advance, it will be necessary to provide 800 m² of temporary build space external to the main building.

4.2.2.7. Diamond Removal

When the shutdown commences all 3 cranes will be involved opening sections of the storage ring roof to expose a complete cell. The total number of roof beams is 1536 with the heaviest weighing 17.6 T and the lightest 7.3 T. They are all individually numbered and are installed in 2 overlapping layers. As the roof beams are removed, they are normally stacked 2 deep either side of the opening.

Stacking roof beams on the roof has the advantage of keeping the foundations loaded thereby reducing risk of the ground relaxing. Also, the journey times of lifting and removing 1536 roof beams in and out of the building to store and back are prohibitive.

Whilst the roof is being opened the Diamond storage ring will be vented and all power supplies isolated. Cooling circuits will be isolated at tunnel labyrinths and drained up to and including the girders. All cables will be disconnected and removed apart from PSS cables, protected in dedicated trunking.

The girders will then be removed by the overhead cranes and transferred to waiting tractor and trailer units and removed from site by the scrap metal contractor who will be responsible for all subsequent dismantling and segregation of metals and recycling. This is the best way to avoid double handling and further storage area. If this cannot be achieved, then an external laydown area of 700 m² will be required to store redundant girders. There is no need to provide cover but it should be within a secure site. It is NOT anticipated that any vacuum equipment, pumps, valves, gauges, diagnostics or MPS equipment will be recovered. However until this is finally agreed a budget space of 200 m² under cover is allowed for.

The girder pedestals may be re-used depending on the design of Diamond-II supports so the current plan is to store them. The motorised movers are not to be re-used and will be removed and scrapped. Pedestal floor plates can be recovered from the floor and re-used.

4.2.2.8. Support Workers

It is estimated that around 100 contract staff will be required to carry out removal and installation tasks over an 18 month period. To provide welfare facilities for these people and office space for supervisors will require 500 m² over 2 floors.

Table 4-1 : Summary of Support Building Areas. (DAB = Diamond-II Assembly Building.)

Building	Purpose	Size m²	Type
1	Vessel clean, bake and Girder assembly	1250	Permanent DAB
2	Storage of delivered components	700	Temporary
3	Front End assembly, bake and test	200	Permanent DAB
4	Temporary storage of assembled girders	700	Off-site
5	Control & magnet PSU racks build space	1200	Temporary
6	Workers' facilities (100 people)	500	Temporary
7	Storage of dismantled components	200	Temporary
8	Storage/dismantling of Diamond girders	700	Open air
9	Entrance points to the building	0	Existing
10	Insertion Devices assembly build and test	650	Existing R79
11	Store Insertion Devices	100	Existing R79
12	Beamline build space	800	Temporary

4.2.2.9. Site Layout

The combination of support building areas both new and existing, permanent or temporary and suggested locations are summarised in Table 4-1 and on a site plan shown in Figure 4-4. The total size is 6950 m², compared to the total for the ESRF-EBS project of 7710 m² excluding RF & Beamline Build Space.
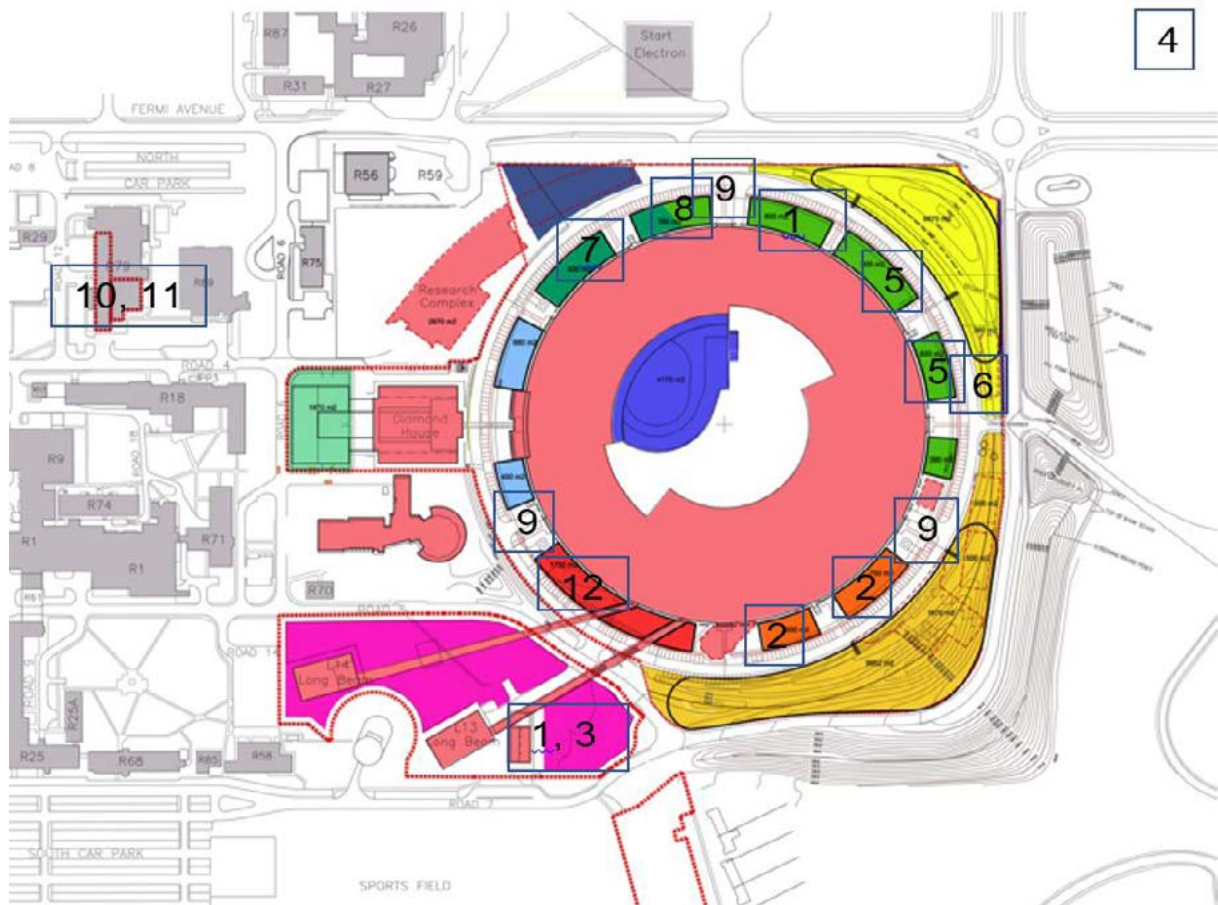

Figure 4-4 : Location of Support Building Areas.

4.3. Services

The following modifications to services will be needed:

4.3.1. Booster Services Modifications

New Booster CIAs will be constructed to serve the new Booster and these will be built during available shutdown periods prior to the 'dark' period of Diamond-II.

New cabling installations and modifications to the process cooling water circuits and electrical supply systems will also be carried out during these shutdown periods.

Once the new Booster is operational, redundant cabling and pipework will be removed and the redundant CIAs converted into storage rooms.

The air conditioning and ventilation system for the Booster will remain unaltered.

4.3.2. Storage Ring Services Modifications

The Diamond-II Machine will be more energy efficient than the current Machine and therefore no major upgrades are envisaged for process cooling water or the electrical infrastructure servicing the Storage Ring.

However, due to the reduced heat load, there may be a requirement to install heat exchangers in each of the ten Storage Ring Air Handling Units to maintain environmental conditions.

Reconfiguration of the respective process cooling water and electrical supply systems will be required to serve modifications to the radio frequency systems where superconducting cavities and IOT amplifiers are to be replaced with normal conducting cavities and solid state amplifiers.

4.3.3. External Manpower/Agency Resource

As with the build of the current Machine, a significant amount of external manpower will be required to provide adequate resourcing for the construction phase of the programme. There will be three main packages of work, namely:-

Pipework: for modifications required to reconnect the new Booster and Storage Ring components to the existing infrastructure. A 'pipework contract' will be awarded for this work.

Electrical: for the new cabling and terminations to reconnect the new Booster and Storage Ring components to new racks within CIAs. This work will be carried out by staff supplemented with agency resource.

General manpower resource: providing an external resource (i.e. electricians, fitters, crane operators, etc.) to supplement staff effort for Diamond-II. A 'manpower contract' based on a 'call off' process will be awarded for this work.

Space has been allocated for contractor accommodation and hygiene facilities for ~100 people (see Section 4.1). The exact contract requirements will be defined during the TDR stage.

4.4. Radiation Safety

The current Diamond storage ring and beamlines are shielded to run at an energy of 3.0 GeV and a stored current of 500 mA. This Section assesses if the current shielding will be adequate for Diamond-II which will run at an energy of 3.5 GeV and 300 mA stored current.

For the assessment we will use the current dose constraint of 1 mSv/year, the justification for this is set out in TDI-HP-GEN-PRO-0003[*].

4.4.1. Sources of Ionising Radiation in Diamond-II Accelerators

There are several processes that produce ionising radiation within the booster, storage ring, and beamlines.

4.4.1.1. Electron Losses

High energy electrons can impact parts of the machine they strike, this sets off an electromagnetic cascade of Gamma and Neutron radiation, which dominates the shielding requirement.

Electrons are lost in a number of ways:

- Beam dump, these can be intentional i.e. beam dump prior to machine development, or unintentional i.e. RF trip.
- Losses of the stored beam due to finite lifetime.
- During injection, and extraction from the booster, because of less than 100% injection/extraction efficiency.

4.4.1.2. Gas Bremsstrahlung

When high energy electrons interact with residual gas molecules within the vacuum vessel they emit high energy X-rays up to the energy of the incident electron. The X-rays are highly focused in the direction of travel of the electrons, this therefore dominates in the calculation of the thickness of the front end shutters and to a lesser extent, the upstream ratchet wall.

4.4.1.3. Synchrotron Radiation

This is produced when electrons pass through a bending magnet or insertion device, the direction of the X-rays is tangential to the electron trajectory.

In beamline optical hutches shielding is defined by the Gas Bremsstrahlung and synchrotron radiation, in experimental hutches shielding is defined by synchrotron radiation only. A full assessment is ongoing, but a summary of the work done so far is given below.

4.4.1.4. Activation

High energy electrons can induce radioactivity in parts of the machine that they strike. The current procedures for protecting against exposure from activation products should be sufficient for Diamond-II. This is not a hazard to anyone outside of the shielding and is not considered further in this document.

---

[*] TDI-HP-GEN-PRO0003 Strategy for the Implementation of Radiation Safety Legislation at Diamond

4.4.2. Assessment Methods

4.4.2.1. Electron Losses

We have calculated the dose outside the storage ring and booster shielding using the equations contained in the modelling code SHIELD 11[**] .SHIELD11 is a computer code for shielding analysis around high energy electron accelerators developed by Stanford Linear Accelerator Centre (SLAC). It takes inputs of beam parameters and shielding thicknesses and dimensions, it then outputs dose rates for Neutron (three different energy ranges), direct gamma, and indirect gamma outside the shielding at specified points. For convenience we have taken the equations used in the code and developed an Excel version for the Diamond-II shielding calculations.

4.4.2.2. Gas Bremsstrahlung

The shielding requirement is calculated using several methods:

1. Known expressions, used in other accelerators and synchrotrons to assess photon fluxes and thus shielding requirements. Holbourn[***].

2. Established computer-modelling codes, used in other accelerators and synchrotrons to calculate the dose rate in a semi-empirical manner. Tromba and Rindi[****], Ipe[*****].

3. Monte Carlo modelling using FLUKA (use of this method is in the early stages and is not used for the calculations in this document).

Several expressions in published papers were compared and the average shielding thickness taken. Some assumptions have been made as the quantities required in the expressions are not currently known. These include vacuum pressure and residual gas composition.

4.4.2.3. Synchrotron Radiation

The shielding requirement for beamlines is calculated using a Fortran code developed at SPRING 8 called STAC8. By inputting machine, ID, mirror, filter, and shielding parameters the dose rate at any point on the outside of the shielding can be calculated. A trial and improvement method is used to calculate how much shielding is needed to reduce the instantaneous dose rate to <0.5 μSv/h (1 mSv per 2000 hour working year).

4.4.3. Results

4.4.3.1 Storage ring

Table 4-2 shows the current shielding thickness of the storage ring concrete walls and roof. Annual doses outside of the shielding due to electron loss have been calculated using the SHIELD11 code. The dose rates are calculated at a number of angles from the loss point, the dose rate stated below is highest out of all the angles calculated. We have assumed that the machine will run for 5160 hours per year and the total electron loss over the run time is 1.54×10^{16} (corresponding to 8.27×10^{8} electrons/s). We have calculated the average annual dose for both the machine run time and a typical 2000 hour working year. The target dose rate is <1 mSv per year.

[**] The SHIELD11 Computer Code.
[***] Holbourn, M. P. Gas Bremsstrahlung Measurements at the ESRF, 1994.
[****] Tromba, G and Rindi, A. Gas Bremsstrahlung From Electron Storage Rings: A Monte Carlo Evaluation and Some Useful Formulae. Nuclear Instruments and Methods in Physics Research A292, 1990.
[*****] Ipe, N and Fasso, A. Impact of Gas Bremsstrahlung on Synchrotron Radiation Shielding at the Advanced Photon Source. SLAC-PUB-6410, 1994.

Table 4-2 : Storage ring wall shielding and dose distribution.

Location	Current material thickness (mm)		Occupation (2000 hrs)	Machine run time (5160 hrs)
Storage ring shield wall	Ordinary concrete	Barytes concrete	Total (mSv/y)	Total (mSv/y)
Inner wall	1250		0.0043	0.01
Side wall		950	0.0325	0.08
End wall		1550	0.0000	0.00
Roof	1430		0.0054	0.014

4.4.4. Booster

4.4.4.1. Booster Wall

The booster is also undergoing a change of design, not only will the maximum electron energy increase to 3.5 GeV, the booster circumference is increasing. As it will be housed in the existing shielding, the vacuum vessel will be closer to the shield wall.

We estimate only a factor 2.8 times more loss in the Diamond-II booster than the current Diamond booster; calculated doses are in Table 4-3 below.

Table 4-3 : Booster wall shielding and dose distribution.

Location		Current material thickness /mm ordinary concrete	Total annual dose (mSv/y)
Booster	Outer wall	1900	0.010
	Roof	2050	0.012

The figures above were calculated using a larger loss rate than the current estimate, so the existing shielding will be adequate, which is consistent with the fact that it is rare that any dose outside the booster is recorded.

4.4.4.2. Booster to Storage (BTS) ring shutter

So that the storage ring can be entered when the booster is running, a shutter is in place in the booster enclosure on the BTS line. Electrons are deflected away from this shutter into the Faraday cup if they are not injected into the storage ring. This shutter will need to stop gas bremsstrahlung that will be generated in the BTS line. Table 4-4 shows that the current thickness of the shutter exceeds the requirements for Diamond-II.

Table 4-4 : BTS shutter thickness. Material is Mallory 1000, a tungsten alloy.

Straight Section leading to BTS shutter	Current thickness (mm)	Diamond-II required thickness (mm)
8.6 m	316	271

The above calculations will be checked against the final booster design in the TDR phase.

4.4.4.3. Port/Optics Shutters

Port/optics shutters or front end shutters are located at the downstream end of the front end, each shutter can operate independently. The thickness required is dominated by gas bremsstrahlung.

Table 4-5 shows the current thickness and the minimum thickness required for Diamond-II for the various ID straight lengths.

Table 4-5 : Port/Optics shutter thicknesses. Material is Mallory 1000, a tungsten alloy.

Diamond, bending magnet or ID straight length	Diamond current thickness (mm)	Diamond- II bending magnet to bending magnet length	Diamond-II required shutter thickness (mm)
Bending magnet	180	3.95 m	271
18.581 m	316	6.59 m	279
15.581 m		9.59 m	286

Front end shutters on all ID beamlines are therefore adequate for Diamond-II. In the case of bending magnet beamlines however, the majority, or possibly all, will move to insertion devices located in the new mid straights, and therefore will require an upgrade of the shutters.

4.4.5. Beamline shielding

Calculations of beamline shielding is currently incomplete as not all the information required for the calculations is currently available.

4.4.5.1. Optics Hutches

The lead thicknesses required to reduce the dose rate to below 1 mSv/y in Diamond-II are shown in Table 4-6. All existing Optics hutches on insertion device beamlines have been built to '9.5 m straight' specifications, and therefore require no modification, with the following exceptions. I19 and I24 have reduced thickness optics hutches as canting has been used, if canting is not employed on Diamond-II this may need to be increased. The superconducting wiggler beamline I12 needs some additional shielding to that stated above and it is anticipated that I15, also a superconducting wiggler beamline, will also need additional shielding; calculations have not yet been finalised.

Table 4-6 : Optics hutch shielding required for the three lengths of ID straight in Diamond-II.

Location	Lead thickness required for Diamond-II (mm)		
	9.59 m straight	6.59 m straight	3.95 m straight
End wall	50	43	31
Additional lead 1m² around beampipe	50 (100 total)	15 (58 total)	13 (44 total)
Lateral wall	30	18	10
Roof (assuming 2.6 m above beampipe)	10	10	8
GB collimator/stop thickness (Mallory 1000)	286	279	271

The current shielding on bending magnet beamlines is 8 mm lead for all walls and roof, with an additional 25 mm around the beam pipe. All bending magnet beamlines that move to an insertion device on the new mid straights will therefore require additional shielding on the end wall, lateral wall and beam pipe.

The required thickness of the collimators and stops are listed above. All existing GB collimators/stops in insertion device beamlines and B16 are thicker than '9.5 m straight' specifications, and therefore require no modification. B24 has 370 mm thick Bremsstrahlung stops in the front end. The current thickness on all other bending magnet beamlines is 180 mm and so all beamlines that move to an insertion device on the new mid straights will require thicker GB collimator/stops.

All other dimensions of GB collimators and their location will be determined by ray trace.

4.4.5.2. Experimental Hutches

Experimental hutch shielding is calculated on a case-by-case basis and is dependent on not only the machine parameters but also the insertion device, mirrors, and hutch dimensions. Calculations have not been concluded, as specifications have not been finalised.

Based on what has been done so far the current shielding of most experimental hutches is sufficient for machine operation at 3.5 GeV, 300 mA. The shielding was originally calculated for 3 GeV and 500 mA.

Some beamlines with more powerful insertion devices will need thicker experiment shutters of the order of a few mm.

As with its optics hutch I12 will need thicker shielding in some areas. It is anticipated that I15 will also need additional shielding. Calculations have not yet been finalised.

4.4.6. Conclusions

The results above show that the current concrete shielding for the storage ring and booster is adequate for operation at 3.5 GeV and that most shutter thicknesses are also adequate to shield the highly penetrating Gas Bremsstrahlung X-rays.

Most beamlines will not need any additional shielding.

Many factors can affect the intensity of the scattered radiation. While simulations have been shown to predict dose rates to a fair degree of accuracy, certain factors cannot be predicted. Of particular concern is the level of vacuum in long narrow insertion device (ID) straights of the storage ring. For these calculations, a vacuum of 10^{-8} mbar has been used. The vacuum will be worse than this during the initial conditioning of the machine until several ampere hours have elapsed. In the early stages, whilst the storage ring is undergoing conditioning, it will be necessary to run the machine with the shutters closed and to possibly restrict access to synchrotron building until sufficient experience has been gained of the machine's performance. The machine is likely to require several tens of ampere-hours of conditioning before the vacuum has reached an adequate level to permit the port shutters to be opened without producing excessive radiation. Health Physics will need to perform extensive measurements once the machine starts operation to ensure that radiation levels are kept As Low As Reasonably Practicable (ALARP).

Further work to be carried out during the TDR phase is as follows:

- **Monte Carlo Models**

  To confirm the above calculations we are developing a Monte Carlo model of Diamond-II using MCNP (Monte Carlo N-Particle Transport Code).

We have also started modelling the various interactions using FLUKA (Monte Carlo code developed by CERN).

- **Beamline Shielding**

  Continue with calculation of the adequacy of the current beamline shielding as new ID and mirror specifications are submitted.

- **Ray Tracing**

  Ray tracing will need to be performed on all front ends and beamlines to ensure sufficient gas bremsstrahlung and synchrotron radiation collimation.

- **Environmental Impact Assessment**

  An assessment will need to be made of the potential for activation of the air, cooling water and ground water. This was done for Diamond and will be repeated for Diamond-II using the new machine parameters.

KCI KONECRANES   20t

11

EXPERIMENTAL HALL